Investigating the representation of smoke and its implications for air quality and climate

by

Thérèse (Tess) Carter

Sc.B. in Chemistry, Brown University, 2016

Submitted to the Department of Civil and Environmental Engineering in partial fulfillment of the requirements for the degree of

Doctor of Philosophy in Civil and Environmental Engineering

at the

Massachusetts Institute of Technology

September 2022

Signature of Author:……
Department of Civil and Environmental Engineering
August 12, 2022

Certified by: ……...……...
Colette L. Heald
Professor of Civil and Environmental Engineering
And Earth, Atmospheric, and Planetary Sciences
Thesis Supervisor

Accepted by: …….
Colette L. Heald
Professor of Civil and Environmental Engineering
And Earth, Atmospheric, and Planetary Sciences
Chair, Graduate Program Committee

Investigating the Representation of Smoke and its Implications for Air Quality and Climate

by

Therese S. Carter

Submitted to the Department of Civil and Environmental Engineering on August 12, 2022, in partial fulfillment of the requirements for the degree of Doctor of Philosophy in Civil and Environmental Engineering

Abstract

Smoke from biomass burning (both wildfires and prescribed and agricultural burns) is important for atmospheric chemistry and composition, air quality, and climate. These impacts are associated with substantial societal implications such as large detrimental health burdens, lost work and school days, and diminished visibility and ability to use the outdoors. However, there are large uncertainties in the magnitude and characteristics of smoke, stemming from considerable unknowns in all parts of the fire system, and thus in our representation of this in models. This thesis aims to address many of these uncertainties with a multipronged approach using models and observations across scales.

The scope of the research completed herein is introduced and described in Chapter 1. Chapter 2 focuses on how smoke emissions uncertainties carry through to air quality and radiative impacts with an emphasis on North America using four commonly used smoke inventories, a chemical transport model, and observational constraints, including surface networks, aircraft, and satellites. We show that two of the inventories (GFED4s and GFAS) direct the model closest to observations. While most air quality and climate studies only use one smoke inventory, we find that there is a large range across the inventories in health-relevant surface smoke concentrations and climate-relevant direct radiative effects. Chapter 3 investigates carbonaceous aerosol and its absorption properties from fires in two large fire source regions, the western US and Africa, using observations from three aircraft campaigns focused on fires. We find that smoke from African fires is more absorbing than that in the western US and thus that global climate models need to represent regional heterogeneity in absorption properties. We also show that a 1-day whitening lifetime of brown carbon matches observations well and substantially decreases the warming contribution of biomass burning. Chapter 4 expands the model representation of non-methane organic gases (NMOGs) from fires and investigates how important fires are for atmospheric reactivity. This is the first global estimate of the impact of fire on atmospheric reactivity. Chapter 5 focuses on two quantifiable human levers (human-ignited wildfires and agricultural fires) on smoke particulate matter under 2.5 microns in the US. We calculate that these two human drivers account for over 80% of important health metrics (population-weighted exposure and premature mortality) associated with fires, suggesting large mitigation potential of smoke impacts. Finally, Chapter 6 summarizes the work completed in this thesis.

Thesis Supervisor: Colette L. Heald
Title: Professor of Civil and Environmental Engineering and Earth, Atmospheric, and Planetary Science

Acknowledgements

I want to thank my family and friends for all that they have done to make this PhD happen.

There were several educators and mentors who led me in this direction that I would like to thank:

Scott Morris, my high school chemistry teacher, for making science fun and for providing my first research experience.

Glynis Lough, my first boss on the National Climate Assessment, for showing me what cool things one can do with an atmospheric chemistry PhD beyond academia.

Meredith Hastings, my undergrad research mentor, for her never-ending support in science, policy, and beyond.

Colette Heald, my PhD advisor, for inspiring me to be a better scientist and for her support and guidance throughout my PhD.

Table of Contents

Chapter 1 Introduction *6*

Chapter 2. How emissions uncertainty influences the distribution and radiative impacts of smoke from fires in North America *9*

Chapter 3. Investigating Carbonaceous Aerosol and its Absorption Properties from Fires in the western US (WE-CAN) and southern Africa (ORACLES and CLARIFY) *49*

Chapter 4. An Improved Representation of Fire Non-Methane Organic Gases (NMOGs) in Models: Emissions to Reactivity *90*

Chapter 5 Large mitigation potential of smoke $PM_{2.5}$ in the US from human-ignited wildfires and agricultural fires *115*

Chapter 6. Conclusions and Implications *129*

References *136*

Appendix 1. Supplement to Chap. 2: How emissions uncertainty influences the distribution and radiative impacts of smoke from fires in North America *160*

Appendix 2. Supplement to Chap. 3: Investigating Carbonaceous Aerosol and its Absorption Properties from Fires in the western US (WE-CAN) and southern Africa (ORACLES and CLARIFY) *171*

Appendix 3. Supplement to Chap. 4: An Improved Representation of Fire Non-Methane Organic Gases (NMOGs) in Models: Emissions to Reactivity *174*

Appendix 4. Supplement to Chap. 5: Large mitigation potential of smoke $PM_{2.5}$ in the US from human-ignited wildfires and agricultural fires *184*

Appendix 5. A brief investigation of using fire temperature from a geostationary satellite to parameterize fire volatile organic compound emissions *191*

Chapter 1 Introduction

Fires have occurred on earth over the last several millennia, increasing and decreasing in response to different natural and human factors. Three major factors control fires and their extent: ecosystem productivity (fuel), climate (e.g., fire weather or wet vs. dry conditions and ignition potential), and humans (colonization; land use; industrial, agricultural, and domestic combustion; fire suppression; and fire ignition) (Bowman et al., 2011). The relative importance of these drivers has changed over time, and climate, land use, and demography will all impact future fires. For example, Kloster et al., (2012) showed that overall global future (2075-2099) fire emissions will increase by 17-62% with climate responsible for increases of 22-66%; harvest and land use for decreases of 5-20%; human ignition for increases of 20%; and fire management (suppression) for decreases of 6%.

Fires (wildfires as well as prescribed and agricultural burns) emit a large suite of both primary gas and particle phase chemicals into the atmosphere, including CO, CO_2, NO_x, volatile organic compounds (VOCs), black carbon (BC), and primary organic aerosol (POA). Many of these species can then react with each other to form secondary pollutants, ozone (O_3) and secondary particulate matter under 2.5 microns ($PM_{2.5}$). The magnitude and properties of many of these emitted and formed species remain challenging to fully capture because they depend on underlying fuel and fire type.

Smoke (which comprises a complex mixture of these chemicals) impacts air quality, health, climate, and beyond (e.g., visibility, the economy, and our ability to use the outdoors). Because of their small size and associated ability to lodge deeply in lungs, $PM_{2.5}$ can have significant health impacts (respiratory infections, asthma, cardiovascular disease, and lung cancer) (e.g., Pope and Dockery, 2006; Brook et al., 2010), especially the high levels of $PM_{2.5}$ from fires (Liu et al., 2015a; Reid et al., 2016; Williamson et al., 2016). Ozone can cause similar respiratory health problems and, in particular, aggravate asthma especially in vulnerable populations (CDC, 2022). Fire $PM_{2.5}$ can also impact the climate system via absorbing and scattering radiation (Bond et al., 2013); BC deposition on ice lowers the surface albedo; and gases from fires (e.g., CO_2, CO, and CH_4) can lead to warming.

However, nearly all components of the fire system in addition to their subsequent impacts are uncertain. The modelling of fires themselves is complex, including their prediction, detection, and spread (Pham et al., 2020); risks associated with wildfire drivers and impacts (Oliveira et al., 2021); and interactions with the atmosphere (Bakhshaii and Johnson, 2019). The advent of satellites has provided much finer spatial and temporal scale observations of fire activity, burned area, and other indirect fire variables globally in the last several decades (van der Werf et al., 2017). This has enabled the development of global smoke emissions inventories for use representing smoke in air quality and climate models. Fires and their smoke are a global problem with regional differences and effects, and so this work attempts to bridge scales and provide insights that are globally relevant and regionally specific as appropriate.

Both the air quality and climate research communities need to represent fires and the resulting smoke accurately. However, uncertainties abound, and most studies do not use observations to constrain the model that they then use to inform decision making. Most air quality studies rely on only one smoke emissions inventory without considering the implications of their choice. The assessment of the radiative forcing impacts of fires relies on the attribution of human vs. natural fires, which is complex and challenging to quantify. The Intergovernmental Panel on Climate Change reports prior to the most recent, the Sixth Assessment Report (AR6), only used one stitched together fire inventory. Using this one fire dataset, the IPCC estimated that the biomass burning component of aerosol radiative forcing hovers right around zero but with large uncertainty bars (Intergovernmental Panel on Climate Change, 2014). For AR6, a fire modeling intercomparison systematically compared a number of models, providing a better representation of the uncertainty in emissions (Rabin et al., 2017). In addition, the underlying models used in the IPCC generally do not consider that a subset of POA (brown carbon or BrC) can absorb incoming radiation, leading to potentially additional warming. Field observations suggest that this BrC can photochemically whiten in the atmosphere, but this is poorly understood. While we know that fires emit a complex mixture of organics, chemical transport models (CTMs) typically include a very limited subset of fire emissions – limited by both knowledge of their emissions and their chemical fate in the atmosphere. The limited representation of NMOGs suggests that models are likely unable to capture secondary pollutant formation (i.e., O_3 and SOA) from fires. In this dissertation, we use models (smoke inventories; a global chemical transport model,

GEOS-Chem; and a radiative transfer model, RRTMG) and observations across scales (lab experiments, surface networks, aircraft and tower campaigns, and satellites) to constrain, inform, and improve our representation of smoke (e.g., emissions, chemical and physical processes, and optical properties) and its air quality and climate impacts.

This thesis begins in Chapter 2 by quantifying how uncertainty in our fire particle emission estimates carries through to air quality and climate impacts and delves into where some of this uncertainty comes from. Further, we constrain the model, driven by four different smoke inventories, with available observations in North America and show that two inventories (GFED4s and GFAS1.2) drive GEOS-Chem closest to observations. A subsequent study showed that GFED also drives the ACCESS-UKCA model closest to observations (Desservettaz et al., 2022). Chapter 3 explores how the magnitude and properties of carbonaceous aerosol (BC and OA) differ in two large fire regions (the western US and central Africa), the absorption and whitening of brown carbon, and the global implications of what we learn.

In Chapter 4, we explore fire non-methane organic gases (NMOGs) and provide a first estimate of the importance of fires for atmospheric reactivity. We update and expand the emissions factors and improve the chemistry of NMOGs from fires in the model and constrain these updates with available observations from large fire regions (US, boreal Canada, Amazon, and Africa). We ultimately show that fires are responsible for a large contribution of surface atmospheric reactivity both near source regions (> 75%) and broadly across the globe (~25%).

In Chapter 5, we explore two quantifiable human levers (agricultural fires and human ignited wildfires) on smoke $PM_{2.5}$ in the contiguous US (CONUS). Through this work, we show that humans are responsible for a large portion of smoke and its impacts in specific regions and across CONUS (>80% of fire-associated population-weighted $PM_{2.5}$ exposure and premature mortality come from these two human levers). Thus, there is a large mitigation potential for lessening associated air quality impacts.

Chapter 6 summarizes the conclusions of this work, briefly discusses two studies complementary to my thesis, and provides an outlook on future research needs.

Chapter 2. How emissions uncertainty influences the distribution and radiative impacts of smoke from fires in North America

Adapted from: Carter, T.S., C.L. Heald, J.L. Jimenez, P. Campuzano-Jost, Y. Kondo, N. Moteki, J.P. Schwarz, C. Wiedinmyer, A.S. Darmenov, A.M. da Silva, and J.W. Kaiser (2020) How emissions uncertainty influences the distribution and radiative impacts of smoke from fires in North America, Atmos. Chem. Phys., 20, 2073–2097, https://doi.org/10.5194/acp-20-2073-2020.

2.1 Introduction

Biomass burning (BB), which includes wildfires in addition to agricultural and other prescribed burning, emits a variety of trace gases and aerosols, including carbon dioxide, oxides of nitrogen, VOCs, and $PM_{2.5}$ (Akagi et al., 2011) with large associated air quality and climate impacts. Particulate matter from fires (or smoke) is dominated by carbonaceous aerosol (BC and OA) (Akagi et al., 2011; Bond et al., 2013). As these emissions are transported through the atmosphere, they deteriorate air quality in a variety of ways. Because of their small size and associated ability to lodge deeply in lungs, aerosols can have significant health impacts (respiratory infections, asthma, and lung cancer) and increase cardiovascular disease (e.g., Brook et al., 2010; Pope and Dockery, 2006), especially the high levels of PM from fire events (Liu et al., 2015; Reid et al., 2016; Williamson et al., 2016). Deep penetration of the lungs and most acute health impacts are generally associated with the fine PM (under 2.5 microns) fraction of PM. Biomass burning aerosols (BBA) can also impact the climate system via absorbing and scattering radiation (Bond et al., 2013). In an era of increasing wildfire activity in the western US (Westerling, 2016; Westerling et al., 2006), there is a pressing need to understand how smoke from fires impacts air quality and alters atmospheric radiation.

Globally, BB is responsible for roughly 30% of BC and nearly 90% of primary OA emissions (POA), contributing an estimated 34 Tg yr^{-1} of aerosol to the atmosphere annually (Bond et al., 2013). In addition, fires may be an important source of secondary organic aerosol (SOA), which form from the oxidative aging of gas-phase organics emitted during combustion. Our current understanding of SOA formation is incomplete. Recent studies demonstrate that there is no clear

consensus on the magnitude of SOA from fires, with estimates that range from virtually none to 95 Tg yr^{-1} (Shrivastava et al., 2017; Vakkari et al., 2018). Much of this spread comes from diverging results from field versus laboratory studies: the majority of field studies have reported no secondary aerosol formation (above dilution-corrected POA concentrations; Hodshire et al., 2019) or even a decrease in OA (Akagi et al., 2012; Collier et al., 2016; Forrister et al., 2015; Garofalo et al., 2019; Jolleys et al., 2014; Liu et al., 2015b; May et al., 2014, 2015), while a few field studies observed significant SOA formation from biomass burning emissions (Vakkari et al., 2014, 2018; Yokelson et al., 2009). Laboratory studies, to the contrary, almost always report substantial SOA formation from fires (Grieshop et al., 2009; Hennigan et al., 2011; Lim et al., 2019; Ortega et al., 2013; Tkacik et al., 2017). The reasons for the discrepancy across studies are not understood (Hodshire et al., 2019; Shrivastava et al., 2017) and should be the focus of further research.

Biomass burning aerosols (BC, POA, and SOA) can have major impacts on radiation. Black carbon has a strong warming or positive direct radiative effect (DRE) (instantaneous radiative impact), both globally and regionally, and some studies suggest its warming direct radiative forcing (DRF) (the change in DRE from pre-industrial to present day, not including climate feedbacks) (Heald et al., 2014) is second only to CO_2 (Bond et al., 2013). Black carbon from BB and gas flares also lowers the snow and ice albedo in the Arctic, leading to additional warming (Stohl et al., 2013). Organic aerosol, because it scatters radiation, has a negative or cooling DRE (Bond et al., 2013). It is therefore the sum of the warming from absorption and the cooling from scattering that dictates the climate effect of BBA, leading to uncertainty in even the sign of the net radiative effect of fires. Previous estimates of BBA DRE range from -0.01 to 0.13 W/m^2 (Rap et al., 2013; Ward et al., 2012). Furthermore, when quantifying BBA impacts on radiation, differentiating anthropogenic and natural fires is central to quantifying the climate forcing, or the DRF of fires which reflects human influence (e.g. via ignition, suppression or changes in fuel availability). The uncertainty in fire radiative impacts has not been assessed in detail.

North America, in particular the western US, is one of the few regions in the world where more intense and frequent wildfires have been directly tied to climate change impacts (e.g., hotter temperatures and less snowpack) (Abatzoglou and Williams, 2016; USGCRP, 2017). In addition

to climate change, historical fire suppression efforts in the US have led to increased fuel loads for fires (Marlon et al., 2012). Consequently, BBA emissions there are likely to increase in future decades (Yue et al., 2013). Already, boreal forest fires are responsible for only 2.5% global burned area but 9% of global BBA emissions (van der Werf et al., 2017). Biomass burning in Alaska has also accelerated in the last decade through increases in both burned area and fire frequency leading to increases in carbon loss associated with late-season burning (Turetsky et al., 2011). Both relative and total impacts of BB on air quality and climate forcing are expected to increase as controls continue to reduce fossil fuel emissions and a changing climate potentially leads to more fires (Fuzzi et al., 2015; Val Martin et al., 2015). It is, therefore, becoming increasingly important to have models and emission inventories that can accurately characterize the impact that current and future fires and their emitted aerosols have on the environment, climate, and human health. Several recent laboratory studies (e.g., Jolleys et al., 2014; Levin et al., 2010; McMeeking et al., 2009), including the recent NOAA Fire Lab 2016 experiments in Missoula, MT (e.g., Jen et al., 2018; Koss et al., 2018; Selimovic et al., 2018), have explored the BB of North American fuels, providing key constraints on smoke emissions, aging, and properties.

Because BBA emissions cannot routinely be measured directly, a variety of global fire emission inventories have been developed over the last decade(s) based on satellite observations. These inventories use different empirical approaches and underlying data to represent gas and aerosol emissions from fires - each with inherent uncertainties. Aerosol emissions from these inventories often vary by large factors depending on the region, do not agree spatially, and sometimes do not reflect observations of concentrations and AOD well either when integrated into a model (Petrenko et al., 2012; Reddington et al., 2016, 2019). In this analysis, we focus on four commonly used, but theoretically distinct inventories: the Global Fire Emissions Database version 4 (GFED4s) (van der Werf et al., 2017) with small fires, the Fire INventory from NCAR version 1.5 (FINN1.5) (Wiedinmyer et al., 2011), the Quick Fire Emissions Database version 2.4 (QFED2.4) (The Quick Fire Emissions Dataset (QFED) – Documentation of versions 2.1, 2.2 and 2.4, NASA Technical Report Series on Global Modeling and Data Assimilation, NASA TM-2013-104606, 2020), and the Global Fire Assimilation System version 1.2 (GFAS1.2) (Kaiser et al., 2012). The two main approaches are a fire detection/burned area (FD/BA) method that relies

upon burned area, which GFED4s uses, or active fire counts, which FINN1.5 uses, and the fire radiative power (FRP) approach, which relies upon fire radiative energy observations, an approach which both QFED2.4 and GFAS1.2 use. Comparisons among these different types of inventories suggest that there is significant variability in the amount of dry matter burned associated with an individual active fire detection, which is one explanation for why FD/BA and FRP inventories do not align (van der Werf et al., 2017 and references therein). Studies using AOD to interrogate BB emission inventories give varied results but suggest that FD/BA BBA estimates are roughly a factor of 3 too low in large BB regions (e.g., boreal North America, South America, southern Africa, and equatorial Asia) and globally (Johnston et al., 2012; Kaiser et al., 2012; Petrenko et al., 2012; Tosca et al., 2013). In this study we will refer to the spread across these inventories as the "uncertainty" in emissions; however, we note that additional factors, not represented by any of these inventories, may increase the true uncertainty in the estimated emissions.

Here we use the GEOS-Chem chemical transport model and a suite of fire emission inventories to investigate the emissions uncertainties associated with impacts of BBA on air quality and radiation. We explore the interannual and geographic variability of fire emissions and dry matter (DM) consumed from 2004-2016 across inventories and discuss how the uncertainty in emissions carries forward to concentrations, exposure, aerosol optical depth (AOD), and DRE with a focus on 2012 - 2014. We also explore the impact of a new model parameterization for SOA from fires.

2.2 Model and observations descriptions

2.2.1 The GEOS-Chem model

We use GEOS-Chem (www.geos-chem.org), a global chemical transport model, coupled with the rapid radiative transfer model for global circulation models (RRTMG, Iacono et al., 2008), a configuration known as GC-RT (Heald et al., 2014), to explore the air quality and climate impacts of BBA. GEOS-Chem is driven by assimilated meteorology from the Modern-Era Retrospective analysis for Research and Applications, Version 2 (MERRA-2) at the NASA Global Modeling and Assimilation Office (GMAO). We run version 12.0.0 of GEOS-Chem (https://doi.org/10.5281/zenodo.1343547) with a horizontal resolution of 2x2.5° and 47 vertical

levels with a chemical timestep of 20 minutes and a transport timestep of 10 minutes and with six month spin up simulations prior to the time periods of interest, 2012-2014 and June-July 2008. We also perform nested simulations over North America at 0.5x0.625° (with boundary conditions from the global simulation) for comparison against observations (IMPROVE and aircraft campaigns, see Sect. 2.3) with transport and chemistry timesteps of 5 and 10 minutes, respectively.

GEOS-Chem employs SO_4^{2-}–NO_3^-–NH_4^+ thermodynamics (Fountoukis and Nenes, 2007) coupled to an ozone–VOC–NO_x–oxidant chemical mechanism (Chan Miller et al., 2017; Mao et al., 2013; Travis et al., 2016) with integrated Cl-Br-I chemistry (Sherwen et al., 2016). The model includes schemes for fine and coarse sea salt aerosols (Jaeglé et al., 2011) and mineral dust in four size bins (Fairlie et al., 2007; Ridley et al., 2012). The standard simulation of BC in GEOS-Chem is described in Park et al., (2003). We update this simulation per Wang et al. (2014), as follows: we update the initial hydrophilic fraction from BB to 70% based on field observations (Wang et al., 2014 and references therein). Fossil-BC is aged from hydrophobic to hydrophilic using the Liu et al. (2011) BC aging scheme with dynamic [OH] and [SO_2] per Wang et al. (2014), and biofuel/biomass-BC is aged with an e-folding time of 4 hours. For hydrophilic BC, we use an absorption enhancement from coating of BC of 1.1 for fossil-BC and 1.5 for biofuel/biomass-BC. We also update the BC properties for optical calculations per Wang et al. (2014).

The standard POA simulation emits 50% of POA as hydrophilic and ages hydrophobic POA to hydrophilic POA with an atmospheric lifetime of 1.15 days (Chin et al., 2002; Cooke et al., 1999). We use an organic matter (OM) to OC ratio of 1.4 for hydrophobic OC and 2.1 for hydrophilic. The baseline model formation of SOA from BB follows the simple scheme implemented by Kim et al. (2015) based on field results from six large campaigns summarized by Cubison et al. (2011). This emits 0.013g SOA precursor (SOAP) per g CO emitted, which then forms non-volatile SOA on a fixed timescale of one day. SOAP is not lost by dry or wet deposition. Recent laboratory results from the NOAA Fire Lab 2016 campaign suggest much greater SOA formation from the burning of North American fuels (Lim et al., 2019); however, we note that, as previously discussed, uncertainties surrounding this source of SOA remain large.

Based on this study, we perform a sensitivity analysis for a new parameterization for SOA production from fires, where SOAP is estimated as POA fire emissions scaled by a factor of 2.48. We note that this is 13 times larger than the field-based estimate of Cubison et al. (2011), which combines the effects of POA evaporation and SOA formation (see Sect. 5 for further details).

Anthropogenic emissions (including fossil and biofuel sources) of both BC and POA follow the CEDS global inventory (Hoesly et al., 2018) with regional inventories used when available, including NEI2011v1 over the US (Air Pollutant Emissions Trends Data, 2020), APEI over Canada, and DICE-Africa over Africa (Marais and Wiedinmyer, 2016). Trash burning emissions are from Wiedinmyer et al. (2014). Aircraft emissions are from the AEIC inventory (Simone et al., 2013; Stettler et al., 2011). Global annual anthropogenic emissions are 4.5 Tg yr^{-1} of BC and 8.7 Tg yr^{-1} of POA in 2012. Biogenic emissions are calculated online from the MEGANv2.1 emissions framework (Guenther et al., 2012).

Fire emission inventories (GFED4s, FINN1.5, QFED2.4, and GFAS1.2) are specified on a daily timescale, the frequency at which all four inventories were available. The standard version of GEOS-Chem, which we use, emits all fire emissions from the surface into the boundary layer. Diurnal scale factors from the Western Regional Air Partnership (WRAP, 2005) were applied to all inventories per Kim et al. (2015). Additional information on each fire inventory is provided in Sect. 2.2.

We quantify simulated AOD at 550 nm, assuming that aerosols are externally mixed with a fixed lognormal size distribution for each species and that AOD is a function of relative humidity to account for hygroscopic growth, which also varies by species (Martin et al., 2003). Aerosol optical properties are from the Global Aerosol Data Set (GADS) database (Köpke et al., 1997) with updates from Drury et al. (2010) and Wang et al. (2014). RRTMG calculates both longwave and shortwave atmospheric radiative fluxes. When coupled to GEOS-Chem, this calculation is performed every 3 hours. Long and shortwave DRE at the top of the atmosphere are summed and reported as total DRE.

2.2.2 Description of fire emission inventories

Here we describe the differences and similarities of the four fire emission inventories investigated in this study: two FD/BA approaches (GFED4s and FINN1.5) and two FRP-based (QFED2.4 and GFAS1.2). GFED4s is the most widely used of fire emission inventories (other inventories are sometimes scaled to it), and it employs a FD/BA approach based on the Moderate Resolution Imaging Spectroradiometer (MODIS)-observed burned area complemented by the Carnegie–Ames–Stanford Approach (CASA) biogeochemical model. CASA provides estimated biomass factors (i.e., combustion completeness and fuel load) in a variety of carbon pools (e.g. leaves, grasses, litter, etc.), depending on pool-specific and environmental conditions, which are combined with emission factors (EFs) and MODIS burned area to produce emissions (van der Werf et al., 2017). GFED4s therefore estimates emissions as:

$$M_s = A\ x\ \rho\ x\ \gamma\ x\ EF_s, \quad (1)$$

where M_S is the mass of the species of interest (g), A is burned area (m^2), γ is combustion completeness (%), ρ is fuel load (kg DM/m^2), and EF_S is the species-specific emission factor (g species/kg DM).

The fourth and most recent version of GFED (GFED4s) provides emissions at a 0.25° resolution from 1997 in near real time, and boosts emissions to include small fires (Randerson et al., 2012). Burned area estimates from 2000 onwards are from the MODIS MCD64A1 500m burned area maps aggregated at 0.25° resolution and a monthly time step (Giglio et al., 2013). Because of measurement limitations, EFs, in general, are very uncertain (see Sect. 3), but GFED4s employs a recent compilation of EFs (Akagi et al., 2011) with some updates, such as for the temperate forest biome. GFED4s emissions are available monthly with scalars also available to distribute emissions over daily or three-hour intervals. These scalars are only available from 2003 onwards.

FINN1.5 follows the same FD/BA approach as GFED4s but with some differences, including: burned area is estimated from active fire detection identified with the MODIS Thermal Anomalies Product (Giglio et al., 2006), EFs are based on the 2015 updates from Akagi et al. (2011) (http://bai.acom.ucar.edu/Data/fire/), and different land cover maps are used. FINN1.5

emissions uncertainty comes from the use of fire hot spots, assumed area burned (each fire hot spot is equivalent to 1km^2 burned area except grasslands, which are 0.75 km^2), land cover maps, biomass consumption estimates, and EFs (Wiedinmyer et al., 2011). The original emission estimates are available at 1 km^2 spatial resolution and from 2002 – 2016 at both daily and monthly mean temporal resolution. Within the GEOS-Chem model, FINN1.5 input files are available at 0.25°, and CO_2 emissions are produced with FINN1.5 and then other emitted species are scaled based on emission factors and land cover type.

QFED2.4 and GFAS1.2 employ an FRP-based method, which estimates emissions using satellite observations of fire radiative power (FRP), relying upon the following theoretical approach:

$$M_s = \alpha \, x \, EF_s \, x \, FRE = \alpha \, x \, EF_s \, x \int_{t_1}^{t_2} FRP(t)dt, \qquad (2)$$

where α is the emission coefficient (kg DM J^{-1}), EF_S is the species-specific emission factor (g species/kg DM), and FRE in joules (is fire radiative energy or the integral of fire radiative power (FRP in J s^{-1}) over time.

This FRP-based approach takes advantage of an empirically derived linear relationship between the energy released as thermal radiation (FRE) and the mass of fuel or DM consumed during combustion (Ichoku and Kaufman, 2005; Wooster, 2002; Wooster et al., 2005). This basic relationship is supported by the fact that the energy released by burning the same amount of a fuel is similar regardless of vegetation type (Wooster et al., 2005). The energy from combustion processes not transferred into the environment (through conductive, evaporative, and convective processes) is released as infrared radiation, which is then assumed to be proportional to the total energy produced during combustion. One can then relate the amount of fuel burned with the time-integrated FRE using an emission coefficient (α). In laboratory studies, the coefficient appears to be universal, i.e. independent of fuel type (Wooster et al., 2005). For satellite-observed FRE, however, different values are associated with different broad classes of fire types (Kaiser et al., 2012).

QFED2.4 uses the MODIS Active Fire Level 2 product (MOD14 and MYD14) and the MODIS Geolocation product (MOD03 and MYD03) for FRP and the location of fires. A linear

regression between the QFED2.4 dataset, starting with an emission coefficient (α_{0}) from Kaiser et al. (2009), and version 2 of GFED was used to calculate the α used in QFED2.4. The location of the fire in addition to a vegetation land type mask was used to assign the FRP to a QFED2.4 vegetation type, which was based on an aggregated version of the International Geosphere-Biosphere Programme (IGBP) vegetation mask with four basic classes: tropical forest, extratropical forest, savanna, and grassland. GFAS1.2 also uses the MOD14 fire product. GFAS1.2 utilizes land cover maps based on the dominant vegetation type from GFED3 and additional organic soil and peat maps (Kaiser et al., 2012). GFAS1.2 also derives conversion factors linking FRP and the GFEDv3.1 dry matter combustion rates based on linear regressions between the two.

QFED2.4 and GFAS1.2 utilize EFs from Andreae and Merlet (2001). An update to this EF compilation is now available (Andreae, 2019) but is not yet used in these inventories. QFED2.4 scales its aerosol emissions to better represent MODIS-observed AOD, using biome-dependent strength factors. It should be noted that these enhancement factors were based on the GEOS model, and depend on the underlying model configuration, most importantly, the single assumed OM:OC ratio of 1.4, but also the specific anthropogenic emissions and the radiative properties of aerosols in the model. Thus, these enhancement factors that scale to AOD could differ substantially in a model that treats these factors differently. To our knowledge, these differences have not been accounted for in previous model studies that have used QFED (e.g., Kim et al., 2015; Lu et al., 2015; Marais et al., 2016; Saide et al., 2016; Zhang et al., 2014). We make no effort to re-derive the biome-specific enhancement factors for GEOS-Chem. In an effort to ensure that global totals of emitted BC and OA are consistent with those reported by QFED2.4, we scale down emissions by a uniform factor of 0.69 (1.4/average OM:OC ratio in GEOS-Chem in 2012). QFEDv2.4 provides daily mean emissions and is available at 0.1° resolution from 2003 – 2016. GFAS1.2 provides daily mean emissions and is available from 2003 – 2019 at 0.1° resolution.

Some advantages of QFED2.4, GFAS1.2, and other FRP-based inventories are that the uncertain factors used in FD/BA inventories to convert burned area to DM consumed (fuel load and combustion completeness) can be bypassed, and that FRP observations are more sensitive to

small fires than burned area observations (MODIS has detection limits of ~5MW and 50m^2, respectively). However, FRP-based approaches face significant challenges associated with the sparse temporal coverage of the underlying polar-orbiting MODIS observations of FRP. The daytime overpass of Terra and Aqua (10:30 LT and 13:30LT, respectively), generally miss the period of peak fire activity in the western US and Canada. In addition, active fire observations (both active fire counts and FRP) can only detect fires during the burning phase, while the accumulated burned area can be detected for an extended period of time after the burning phase. FRP-based emission estimates therefore contain errors due to assumptions on undetectable fire activity under cloud cover and between satellite overpasses (for low-earth orbiting instruments like MODIS). Smouldering and peat fires are difficult to quantify with both methods: FRP-based approaches suffer from weak thermal signatures and uncertain emission coefficients (Darmenov and da Silva, 2013), and FD/BA-based approaches suffer from missing information on burn depth and thus combustion completeness.

2.2.3 In-situ observations

The ARCTAS (Arctic Research of the Composition of the Troposphere from Aircraft and Satellites) summer airborne campaign surveyed large swaths of the Arctic with an emphasis on probing forest fire smoke plumes using the NASA DC-8 aircraft from June 18 to July 13, 2008 (Jacob et al., 2010) (see Fig. 2.1 for flight tracks). Black carbon mass concentrations were measured with a single particle soot photometer (SP-2, Schwarz et al., 2008). For ARCTAS, the SP-2 detection range for particle diameter is 80-860nm, and the uncertainty is estimated to be 10% (Kondo et al., 2011). Organic aerosol was measured using a high-resolution time-of-flight aerosol mass spectrometer (CU-Boulder Aerodyne HR-ToF-AMS, Canagaratna et al., 2007; Cubison et al., 2011; DeCarlo et al., 2006) with a 2σ estimated uncertainty of 38% for OA (Bahreini et al., 2009) and a size detection limit extending down to 35nm vacuum aerodynamic (about 25 nm geometric diameter for typical BBOA densities) (DeCarlo et al., 2006, 2008). Concentration detection limits for OA for 1 min. data are ~0.16 $\mu g\ m^{-3}$ (DeCarlo et al., 2006; Dunlea et al., 2009), several orders-of-magnitude lower than typical field BBOA concentrations (>= 10 $\mu g\ m^{-3}$). The model structural and emission uncertainties for fire OA likely far outweigh measurement uncertainties, and thus, these measurement uncertainties are not germane to the analysis presented here. Acetonitrile, a useful tracer for BB, was measured using a Proton-

Transfer-Reaction Mass-Spectrometer (PTR-MS, Hansel et al., 1995; Wisthaler et al., 2002) and used as a filter to help isolate BB influence.

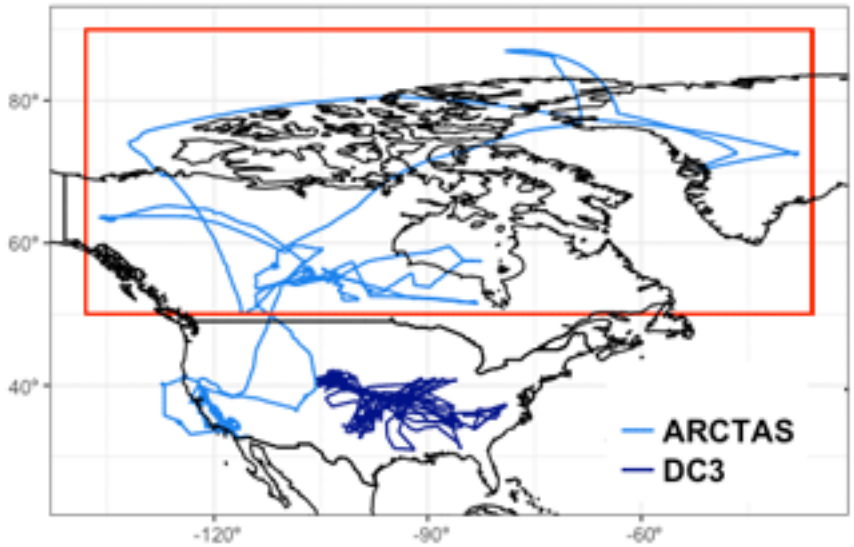

Figure 2.1 Flight tracks of the ARCTAS and DC3 aircraft campaigns. The red box indicates the boreal region of the ARCTAS flights used here.

Observations from the Deep Convective Clouds and Chemistry (DC3) campaign are also included in our analyses. DC3 focused on thunderstorms and their impact on the chemical composition of the troposphere and documented BB plumes and their interactions with deep convection in the Southern Great Plains, the Colorado Front Range, and the southeastern US. Flights occurred from May 18 to June 22, 2012 (Barth et al., 2015) (Fig. 2.1). As in ARCTAS, BC was measured using the SP-2, and OA was measured using an HR-ToF-AMS. The detection range for BC mass from the SP-2 corresponds to 90-550 nm volume equivalent diameter, assuming 1.8 g cm^{-3} density, with ± 30% total uncertainty in the accumulation mode BC mass mixing ratio (Schwarz et al., 2013). Acetonitrile was again measured using a PTR-MS (Hansel et al. 1995; Wisthaler et al. 2002). For comparison with airborne measurements, the model was sampled to the nearest grid box both temporally and spatially to each flight track using 1-minute aircraft data. We then average both the model and the observations to the model grid box.

As the spatial and temporal coverage of aircraft campaigns is limited, we also include surface observations from 168 sites in the contiguous United States (CONUS) that are part of the

IMPROVE aerosol network (Interagency Monitoring of Protected Visual Environments, http://vista.cira.colostate.edu/improve/) from 2012 and compare against 24-hour averaged model results. Black carbon and OC are measured using a $PM_{2.5}$ size-selective filter-based thermal method in this network (Chow et al., 2007). We use a conversion factor of 1.8 from OC to OA mass (Malm and Hand, 2007), which is the average of fresh and more aged OA in the model, to represent average surface conditions (note that the same OM:OC is applied to the model simulation when compared against IMPROVE).

2.2.4 MODIS AOD observations

Aerosol optical depth (AOD), the column total aerosol extinction, is directly proportional to the total mass concentration of aerosol in an atmospheric column (Levy et al., 2007, 2010) and is commonly measured by satellites. AOD measurements capture all aerosol contributions and, therefore, do not provide a unique quantitative constraint on BBA, but they can be a used to understand spatial and interannual BB patterns.

We use the MODIS Collection 6 level 3 daily product of satellite AOD retrievals at 550nm and 10km resolution (Levy et al., 2013; Sayer et al., 2014) from the Aqua platform and re-grid MODIS AOD from 1x1° to the model grid of 2x2.5° for further comparison with GEOS-Chem AOD. AOD retrievals from Aqua are used because the cross-over time of Aqua (early afternoon) typically coincides with peak burning activity and a well-mixed boundary layer. We use a merged AOD product (Dark Target-Deep Blue Combined Mean) from the Collection 6 MODIS data that combines ocean and vegetated land surface retrievals (Dark Target) and bright land surface retrievals (Deep Blue) to maximize coverage. Retrieved AOD (τ) is estimated to be accurate to $\pm 0.03 \pm 0.05\tau$ over the ocean (Remer et al., 2005), to $\pm 0.05 \pm 0.15\tau$ over dark land surfaces (Levy et al., 2010), and to $\pm 0.05 \pm 0.20\tau$ over bright surfaces (Hsu et al., 2006; Sayer et al., 2014). The model was sampled at the satellite overpass time (1330 local time). In addition, we filter out AOD values from both MODIS and the model for which the cloud fraction from MODIS is greater than 80% to eliminate potential cloud contamination.

2.3 Underlying emissions and dry matter uncertainty

Figure 2.2 demonstrates the large differences in total annual BBA emissions estimated by the four different fire emission inventories from 2004-2016 for boreal North America (BONA, Canada and Alaska), the contiguous US (CONUS), and the globe. Emission totals over other large BB regions that are not the focus of this study (Amazon, Africa, and Asia) are shown in Fig. 2.S1. We focus on BC and OC (note that inventories provide OC, not OA) emissions in our analysis, but also provide a summary of CO for context, which generally follows the trends observed for OC (as does NO_x, not shown). Globally, emissions of BC and OC are highest in QFED2.4 (3.1Tg yr^{-1} and 28.3Tg yr^{-1}, respectively), but emissions are also most variable in this inventory (i.e., more variability from 2004-2016 as evidenced by the wider range between the 25^{th} and 75^{th} percentiles) (Fig. 2.2). Average global annual emissions are smallest in GFED4s for BC, and, for OC and CO, FINN1.5 emissions are smallest – though very similar to GFED4s for OC and similar to QFED for CO. Global mean total annual BC emissions differ by roughly a factor of 2.3 across the inventories while mean total annual OC emissions differ by less (~ a factor of 1.7). The inventories show a smaller range in mean total annual CO emissions (~ a factor of 1.1): from GFAS1.2 (360Tg yr^{-1}) to FINN1.5 (327Tg yr^{-1}).

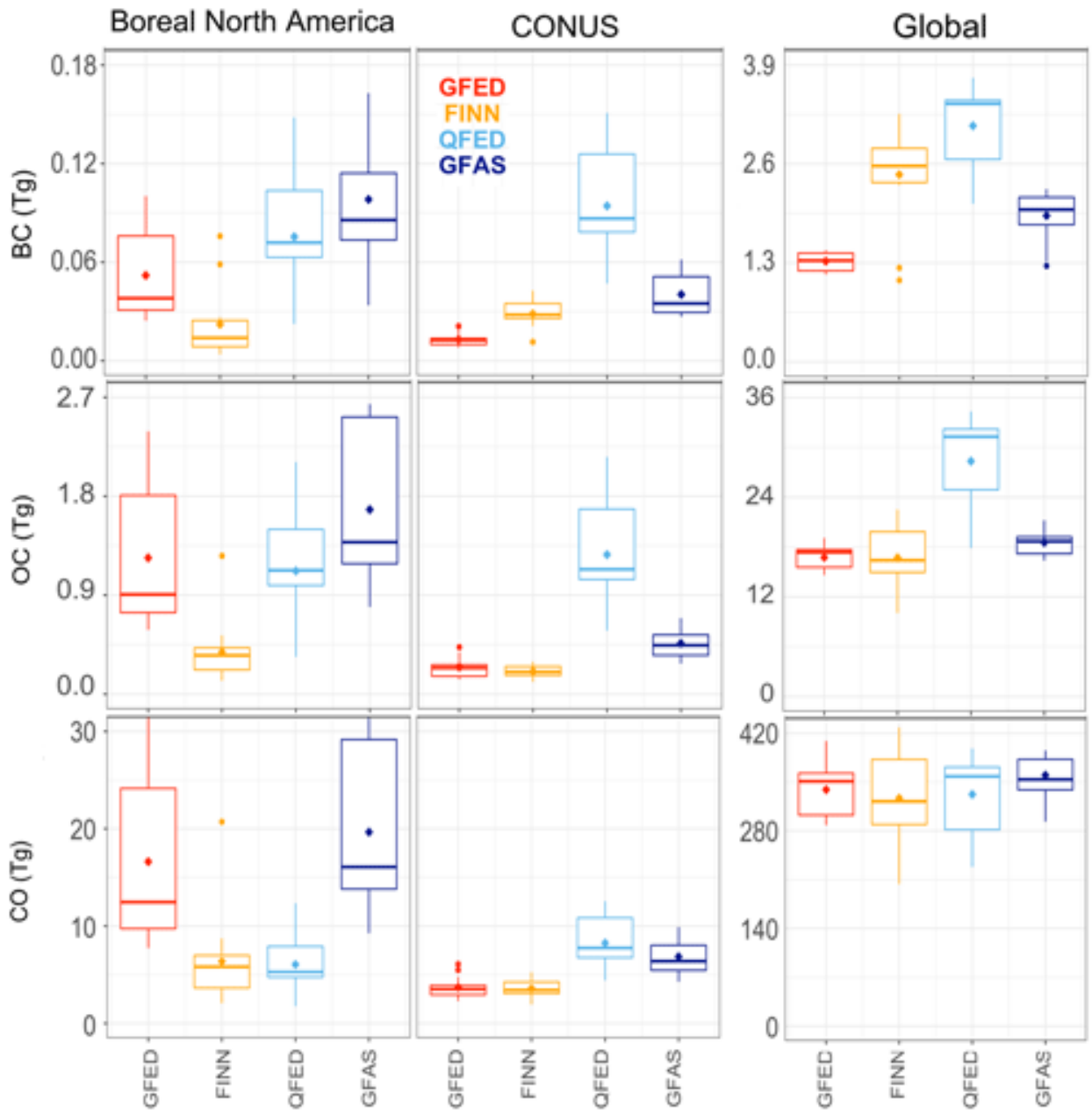

Figure 2.2 Boxplot summaries of each inventory's total annual emissions of BC, OC, and CO globally and for boreal North America and CONUS from 2004 to 2016. Diamonds indicate means. The horizontal bar is the median. The box shows the 25th to the 75th percentile, and the whiskers show 1.5 times the interquartile range. Points outside 1.5 times the interquartile range are shown as dots. GFED4s emissions are in red, FINN1.5 emissions are in orange, QFED2.4 emissions are in light blue, and GFAS1.2 emissions are in dark blue.

The spread in BBA emissions across North America is larger than that seen globally. In BONA, mean annual BC and OC emissions show a factor of roughly five and four range, respectively, from the smallest, FINN1.5 (0.02Tg yr^{-1} and 0.4Tg yr^{-1}, respectively), to the largest, GFAS1.2 (0.1Tg yr^{-1} and 1.7Tg yr^{-1}, respectively). The relative magnitudes of the four inventories are consistent across species for CONUS with QFED2.4 largest (0.09Tg yr^{-1} and 1.3Tg yr^{-1}, for BC and OC respectively), followed by GFAS1.2 (0.04Tg yr^{-1} and 0.5Tg yr^{-1}, for BC and OC respectively), and then FINN1.5 (0.03Tg yr^{-1} and 0.2Tg yr^{-1}, for BC and OC respectively) and GFED4s (0.01Tg yr^{-1} and 0.3Tg yr^{-1}, for BC and OC respectively) – where the exception is that the mean OC emissions from GFED4s are slightly larger than those of FINN1.5. The range of values is very similar for BC and OC in CONUS (a factor of ~7 for BC and ~6 for OC). For CONUS, GFED4s, GFAS1.2, and QFED2.4 show similar spatial patterns; FINN1.5 continues to show very little fire influence.

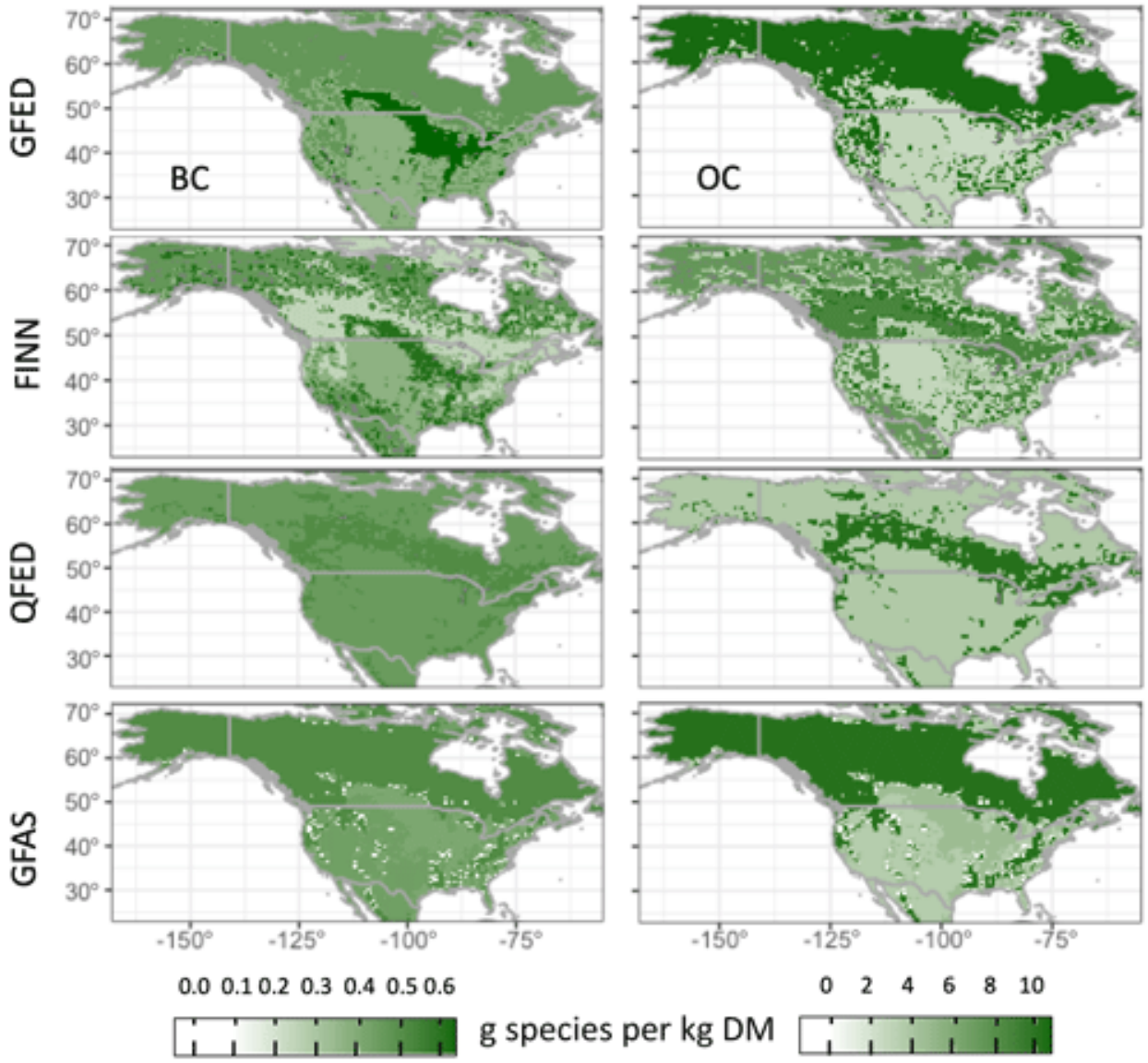

Figure 2.3 Emissions factors in g species per kg DM (shown only for vegetated land) for each inventory over North America; BC is shown on the left, and OC is shown on the right.

Emission factors across inventories and vegetation types (g species per kg dry matter)										
Types	BC					OC				
	GFED4s	FINN1.5	QFED2.4^{AM}		GFAS1.2^{AM}	GFED4s	FINN1.5	QFED2.4^{AM}		GFAS1.2^{AM}
Temperate forest	0.5^{AM}	0.56^{An}	2.52	0.56	0.56	9.6^{AM}	7.6^{An}	28.38*	9.14	9.1
Boreal forest	0.5^{AM}	0.2^{Mc}	2.52	0.56	0.56	9.6^{AM}	7.8^{Mc}	28.38*	9.14	9.1
Savanna, grass, shrub	0.37^{Ak}	0.37 (SG)/ 0.5 (WS)^{Ak}	0.86	0.48	0.46	2.62^{Ak}	2.62 (SG)^{Ak}/ 6.6 (WS)^{Mc}	4.22*	3.40	3.2
Tropical forest	0.52^{Ak}	0.52^{Ak}	1.65	0.66	0.57	4.71^{Ak}	4.71^{Ak}	8.97*	5.20	4.3
Agricultural	0.75^{Ak}	0.69^{AM}	–	–	0.42	2.3^{Ak}	3.3^{AM}	–	–	4.2

Table 2.1 Emissions factors used in each inventory. Superscripted AM is from Andreae and Merlet (2001), Ak is from Akagi et al. (2011), An is Andreae and Rosenfeld (2008), and Mc is McMeeking et al. (2009). Note that QFED2.4 and GFAS1.2 EFs shown here for BC and OC are entirely from Andreae and Merlet (2001). * The first QFED2.4 column shows the underlying EFs (shown in the second QFED2.4 column) multiplied by their biome-specific enhancement factor. We also adjust this factor down by the ratio of 1.4 (the OM : OC ratio used in the GEOS model) to the average OM : OC ratio used in GEOS-Chem in 2012 (see Sect. 2.2 for details).

Multiple studies (e.g., Akagi et al., 2011; Alvarado et al., 2010; Urbanski et al., 2011) have identified uncertainties in EFs as a large source of uncertainty in BB emissions. Table 2.1 confirms that there are large differences in the EFs used in the four inventories explored here in North America, particularly in boreal and agricultural regions. For example, OC boreal forest EFs range from 7.8 to 9.6 g/kg DM and BC from 0.2 to 0.56g/kg DM. The EFs used in each inventory are shown spatially over North America in Fig. 2.3. Updated EFs have also become recently available – from a large recent EF compilation (Andreae, 2019) to multiple studies focused on western fuels because of recent field intensives there. Some of this work has suggested that the PM EFs for western US fuels may be higher than those used in the inventories explored in this work (Liu et al., 2017). For example, the OA EFs measured by Liu et al. 2017 are roughly a factor of 1.5 to 4 larger than those used by the four inventories in this work. The uncertainty in EFs is associated with: measurement technique, variation in the experimental conditions used to measure species' EFs in a laboratory, post-processing and aging that can change smoke composition rapidly but is likely not yet fully mechanistically understood, and poorly characterized combustion and fire types (Akagi et al., 2011). Measured EFs vary considerable from different fuels (Jolleys et al., 2014; McMeeking et al., 2009); however, only coarse vegetation types (e.g., boreal forests) are typically delineated in emission inventories, making it difficult to apply laboratory-measured EFs. Of relevance to this study, relatively few measurements of BB have been made in temperate regions, such as large portions of the US, where much of the BB is prescribed for land management but controlled to protect air quality(Akagi et al., 2011), conditions which may lead to substantially lower BBA emissions(Liu et al., 2017). Another potential source of uncertainty in EFs is that experimentally-derived OC EFs may represent SOA as well as POA; EFs presented in compilations (Akagi et al., 2011;

Andreae and Merlet, 2001) are generally calculated from fresh smoke where the quantity of SOA production is not well constrained.

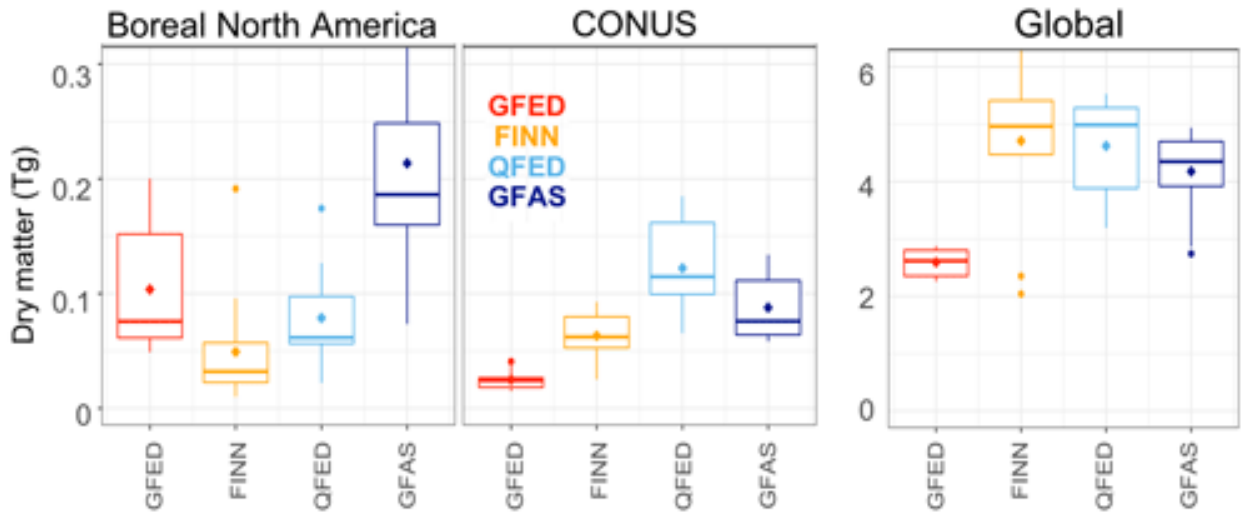

Figure 2.4 Boxplot summary of each inventory's underlying total annual dry matter (DM) globally and for boreal North America and CONUS. The conventions of this boxplot are described in Fig. 2.2. GFED4s DM emissions are in red, FINN1.5 emissions in orange, QFED2.4 effective DM emissions in light blue, and GFAS1.2 effective DM emissions in dark blue.

We quantify how the range in EFs contributes to the overall spread in BBA emissions. First, we divide emissions by the applied EFs to estimate the underlying dry matter (DM) consumed across inventories in the same regions and years as our emissions analysis (Fig. 2.4) to isolate the importance of EFs. We note that the two-FD/BA inventories (GFED4s and FINN1.5) quantify DM consumption in the construction of the inventory; however, for the FRP-based inventories (QFED2.4 and GFAS1.2) this division results in an effective DM consumed (FRE multiplied by an emission coefficient). We show DM calculated from BC emissions except for QFED2.4, where we use the effective DM calculated from the CO emissions so as to avoid any confounding issues with the aerosol strength scaling factors discussed briefly in Sect. 2.2.2. Across all regions, the range in DM tracks very closely the range observed across emissions, suggesting that the uncertainty in the underlying DM, not EFs, is the predominant factor in emissions uncertainty. We note that the large range in the DM consumed globally alongside the

similar global CO emissions indicates that large differences in the EFs of CO and different vegetation classifications offset the DM differences for this species.

To further illustrate the role of EFs, Fig. 2.5 shows the time series of total annual emissions from 2004-2016 for GFED4s, alongside the estimated emissions obtained by applying the GFED4s EFs to the estimated DM for the other three original inventories (applied using each inventories' respective vegetation mask). We then compare total annual emissions from the original inventories (dashed lines) with their GFED4s-EF counterparts (solid lines) and with the original GFED4s inventory from 2004-2016 (Fig. 2.5). While eliminating the variation in assumed EFs does constrict the range in emissions across the inventories across North America and globally, there remain substantial differences. This suggests that EFs are important but that underlying DM burned is the largest source of fire emissions uncertainty – consistent with previous work (Van Leeuwen et al., 2014). One reason for this is that substantial uncertainties are associated with using biome-averaged values to represent DM consumed for whole biomes (Van Leeuwen et al., 2014; Veraverbeke et al., 2015) and that satellite products and assumptions used to capture fuel burned vary significantly (van der Werf et al. 2017 and references therein).

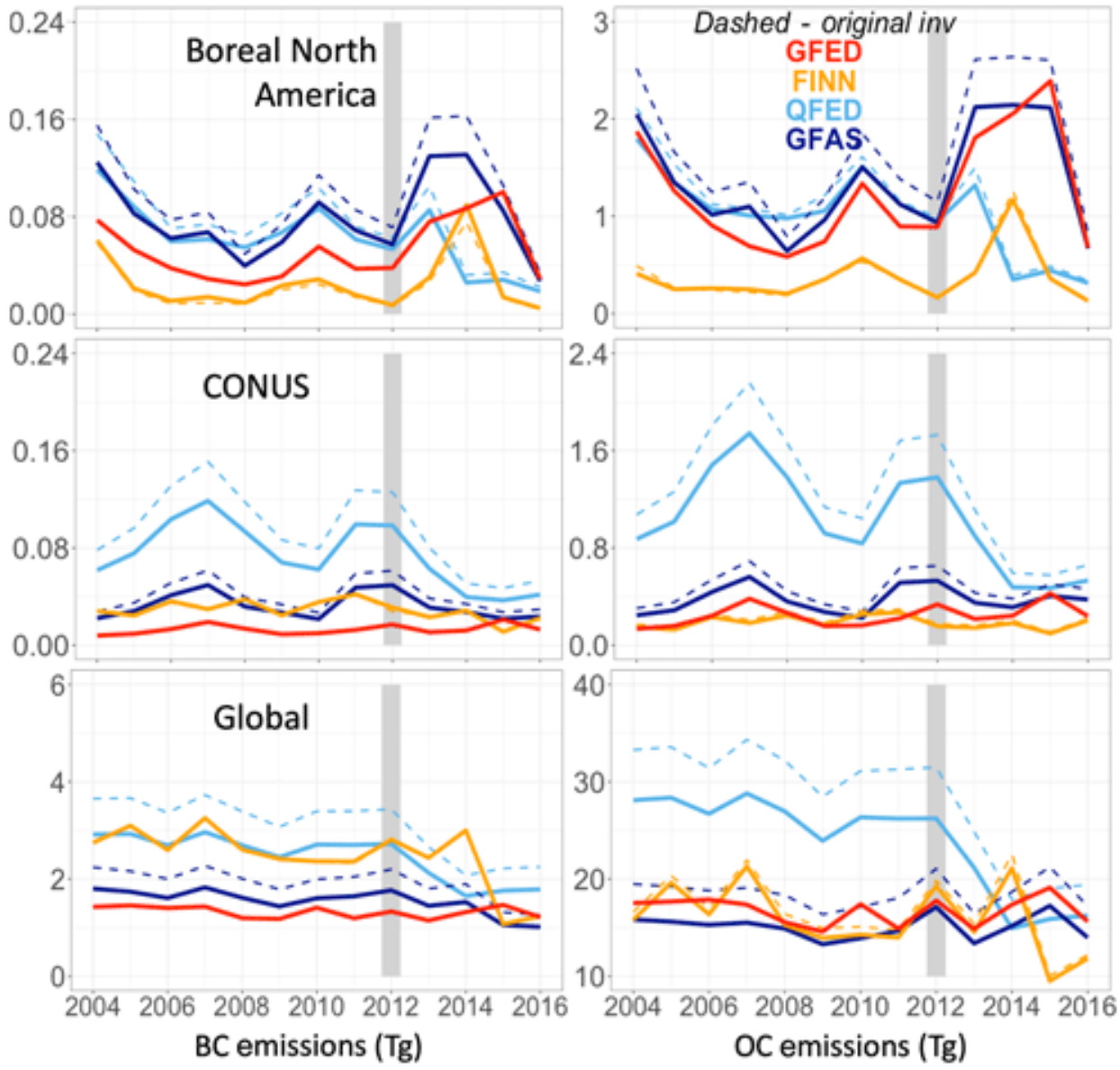

Figure 2.5 Annual emissions scaled to GFED4s emissions factors from 2004 to 2016. The original inventory emissions from FINN1.5 (orange), QFED2.4 (light blue), and GFAS1.2 (dark blue) are shown as dashed lines, while their annual values using GFED4s (red) emissions factors are shown as solid lines. The year 2012 is marked with a gray rectangle.

Furthermore, assuming that the EFs used in the four inventories are all equally reasonable values, we can estimate a much larger range in plausible fire emissions by multiplying the minimum and the maximum DM consumed across the inventories by the smallest and largest EFs (Table 2.1) using the GFED4s vegetation mask. Globally, this calculation suggests a plausible range that

spans a factor of 24 for BC and 18 for OC compared to the inventory spread of 2.3 and 1.7, respectively. This suggests that using the range across these four inventories may be a modest estimate of the uncertainty in fire emissions.

Interannual differences, especially in North America, are fairly consistent across the inventories except for 2014 (Fig. 2.5) where QFED2.4 trends down while the other three increase. It should be noted that an updated version of QFED (v2.5r1) does not show this decreasing trend in 2014. Globally and in CONUS, GFED4s, GFAS1.2, and QFED2.4 show similar interannual differences while FINN1.5 shows the greatest interannual variability and different maximum and minimum years. We note that 2012 is a fairly typical fire year (see Fig. 2.5), and much of the following analysis will focus on this year.

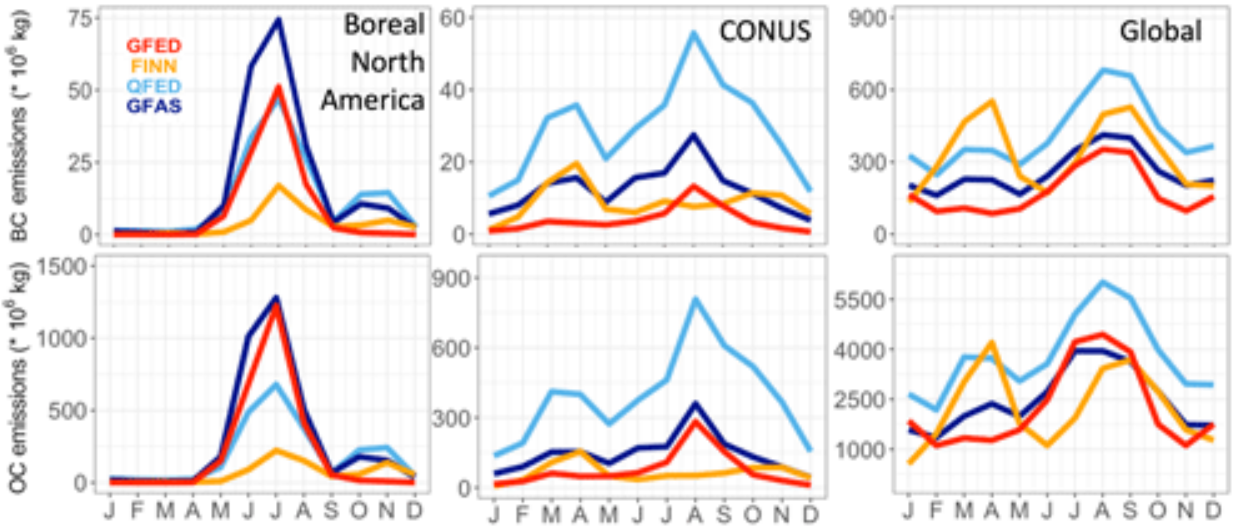

Figure 2.6 Seasonal mean BC and OC emissions from 2004 to 2016 for boreal North America, CONUS, and the globe. GFED4s emissions are in red, FINN1.5 emissions are in orange, QFED2.4 emissions are in light blue, and GFAS1.2 emissions are in dark blue.

We also explore the seasonality of BC and OC emissions represented in the inventories for BONA, CONUS, and globally across the same 13 years (Fig. 2.6). The seasonality, including relative magnitude, is generally consistent across regions and species. Some seasonal features (e.g., the October-November enhancement in BONA and the springtime enhancement in CONUS) are only visible in the three inventories that rely on active fire counts or FRP –

FINN1.5, QFED2.4, and GFAS1.2 – which is consistent with work suggesting that these methodologies pick up small fires better than GFED4s (Kaiser et al. 2012). The fall peak in the boreal region is driven by fires in eastern British Columbia. The seasonal CONUS springtime peak is primarily associated with small fires (as identified in GFED4s), likely linked to agricultural and prescribed burns in the southeastern US.

2.4 How emissions uncertainty impacts mass concentrations and AOD

Given the large range in fire emissions, we use observations to try to assess which, if any, inventory is most realistic. We use IMPROVE surface observations and two airborne campaigns to compare with model simulations driven by each inventory. As another constraint on aerosol abundance, we also compare model AOD with MODIS-observed AOD in North America.

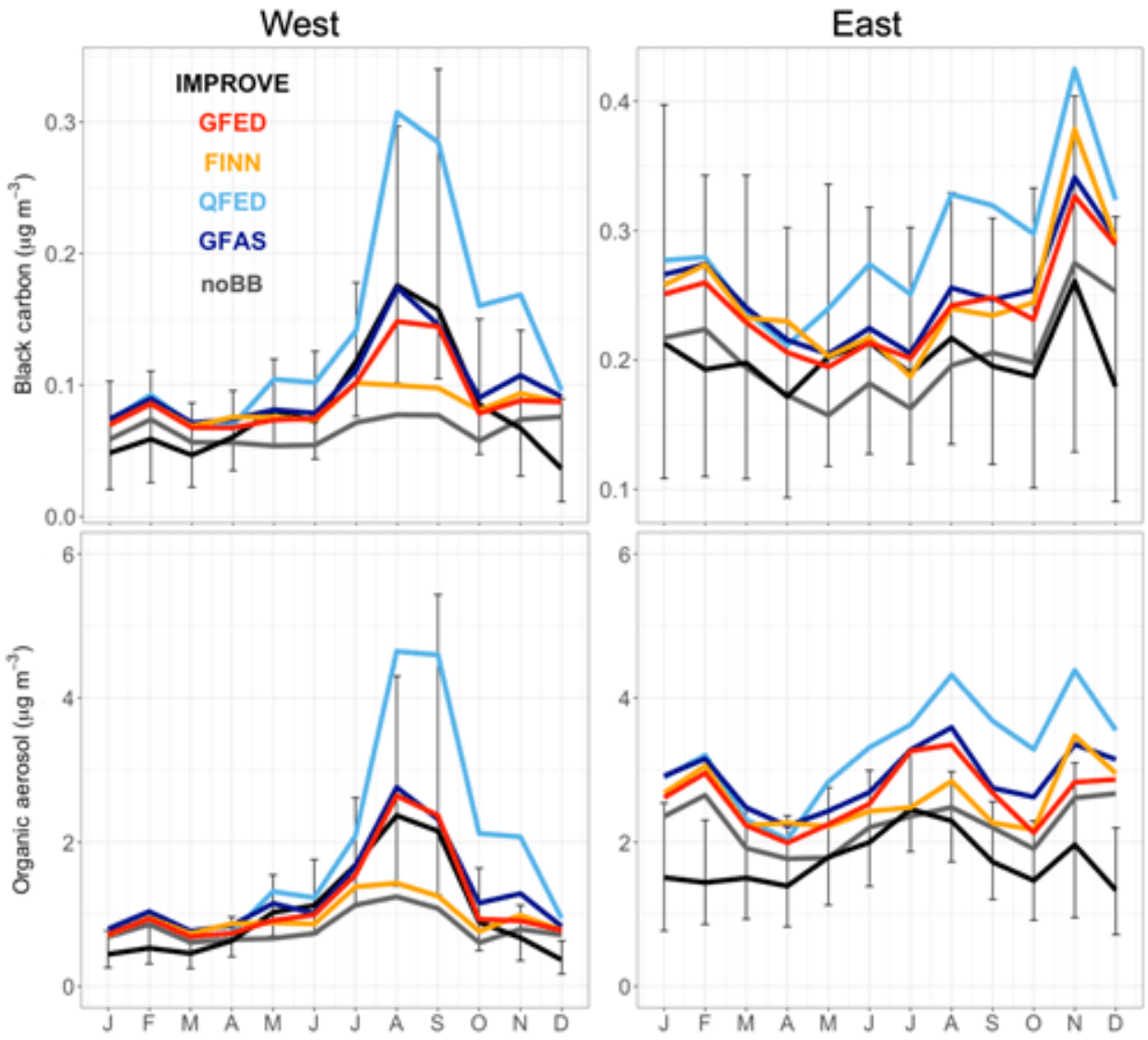

Figure 2.7 The 2012 monthly comparison of simulated and observed median surface concentrations at IMPROVE sites in CONUS split between east and west at −104° W longitude. Observations in black are compared with concentrations simulated using GFED4s in red, FINN1.5 in orange, QFED2.4 in light blue, GFAS1.2 in dark blue, and a simulation with no biomass burning (noBB) in gray. Error bars show the 25th to 75th percentile range of observations. Note the different scales among panels.

We test the model against IMPROVE observations of surface concentrations across the US and find significant variation in model skill across the inventories with QFED2.4 generally biased high and FINN1.5 low (Fig. 2.7 & 2.8). Seasonal comparisons of IMPROVE surface

concentrations with simulated concentrations driven by the four different inventories show similar patterns across aerosol species but significant differences between the western and eastern US (Fig. 2.7). This is likely related to how well the inventories capture the differences in burning regimes in the western (predominantly wildfires) and eastern (mostly prescribed and agricultural burns) US (Brey et al., 2018a). The southeastern US, in particular, is of interest to the public health and policy communities because a prevalence of agricultural and prescribed burning there, which dominates burned surface area (Nowell et al., 2018), may have a stronger impact on low altitude air quality in a relative sense than large wildfires that inject higher into the air. We also analyse the western and eastern US separately because, in the east, the magnitude of fire emissions is lower and BC, in particular, is dominated by anthropogenic sources. In the western US, GFED4s and GFAS1.2-driven concentrations of both BC and OA match the seasonality and magnitude of IMPROVE observations well. QFED2.4 is biased high, particularly during the peak in the wildfire season (August-September). FINN1.5-based concentrations are biased low and are virtually indistinguishable from simulations with no BB. In the eastern US, because fire is a smaller relative source of carbonaceous aerosol, there is less of a spread between the simulations. All inventories other than QFED2.4 do a reasonable job capturing observations with a general tendency for simulated BC and OA to be a bit too high, suggesting an overestimate in anthropogenic emissions in the eastern US. However, the 25th to 75th percentile bars on the observations show that across the US for BC and in the west for OA, virtually all the simulations fall within this range of the measurements. QFED2.4 overestimates OA well beyond the 25th to 75th percentile range in the eastern US, starting with the northern hemispheric wildfire season in May and continuing the overestimate through the end of the calendar year.

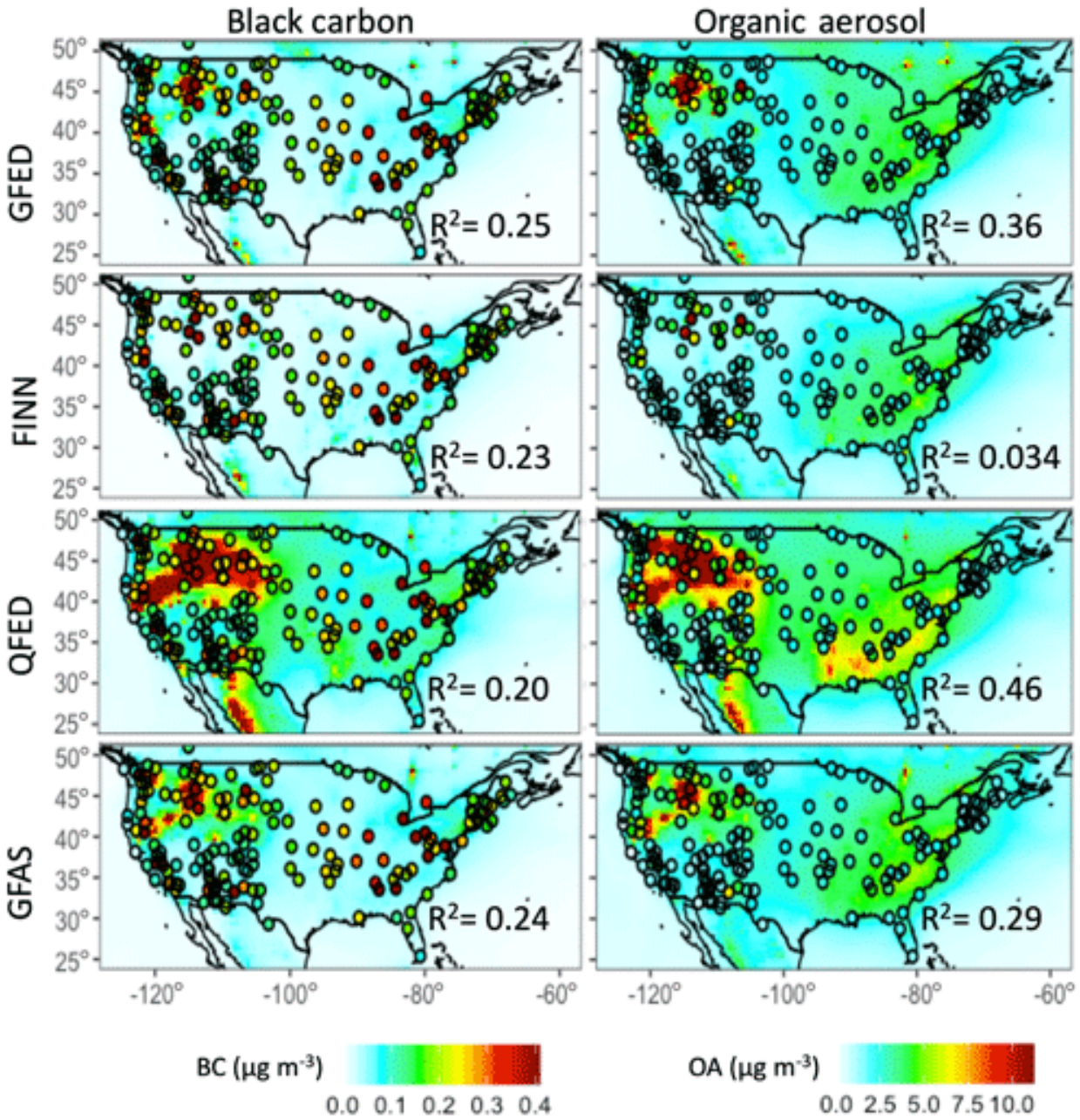

Figure 2.8 Fire season (May–September) 2012 mean surface BC and OA concentrations in CONUS with the model driven by each inventory. The circles show the mean observed surface concentrations at IMPROVE sites.

Figure 2.8 illustrates the ability of these simulations to capture the spatial distribution of observed surface concentrations during the fire season (May-September). Similar skill is seen across both aerosol species for GFED4s and GFAS1.2 (R^2 for BC, 0.25 and 0.24, respectively,

and, for OA, 0.36 and 0.29, respectively), but FINN1.5 matches observed BC somewhat better than OA (R^2 of 0.23 and 0.034, respectively) and QFED2.4 matches OA somewhat better than BC (R^2 of 0.46 versus 0.20). Consistent with the seasonal IMPROVE analysis, simulations driven by GFED4s, QFED2.4, and GFAS1.2 have greater skill in the western US than the eastern US while the FINN1.5-driven simulation performs better in the east. QFED2.4 is generally biased high, especially in the Pacific Northwest and, to some extent, in the southeastern US. However, QFED2.4 also has the highest skill in reproducing the spatial patterns of the highest concentrations when compared against the 95th percentile of observed concentrations (not shown).

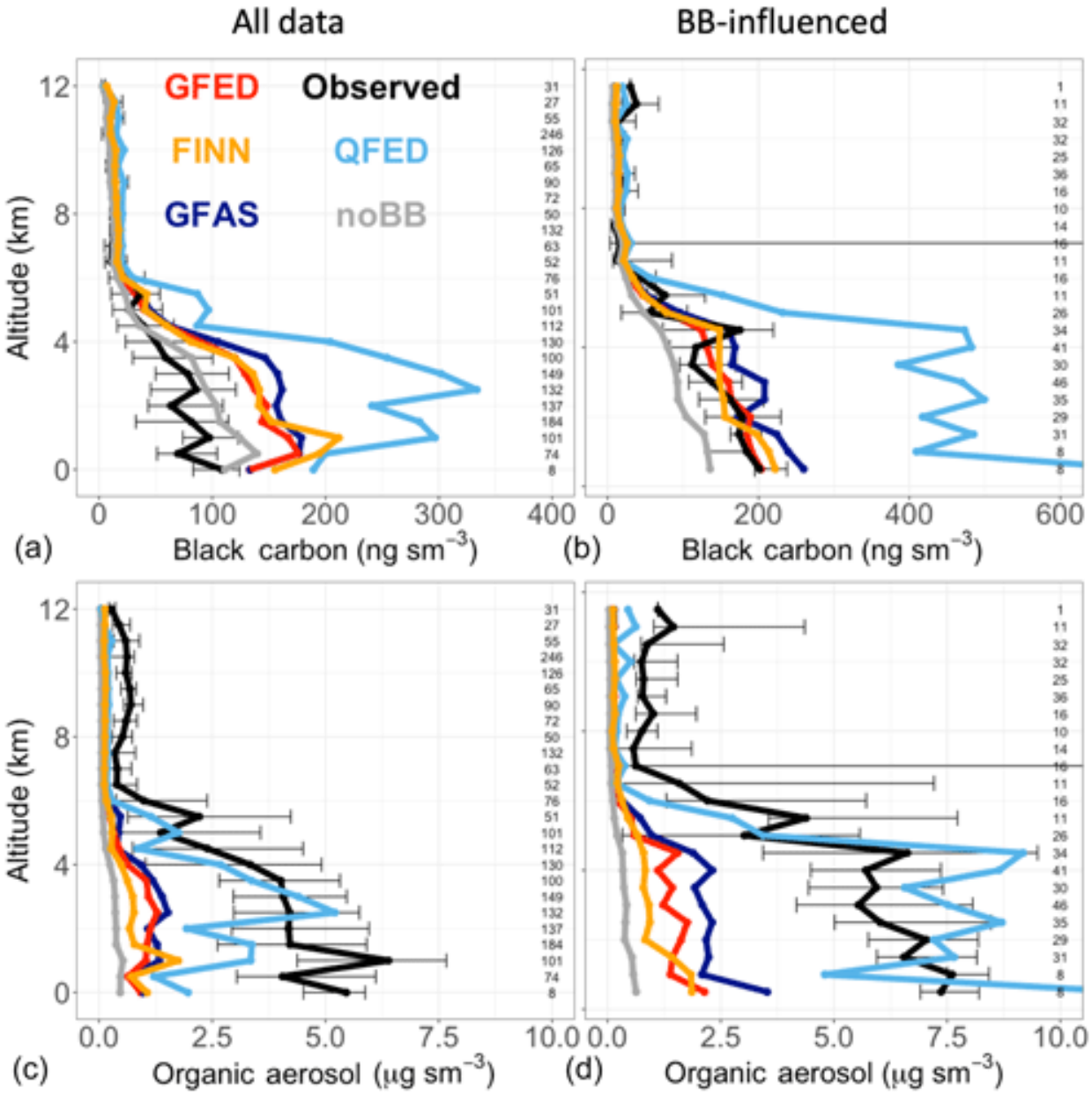

Figure 2.9 The median vertical profiles of BC and OA mass concentrations (shown in 0.5 km bins) from the DC3 campaign. Observations (black) are compared with simulations using the four fire inventories – GFED4s (red), FINN1.5 (orange), QFED2.4 (light blue), and GFAS1.2 (dark blue) – and a simulation with no fire emissions (noBB) in gray. Error bars show the 25th–75th percentile range of measurements averaged in each vertical bin. The number of observations in each bin is given on the right side of each panel. Panels **(a, c)** show total results for the campaign. Panels **(b, d)** show results filtered for the top 25th percentile of observed acetonitrile. Note the different scale between BC panels.

The ability of models to accurately represent aerosol concentrations aloft is also important for both air quality and climate, and we use two fire-influenced aircraft campaigns, DC3 and ARCTAS, to explore the model skill in this dimension. These campaigns provide observations from two very different fire regimes across North America (See Sect. 2.2.3) – DC3 in the central/southeastern US and a subset of ARCTAS focusing on boreal Canada. In addition to median vertical profiles for both BC and OA for each campaign, we also show median vertical profiles filtered by the top 25th percentile of acetonitrile (equivalent to a concentration cut off of 167 ppt for DC3 and 213 ppt for boreal ARCTAS), a useful BB tracer that allows us to investigate the most BB-influenced data.

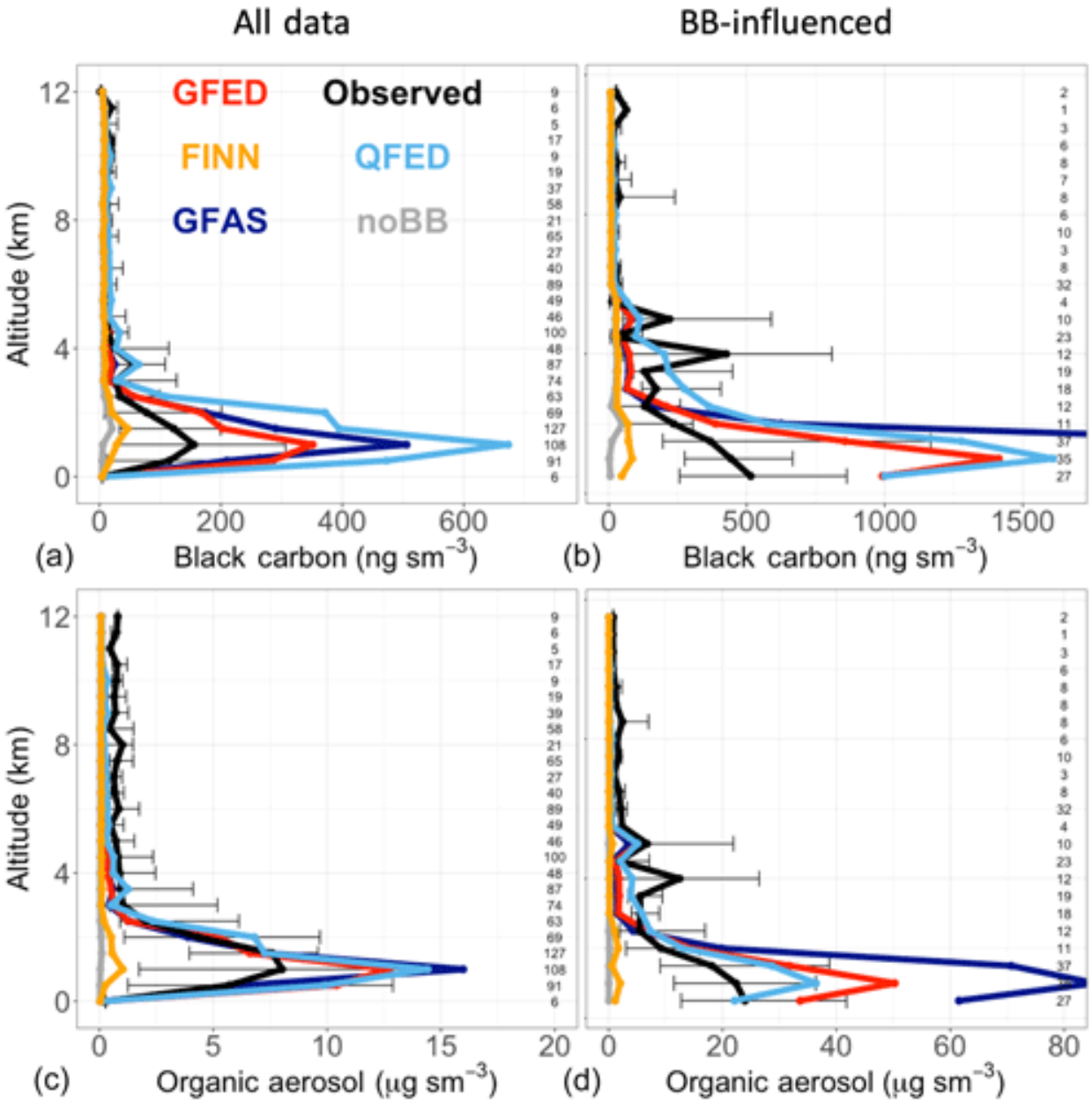

Figure 2.10 The median vertical profiles of BC and OA mass concentrations (shown in 0.5 km bins) from the boreal part of the ARCTAS campaign. Observations (black) are compared with simulations using the four fire inventories – GFED4s (red), FINN1.5 (orange), QFED2.4 (light blue), and GFAS1.2 (dark blue) – and a simulation with no fire emissions (noBB) in gray. Error bars show the 25th–75th percentile range of measurements averaged in each vertical bin. The number of observations in each bin is given on the right side of each panel. Panels **(a, c)** show total results for the campaign. Panels **(b, d)** show results filtered for the top 25th percentile of observed acetonitrile. Note the different scale among panels.

We find that concentrations driven by the various inventories perform somewhat differently against each of the campaigns (Fig. 2.9 & 2.10). Across both campaigns, QFED2.4-driven modelled concentrations are generally biased high, particularly towards the surface, while FINN1.5 simulations are nearly always biased low (Fig. 2.9 & 2.10). QFED2.4 has been constrained to observed AOD, so one could assume that it would perform best. We find that after adjusting the QFED2.4 emissions downward to account for our different OM:OC ratio, QFED2.4 simulations of OA do match observed concentrations fairly well; however, BC concentrations remain much too high. This suggests that the QFED2.4 biome-specific adjustment factors should not be applied to BC and that the scaling factor applied in this inventory to match AOD constraints may be accounting for errors in other properties (i.e. optical properties or background aerosol), not fire emissions. This is consistent with recent work showing that even when observed and modelled concentrations agree in the Amazon, observed and modelled AOD sometimes do not (Reddington et al., 2019). Over the continental US (Fig. 2.9) QFED2.4 emissions result in the highest concentrations of OA and BC; however, in the boreal region (Fig. 2.10), simulations driven by GFAS1.2 (as well as GFED4s to a lesser extent) produce more smoke than QFED2.4, consistent with the relative emissions magnitudes shown for these regions in Figures 2.2 & 2.5. As a result, both GFAS1.2 and GFED4s significantly overestimate both BC and OA concentrations towards the surface in the boreal region.

In DC3, all four inventories, and even the noBB run, overestimate the BC median vertical profile, suggesting that anthropogenic emissions are overestimated in the southeastern US, consistent with the IMPROVE analysis. This is reinforced by the DC3 BC vertical profile filtered for fire influence where three of the inventories (GFED4s, FINN1.5, and GFAS1.2 to a lesser extent) match observations quite well. Similarly, in boreal ARCTAS, all the inventories but FINN1.5 overestimate BC concentrations, especially towards the surface.

This analysis suggests that anthropogenic emissions of BC may be overestimated throughout the U.S., that the two FRP-based inventories and GFED4s, to some extent, may overestimate boreal emissions, and that FINN1.5 emissions are too low throughout, but particularly in boreal regions. In concert with the analysis at IMPROVE sites, this indicates that GFED4s-driven simulations

generally provide the best match to observations, but with substantial under/over-estimates in some regions and species.

Our comparisons with in situ mass concentrations, both at the surface and aloft, consistently suggest that the FINN1.5 inventory substantially underestimates fires over North America. Scaling relationships between fire activity and dry matter consumed should be re-visited for this inventory for North American fuels. One likely cause of the underestimation of North American fires by FINN1.5 is that the MODIS Land Cover Type (LCT) data used to define burned ecosystems assigns shrubs where other classifications assign forest, leading to lower fuel burned estimates. A second likely contributor to this underestimate is that the way in which burned area is calculated from active fire counts underestimates large wildfires, which is particularly relevant for the western US. This underestimation was also seen in earlier work by Pfister et al. (2011), using FINN1.5 to explore CO from fires in California.

Some of the disagreement aloft with the baseline model across inventories may be related to the model failure to capture injection heights for some fires which loft aerosols above the boundary layer. This is not represented in the simulations shown here, but typical approaches put too much aerosol at the top of boundary layer (~2km) (Zhu et al., 2018) (See Fig. 2.S3 for an injection height sensitivity test). It is also worth noting that sampling in the DC3 campaign was biased towards convective outflow given campaign goals, and it is possible that the model may also have errors in convection and convective removal.

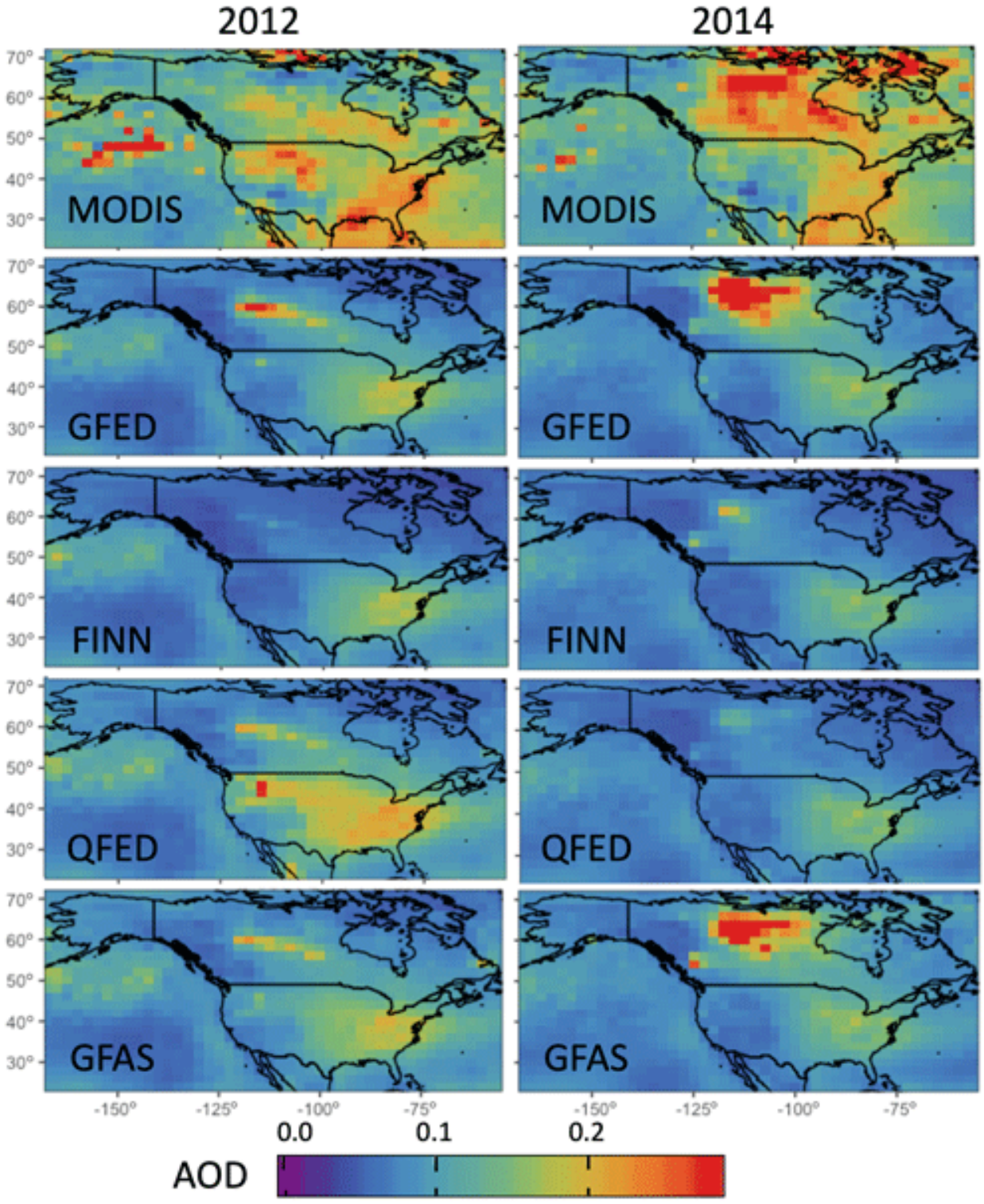

Figure 2.11 The mean Northern Hemispheric fire season (May–September) simulated AOD at 550 nm sampled to and compared with daily MODIS-observed AOD from the Aqua satellite for 2012 and 2014.

Figure 2.11 shows the spatial distribution of average AOD over North America during the northern hemispheric fire season (May – September) in both 2012 and 2014 compared to MODIS-observed AOD. In general, the model simulation underestimates observed AOD, which may result from a combination of errors in model optics, background aerosol, or cloud contamination in the MODIS product. We note that Reddington et al. (2019) similarly show that their model underestimates AOD, even when it captures the observed mass concentrations of PM over the Amazon. Here we focus on the fire-driven AOD features. Across both years, FINN1.5 AOD is low compared to MODIS in CONUS and does not capture the fires in BONA. GFED4s and GFAS1.2-driven AOD look quite similar to each other across years and include the large fire signatures in BONA that MODIS observes. AOD driven by QFED2.4 identifies the boreal, and potentially Pacific Northwest, fire signatures in 2012 but misses the large boreal hot spot in 2014 that is evident in both MODIS-observed and GFED4s and GFAS1.2 AOD.

2.5 Secondary organic aerosol from biomass burning and its implications

Previous simulations in Sect. 2.4 included the GEOS-Chem default minor source of SOA from fires. The recent NOAA Fire Lab 2016 experiment (Lim et al., 2019) reported large increases in OA mass when fire emissions were oxidatively aged, as have many other laboratory studies; though, this has not been observed in the majority of field campaigns (see Sect. 2.2.1). While uncertainties on this potential source of additional OA mass are large, we test the sensitivity of our results to this additional source. The default scheme ((0.013 times CO emissions) (Cubison et al., 2011; Kim et al., 2015)) results in a mean annual global source of BB SOA (~5 Tg yr^{-1}) from GFED4s, which is at the lower range of potential annual global fire SOA source amounts reported in Shrivastava et al. (2017). We implement a new parameterization from the NOAA Fire Lab 2016 lab studies for SOA production from BB based on Lim et al. (2019) (2.48 times POA emissions). This new scheme produces a mean annual global GFED4s source of BB SOA of ~41 Tg yr^{-1}, which is roughly in the middle of estimates reported in Shrivastava et al. 2017. In principle, such a large additional source of OA should be distinguishable from observations. However, our previous analysis using the default scheme demonstrates that the range in estimated POA is so large that it is challenging to say how much additional OA mass from SOA from BB would be consistent with the observations. In particular, even with negligible SOA the

model already matches observed OA with at least one inventory (QFED2.4). With this new parameterization, we show a roughly order of magnitude increase in the BB SOA burden (and thus more than a doubling of total OA) from GFED4s in 2012 with similar increases across the other inventories. Figure 2.12 shows how this new SOA impacts model-observation agreement with the DC3 and ARCTAS campaigns. The QFED2.4 simulations now overestimate OA across campaigns while FINN1.5 simulations improve against observations modestly, consistent with its smaller BB OA burdens to start with. It is possible that the AOD-based scaling of QFED2.4 emissions previously compensated for underestimated SOA. With the new SOA parametrization, GFED4s and GFAS1.2 simulations are better able to capture the magnitude of the mean concentrations observed during DC3. However, for boreal ARCTAS, GFED4s and GFAS1.2-driven simulations with the default scheme captured observed OA concentrations and indeed overestimated (Fig. 2.10); thus, this new large source of fire SOA exacerbates this overestimate.

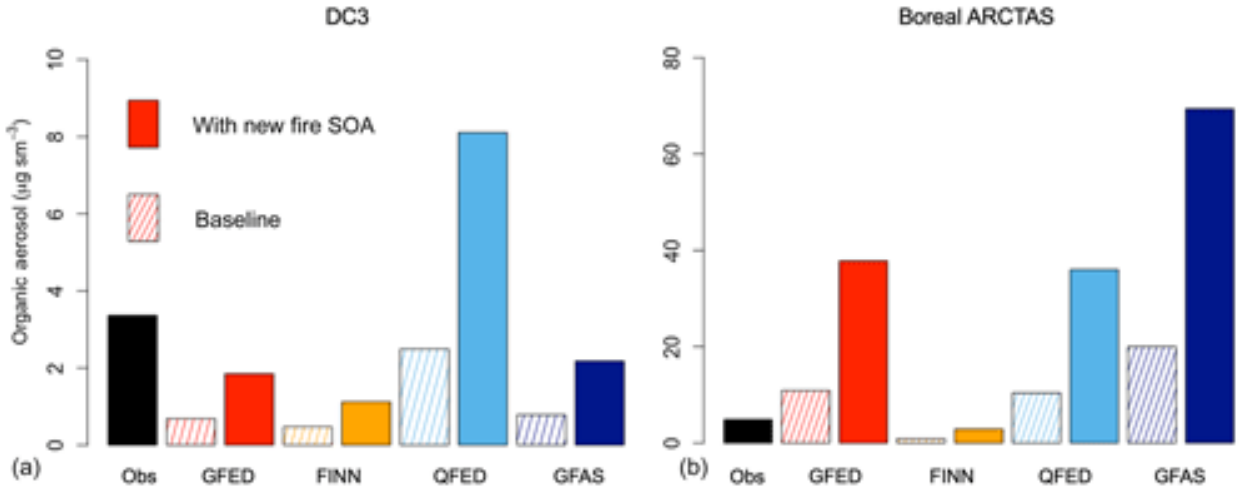

Figure 2.12 Bar plots of mean OA mass concentrations from the DC3 **(a)** and boreal ARCTAS **(b)** campaigns. Observations (black) are compared with simulations using the four fire inventories: GFED4s (red), FINN1.5 (orange), QFED2.4 (light blue), and GFAS1.2 (dark blue). The hatched version of each inventory denotes OA mass concentrations using the baseline fire SOA scheme while the full color of each shows OA with the new SOA from fire parameterization.

Our analysis of observations over North America can neither preclude nor confirm the presence of a large source of SOA from fires, given the uncertainty in POA emissions over the region.

This additional SOA source is not included in the assessment of air quality and radiative impacts of fires in Sections 2.6 and 2.7.

2.6 How emissions uncertainty translates to air quality and fire PM exposure

We next explore how uncertainty in fire emissions affects estimates of air quality impacts. We show the differences in fire $PM_{2.5}$ (calculated as the sum of the BB-only BC and OA mass fractions for aerosol under 2.5 microns) exposure spatially (Fig. 2.S5) and quantify the range in population-weighted fire $PM_{2.5}$ exposure in 2012 across North America (Canada and CONUS only) given by the four inventories. We calculate fire $PM_{2.5}$ exposure by averaging surface concentrations of the sum of BC and OA from BB across North America in 2012. We then calculate population-weighted annual fire $PM_{2.5}$ for each inventory by using population data from the Gridded Population of the World, Version 4 (GPWv4), created by the Center for International Earth Science Information Network (CIESIN) and available from the Socioeconomic Data and Applications Center (SEDAC) (Accessed 6 February 2019). We linearly interpolate the gridded UN-adjusted population count dataset, which has a native resolution of 30 arc-seconds and provides population estimates for 2000, 2005, 2010, 2015, and 2020, to 2012 and grid the data to the GEOS-Chem nested grid (0.5x0.625°). Figure 2.13 shows that the range in BBA emissions carries forward to uncertainty in 2012 North America fire annual mean $PM_{2.5}$ exposure with a range of 0.5 – 1.6μg m^{-3}. The World Health Organization (WHO) air quality guidelines for annual mean $PM_{2.5}$ are 10 μg m^{-3}, and the US EPA annual standard for $PM_{2.5}$ is 12 μg m^{-3}. Thus, the range in fire $PM_{2.5}$ exposure across the inventories in North America is equivalent to roughly 10% of these air quality standards. The population-weighted mean $PM_{2.5}$ exposure due to fires in North America varies by about a factor of two between different years, reflecting the location and intensity of different fire events (see Fig. 2.S6 and 2.S7 for an analysis of 2012 – 2014 at 2x2.5º).

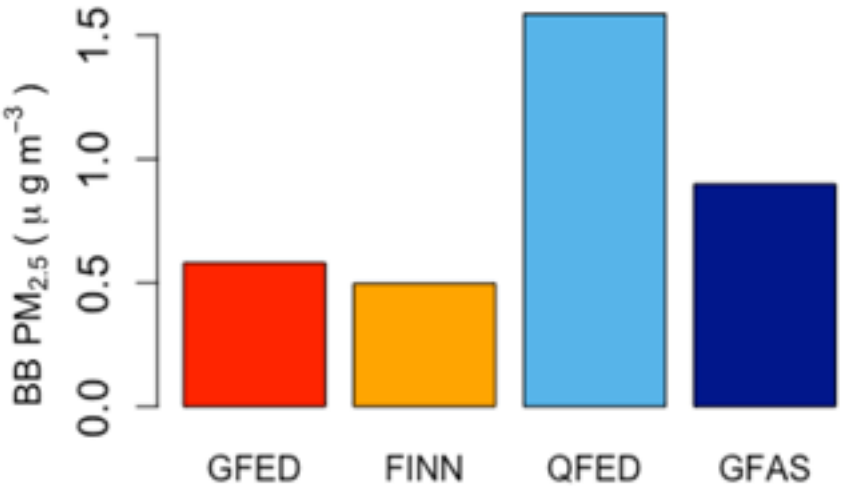

Figure 2.13 Bar plots of the 2012 annual mean population-weighted fire $PM_{2.5}$ exposure across the four inventories (GFED4s in red, FINN1.5 in orange, QFED2.4 in light blue, and GFAS1.2 in dark blue) across North America (Canada and CONUS only) at nested resolution. See Figure 2.S6 for an analysis from 2012 to 2014 and for bar plots split out for Canada and the US at 2×2.5°.

Because the 24-hour average $PM_{2.5}$ reflects acute exposure, we also looked at the differences in this metric when driven by each inventory. Over the United States, the simulated daily $PM_{2.5}$ from fires in 2012 ranges up to 1778 μg m^{-3} as simulated by QFED2.4 while FINN1.5-driven simulations show the smallest maximum BBA concentration at 55 μg m^{-3}. A number of regions experience well over the $PM_{2.5}$ daily standard (35 μg m^{-3}) due to fires alone for more than ten days a year, and in some locations for several weeks (see Fig. 2.S8), highlighting smoke as a major cause for air quality degradation in the United States. These regions and the magnitudes of daily fire influence are highly variable year to year.

2.7 Impacts on the direct radiative effect

Across North America and globally, we compare the mean annual top-of-atmosphere (TOA) all-sky DRE of BB-only BC and OA driven by each of the inventories with the OA DRF reported in the Fifth Assessment Report (AR5) of the Intergovernmental Panel on Climate Change (IPCC). We quantify the annual mean BBA DRE in 2012 (Fig. 2.14) and the Northern Hemispheric fire season (May – September) average DRE in each year from 2012 to 2014 (Fig. 2.S9) to investigate interannual variability. The differences across inventories seen in the sections above

translate to the large ranges in DRE estimated for BONA and CONUS with smaller, but still significant, ranges seen globally.

For 2012, GFAS1.2-driven global DRE is largest in absolute magnitude for BBA (-0.11 W/m^2) with FINN1.5 smallest (-0.048 W/m^2) (See Table 2.S1 for underlying values). These values are significantly more negative than previous estimates of BBA DRE, which ranged from -0.01 to 0.13 W/m^2 (Rap et al., 2013; Ward et al., 2012). Previous work suggests that the whitening of fire-generated brown carbon (BrC) may limit the global absorption from BrC (Forrister et al., 2015; Wang et al., 2016). Wang et al. (2018) estimate a modest global mean DRE of BrC of +0.048 Wm^{-2} when accounting for this whitening; however, uncertainties on the magnitude and the evolution of absorption of BrC remain large. We treat OA as scattering here, which may lead to a positive bias in the total DRE of carbonaceous aerosol from smoke; thus we focus on the range in values associated with the use of various fire inventories rather than the absolute magnitude of the DRE. The range across the 2012 annual global mean inventory-driven BBA DRE is -0.062 W/m^2, which is comparable to the magnitude of the direct radiative forcing of OA (-0.09 W m^{-2}) reported in the in AR5 (Intergovernmental Panel on Climate Change, 2014). Only some fires contribute to the DRF, but we have shown here that the uncertainty in BBA DRE as represented by the spread in values driven by different inventories is on a comparable scale to the anthropogenic influence on OA forcing. While we have not assessed the annual global mean BBA DRE across other years, we have quantified the northern hemispheric fire season BBA DRE from 2012-2014, which show generally similar trends across years with some variability; larger boreal fire years generally affect the DRE driven by GFED4s and GFAS1.2 the most (see 2014 in Fig. 2.S9). 2014 also appears to be an outlier year where GFED4s and GFAS1.2-driven OA DRE is larger than QFED2.4-driven DRE across both BONA and CONUS and also globally, consistent with our emissions analysis (See Fig. 2.5).The IPCC estimate of aerosols' contributions to the DRF only includes one set of historical fire emissions and one for each RCP – this choice allows for better intermodal comparisons but masks underlying uncertainty from fire emissions, which we have shown here to be important.

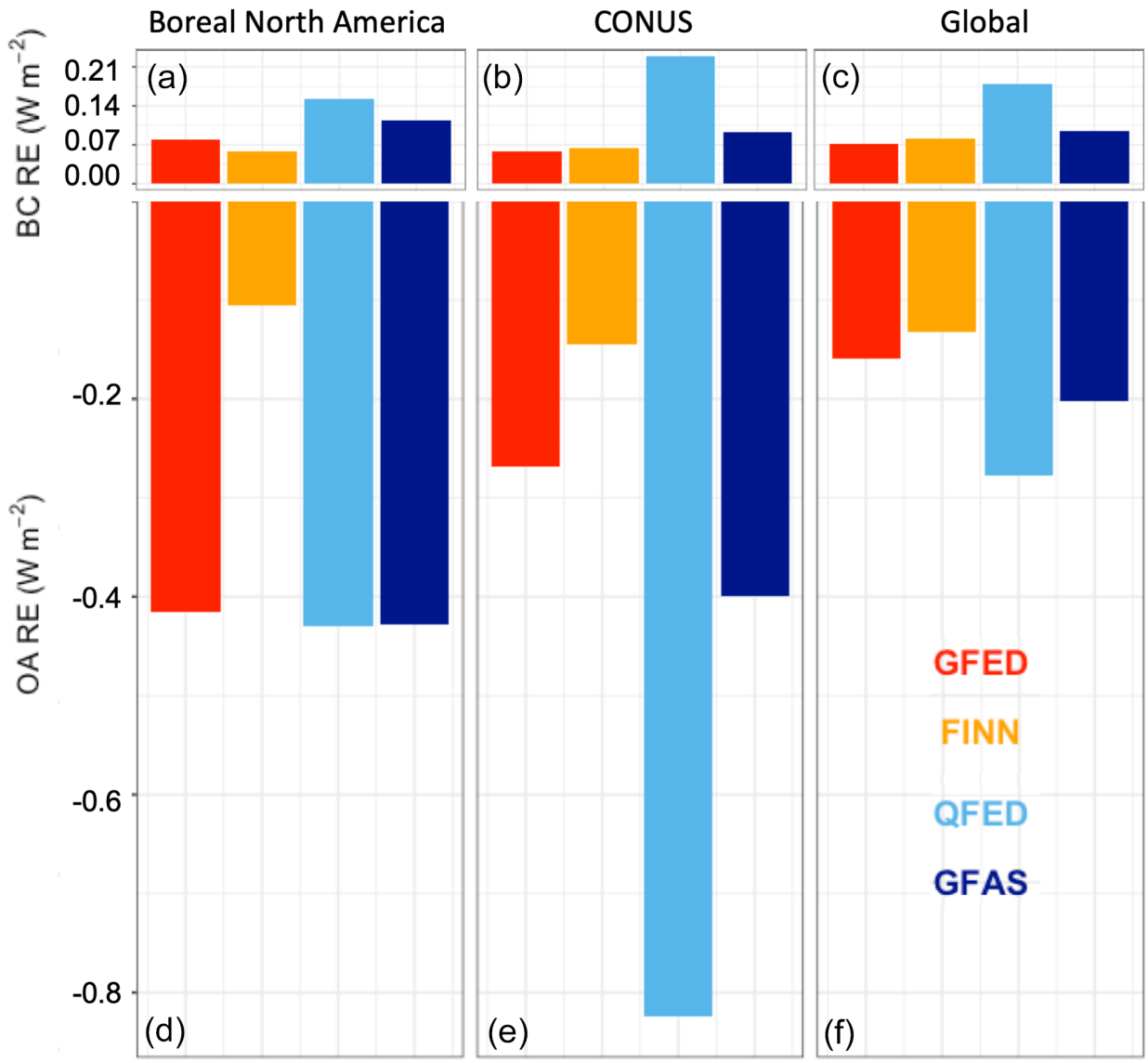

Figure 2.14 Top-of-atmosphere all-sky direct radiative effect of BB-only BC **(a–c)** and OA **(d–f)** averaged over 2012 in BONA, CONUS, and globally. GFED4s is shown in red, FINN1.5 is orange, QFED2.4 is light blue, and GFAS1.2 is dark blue (the size of BC versus OA panels is not to scale).

2.8 Conclusions

Most models do not test basic uncertainty associated with fire emissions both in air quality and climate studies – our work suggests that this uncertainty is large and may substantially impact our understanding of fire impacts. We note that, while we refer to the spread across these inventories as the "uncertainty" in emissions, additional factors, not represented by any of these

inventories, may increase the true uncertainty in the estimated emissions beyond what we have shown in this work. We provide an evaluation of this uncertainty by comparing multiple, commonly-used fire emission inventories (GFED4s, FINN1.5, QFED2.4, and GFAS1.2) that have become available in the last five to ten years. We show that the four inventories perform differently depending on species, location, and season. We also calculate that average BC and OC emissions differ by roughly a factor of five and four, respectively, across the inventories in BONA. The range in BC and OC emissions in CONUS is even larger (a factor of ~7 and 6, respectively). Global ranges in BC emissions are smaller than those in North America (~2.3) with a somewhat more modest spread (~1.7) in OC emissions, possibly because of emission factor differences. We also show that dry matter, not emission factor, differences are the driving force for emissions variation across inventories.

With such large differences in emissions, we test which of these inventories drives model simulations closest to observations over North America. We show that modeled concentrations both at the surface and aloft show variable skill across inventories when compared to in situ observations (IMPROVE, DC3 and ARCTAS campaigns) with FINN1.5 biased low for BC and OA and QFED2.4 biased high against observed BC. GFED4s and GFAS1.2-driven AOD also do a better job matching MODIS-observed AOD over the regions, in general and with specific features, than FINN1.5 and QFED2.4. QFED2.4 emissions may be biased high because they were scaled up to ensure that the GEOS model AOD simulation matches satellite-observed AOD, potentially mis-attributing biases in aerosol extinction efficiency and SOA formation in the GEOS model to emission; MODIS AOD has also been shown to be high in some environments (Lapina et al., 2011). That these enhancement factors are too high is further reinforced by the fact that, after adjusting the QFED2.4 emissions downward to account for our different OM:OC ratio, QFED2.4 simulations of OA match observed concentrations fairly well across campaigns – while BC concentrations remain much too high. The assumptions that FINN1.5 uses to compute burned area from active fire counts likely contribute to its low bias and should be revisited, especially for regions with large wildfires (e.g., boreal Canada and the western US). We also show that a laboratory-based parameterization for fire SOA, scaled from fire POA emissions, does improve model agreement with observations in some regions.

However, from our comparisons, the range in POA emissions makes it challenging to discern whether SOA from fires is significant.

This range in fire emissions also carries through to uncertainties in the air quality and radiation impacts of fires, which we have shown to be large and significant. Over North America depending on the inventory used, large differences in both the spatial extent and magnitude of BBA-only annual and daily surface concentrations and also in population-weighted annual fire PM2.5 exposure (0.5 - 1.6 μg m^{-3} for 2012) arise. We have also shown that fire emissions uncertainty produces a considerable envelope in global BBA DRE (-0.062 W m^{-2}), roughly comparable to the direct radiative forcing of OA (-0.09 W m^{-2}) reported in AR5.

Additional evaluation of satellite-based fire emission inventories, particularly in other large BB source regions, would help to provide insight into fire emissions uncertainty. Observations at all scales (surface, aloft, and satellite) are needed to better constrain our understanding of fire emissions and processing. To bridge fire emissions and subsequent impacts, additional investigation of uncertainties in fire aerosol aging and processing (e.g., injection heights, mixing state, SOA formation, etc.) is needed. Our work suggests that emissions uncertainty is a major factor in our ability to model the air quality and climate impacts of fires and should be incorporated into modeling studies of both.

Chapter 3. Investigating Carbonaceous Aerosol and its Absorption Properties from Fires in the western US (WE-CAN) and southern Africa (ORACLES and CLARIFY)

Adapted from: Carter, T.S., C.L. Heald, C. D. Cappa, J. H. Kroll, T. L. Campos, H. Coe, M. I. Cotterell, N. W. Davies, D. K. Farmer, C. Fox, L. A. Garofalo, L. Hu, J. M. Langridge, E. J.T. Levin, S. M. Murphy, R. P. Pokhrel, Y. Shen, K. Szpek, J. W. Taylor, H. Wu (2021), Investigating Carbonaceous Aerosol and its Absorption Properties from Fires in the western US (WE-CAN) and southern Africa (ORACLES and CLARIFY), J. Geophys. Res.,126, e2021JD034984.

3.1 Introduction

Biomass burning (BB), both wildfires and prescribed burns, emits large quantities of $PM_{2.5}$ globally (Akagi et al., 2011) with air quality and climate impacts across regional to global scales. Air quality degradation from smoke impairs visibility and is detrimental to human health (Johnston et al. 2012; Liu et al. 2015; O'Dell et al. 2020; Reid et al. 2016; Williamson et al. 2016) with substantial associated economic costs (e.g., Jones, 2017). Climate impacts of BB emissions include heating and cooling of Earth's atmosphere and surface caused by aerosol-radiation and aerosol-cloud interactions, as well as a decrease in planetary albedo associated with BC deposition on snow (Bond et al. 2013). These impacts remain uncertain and poorly constrained – in large part because the magnitudes and characteristics of different BB aerosol (BBA) species from varied fire and fuel types are not well understood.

Particulate matter from BB is dominated by carbonaceous aerosol; previous work has estimated that BB adds between ~16 – 34 Tg yr^{-1} of aerosol to the atmosphere (Akagi et al., 2011; Bond et al., 2013; Carter et al., 2020). Globally, BB is responsible for roughly one third of all BC emissions and between 65 – 90% of OA emissions (Bond et al., 2013; Carter et al., 2020). However, uncertainties on these emissions are high; for example, estimates of BBA from the four most commonly used fire emissions inventories differ by roughly a factor of two globally with larger differences regionally (Carter et al., 2020). Important BB source regions can have both very different dominant combustion types and also fuel types - both of which are difficult to

globally characterize, and thus are not adequately captured by emission inventories, particularly at high spatial and temporal resolution.

Biomass burning aerosol has three major carbonaceous constituents, which interact directly with radiation in different ways: BC, which is largely absorbing; POA, which generally scatters but which may also absorb, and which is then referred to as brown carbon (BrC); and SOA, which has been shown to mostly scatter (Laskin et al., 2015). Inorganic, non-carbonaceous components are also present in BBA, but in relatively small quantities (typically <15% of total submicron aerosol in fresh wildfire emissions) (Garofalo et al. 2019). Unlike BC, which is also emitted in low quantities (typically ~2 – 10 % of submicron mass) (Garofalo et al., 2019), these non-carbonaceous components play a minor role in radiative effects beyond direct light scattering and are not considered here. The net radiative impact of smoke is thus a complex combination of the different abundance and properties of BBA species. Previous work has reported a large spread with uncertainty in even the sign of the possible direct radiative effect (DRE or the instantaneous radiative impact) (Heald et al., 2014) of BBA from −0.01 to +0.13 W m^{-2} (Rap et al., 2013; Ward et al., 2012). The IPCC Fifth Assessment report concludes that the absorption and scattering from fires effectively offset each other, but the underlying models used do not generally have an explicit representation of BrC (IPCC, 2014).

Recent work on BBA absorption properties has provided key insights, but further work is needed to better constrain the DRE of BBA. The ability of a species to absorb light is commonly represented by the mass absorption coefficient (MAC, the absorption cross-section per unit mass with a unit of m^2 g^{-1}), which depends on the molecular form (Liu et al., 2020) of the absorbing species as well as aerosol shape and size. Bond & Bergstrom (2006) determined that the MAC of BC from combustion sources is 7.5 m^2 g^{-1} at a wavelength of 550 nm for uncoated particles based on an average of ~20 measurements. This translates to a MAC of 6 m^2 g^{-1} at a wavelength of 660 nm, assuming an absorption Ångstrom exponent (AAE) of 1. Wang et al. (2014) showed that the direct radiative forcing (DRF) of BC had been previously overestimated due to an overestimate of the BC lifetime and an incorrect attribution of BrC absorption to BC. Wang et al. (2018) discussed how representing BBA as externally mixed (i.e., that the majority of OA is externally mixed with BC) is reasonable considering the low BC:OA emission ratio from BB and

biofuel and typical coating thickness (Moffet & Prather, 2009; Perring et al., 2017; Schwarz et al., 2008b). Based on several field studies (Cappa et al., 2012; Lack et al., 2012; Moffet & Prather, 2009; Schwarz et al., 2008a; Schwarz et al., 2008b), Wang et al. (2014) showed that applying different absorption enhancement (AE, i.e., the MAC of the internally mixed BC with coating species such as OA and inorganics, relative to the MAC of the corresponding uncoated BC) factors for the hydrophilic components of BB-emitted BC (1.5) and fossil fuel (FF)-derived BC (1.1) could help approximate the mixing state of BC and OA and thus lensing effects, and improve agreement with observations. The so-called lensing effect is when a coated BC particle with a non- or weakly-absorbing shell (in fire emissions, this shell is generally composed of OA) absorbs more than the BC core alone (Bond et al., 2006; Fuller et al., 1999; Jacobson, 2000). The AE is assumed to result from coatings on BC, distinct from absorption by BrC. Other recent work that focused on combustion of fuels native to the western US and primary particles emitted found AE factors of 1.2 to 1.5 for BB BC (McMeeking et al., 2014) and no larger than 1.19 (McClure et al., 2020), suggesting that the assumption of Wang et al. (2014) (used in this work) is at the high end of the estimated range. However, given that the studies cited here are mostly focused on North and central America, it is possible that the AE for smoke from Africa (where BC:OA is higher) may differ from that in the western US. A recent study of observations downwind of Africa reported AE factors as high as 1.85 (Taylor et al. 2020).

Substantial uncertainties exist around the emission, production, and absorption properties of BrC. Biomass burning POA has been shown to be the dominant source of BrC globally. Laboratory work has shown that some SOA can also absorb (Laskin et al., 2015). Palm et al. (2020) showed, with a combination of lab and field data, that the contribution of nitroaromatics, specifically nitrocatechol, to aerosol absorption is outsized compared to its mass. However, in general, SOA has been found to be considerably less absorbing than BB POA (see for example Figure 1 in Wang et al. (2014)). Some work has suggested that BrC absorption may constitute up to ~40% of total absorption of carbonaceous aerosol, but there is a large range for this value and that of BrC DRE (+0.03 to +0.6 W m^{-2}) in the literature (Feng et al., 2013; Lin et al., 2014; Wang et al., 2014; Wang et al., 2018). The MAC of OA is smaller than that of BC (e.g., OA MAC at 550 nm is estimated to be 0.35 m^2 g^{-1} versus 7.5 m^2 g^{-1} for uncoated BC discussed above (Bond & Bergstrom, 2006; Wang et al., 2018)). However, BrC absorption has a strong wavelength

dependence with increasing absorption in the UV; studies show a range in OA MAC from 0.65 to 5.01 $m^2 g^{-1}$ at 365 nm (Jo et al., 2016; Wang et al., 2018). Brown carbon may also undergo whitening (a decrease in absorptivity over time); limited field work to date suggests that this occurs with an e-folding time of ~ 1 day (Forrister et al., 2015; Wang et al., 2016).

Biomass burning aerosol emitted from fires with various fuel and combustion types has been shown to have different absorption characteristics (e.g., more flaming fires may lead to more absorbing BrC (McClure et al., 2020; Saleh et al., 2014)). However, global modeling studies have typically assumed globally uniform properties independent of combustion phase (Chung et al., 2012; Feng et al., 2013; Jo et al., 2016; Park et al., 2010; Wang et al., 2014). In addition, very little work has been done to validate model simulations of aerosol absorption, particularly from BrC (Liu et al., 2020). Challenges exist with the measurement techniques used for BBA absorption that would subsequently be used to constrain models (Liu et al., 2020). Filter-based techniques like aethalometers (Hansen et al., 1983), particle soot absorption photometers (PSAPs) (Bond et al., 1999), and continuous light absorption photometers (CLAPs) (Ogren et al., 2017) are commonly used measurement techniques but are susceptible to a variety of biases (Davies et al., 2019; Lack et al., 2008), including multiple scattering within the filter and loadings on saturated filters leading to nonlinear responses and backscatter variability due to particle size distributions (Foster et al., 2019 and references therein). An alternative approach to measuring absorption is to take the difference between extinction and scattering, as done by the cavity-attenuated phase shift PM single-scattering albedo (CAPS PM_{SSA}) instrument. The CAPS PM_{SSA} has high accuracy and precision but only when measured aerosol has a low single scattering albedo (Foster et al., 2019). Alternatively, photoacoustic spectroscopy (PAS), has been shown to be an unbiased and sensitive approach to measuring the absorption of dry aerosol but requires a more complex calibration (Cotterell et al. 2020, 2021; Davies et al. 2018; Foster et al. 2019 and references therein).

In the last few decades, burned area has decreased globally by 25%, but increased in some important BBA source regions like southern Africa and the western US (Andela et al., 2017). Previous work has suggested that future trajectories in fire impacts will vary across regions (e.g., Ford et al., 2018; Val Martin et al., 2015; Yue et al., 2013). Thus, with different fire and fuel

properties leading to varying smoke absorption properties and with BB regions already experiencing a range of fire trends, it is essential that we better understand the quantity of BBA and its absorption properties globally, with at least regional granularity.

In this study, we use the GEOS-Chem chemical transport model, satellite observations, and data from three aircraft campaigns that surveyed very different fire regimes (western US and southern Africa) to contrast the abundance and properties of carbonaceous aerosol from fires in two important BB source regions and to test the model representation of these properties.

3.2 Model and Observation Descriptions

3.2.1 The GEOS-Chem model

We use GEOS-Chem (https://geos-chem.org, last access: April 24, 2019), a global chemical transport model, coupled with the rapid radiative transfer model for global circulation models (RRTMG, Iacono et al., 2008), a configuration known as GC-RT (Heald et al., 2014), to explore BBA and its absorption properties in the western US and off the coast of southern Africa. GEOS-Chem is driven by assimilated meteorology from the Modern-Era Retrospective analysis for Research and Applications, Version 2 (MERRA-2), at the NASA Global Modeling and Assimilation Office (GMAO). We run version 12.3.0 of GEOS-Chem (https://doi.org/10.5281/zenodo. 2620535) with a horizontal resolution of 2°×2.5° and 47 vertical levels with a chemical time step of 20 min and a transport time step of 10 min as recommended by Philip et al. (2016). We perform 6-month spin-up simulations prior to the time periods of interest, July-August 2016, August-September 2017, and July-September 2018. We also perform nested simulations over North America at 0.5°×0.625° (with boundary conditions from the global simulation) for comparison against WE-CAN observations (see Sect. 3.2.2) with transport and chemistry time steps of 5 and 10 min, respectively.

GEOS-Chem includes $SO_4^{2-}/NO_3^-/NH_4^+$ thermodynamics (Fountoukis and Nenes, 2007) coupled to an O_3–VOC–NO_x–oxidant chemical mechanism (Chan Miller et al., 2017; Mao et al., 2013; Travis et al., 2016) with integrated Cl-Br-I chemistry (Sherwen et al., 2016). Aerosols are modeled as fixed log-normal size distributions. Aerosol optical properties are generally from the Global Aerosol Data Set (GADS) database (Köpke et al., 1997) with updates from Drury et al.

(2010) and Wang et al. (2014; 2018), which are detailed below. RRTMG calculates both longwave and shortwave atmospheric radiative fluxes. When coupled to GEOS-Chem, this calculation is performed every 3 h. Longwave and shortwave DRE at the top of the atmosphere are summed and reported as total DRE.

The standard simulation of BC in GEOS-Chem is described in Park et al. (2003). We update this simulation as described by Wang et al. (2014), including the following: the initial hydrophilic fraction for BC is set to 20% for FF/biofuel (BF) and to 70% for BB; FF BC aging is proportional to the concentration of SO_2 and OH; BB/BF BC aging is specified with a 4h e-folding time; and the BC size (log-normal distribution) for FF BC is set to a geometric mean diameter (GMD) = 60 nm and standard deviation (δ) = 1.6 and for BF/BB BC to GMD = 140 nm and δ = 1.4. To account for differences in mixing state, we apply an AE from coating of BC of 1.1 for FF BC and of 1.5 for BF/BB BC. With these updates, including the AE, and using Mie Theory with input from the Global Aerosol Data Set (GADS, http://opac.userweb.mwn.de/radaer/gads.html)(Köpke et al., 1997), Wang et al. (2014) estimate the "best" dry MAC at 550 nm for FF BC of 7.0 $m^2\ g^{-1}$ and for BB BC of 9.5 $m^2\ g^{-1}$ (corresponding to uncoated MAC values of 6.3 $m^2\ g^{-1}$ without the AE, which is substantially lower than the "best" estimate from Bond & Bergstrom 2006 and smaller than McClure et al. 2020). The wavelength dependence of the refractive index of BB BC that we use is based on the GADS (http://opac.userweb.mwn.de/radaer/gads.html)(Köpke et al., 1997), a database used by many global models because it covers wavelengths from near-UV to IR. Table 3.1 provides more details on the MAC values for BB BC and BrC used in this work. We note that the associated AAE of BC decreases with wavelength, and is well below 1 for all visible wavelengths (referenced to 405 nm); this may underestimate the BC MAC at shorter wavelengths as discussed in Sections 3.3.2 and 3.4.

	Intrinsic	Intrinsic MAC_{BC}	Baseline	Saleh parameterization MAC_{OA} ($m^2\ g^{-1}$) for BrC	FIREX parameterization MAC_{OA} ($m^2\ g^{-1}$) for BrC

λ (nm)	MAC_{BC} ($m^2\ g^{-1}$)	times absorption enhancement (1.5) ($m^2\ g^{-1}$)	MAC_{OA} ($m^2\ g^{-1}$) for BrC	WE-CAN	ORACLES-2016	CLARIFY	WE-CAN	ORACLES-2016	CLARIFY
660	5.3	8.0	0.13	0.11	0.11	0.11	0.06	0.14	0.15
470	6.6	10.0	0.74	0.61	0.85	0.90	0.64	0.76	0.80
405	6.9	10.4	0.95	1.1	1.5	1.6	0.90	1.2	1.3

Table 3.1. BB carbonaceous aerosol mass absorption coefficient (MAC) values used in the GEOS-Chem model at wavelengths relevant to comparison with observations from the three aircraft campaigns investigated in this study.

The standard POA simulation, used here, emits 50 % of POA as hydrophobic and ages hydrophobic POA to hydrophilic POA with an atmospheric lifetime of 1.15 d (Chin et al., 2002; Cooke et al., 1999). We use OA to OC (organic carbon) ratios of 1.4 and 2.1 for hydrophobic and hydrophilic OC, respectively. The model formation of SOA follows the simple scheme described in Pai et al. (2020); SOA precursor gases from fires are emitted at 0.013 g per g CO emitted. The SOA precursor gases are then aged to SOA based on a first-order rate constant (lifetime of 1 d). We use the optical properties for "white" carbon as described in Wang et al. (2018) for SOA and FF POA. We simulate BrC by assuming that emitted BB POA is BrC, using optical properties for absorbing OA as described in Wang et al. (2018): for a dry BB POA, the MAC equals 1.33 $m^2\ g^{-1}$ at 365 nm, 0.35 $m^2\ g^{-1}$ at 550 nm, and 0.13 $m^2\ g^{-1}$ at 660 nm, which decreases with aging. The wavelength dependence of BrC is also based on Wang et al. (2018), which used the Saleh parameterization and one average BC:OA ratio globally. See Table 3.1 for these baseline values of MAC_{OA} at wavelengths relevant to our model-observation comparisons. We implement the whitening parametrization from Wang et al. (2018) that assumes the absorptivity of OA decreases at a rate related to the concentration of OH (with a rate constant corresponding to a 1-day whitening e-folding time when assuming [OH] equal to 5 x 10^5 molec

cm^{-3}) and that absorptivity does not drop below 25% of the starting value. Alternative parameterizations for the properties of BrC are considered in Section 3.4.

Anthropogenic emissions (including fossil and biofuel sources) of both BC and POA follow the CEDS global inventory (Hoesly et al., 2018) with regional inventories used instead when available, including NEI2011v1 over the US (Air Pollutant Emissions Trends Data, 2020) scaled to 2013 (scale factors were not available beyond 2013), APEI over Canada, and DICE-Africa over Africa (Marais and Wiedinmyer, 2016). Trash burning emissions are from Wiedinmyer et al. (2014). Aircraft emissions are from the AEIC inventory (Simone et al., 2013; Stettler et al., 2011). Biogenic emissions are calculated online from the MEGANv2.1 emissions framework (Guenther et al., 2012). Fire emissions, emitted into the boundary layer, are from the GFED4s inventory (Giglio et al., 2018; van der Werf et al., 2017), specified on a daily timescale. GFED4s was selected because previous work has shown that it generally matches observations well and is typically in the middle of the range of emission estimates across inventories (Carter et al., 2020). Global total emissions of BC are 9.0 Tg and of OC are 32.5 Tg in 2018 in our simulations, but it is important to note that emissions vary year to year.

3.2.2 In situ observations

The WE-CAN (Western Wildfire Experiment for Cloud Chemistry, Aerosol Absorption, and Nitrogen) summer campaign used the NSF/NCAR C-130 aircraft to survey wildfires (mostly forest fires) in the western US from July 24 to September 13 2018 (see Fig. 3.1 for flight tracks). Several of the large fires in California and Oregon in the summer of 2018 are visible in the smoke emissions shown in Fig. 3.1, including the Mendocino Complex, Carr, and Ferguson Fires. WE-CAN targeted smoke in the near-field (<6 hours since emission) by sampling close to the fire and systematically sampling downwind to intercept the same parcel of air multiple times to track evolution of smoke over time. Black carbon mass concentrations were measured using a single-particle soot photometer (SP2; DMT; Schwarz et al., 2008a). For WE-CAN, the SP2 detection range for BC mass equivalent diameters is ~90 – 500 nm, and the calibration uncertainty is estimated to be 30%. BC mass outside the SP2 detection range was not estimated for the WE-CAN data set. However, based on observations of BC size distributions from biomass burning (Schwarz et al. 2008a), it is expected that the SP2 measurements captured the

majority of the BC mass; this is similarly true for the ORACLES and CLARIFY campaigns. When sampling in plumes, the SP2 sample line was diluted with HEPA-filtered, ambient air to prevent signal saturation. Organic aerosol mass concentrations were measured using a high-resolution time-of-flight aerosol mass spectrometer (HR-AMS; Aerodyne Inc.) with a detection range for vacuum aerodynamic particle diameter of 70 – ~1000 nm and an estimated uncertainty of 35% (Garofalo et al., 2019). Carbon monoxide (CO) was measured using two instruments: a quantum cascade laser instrument (QCL; CS-108 miniQCL, Aerodyne, Inc.) and a gas analyser utilising cavity ring-down spectroscopy (G2401-m WS-CRD; Picarro). Garofalo et al. (2019) noted that the QCL instrument had a better measurement precision for CO concentrations than that of the Picarro gas analyzer. Therefore, we use the concentration measurements from the QCL instrument in our analyses here. Acetonitrile, a useful BB tracer, was measured using a proton transfer reaction time of flight mass spectrometer with an uncertainty in mixing ratios of 15% (PTR-ToF-MS 4000; Ionicon Analytik; (Müller et al. 2014)). A photoacoustic absorption spectrometer (PAS) was used to measure total absorption with two dry (RH < 15%) channels at 405 and 660 nm (Foster et al. 2019).

ORACLES (ObseRvations of Aerosols above CLouds and their intEractionS) was a five-year investigation with three intensive observation periods in roughly August – September of 2016, 2017, and 2018 that surveyed off the Atlantic coast of southern Africa. This campaign was designed to study key processes that regulate the climate impacts of African BBA – a large global source of particles, responsible for ~1/3 of all global BBA emissions, but one that is severely understudied. The smoke sampled during this campaign was primarily aged outflow from savanna fires and some agricultural fires (~2-15 days after emission (Pistone et al. (2019)). In this work, we focus on the 2016 deployment out of Walvis Bay, Namibia; although, we also compare simulations with 2017 data with very similar results (not shown) – consistent with small interannual variability in southern African fires. The BBA measured during the 2018 deployment were of a lower concentration compared to other years of the ORACLES campaign, likely because most of the 2018 sampling was in October as opposed to the more dominant fire months of August and September (African Biomass Burning and Its Atmospheric Impacts, 2021; Zuidema et al., 2018). We use data from 13 flights performed by the NASA P-3 aircraft in 2016. Fig. 3.1 shows that emissions are geographically more extensive in the southern African region

than the region sampled in WE-CAN but that peak emission rates in the ORACLES region are lower. We note here that we have saturated the WE-CAN plot in Fig. 3.1 to the same scale as that for ORACLES, but the maximum fire emissions are ~2 times larger for the WE-CAN campaign. BC mass concentrations were measured using an SP2 with a particle size detection range of 70 – 700 nm and an uncertainty of 25%. A Time of Flight Aerosol Mass Spectrometer (ToF-AMS) was used to measure OA mass concentrations for particles with diameters within the detection range of 30 – 1000 nm and an uncertainty of 30%. An ABB/Los Gatos Research $CO/CO_2/H_2O$ analyzer was used for CO concentration measurements with an uncertainty of 1%. Two Radiance Research Particle Soot Absorption Photometers (PSAPs) were used to measure dried aerosol total absorption at 470, 530, and 660 nm. Instrument noise levels were 0.5 Mm^{-1} for a 240-300 s sample; additional details are given in Pistone et al. (2019). During this campaign, the multiple scattering from this filter-based measurement potentially led to a high bias in the PSAP signal (Pistone et al., 2019). To partially address this, we use the average wavelength-corrected PSAP observations provided by Pistone et al. (2019), which have been shown to be less biased than the wavelength-specific values whose use resulted in an unphysical increase in the absorption Ångström exponent (Pistone et al., 2019; Zuidema et al., 2018); this does not alter the conclusions presented here.

The CLARIFY (Cloud-Aerosol-Radiation Interactions and Forcing for Year 2017) campaign aimed to improve model estimates of the direct, semi-direct, and indirect radiative forcings of BBA. Full details of the campaign are given in Haywood et al. (2021). We use data from 13 flights from the deployment of the FAAM Bae-146 aircraft out of Ascension Island for 4 weeks during August 2017. This deployment sampled the same broad source region as ORACLES-2016 but further west; thus the air had been transported and therefore aged further (~4-8 days from emission (Taylor et al. 2020). BC mass concentrations were measured using an SP2 with a particle size detection range of 102 – 533 nm, an uncertainty of 17% (Taylor et al., 2020), and a 100% detection efficiency for particles with 1-143 fg BC per particle. A compact Time of Flight Aerosol Mass Spectrometer (cToF-AMS) was used to measure OA mass concentrations with a detection range for particle vacuum aerodynamic diameter of 50 – 700 nm (Taylor et al., 2020) and an uncertainty of 30%. An Aero-Laser AL5002 was used to measure CO concentrations with an uncertainty of ±2.8 ppb at 1 Hz. Measurements of dry (RH <10%) aerosol absorption at 405,

514, and 660 nm were made using photoacoustic spectroscopy using the EXSCALABAR PAS instrumentation described by Davies et al. (2018, 2019) and Cotterell et al. (2020, 2021) with an uncertainty on the absorption instrument of 8% (Davies et al. 2019).

All aerosol mass concentrations across campaigns are shown at standard temperature and pressure: STP (273K, 1 atm). For comparison with airborne measurements, the model was sampled to the nearest grid box both temporally and spatially to each flight track using 1 min aircraft data. We then average both the model and the observations to the model grid box.

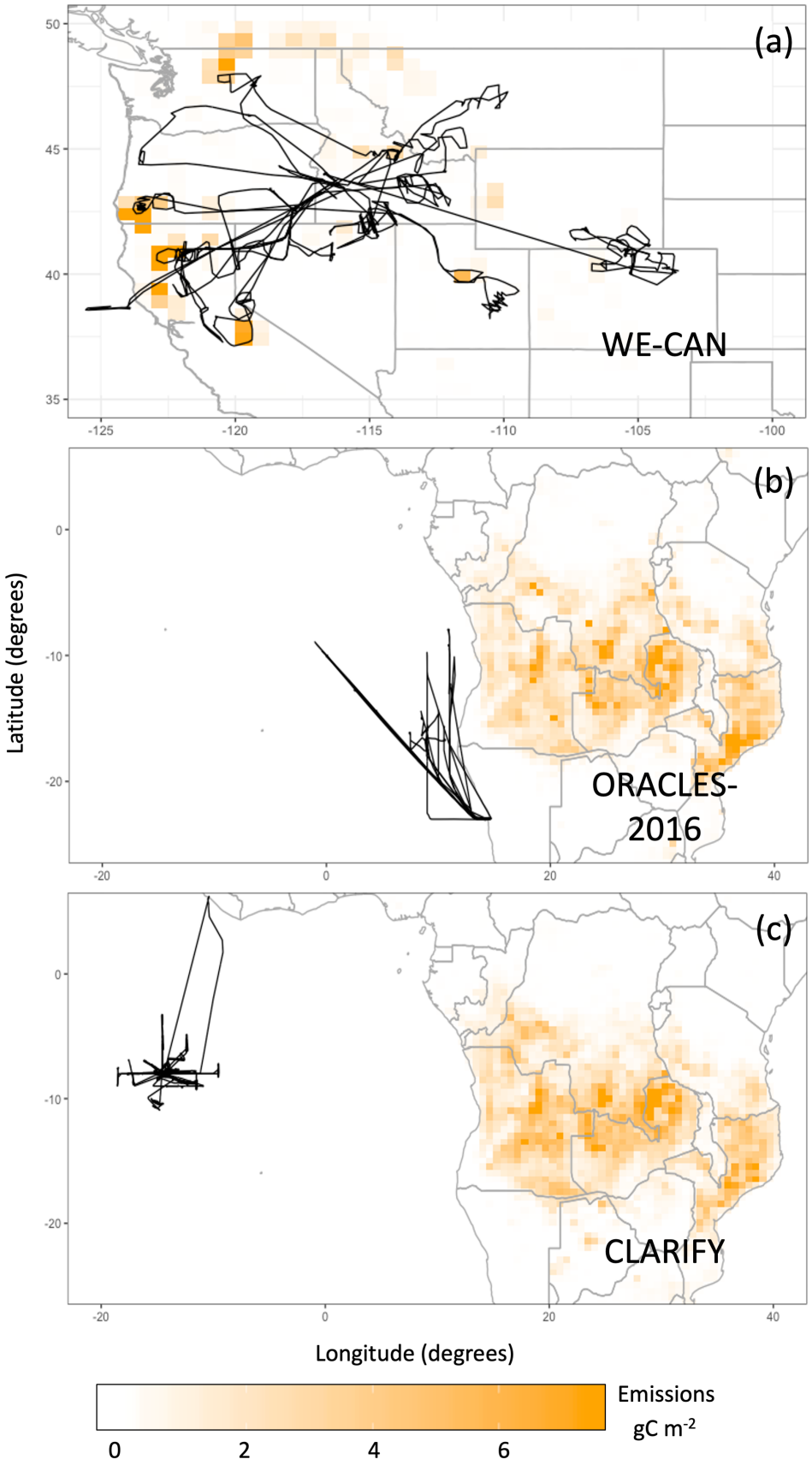
(a)
WE-CAN
(b)
ORACLES-
2016
(c)
CLARIFY
Latitude (degrees)
Longitude (degrees)
Emissions
gC m-2
0
2
4
6

Figure 3.1. Flight tracks of the (a) WE-CAN, (b) ORACLES-2016, and (c) CLARIFY campaigns overlaid on total BBA emissions from GFED4s during the months of each respective campaign (July – September 2018 for WE-CAN, August – September 2016 for ORACLES-2016, and August 2017 for CLARIFY). Note that the underlying maps are not on the same scale.

In addition to the WE-CAN flight observations in the contiguous US (CONUS), we also use IMPROVE (Interagency Monitoring of Protected Visual Environments, http://vista.cira.colostate.edu/improve/, last access: 24 February 2020) surface observations from 155 sites in 2018 and compare against 24 h averaged model results to further constrain anthropogenic BC in CONUS. Black carbon is measured using a $PM_{2.5}$ size-selective filter-based thermal method in this network (Chow et al., 2007).

3.3 Campaign comparisons

We use observations from the WE-CAN, ORACLES-2016, and CLARIFY campaigns to test how well our model captures mass concentrations and absorption properties of BBA from different fire source regions. In Sections 3.3.1 and 3.3.2, we compare observations with our baseline simulation.

3.3.1 Mass concentration comparisons

3.3.1.1 WE-CAN

We first compare median vertical profiles of BC, OA, and CO concentrations observed during WE-CAN with model-simulated concentrations (Fig. 3.2). We find that the model is biased substantially low for OA and CO across most altitudes but matches observed BC quite well from roughly 3 km to the surface with some underestimate at higher altitudes. Below 3 km, simulated OA is biased low by 30% and CO by 41% while BC is only biased low by 7%. We note that SOA contributes ~5% of the simulated OA at all altitudes, in good agreement with observed percentages (Palm et al. (2020). Because this is a strongly plume-targeted campaign, BB is the dominant emission source for all 3 species, as indicated by a noBB simulation in grey, which shows much lower concentrations. Thus, given that fires are the dominant source for all three, one might expect similar model performance for all three species.

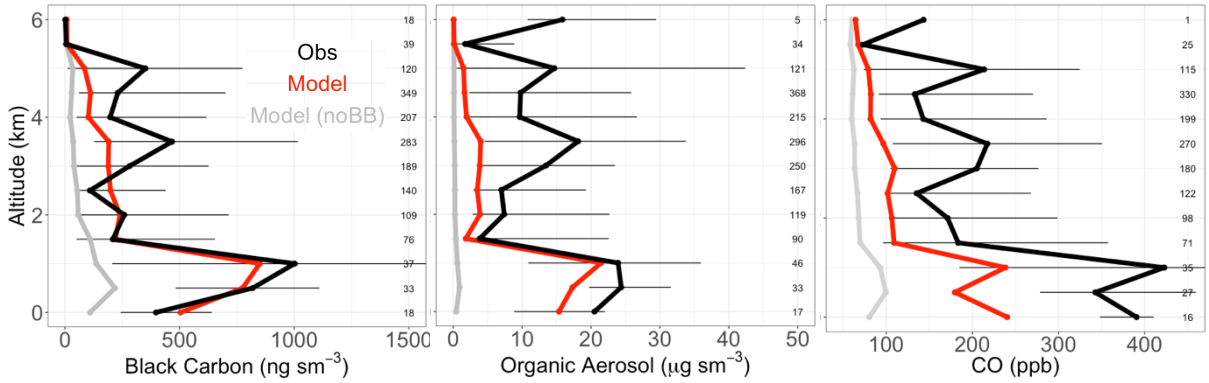

Figure 3.2. The median vertical profiles of BC, OA, and CO concentrations (shown in 0.5 km bins) from the WE-CAN campaign. Observations (black) are compared with model simulations (red) and a simulation with no fire emissions (noBB) in gray. Horizontal bars show the 25th-75th percentile range of measurements in each vertical bin. The number of observations in each bin is given on the right side of each panel. Aerosol concentration measurements and simulations are reported at standard conditions of temperature and pressure (STP: 273K, 1 atm).

The low bias of OA and CO is consistent with a campaign that targeted many fresh fire plumes, given that Eulerian models generally have trouble reproducing sub grid features (Eastham and Jacob, 2017; Rastigejev et al., 2010). The comparisons of Figure 3.2 suggest that the higher resolution nested grid used here is not sufficient to capture near-field plumes sampled during WE-CAN. Figure 3.S1 shows that concentrations of acetonitrile (a useful BB tracer) during WE-CAN are considerably higher (254 ppt median) than during two other well-characterized, fire-influenced campaigns: DC3 (167 ppt, May-June 2012 in the southeastern and south-central US) and the boreal portion of ARCTAS (213 ppt, June-July 2008 in boreal Canada). Furthermore, the WE-CAN measurements show a pronounced tail extending to very high acetonitrile concentrations that are not present in the observations for the DC3 and ARCTAS campaigns. For reference, previous work has suggested that 225 ppt is a potential cutoff for fire influence (Aruffo et al., 2016), indicating that more than half of the observations during WE-CAN are within concentrated smoke plumes that are challenging for the model to resolve. This plume-targeted sampling strategy likely accounts for the low model bias for OA and CO.

While the model is biased low with respect to observations of both OA and CO, as previously noted, model-simulated BC better captures observations in this fire-influenced regime. Figure 3.3

shows the same comparisons for BC, OA, and CO when filtered to include only the lowest 25th percentile (< 159 ppt) acetonitrile to isolate the observations with the least fire influence (or more aged/diluted fire influence). We note that concentrations filtered for the lowest 25th percentile of acetonitrile are considerably lower (roughly an order of magnitude) than the medians for the full dataset shown in Fig. 3.2. We see from the noBB (grey lines) simulations, that even for the lowest acetonitrile concentrations, much of the OA and CO is due to fires, whereas the BC is largely due to other sources (fossil fuels). We show that the model is better able to capture the least fire-influenced OA and CO between 3 and 5.5 km (compared to Fig. 3.2), though an underestimate persists in the lowest 2 km given the predominance of fire OA and CO even at these lower acetonitrile levels. However, the model clearly overestimates the least fire-influenced BC, indicating that anthropogenic BC emissions from the 2011 NEI may be overestimated in this region.

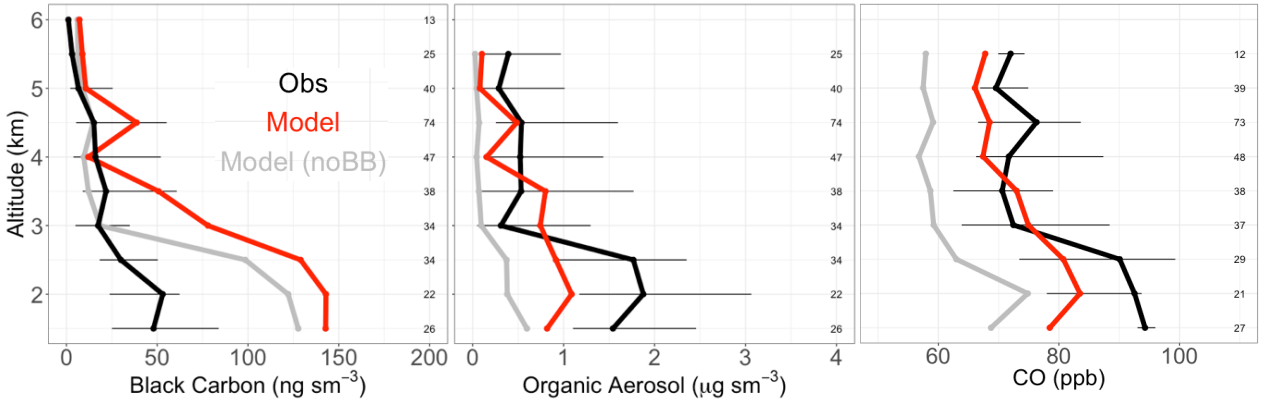

Figure 3.3. The median vertical profiles of BC, OA, and CO concentrations with the same conventions as Fig. 3.2 with results filtered to include only data coincident with the bottom 25th percentile of observed acetonitrile. We note that the y axis starts at 1.5 km because the lowest quartile of acetonitrile is found above this altitude.

To investigate the suggestion from Figure 3.3 that the anthropogenic BC emissions are overestimated, we compare simulated surface BC concentrations with observations from the IMPROVE network. To focus on anthropogenic emissions, we compare modeled and observed mean surface wintertime (December 2017 to February 2018) BC concentrations in CONUS when fire emissions should be negligible, with a few notable exceptions outside of the "WE-CAN region" including the Thomas fire in Southern California. In the wintertime, biofuel BC

from home heating/fireplaces may be more important in certain regions; based on the inventories used here, and, in this example, BF BC contributes ~13% of all US BC emissions at this time of year. Figure 3.S2 shows that, spatially, the model is in reasonable agreement with the IMPROVE observations, but with a large positive bias (34% normalized mean bias (NMB) for CONUS and 90% for the specific geographic region where WE-CAN sampled). Taken together, our analysis indicates that anthropogenic BC emissions are too high in the 2011 NEI. This is consistent with previous work that also used NEI 2011 for anthropogenic BC emissions (e.g., Carter et al., 2020; Kim et al., 2015; Wang et al., 2018); although, our work suggests that the overestimate is even higher than in these previous studies, perhaps because we use 2013 emissions here (see Section 2.1). Annual anthropogenic BC emissions in the recently released (full release in April 2020) 2016 NEI inventory are ~40% lower than in the 2011 NEI, suggesting that updated inventories may be more consistent with our analysis. A more detailed spatial and temporal exploration of anthropogenic BC emissions across the U.S. is needed.

In an effort to minimize the impact of any fossil fuel emissions bias on our analysis of BBA, we remove the data associated with the bottom 25th percentile acetonitrile in the analysis that follows. The filtered modeled BC vertical profiles (not shown) demonstrate the same low bias as shown in Figure 3.2 for OA and CO. Using this filtered data, we find that the observed median vertical profile of the BC:OA ratio is well captured by the model with only a slight overestimate, likely due to the residual influence of overestimated fossil fuel emissions (Fig. 3.4). Thus, when focusing on fire-influenced points, the model captures well the observed BC:OA ratio while underestimating the magnitude of observed mass concentrations of both.

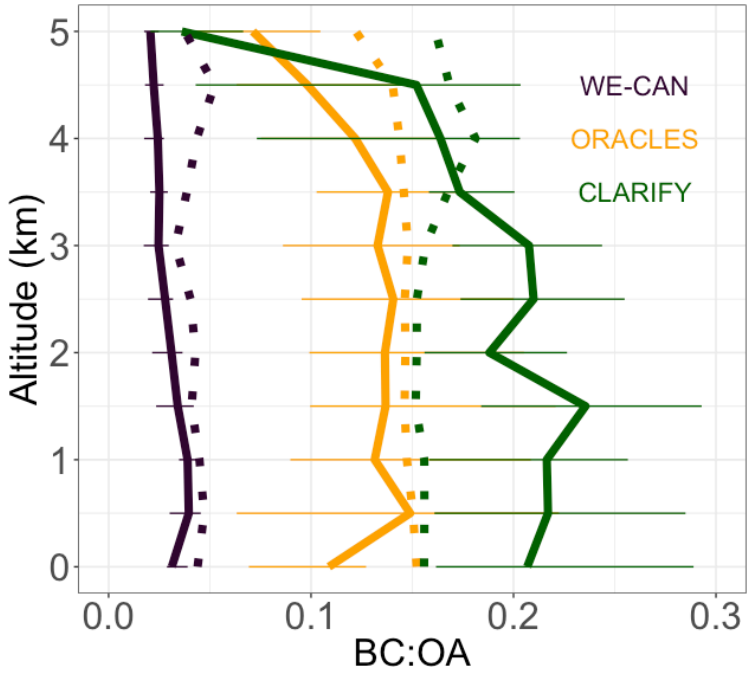

Figure 3.4. The median vertical profiles of the BC:OA ratio (shown in 0.5 km bins) from WE-CAN (in purple), ORACLES-2016 (in orange), and CLARIFY (in green) with both ORACLES-2016 and CLARIFY using scaled up BB BC emissions. Observations (solid lines) are compared with model simulations (dotted lines). The WE-CAN comparisons have been filtered to remove the data corresponding to the lowest 25th percentile of acetonitrile (see Section 3.2.1). Horizontal bars show the 25th-75th percentile range of measurements averaged in each vertical bin.

3.3.1.2 ORACLES-2016 and CLARIFY

The ORACLES-2016 and CLARIFY campaigns sampled downwind (by generally two or more days) of fires in southern Africa. CLARIFY is substantially downwind from ORACLES-2016 (i.e., the plume is likely to have descended further and become more aged). Stratocumulus sheets also tend to be more broken in the CLARIFY region around Ascension Island. This sampling of aged smoke provides a better opportunity for the model to reproduce observations, in contrast to WE-CAN's sampling of sub-model grid plumes. Fig. 3.5 shows a comparison of vertical profiles of simulated and observed concentrations of BC, OA, and CO during the 2016 ORACLES and 2017 CLARIFY campaigns. The noBB simulation (shown in grey) demonstrates that BC, OA, and CO concentrations are all dominated by smoke in these campaigns.

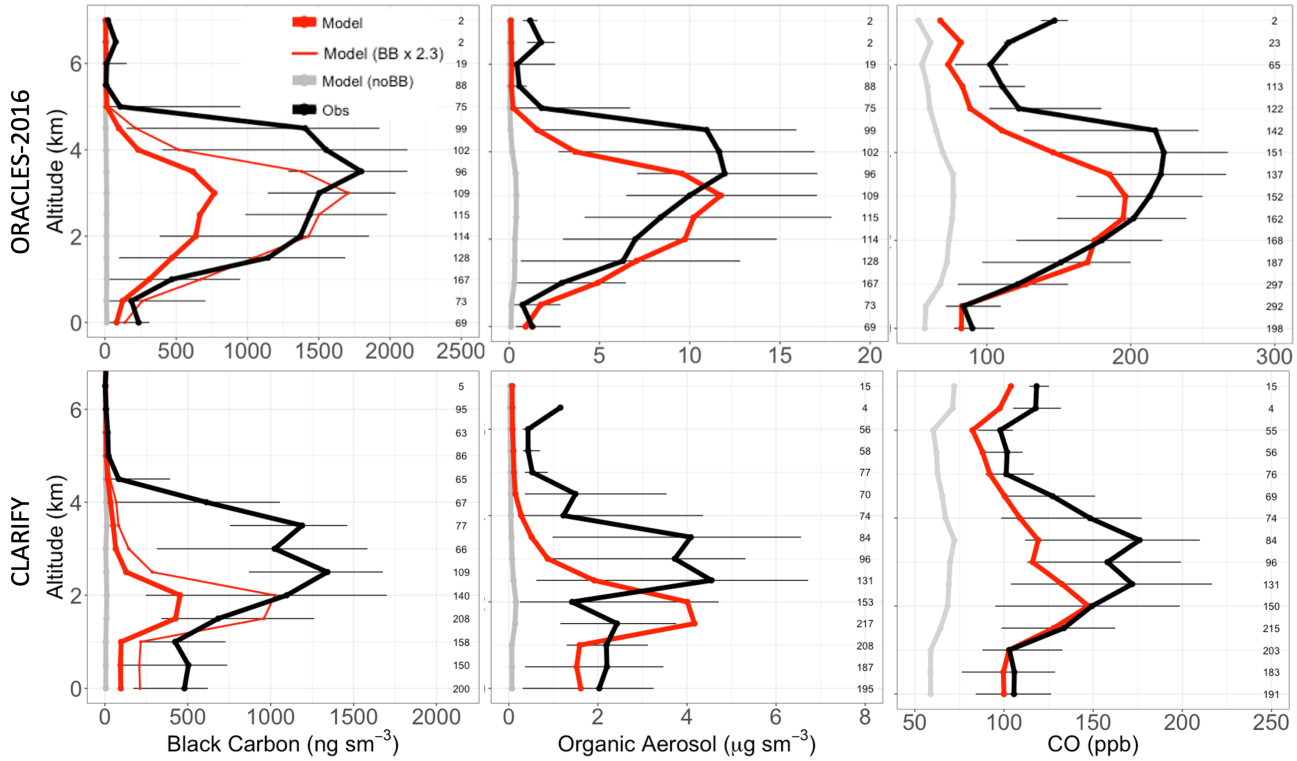

Figure 3.5. The median vertical profiles of BC, OA, and CO mass concentrations (shown in 0.5 km bins) from the ORACLES-2016 (top) and CLARIFY (bottom) campaigns. Observations (black) are compared with model simulations (red; thinner red line shows simulation with BB BC emissions scaled up by a factor of 2.3) and a simulation with no fire emissions (noBB) in gray. Horizontal bars show the 25th-75th percentile range of measurements averaged in each vertical bin. The number of observations in each bin is given on the right side of each panel. Aerosol concentration measurements and simulated values are reported at standard conditions of temperature and pressure (STP: 273K, 1 atm).

Figure 3.5 shows that the model generally captures the magnitude of observed OA and CO mass concentrations during ORACLES-2016 and CLARIFY, with the exception of a substantial low bias aloft from ~3 - 5 km. This underestimate likely results from the representation of clouds in the MERRA-2 assimilated meteorology used in GEOS-Chem. A multi-model study investigating ORACLES-2016 found that cloud cover was significant during many flights and that both GEOS-5 and GEOS-Chem underestimate the top of smoke plumes (Shinozuka et al., 2020). Haywood et al. (2021) also showed significant cloud cover during the CLARIFY campaign. Das et al. (2017) show that GEOS-Chem (using MERRA meteorology) aerosol transport off the coast

of southern Africa is characterized by a sharp descent in aerosol plumes from ~4 – 5 km due to excessive subsidence over the ocean in the MERRA product, producing an aerosol layer which is located closer to the surface than observed with CALIOP. This vertical displacement is similar to the low bias shown in our simulation of ORACLES-2016 and CLARIFY (Fig. 3.5). This low bias is somewhat larger for CLARIFY, potentially because the CLARIFY observations are further from the source and are thus affected by longer subsidence timescales. Given our use of assimilated meteorology, it is not possible to explore how BC and OA might respond to differences in entrainment and other cloud related processes. However, we do find that the model bias is highest under high humidity conditions, supporting a cloud-related mechanism for this biased vertical profile. We tested the impact of recent wet deposition updates related to cloud liquid water and scavenging efficiencies for GEOS-Chem (Luo et al., 2019), which minimally impacted our comparison. An injection height sensitivity test based on Fischer et al., (2014), which emits a percentage of emissions into the free troposphere, yielded little change in the simulated vertical profile. Thus, the bias aloft is likely associated with cloud representation in MERRA-2 and not injection height issues. Self-lofting of the absorbing aerosol may also contribute to the discrepancies above boundary layer (Haywood et al., 2021), and more work is needed to explore this mechanism.

Figure 3.5 shows a model underestimate of observed BC mass concentrations by a factor of ~2.3 during ORACLES-2016, which can be attributed to fire emissions given the negligible anthropogenic influence on BC (grey lines). A study exploring the DACCIWA campaign in western Africa provides additional evidence for underestimated BB BC emissions in this region; they scale fire emissions (in this case from the GFAS inventory, which, for this region and season, are within 25% of the GFED4s inventory) by 3.4 in GEOS-Chem to match observations (Haslett et al., 2019). Ramo et al. (2021) suggest that burned area in sub-Saharan Africa is underestimated by 63% (compared to GFED4s in 2016) due to missing contributions from small fires, which can be better detected with higher resolution satellite products. In addition, a recently updated emission factor (EF) compilation (Andreae, 2019) confirms that a higher BC EF is reasonable for the vegetation type fires (savanna) dominating the ORACLES-2016 and CLARIFY campaigns. The inventory that we use (GFED4s) uses 0.37 g/kg dry matter (DM) burned for savanna BC emissions while the updated Andreae (2019) paper suggests a value of

0.53 g/kg DM with a standard deviation across studies of 0.35 g/kg DM. Scaling up the BC savanna EF by a factor of ~2.3 falls within the range presented in Andreae (2019). Scaling up BB BC emissions by this factor does not entirely remedy the CLARIFY model-observation bias (Fig. 3.5), potentially because different fires were sampled than during ORACLES-2016. Observations of additional chemical tracers for anthropogenic and biomass burning activity are needed to understand these source differences from Africa, as well as additional observations over the source region.

In the following analyses for ORACLES-2016 and CLARIFY, we scale up BB BC emissions in southern Africa by a factor of 2.3. While this scaling factor is somewhat arbitrary, it is supported by 3 years of comparison against ORACLES data and additional literature evidence detailed above. It is not sufficient to explain the CLARIFY underestimate, but a more sophisticated inverse model would be needed to correct emissions to match both ORACLES and CLARIFY. This is beyond the scope of this work. While we do not scale savanna EFs elsewhere as we do not have the observations to test such scaling, it is possible that savanna BB BC EFs are similarly underestimated in other regions, and more work is needed to investigate this. The BC:OA ratio is particularly well captured during ORACLES-2016 (Fig. 3.4) when including these scaled up BB emissions, so we focus on the ORACLES-2016 dataset in our discussions of the smoke absorption properties downwind of Africa in addition to including a comparison with CLARIFY. For ORACLES, we show comparisons here only for data collected during the 2016 deployment, but given the limited interannual variability in fires in the region, the observed magnitudes and the model comparisons are consistent for 2017 and 2018 albeit with small differences discussed in Section 3.2.2.

3.3.2 Absorption comparisons

Comparisons of vertical profiles of simulated and observed total absorption (not shown) demonstrate model underestimates consistent with the aforementioned low model bias of mass concentrations (Fig. 3.2 & 3.7). We, therefore, focus on the mass-normalized absorption (i.e. the MAC) under dry conditions, as the MAC is an intrinsic aerosol optical property independent of mass loadings and associated biases. This minimizes the effect of mass underestimates

associated with WE-CAN plume sampling, vertical transport biases off of Africa, and BC emissions biases affecting CLARIFY.

Because the total absorption measurements do not distinguish between BC and OA contributions to absorption, our strategy is to first look at the MAC_{BC} (i.e., the absorption coefficient divided by the BC mass concentration) at 660 nm where BC absorption should dominate. We then explore the MAC of total BBA or MAC_{BC+OA} (i.e., the absorption coefficient divided by the summed mass concentrations for BC and OA) at shorter wavelengths (where both BC and BrC contribute substantially to absorption). This enables us to investigate the role of BrC absorption informed by our knowledge of BC absorption. Modeled and observed MAC quantities are calculated in the same way to enable comparison. Note that critical to this analysis of the MAC_{BC+OA} is the model's ability to capture the BC:OA observed in these two very different regions of the world, as shown in Fig. 3.4. These ratios are predicted well by our model for WE-CAN and ORACLES but are not captured as well for the CLARIFY measurement region, rendering the CLARIFY comparisons somewhat less useful for constraining the model optical properties. We further note that uncertainty in the average BC:OA ratio increases with altitude with fewer observations and lower concentrations. Here we focus on absorption constraints at two wavelengths only (limited by the observations from WE-CAN); however, additional measurements that can better constrain the wavelength dependence of absorption may provide further insight.

MAC calculations are only performed when the observed and modeled BC mass concentrations (or the combined BC and OA mass concentration, if calculating MAC_{BC+OA}) are greater than 0.6 $\mu g\ sm^{-3}$ and for which the corresponding extinction values, if available from the datasets, are greater than 10 Mm^{-1} (as suggested by Shinozuka et al. (2019) to reduce noise as instruments approach their detection limit). Our results are robust to this filtering; filtering reduces the range of estimated MAC but not central values.

3.3.2.1 WE-CAN

At 660 nm, total aerosol absorption is generally dominated by BC, owing to the low absorptivity of BrC relative to BC at this wavelength (McClure et al., 2020; Pokhrel et al., 2017). Fig. 3.6

shows good agreement between the observed (black) and modeled (red) MAC_{BC} at 660 nm. The median values for observed and simulated MAC_{BC} at 660 nm (11.29 $m^2 g^{-1}$ and 12.03 $m^2 g^{-1}$, respectively) are higher than values for BB-dominated BC absorption alone (see section 3.2.1 for assumptions regarding BB BC absorptivity). While the absorption from OA is much lower at longer wavelengths (see Section 3.2.1), there is so much OA in the smoke sampled during WE-CAN (Fig. 3.2) that its contribution to total absorption at 660 nm is considerable, and its inclusion in the model reconciles the predicted MAC_{BC} with observed values (Fig. 3.6). Our simulations of MAC_{BC} at 660 nm use an AE of 1.5 for BB BC (as in Wang et al. (2014), see Section 3.1 for details). However, our model assumption for the intrinsic BB MAC_{BC} at 660 nm (5.3 $m^2 g^{-1}$, without accounting for the AE) is lower than other values in the literature (e.g., 6.25 $m^2 g^{-1}$; (Bond & Bergstrom, 2006)). As noted in Section 3.1, the AE assumed in our model for BB BC is at the high end of literature estimates from North America, increasing the plausibility that it is partially accounting for a lower intrinsic BB MAC_{BC}.

At 405 nm, the role of BrC absorption is more important than at longer wavelengths. We calculate the MAC_{BC+OA} at this shorter wavelength. These values are inherently much smaller than MAC_{BC} given the preponderance of OA, but overall absolute absorption is higher at 405 nm than at 660 nm. We show in Fig. 3.6 that modeled MAC_{BC+OA} (median value of 1.34 $m^2 g^{-1}$) is biased high at 405 nm and is towards the upper range of observations (median of 0.78 $m^2 g^{-1}$). As shown in Fig. 3.4, the model generally captures the average BC:OA ratio during WE-CAN. Correcting the small high bias due to the residual influence of overestimated fossil fuel emissions reduces the simulated MAC_{BC+OA} by only ~15%. It is also highly unlikely that this difference at 405 nm is the result of overestimates in the absorptivity of BC, given that MAC_{BC} is well captured by the model at longer wavelengths and that, if anything, the GADS BC AAE (0.53 from 405-655 nm) is low. Modelled BrC absorption at this wavelength is substantial (more than 1/2 of total absorption); therefore, photochemical whitening of these particles may play an important role in determining the MAC_{BC+OA}. Alternatively, the prescribed BrC absorption may be overestimated. However, we note that the good agreement at 660 nm makes this less likely.

To investigate the impact of whitening at 405 nm, we use the parameterization from Wang et al. (2018) based on OH exposure. While WE-CAN is characterized by relatively near-field

sampling, air masses in the region contain both fresh plumes and aged emissions from the surrounding fires. As a result, whitening of BrC decreases the simulated MAC_{BC+OA} considerably, bringing our modeled MAC_{BC+OA} (median of 0.83 m^2 g^{-1}) into good agreement with observed MAC_{BC+OA}. This corresponds to a MAC_{OA} of ~0.4 m^2 g^{-1} at 405 nm, or about 40% of the assumed MAC_{OA} for primary BB. The whitening scheme has an effect on the MAC_{BC} at 660 nm (median drops by ~2 m^2 g^{-1}) and remains in agreement with the bottom of the interquartile range of observations. This suggests that, in the western US, whitening should be considered when modeling BrC absorption and that the parameterization of Wang et al. (2018) does a reasonable job in capturing the magnitude of this effect.

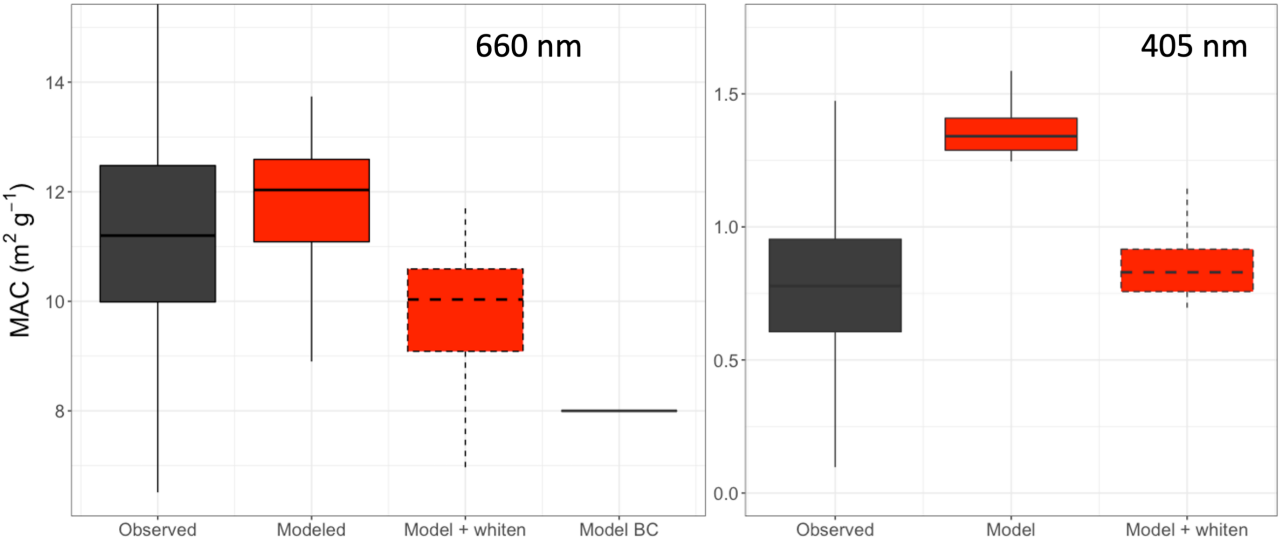

Figure 3.6. Boxplot summaries of the mass absorption coefficient (MAC) observed (black) and modelled with GEOS-Chem (red) for the WE-CAN campaign. Values at 660 nm are shown on the left (MAC_{BC} = total absorption divided by BC mass concentration) and at 405 nm on the right (MAC_{BC+OA} = total absorption divided by the summed BC and OA mass concentration). Model BC refers to the MAC_{BC} when only accounting for absorption from BC in the model. The horizontal bar is the median. The box shows the 25th to the 75th percentile, and the whiskers show 1.5 times the interquartile range. The inclusion of BrC whitening is denoted with dashed lines.

3.3.2.2 ORACLES-2016 and CLARIFY

As in comparisons with WE-CAN observations, we focus on MAC during ORACLES-2016 and CLARIFY because the vertical absorption profiles show the same vertical bias seen in the mass

concentrations. Figure 3.7 shows that the 660 nm MAC_{BC} observed during ORACLES-2016 (median value of 9.30 $m^2\ g^{-1}$) are lower than those during WE-CAN (median 11.29 $m^2\ g^{-1}$). In our framework, this is expected based on the differing BC:OA ratios for these two campaigns (see Fig. 3.4) and thus a smaller contribution to absorption from OA downwind of Africa. The LASIC campaign in 2016 partially overlapped with ORACLES-2016 and found higher MAC_{BC} at 660 nm (10.7 $m^2\ g^{-1}$); the surface site was located on Ascension Island (Zuidema et al., 2018) and thus was further from the fire source and likely sampled more aged aerosol. During CLARIFY, the median observed MAC_{BC} at 660 nm is considerably higher (11.52 $m^2\ g^{-1}$) than during ORACLES-2016. CLARIFY sampled more aged BBA and previous studies report that these BBA exhibit some of the highest levels of coating thicknesses observed in field measurements (and thus have a higher AE due to the lensing effect) as it was transported further from the continental source region (see Fig. 3.1 for the campaign flight tracks) (Taylor et al., 2020). While the uncertainties around sampled aerosol lifetime are large, Taylor et al. (2020) suggest that CLARIFY aerosol was sampled 4-8 days from emissions, potentially larger than some of the estimates from Pistone et al. (2019) and references therein for ORACLES-2016 (2-15 days with potentially an emphasis on 2-5 days). The two campaigns also employ different instrumentation: CLARIFY employed highly sensitive and accurate in-situ measurements (PAS) while ORACLES-2016 employed filter-based measurements (PSAP), which has higher systematic biases, with overestimates of absorption observed up to 45%. The differences in observed MAC_{BC} are within measurement uncertainty; although, it is noteworthy that the ORACLES-2016 MAC_{BC} is lower than the CLARIFY MAC_{BC}, despite the potential for a positive bias in the ORACLES-2016 observations. Other possible explanations for the difference in observed MAC_{BC} at 660 nm include an underlying MAC_{OA} that differs between the two campaigns. However, given the high BC:OA downwind of Africa (Fig. 3.4), OA is not likely to make such a large contribution to total absorption at these wavelengths.

Figure 3.7 shows that the model underestimates the MAC_{BC} at 660 nm downwind of southern Africa. Model values are similar for ORACLES-2016 and CLARIFY (8.91 and 8.72 $m^2 g^{-1}$, respectively), as our current model scheme uses a fixed AE of 1.5 globally, which may not be a good representation of real world conditions downwind of Africa (Ko et al., 2020). Given higher BC:OA ratios for ORACLES and CLARIFY compared to WE-CAN, OA contributes less to the

simulated MAC_{BC} at 660 nm. However, the contribution (~0.9 m^2g^{-1} for ORACLES, ~0.7 $m^2 g^{-1}$ for CLARIFY) is not negligible. Taylor et al. (2020) suggest that a BC AE of 1.85 (applied to an intrinsic MAC_{BC} from Bond and Bergstrom (2006), that is higher than we use here) is required to correctly predict the observed MAC_{BC} during CLARIFY – this AE includes the contribution of OA absorption at 660 nm. Keeping our OA absorption properties fixed, we estimate that we would need to increase our BC AE to 2 (or that the AE applied to an intrinsic MAC_{BC} from Bond and Bergstrom (2006) would need to be 1.8, similar to the values from Taylor et al. (2020)) to match the observed MAC_{BC} at 660nm in CLARIFY. A smaller increase in AE to 1.6 is needed to reconcile the model with observations during ORACLES at 660 nm. This may suggest that the BC in the somewhat fresher ORACLES-2016 outflow was less thickly coated compared to CLARIFY.

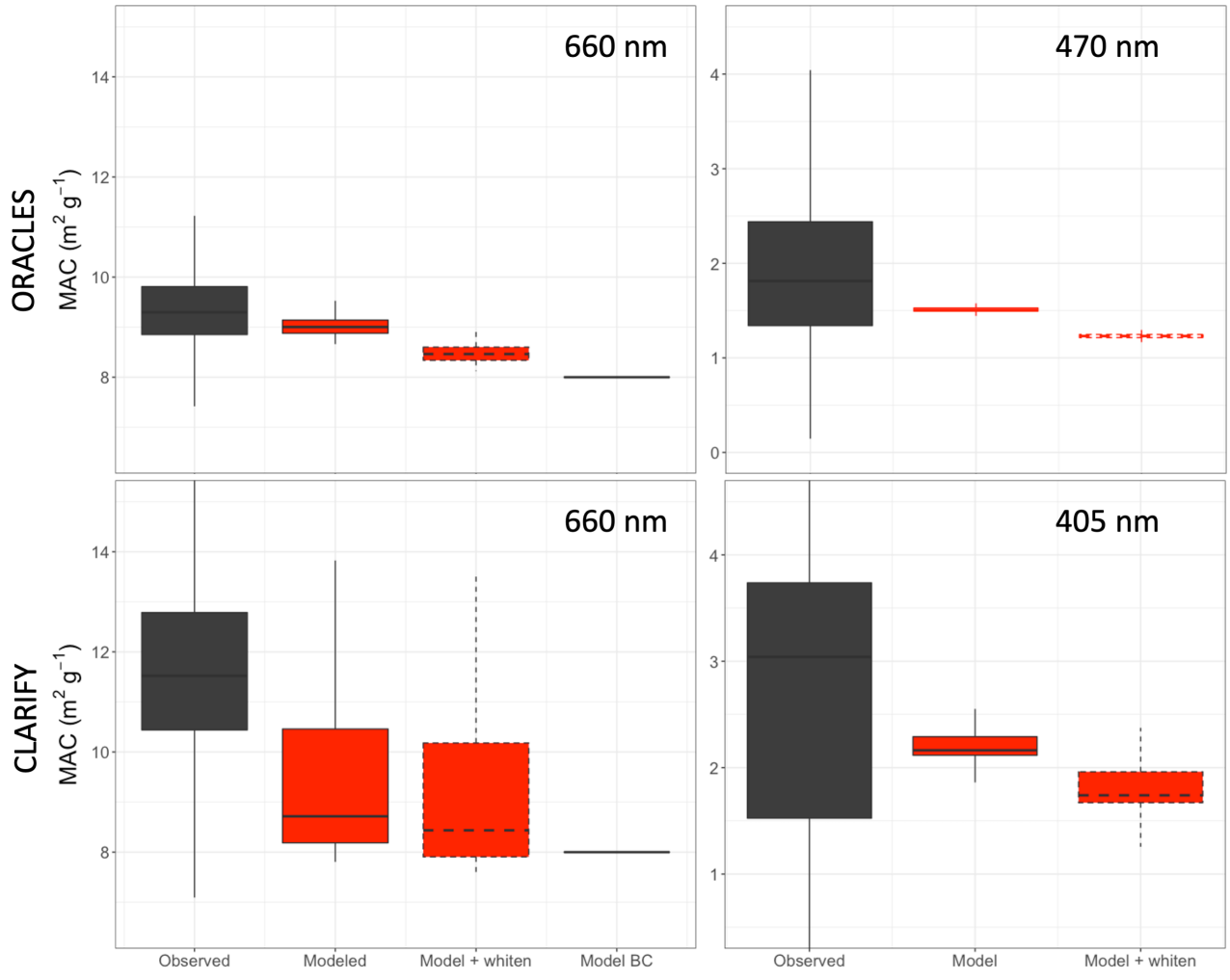

Figure 3.7. Boxplot summary of observed and simulated ORACLES-2016 and CLARIFY MAC_{BC} at 660 nm on the left and MAC_{BC+OA} at 470 and 405 nm, respectively, on the right. The conventions of this boxplot are described in Fig. 3.6.

At shorter wavelengths, the observed MAC_{BC+OA} is higher during CLARIFY (median 3.04 m^2 g^{-1}) than for ORACLES-2016 (median 1.81 m^2 g^{-1}), due largely to the difference in the measurement wavelength (470 nm for ORACLES-2016 and 405 nm for CLARIFY). Given the higher BC:OA ratio downwind of Africa (Fig. 3.4), BC makes a much larger contribution to absorption at shorter wavelengths than seen for WE-CAN. This increases the MAC_{BC+OA} and suggests that the difference in MAC_{BC} seen at 660 nm between ORACLES-2016 and CLARIFY also contributes to the difference in MAC_{BC+OA} seen in Figure 3.7. For ORACLES in 2017 and 2018, the comparisons between observed and modeled MAC are similar to Figure 3.7, with 2018 showing somewhat higher observed MAC_{BC+OA} at shorter wavelengths (not shown).

At these shorter wavelengths, our baseline simulated MAC_{BC+OA} (median value of 1.51 m^2 g^{-1} for ORACLES-2016 at 470 nm and 2.10 m^2 g^{-1} for CLARIFY at 405 nm) also underestimates the observed MAC_{BC+OA} by 16% and 31%, respectively; though, the former is within measurement uncertainties. The larger model bias for CLARIFY compared to ORACLES-2016 can be partly reconciled by considering the model underestimate of the BC:OA for CLARIFY (Fig. 3.4). Scaling up BC concentrations to correct this bias for CLARIFY increases the model value to ~2.37 m^2 g^{-1} (equivalent to a 22% underestimate). The model bias in MAC_{BC} at 660 nm likely contributes to the bias at shorter wavelengths as well. If we apply the BC AE of 1.6 and 2 for ORACLES-2016 and CLARIFY, respectively, estimated from the 660 nm comparisons to the shorter wavelengths, we reduce the model bias at the shorter wavelengths to 10% and 11% for ORACLES-2016 and CLARIFY, respectively. These differences lie within measurement uncertainties. If the model BC AAE (from GADS) is underestimated, the contribution of BC at short wavelengths may in fact be considerably larger. Including BrC whitening exacerbates the discrepancy at all wavelengths. Though, whitening decreases the MAC_{BC+OA} less downwind of Africa than during WE-CAN, consistent with a larger BC:OA downwind of Africa. We conclude that either (1) a higher AAE for BC (and thus more absorbing BC at short wavelengths) or (2) more absorbing BrC (with whitening) or (3) no photochemical whitening of BrC is required

downwind of Africa to fully reconcile the model and observations. It is possible that some combination of these factors may explain the observations. In addition, Figure 3.7 shows that observed MAC_{BC} and MAC_{BC+OA} are much more variable than our simulated MACs. This suggests that using one number for OA MAC and for the AE does not capture the variability in absorption properties. The model also underestimates the variability in the observed BC:OA (particularly for CLARIFY).

The observations demonstrate that BBA from African fires is roughly a factor of 3 more absorbing than from fires in the western US at short wavelengths (at 405 nm, MAC_{BC+OA} of 3.04 $m^2\ g^{-1}$ for CLARIFY, compared to 0.78 $m^2\ g^{-1}$ for WE-CAN). This is due, in large part, to higher BC loadings downwind of Africa relative to OA. This effect is captured by the model, which simulates the higher BC:OA observed downwind of Africa relative to the western US (Fig. 3.4). However, after accounting for the differing BC content, the model absorptivity remains biased low downwind of Africa. Our comparisons at longer wavelengths suggest that increasing the AE of BC (as in Taylor et al., 2020) reduces this gap. We attribute the remaining underestimate of the MAC_{BC+OA} to more absorbing BC (achieved with a higher BC AAE) and/or more absorbing BrC (or little photochemical whitening). We note that mixing state and the resulting absorption enhancement are a complex function of particle size, coating thickness, and morphology. Our model scheme here does not dynamically simulate these factors, but rather applies a fixed AE to BC. While we acknowledge that this is a limitation of such a global model scheme, these mixing state considerations would need to translate to a wavelength dependent effect on absorption to explain the model-observation discrepancies at short wavelengths discussed here. More work is needed to better understand the role of mixing state of smoke and its impact on absorption. However, previous studies have shown that BrC absorption increases with BC:OA ratio (Saleh et al., 2014; McClure et al., 2020), consistent with our contrast of Africa and the western U.S., and we therefore consider this as a possible explanation for our results in what follows.

3.4 Impact of alternate BrC absorption parameterizations

The stronger absorption at shorter wavelengths observed in smoke from African fires compared to western US fires (that cannot be attributed to higher BC content of smoke alone), in addition to the high variation in observed absorption properties from different sources or even years, imply that BrC absorption from fires should not be treated as constant. Saleh et al. (2014) found

that absorption of BrC increases as a function of BC:OA ratio in laboratory measurements. McClure et al. (2020), using data from the FIREX 2016 Lab experiment in Missoula, MT, extended the Saleh work and developed their own parameterization for BrC absorption as a function of BC:OA. Figure 3.4 shows that the ORACLES-2016 and CLARIFY campaigns exhibited significantly higher BC:OA ratios than WE-CAN (by a factor of ~4-7), consistent with generally more flaming fires in southern Africa. The model generally captures the difference between the two campaign regions. These varying BC:OA ratios suggest that a parameterization keyed to this factor has the potential to better describe the difference in BrC absorption in the western US and the southern African outflow as observed in Section 3.3. We note that our baseline BrC absorption properties from Wang et al. (2018) are calculated by using one globally averaged BC:OA ratio within the Saleh et al. parameterization; in this section when we refer to the Saleh parameterization, we are referring to the full parameterization which varies as a function of BC:OA. The Saleh et al. (2014) and McClure et al. (2020) parameterizations are described in detail in the SI, the latter is referred to as the "FIREX" parameterization in what follows. We explore here whether these parameterizations can better capture the observations during WE-CAN, ORACLES-2016, and CLARIFY.

While the BC:OA ratio is much lower in the western US than downwind of Africa, when the Saleh et al. parameterization is applied to WE-CAN and ORACLES-2016, the resulting BrC imaginary refractive index *k* (responsible for absorption) at short wavelengths (405 and 470 nm) is similar (and generally higher) for both regions. This is the result of offsetting changes to both the *k* at 550 nm and the AAE used to calculate the absorption at shorter wavelengths (see SI for further details).

The FIREX parameterization produces MAC_{OA} values more than twice as high downwind of Africa compared to during WE-CAN at 660 nm, and ~50% higher at 405 nm. Thus, while the Saleh et al. parameterization does go beyond assuming fixed absorption properties for BrC, it does not fully achieve our goal of representing the different brownness observed for fires in the western U.S. and downwind of Africa. The FIREX parameterization produces a larger difference between campaigns at longer wavelengths because the MAC_{OA} (and *k*) is more sensitive to the

BC:OA ratio than in the Saleh parameterization at these wavelengths, particularly in the observed and simulated WE-CAN BC:OA range (0.03 to 0.05).

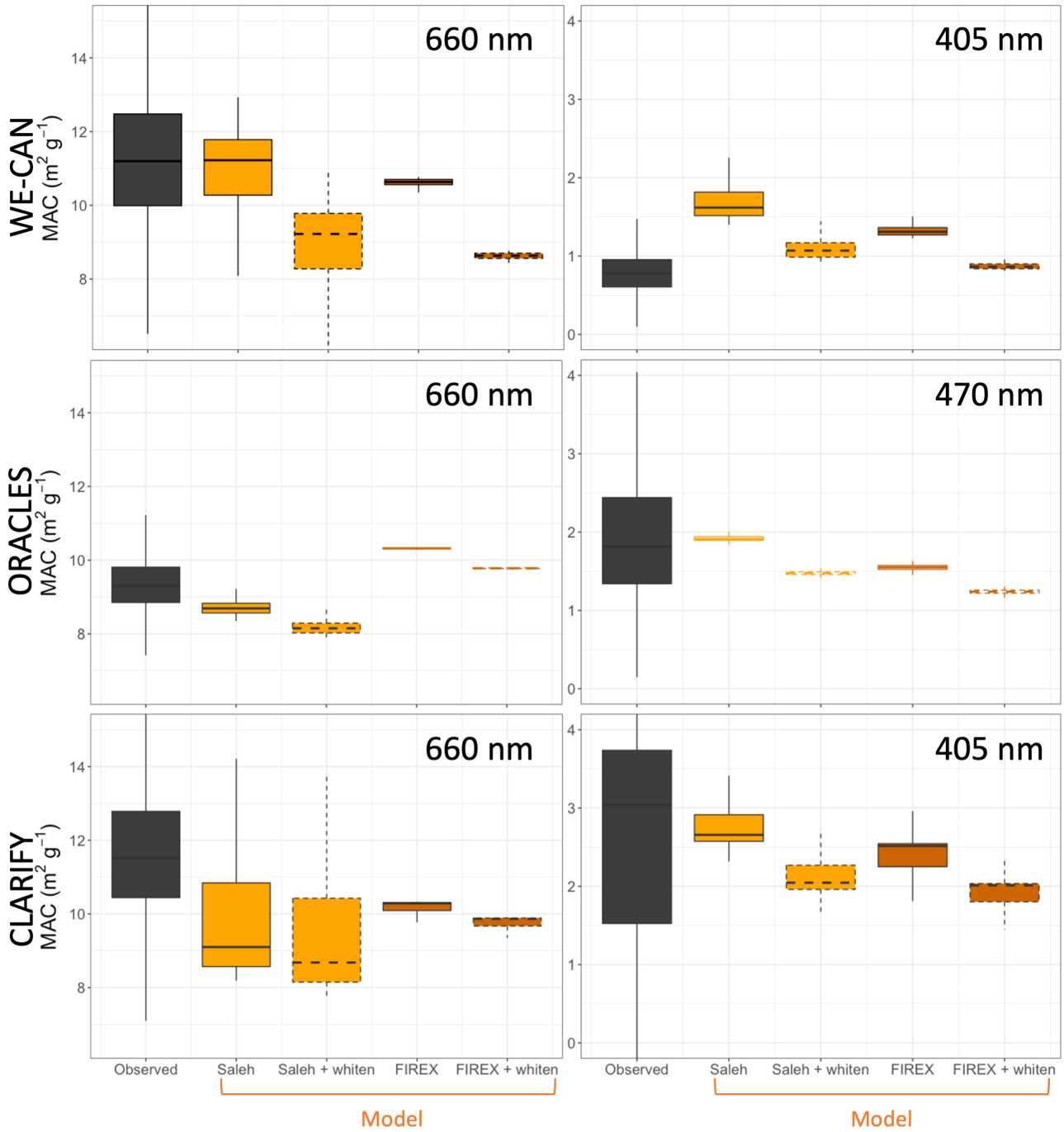

Figure 3.8. Boxplot summary of observed (black) and simulated MAC_{BC} at 660 nm on the left and MAC_{BC+OA} on the right at 405 nm for WE-CAN (top) and CLARIFY (bottom) and at 470 nm for ORACLES-2016 (middle). Simulations using the Saleh et al. (2014) parameterization are

shown in yellow and those using the FIREX parameterization in light brown. The conventions of this boxplot are described in Fig. 3.6.

We implement the Saleh et al. (2014) and the FIREX schemes for BrC absorption in GEOS-Chem for comparison against the three campaigns (Fig. 3.8). We use the modeled BC:POA ratio in these parameterizations given that SOA here contributes < 5% of simulated OA mass. Given that the model generally captures the overall BC:OA ratio, we do not expect this simplification to affect our results. At 660 nm, using the Saleh parameterization does not change the MAC_{BC} significantly from the baseline simulation. At these same wavelengths the FIREX parameterization agrees well with the WE-CAN observations at 660 nm, improves agreement with the CLARIFY observations relative to both the baseline and Saleh, and overestimates observations during ORACLES-2016. The increase in BrC absorption at long wavelengths downwind of Africa with the FIREX parameterization removes much (all) of the earlier underestimate of MAC_{BC} for CLARIFY (ORACLES) seen in Figure 3.7, suggesting that an underestimate of BrC absorption could explain these results.

Figure 3.8 shows that at shorter wavelengths, using BrC parameterizations based on BC:OA ratios leads to overall increases in modeled MAC_{BC+OA} relative to the baseline (labeled "Model") simulations – with the Saleh parameterization producing slightly larger values than the FIREX parameterization. Both parameterizations overestimate MAC_{BC+OA} during WE-CAN and improve model agreement with observations downwind of Africa (compared to our baseline simulation). At these short wavelengths, the FIREX parameterization produces a less biased simulation for WE-CAN, but the Saleh parameterization is a better match for observations downwind of Africa. Adding photochemical whitening reduces the MAC_{BC+OA}, bringing simulated values closer to observations for WE-CAN, but degrading the comparisons downwind of Africa. In particular, photochemical whitening in combination with the FIREX parameterization results in simulated values below the lower bounds of the interquartile range of ORACLES-2016 observations. However, correcting a likely model underestimate in the BC AAE (and thus increasing the intrinsic MAC of BC) could bring us back into agreement with observations at short wavelengths. These comparisons support the need for photochemical whitening during WE-CAN (or a considerably lower intrinsic MAC for BrC than assumed with

any of the FIREX, Saleh, or baseline parameterizations), but make it challenging to draw conclusions as to whether the observations support the use of a whitening parameterization for African fires.

Taylor et al. (2020) suggest that less than 11% of the absorption at 405 nm during CLARIFY was attributed to BrC, using measured MAC at 405 and 514 nm and the AAE of BC from 514 to 655 nm to estimate the absorption fraction due to BrC and an assumption of no BrC absorption at 655 nm. With the Saleh and FIREX parameterizations we attribute 48% and 35%, respectively, of absorption at 405 nm to BrC (when including whitening) during CLARIFY – these estimates are more than triple the contribution estimated by Taylor et al. (2020) for this highly aged aerosol plume, but are similar to other literature estimates of BrC absorption percentages of up to ~40% (Wang et al., 2018 and references therein). Given a likely model underestimate in the AAE of BC, our model values are likely an upper limit.

Our analysis indicates that observed brownness in the two BB regions could be different and that a parameterization that accounts for the observed elevated BrC absorptivity of African fires relative to western US fires may be necessary to capture observations during ORACLES-2016 and CLARIFY. However, using either the Saleh et al. or FIREX parameterizations does not fully account for this difference. Though, the FIREX parameterization better distinguishes smoke properties from fires in the western US and versus Africa at longer wavelengths. At shorter wavelengths, a parameterization that results in lower BrC absorption at low BC:OA (WE-CAN) and higher BrC absorption at higher BC:OA (ORACLES-2016/CLARIFY) would better match these observations. It is possible that we are not representing another potential explanation for the different absorption of BrC in the two regions: recent work has shown that under conditions with very high primary BC:OA ratios from biomass combustion (such as savanna burning in Africa), a first stage of BrC enhancement happens after emission, owing to formation of highly absorbing SOA, and before whitening (the whitening may result from less-absorbing SOA formation in those experiments) (Cappa et al., 2020; Wu et al., 2021).

These results are further complicated by several factors. First, the fire emissions inventory does not allow BC and OA emissions to vary with either burn conditions nor sub-fuel types in the fire

emissions inventory used here; GFED4s does not capture rapidly evolving burn conditions (fire temperature, intensity, etc.) and aggregates major fuel categories, such as savannas, grasslands, and shrubs together. Thus, the simulated BC:POA represents the result of average burn conditions. Variability, or indeed bias, in the representation (or airborne sampling) of these fuel types and burn conditions could drive an inaccurate implementation of the two BC:OA parameterizations. Second, our implementation of the two BC:OA parameterizations in GEOS-Chem also, by necessity, uses total BC:POA rather than the concentrations of carbonaceous aerosols from fires alone (tagging the BC:POA for fires only is an additional computational expense). Because modeled anthropogenic BC is biased slightly high during WE-CAN, using the overall, rather than BB-only, BC concentrations to parameterize BrC absorption is an imperfect representation of this lab-based parameterization. Third, the GEOS-Chem optical properties (MAC) are based on Mie theory which use refractive indices as well as particle size. If there is a mismatch between the particle size in the observations versus the model, this could lead to additional differences and to MAC values that differ between the baseline results and calculations using the FIREX parameterization, especially for Africa. Indeed, Mie theory pertains to homogeneous spheres, while BBA aerosols are known to adopt a wide variety of internal mixing states and particle morphologies (Kahnert and Kanngießer, 2020). These discrepancies with the underlying assumptions for Mie theory are a further potential source of model bias. Finally, the differences in absorption instrumentation used across the three campaigns also complicate our ability to draw broad conclusions from our model-observations comparisons. However, the PAS instruments, used during both WE-CAN and CLARIFY, are known to be more sensitive, much faster (less averaging over long time-scales required for a useable measurement), and less biased than filter-based methods, such as the PSAP used during ORACLES-2016, especially under the dry conditions in these studies. There has been limited observational validation of smoke optical properties used in 3D models as explored here. The challenges outlined above imply that there remain opportunities to bridge laboratory parameterizations, field observations, and models.

3.5 Photochemical whitening and the radiative impact of BrC

We use OMI near-UV aerosol index (AI) observations as a qualitative constraint on the spatial distribution of BrC and the potential role of photochemical whitening. Outflow from central

Africa provides an ideal case study as it is dominated by smoke (e.g., Denjean et al., 2020; Hammer et al., 2018) (Fig. 3.9), unlike the western U.S. where absorption from fires is confounded by anthropogenic sources. There is also minimal dust in the southern African outflow region at this time of year, enabling a focus on BrC in this region (e.g., Hammer et al. 2016). The UVAI is a qualitative parameter for detecting the presence of absorbing and scattering aerosol in the atmosphere and is sensitive to BrC and relatively insensitive to BC (e.g., Hammer et al. 2016). We use the Level-3 Aura/OMI Near UV Global Aerosol Data Products OMAERUVd product of UVAI at 1-degree resolution and regrid to the GEOS-Chem grid of $2^{\circ}\times2.5^{\circ}$ to enable comparison. Larger UVAI values indicate more absorption. UVAI values are higher off the coast of southern Africa relative to the western US generally and during each campaign's deployment year (not shown), consistent with the in situ measurements that suggest BrC produced by flaming fires (e.g., those that dominate African burning (Wu et al., 2020)) is more absorbing than that from less-flaming fires (like the forest fires of the western US) and with previous work (e.g., Hammer et al., 2016, 2018).

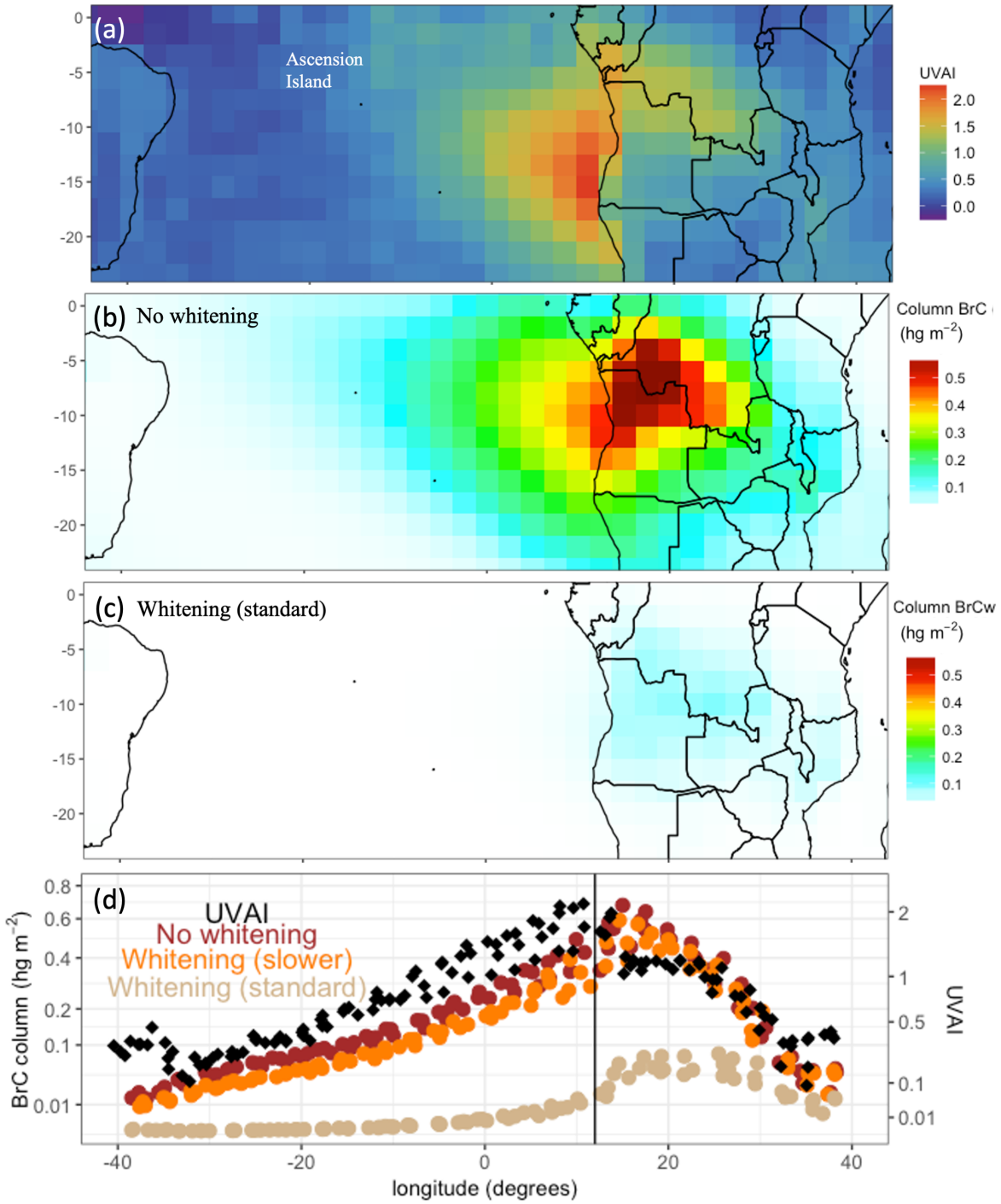

Figure 3.9. The mean August – September 2017 spatial distributions of the OMI UVAI (a), total simulated column burden of BrC (b), and total simulated column burden of BrC with the baseline whitening scheme (c) – all at 2°×2.5°. Column BrC is saturated at maximum values. Panel d shows column-integrated BrC concentrations averaged across August – September 2017 with our baseline BrC in red, our slower whitening lifetime simulation in orange, and our standard

whitening scheme in beige within a box off the coast of southern Africa bounded by latitude = -12° to -5° and longitude = -40° to 40°. OMI UVAI observations for the same region are overlaid in black diamonds. A vertical line at 12 degrees is the approximate edge of the African continent. The y axes have been transformed by a square-root function.

Figure 3.9 shows the region off the coast of southern Africa where the smoke plume is well-defined. The OMI UVAI product shows an abrupt change at the coastline. Two factors may contribute to this, namely that (i) this region is quite cloudy, which complicates retrievals, and (ii) the retrievals are more reliable over land (Hammer et al., 2018; OMI Team, 2012), potentially explaining the observed change. While the values over the ocean may be less reliable, their relative magnitude still provides a good qualitative perspective on the decay of BrC absorption over time. BrC concentrations (as well as the UVAI) decrease due to dilution in the outflow, possible SOA formation that increases the ratio of scattering aerosol in the outflow and whitening of BrC. An increasing inorganic fraction over time may also contribute to increasing scattering. Implementing whitening significantly decreases the total column BrC concentrations relative to a simulation without whitening. Low UVAI value are observed as far west as Ascension Island, especially as compared to the area close to the African coast where a large plume is visible and where ORACLES-2016 generally sampled.

Figure 3.9d compares the BrC column-integrated concentrations from simulations with no whitening, with the standard whitening, and with a slower whitening with the OMI UVAI observations plotted against longitude. The standard whitening scheme is based on two studies in different regions (Forrister et al. (2015) in the western US and Wang et al. (2016) in the Amazon), which both suggested a 1-day photochemical lifetime, indicating that there is not strong regional variance. As described in Section 3.2.1, the GEOS-Chem parameterization of this process is dependent on OH levels, and equivalent to the observed 1 day at global mean average OH levels. However, given the higher [OH] in the southern African region (mean of ~3 x 10^6 molec cm^{-3}), whitening timescales are much faster there (~4 hours using the standard whitening scheme instead of 1 day). We thus run a sensitivity study that fixes the whitening timescale to 1 day globally. Peak simulated column concentrations of BrC in African outflow are roughly a factor of eight larger when neglecting whitening versus using our standard whitening

parameterization, or a factor of 1.15 larger when comparing a simulation without whitening with a simulation using a slower whitening time scale. BrC emissions accumulate as you move westward over the continent (roughly 12° to 40°) in all three simulations, with the whitening process quickly counteracting some of this increase in BrC concentrations (Fig. 3.9d). Thus, with whitening, much less BrC is exported from the continent and a more rapid decline in BrC concentrations is also observed in the outflow. The rate of decrease of the OMI UVAI observations off the coast is best matched by the simulation without whitening; although, the slower whitening simulation shows reasonable agreement as well. This suggests that the whitening time scale for smoke downwind of Africa is likely 1 day (consistent with previous field studies) or longer, and that [OH] may not be a good proxy for whitening timescales in all regions. It is also possible that the slower whitening timescale is, at least partially, accounting for a neglected initial stage of BrC net enhancement after emission mentioned above in Section 3.4. However, we caution that these are qualitative comparisons. It is computationally intensive (and beyond the resources of this study) to repeat the detailed radiative calculations required to directly compare our simulations with the OMI UVAI product as done by Hammer et al. (2016; 2018). Coincident measurements of aerosol composition, size, and absorption within the export plume would be needed to directly constrain the evolution of BrC absorption.

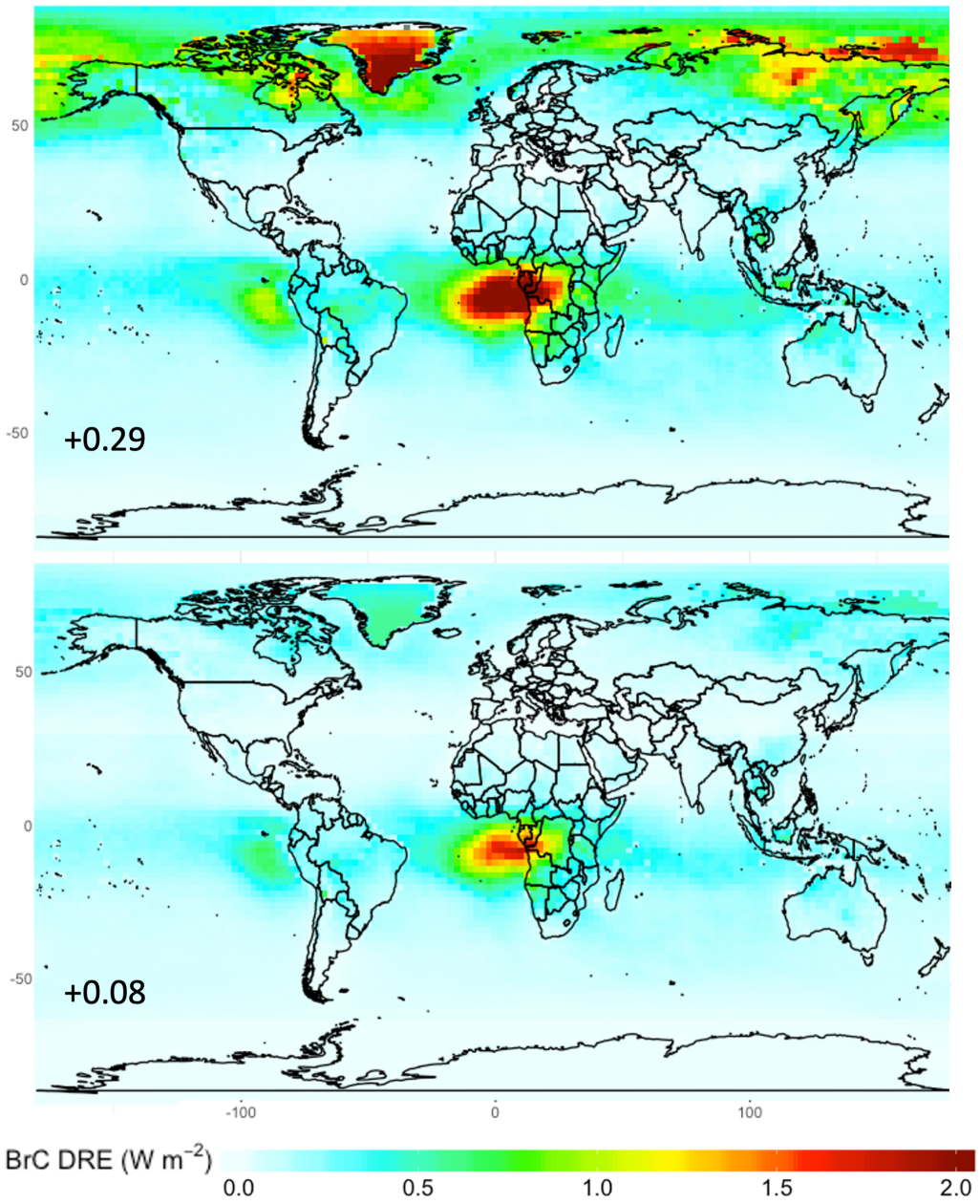

Figure 3.10. The global annual mean all-sky BrC DRE at the top of the atmosphere (TOA) in 2018 from a simulation without whitening (top) and when including whitening with a 1-day whitening scheme (bottom). Numbers indicate the global mean value in W m^{-2}.

We also investigate the global implications of the photochemical whitening of BrC (an optical loss process only and not a physical loss of BrC (e.g., fragmentation and evaporation)). The global burden of BrC without whitening (4.64 Tg) is a factor of three higher than with the 1-day whitening scheme (1.38 Tg) – OA mass is conserved; the whitened BrC is tracked separately as

white POA. Correspondingly, we estimate an annual mean all-sky BrC DRE of +0.29 W m^{-2}, which is reduced to +0.08 W m^{-2} when including whitening using the 1-day whitening scheme (Fig. 3.10). Both values fall within the (large) literature range (+0.03 to +0.6 W m^{-2}) (Feng et al., 2013; Lin et al., 2014; Wang et al., 2014; Wang et al., 2018). Given the model underestimate of smoke concentrations downwind of Africa seen in Figure 3.5, these numbers are likely a lower limit. We calculate that the net effect of all BBA (BC: +0.05 W m^{-2}, BrC given above (with 1-day whitening scheme, white POA: -0.10 W m^{-2}), and SOA: -0.05 W m^{-2} from fires) on all-sky annual mean DRE, which switches from positive without whitening to slightly negative with whitening (+0.19 W m^{-2} without whitening, -0.02 W m^{-2} with whitening). This range suggests that the timescales for photochemical whitening of BrC could dictate a significant change in magnitude and possibly a change in the sign of the net DRE of BBA, highlighting the importance of better observational constraints on this process.

3.6 Conclusions

Significant uncertainties exist around both the abundance and properties of BBA – our work investigates this in two major BB regions, the western US and southern Africa, and explores the implications of this work globally. We show that BB BC is underestimated during ORACLES-2016 and CLARIFY, suggesting an underestimate in BB inventories in southern Africa, and that simulated anthropogenic BC is overestimated in the US when using the 2011 NEI. We address these biases through scaling of emission factors and filtering out of more anthropogenically-influenced air masses, respectively. The resulting model is able to capture the large regional difference in observed BC:OA albeit with an underestimate of CLARIFY. Comparing modeled MAC with observations of absorption from each campaign, we show that our BC optical properties for smoke (which include an AE of 1.5 for BB BC) are generally consistent with observations at longer wavelengths (660 nm) during WE-CAN. However, more absorbing BC (achieved either via a higher baseline MAC (Forestieri et al., 2018; McClure et al., 2020) or a higher AE as in Taylor et al. (2020)), would better capture measurements downwind of Africa. Our analysis of African outflow also suggests that the low bias in the model AAE of BC may contribute to the model underestimate of absorption at shorter wavelengths. We also show that an increase in BrC absorption can help explain these observations at short visible wavelengths.

Our comparisons of the measurements from WE-CAN and ORACLES-2016/CLARIFY demonstrate that African smoke (BC and/or BrC) is substantially more absorbing at shorter wavelengths than suggested by our baseline simulations. Brown et al. (2021) recently suggested that most models overestimate BB absorption, but their work focused on absorption at longer wavelengths (550 and 700 nm). More absorbing BrC downwind of Africa is consistent with a higher BC:OA ratio observed in African outflow and captured by our model simulations. We implement two parameterizations of BrC absorption based on the BC:OA ratio (Saleh et al. 2014; McClure et al., 2020). These schemes improve our ability to simulate the MAC_{BC+OA} at short wavelengths for fires downwind of Africa, but lead to an overestimate in absorption during WE-CAN when not invoking whitening. Thus, neither scheme sufficiently represents the considerably lower absorption of BrC in smoke from the western US and the more absorbing BrC from African fires. One possible explanation is that Mie theory (used in Saleh et al.) may not be a good representation of optical properties for fresh smoke (Womack et al., 2020), as sampled during WE-CAN. Additional multi-wavelength measurements, with a focus on determination of BrC properties from primary BBOA when the BC:OA ratio < 0.1, would be helpful in improving these parameterizations. McClure et al. (2020) showed that the uncertainty increases as the BC:OA ratio increases. Lab observations also suggest that there is some additional dependence on what is burned outside of a simple BC:OA paradigm. We also find that the FIREX parameterization enhances the absorption of BrC downwind of Africa at longer wavelengths, reducing the BC AE needed to explain observations during ORACLES and CLARIFY.

Our analysis relies on the contrast of total absorption measurements at two wavelengths in two different regions. This type of analysis is complicated by convolving the properties of various absorbers, the relevance of fixed assumptions for absorption efficiency, and the use of differing instrumentation across field campaigns. Absorption measurements at more than two wavelengths, and thus multiple AAE determinations, in different environments would offer additional opportunities to constrain models. More comprehensive field observations of the size of BC and BrC along with species-specific absorption measurements (e.g., BrC absorption measured directly from filter extracts, alongside total absorption measurements) at multiple wavelengths could better discern the relative contributions of BC and BrC.

This analysis provides qualitative evidence for the need to include whitening (on a 1-day timescale, or even faster) to capture observations from WE-CAN, but uncertainties in the baseline properties for BC and BrC from African fires make it more challenging to comment on the role of photochemical whitening during the ORACLES-2016 and CLARIFY campaigns. Our qualitative comparisons with the OMI UVAI in African outflows support a whitening timescale of 1 day or longer. These comparisons also suggest that linking the timescale of photobleaching to OH concentrations, as in our standard simulation, may not be appropriate, given the resulting very fast bleaching that would result in the tropics. It is possible that whitening timescales could vary regionally given that different fuel types produce distinct amounts of nitrogen-containing species, which have been associated with BrC (Mohr et al., 2013; Palm et al., 2020; Teich et al., 2017; Yuan et al., 2020). Analyses of WE-CAN show that there were large concentrations of N-containing species during the campaign (e.g., $[NH_3] > 50$ ppb in concentrated smoke plumes; Pollack et al., 2019) and suggest that nitroaromatics are important for BrC (Palm et al., 2020). However, no comparable measurements downwind of Africa exist to test whether the nitrogen content of smoke might dictate whitening timescales. More work is needed to determine the timescale of photochemical whitening in smoke from different fuels, whether OH concentrations or photolysis are controlling parameters, and how model resolution may affect these parameterizations.

Our comparison of smoke optical properties in two important, but very different, regions has implications for aerosol remote sensing algorithms. Typically, such retrievals assume constant properties, but the large differences in absorption shown here, as well as the dynamic properties associated with photochemical whitening, suggest that such an approach may introduce retrieval artifacts. Therefore, further refinement of BrC parameterizations may also help inform the development of remote sensing algorithms.

The global mean DRE of BrC is very sensitive to the timescale of photochemical whitening. This process may dictate the overall importance of the DRE from carbonaceous aerosol in smoke. Using our best estimate of a universal 1-day timescale for whitening (not dependent on OH), we find a global DRE of BBA of -0.02 W m^{-2}, neglecting whitening results in a considerably more

warming DRE for fires (+0.19 W m^{-2}). Additional observations in fire outflow, over long timescales, and from varying fuel types, are needed to better understand the magnitude and evolution of BrC absorption, and thus the global radiative impacts of smoke.

Chapter 4. An Improved Representation of Fire Non-Methane Organic Gases (NMOGs) in Models: Emissions to Reactivity

Adapted from: Carter, T.S., C. L. Heald, J. H. Kroll, E. C. Apel, D. Blake, M. Coggon5, A. Edtbauer, G. Gkatzelis, R. S. Hornbrook, J. Peischl, E. Y. Pfannerstill, F. Piel, N. G. Reijrink, A. Ringsdorf, C. Warneke, J. Williams, A. Wisthaler, and L. Xu (2022), An Improved Representation of Fire Non-Methane Organic Gases (NMOGs) in Models: Emissions to Reactivity, Atmos. Chem. Phys. Discuss., submitted.

4.1 Introduction

Biomass burning (both wildfires and prescribed and agricultural burns) is a large source of non-methane organic gases (NMOGs) (e.g., Akagi et al., 2011; Koss et al., 2018; Coggon et al., 2019; Kumar et al., 2018). Goldstein and Galbally (2007) suggest that, while tens of thousands of organic compounds have been detected in the atmosphere, this may represent only a small subset of the species present in the atmosphere. Only ~100 compounds have typically been measured during field campaigns, but recent advances in mass spectrometry have enabled the online characterization of an expanding suite of organic compounds in the atmosphere, including those from fires (e.g., Koss et al., 2018). Because many NMOGs are quite reactive, they impact tropospheric and stratospheric (Bernath et al., 2022) chemistry and composition. Many NMOGs are toxic themselves (Naeher et al., 2007), and they can also react to form two major air pollutants that are also harmful to human health, ozone (O_3) and particulate matter under 2.5 microns ($PM_{2.5}$) (e.g., Hobbs et al., 2003; Yokelson et al., 2009; Jaffe et al., 2008, 2013, 2018; Xu et al., 2021). NMOGs also modulate oxidant concentrations, which affect the climate through the methane lifetime (Voulgarakis et al., 2013; Mao et al., 2009). The importance of fires to the budget of global NMOGs and to the impacts discussed above is not well understood, as suggested by a recent study (Bourgeois et al., 2021).

Various terms have been used in the literature to describe reactive carbon-containing trace gases, including one of the first, non-methane hydrocarbons (NMHCs), which excludes species with oxygen or other heteroatoms. The term volatile organic compounds (VOCs) encompasses this

broader set of compounds; although, there is no agreed upon, quantitative definition for VOCs or their surrogate, non-methane organic compounds (NMOCs). The European Union defines VOC as any organic compound having an initial boiling point less than or equal to 250° C measured at a standard atmospheric pressure of 101.3 kPa (European Union, 1999). The US EPA defines VOCs as any compound that participates in atmospheric photochemical reactions except for those that they designate as having minimal reactivity. The term oxygenated VOCs (OVOCs) (Goldstein and Galbally, 2007; Kwan et al., 2006) has further blurred these definitions, with colloquial usage sometimes being ambiguous as to whether OVOCs are a subset of VOCs or whether VOCs represent the unoxygenated (i.e., NMHC) suite of compounds. Volatility-based nomenclature separates VOCs from semi-volatile (SVOC) and intermediate-volatility (IVOC) species (Robinson et al., 2007). For this study, we use NMOGs, which encompasses all gas-phase organic compounds (excluding methane), regardless of volatility, degree of oxygenation, or other chemical properties.

While fires emit a significant amount of NMOGs (> 400 Tg yr^{-1})(Akagi et al., 2011; Yokelson et al., 2008), second only to biogenic sources globally (~1000 Tg yr^{-1})(Guenther et al., 2012), modeling efforts, particularly at the global scale, have historically represented only a modest subset of these emissions and their reactivity. This is in part because a large number of reactive fire NMOGs remain unidentified (Kumar et al., 2018; Hayden et al., 2022; Akagi et al., 2011). While progress has been made on measuring emissions of many fire NMOGs, these measurements have not yet been incorporated into models with global coverage. Given the significant, but insufficiently characterized variability in emission with both fuel and fire characteristics, this challenges integration into fire emission inventories. To represent emitted species, fire emissions inventories generally apply emission factors (EFs) to estimates of dry matter (DM) burned. Variation among fire inventories is generally driven by differences in DM, rather than EFs (Carter et al., 2020); though, NMOG EFs often have greater variability amongst inventories. Akagi et al. (2011) estimated both species-specific NMOC EFs, as well as the EF for the total of identified + unidentified NMOC mass (for various ecosystems (e.g., for savannas, the fraction of NMOC emitted mass that is unidentified is ~50% - this number is typical across the other ecosystems). They also identify unknown NMOCs as one of the largest sources of BB emissions uncertainties. The GFED version 4 with small fires (GFED4s) inventory (van der Werf

et al., 2017) includes the Akagi et al. (2011) NMOG EFs. The Fire Inventory from NCAR (FINN) v1.5 also uses the Akagi et al. (2011) species-specific EFs as well as total NMOC, and total non-methane hydrocarbon (NMHC) EFs (Wiedinmyer et al., 2011). Both the Quick Fire Emissions Dataset (QFED)(Darmenov and daSilva, 2014) and Global Fire Assimilation System (GFAS)(Kaiser et al., 2012) rely mostly on an older EF compilation (Andreae and Merlet, 2001) with a few small updates.

Several recent scientific advances, including a new fire EF compilation, improved instrumentation, and fire-focused field campaigns, provide opportunities to enhance our understanding of NMOGs from fires. Andreae (2019) updated the EFs compiled by Akagi et al. (2011) and Andreae and Merlet (2001) and added 28 more chemical species, including many fire NMOGs. Recent improvements in instrumentation, especially proton-transfer-reaction time-of-flight mass spectrometry (PTR-ToF-MS) and gas chromatography (GC), enable high resolution NMOG measurements, providing the exact molecular formulas and isomer distributions of detected NMOGs (Hatch et al., 2015; Gilman et al., 2015) and quantification of a substantial portion of the total carbon mass (Koss et al., 2018). Because OH is generally the dominant oxidant of most fire NMOGs, the inverse of the OH lifetime (or the OH reactivity, OHR) can be a useful metric to understand the reactivity of fires, where a gap between summed observed OHR and calculated OHR based on OH lifetimes can point to unidentified NMOGs or oxidation products (Yang et al., 2016). Lab studies have shown that, from fires, furans, oxygenated aromatics, and aliphatic hydrocarbons (e.g., monoterpenes) contribute substantially to both calculated and measured OHR and that furans and phenolic compounds are among the most reactive (Coggon et al., 2019; Hatch et al., 2015). The contribution of fires to global OHR has not been quantified. Growing interest in the impacts of fires on tropospheric composition has motivated recent fire campaigns in regions with large and growing fire emissions.

These advances suggest that there are opportunities to improve the modeling of NMOGs from fires and their impacts. In this work, we use the GEOS-Chem chemical transport model (CTM) and recent lab and field observations to investigate and improve our simulation of fire NMOGs. We then use this model to characterize the importance of fires to atmospheric reactivity (through their contribution to total NMOG concentrations and OHR) both globally and regionally.

4.2 Model description

The GEOS-Chem model

We use GEOS-Chem (https://geos-chem.org, last access: 15 January 2021), a global CTM, to explore fire NMOGs globally and in specific large fire regions and outflow regions, such as the US, boreal Canada, the Amazon, and Africa. GEOS-Chem is driven by assimilated meteorology from the Modern-Era Retrospective analysis for Research and Applications, Version 2 (MERRA-2), from the NASA Global Modeling and Assimilation Office (GMAO). We use version 13.0.0 (https://zenodo.org/record/4618180) of GEOS-Chem with a horizontal resolution of 2° × 2.5° and 47 vertical levels with a chemical time step of 20 min and a transport time step of 10 min as recommended by Philip et al. (2016). We perform 12-month spin-up simulations prior to the time periods of interest, either our yearlong analysis or for comparison with campaigns: June-July 2008, May-June 2012, April-August 2016, January-December 2017, October 2018, and January-December 2019. We also perform nested simulations over North America at 0.5° × 0.625° (with boundary conditions from the global simulation) for comparison against aircraft campaign DC3, FIREX-AQ, and ARCTAS observations (see Section 4.4) with chemistry and transport time steps of 10 and 5 min, respectively.

GEOS-Chem includes $SO_4^{2-}/NO_3^-/NH_4^+$ thermodynamics (Fountoukis and Nenes, 2007) coupled to an O_3–VOC–NO_x–oxidant chemical mechanism (Chan Miller et al., 2017; Mao et al., 2013; Travis et al., 2016) with integrated Cl-Br-I chemistry (Sherwen et al., 2016). We add aromatic oxidation updates (with benzene, toluene, and xylenes (C8 aromatic compounds including o-, m-, p- xylenes and ethylbenzene) emissions) per Bates et al. (2021) and ethene and ethyne chemistry updates per Kwon et al., (2021); both were developed in GEOS-Chem, but not yet implemented in the standard model. These aromatic and ethene/ethyne chemistry updates modify oxidant levels, particularly NO_3, which overall decreases NMOG lifetimes. Bates et al. (2021) estimate an annual global mean increase of +22% for NO_3. In general, species not directly involved in the new chemistry are modestly impacted by these changes while, for example, species like glyoxal and glycolaldehyde, which are important products of the ethene/ethyne chemistry, undergo large increases.

Baseline fire emissions are from the Global Fire Emissions Database version 4 with small fires (GFED4s; (van der Werf et al. 2017)) and are specified on a daily timescale. Additional details on fire NMOG emissions are provided in Sect. 4.3. A sensitivity analysis, described in Sect. 4.4, uses FINNv1.5. Anthropogenic emissions (including fossil and biofuel sources) follow the year-specific CEDS global inventory (Hoesly et al., 2018). Trash burning emissions are from Wiedinmyer et al. (2014). Aircraft emissions are from the Aviation Emissions Inventory Code (AEIC) inventory (Stettler et al. 2011; Simone et al. 2013). Biogenic emissions are calculated online from the MEGANv2.1 emissions framework (Guenther et al. 2012).

A typical source attribution method in models zeroes out a specific source and differences that simulation from the baseline. This brute force method is ideal for linear systems, but for non-linear chemistry, large perturbations to emissions will feed back onto the chemistry (and thus impact lifetimes). For example, zeroing out fire emissions increases OH concentrations because the OH sink has been decreased, thereby increasing the rate of oxidation of other species, such as from biogenic sources. Such a depression in isoprene concentrations, for example, may then increase or decrease ozone concentrations, depending on the chemical regime. The HTAP modeling experiments, which were focused on O_3, address this issue with 20% emission perturbation sensitivity studies – a number chosen to produce a discernable (larger than numerical noise) and realistic impact while minimizing non-linearities (Huang et al., 2017). To isolate the influence of fires in our model and minimize these nonlinearities, we run emissions sensitivity simulations with 5% more and less fire emissions (0.95 and 1.05 times fire emissions) and scale up the difference to equate to a 100% perturbation. We compare these runs with the more typical noFires brute force simulation in the SI (see Figs. 4.S1, 4.S2, and 4.S3) and show, for example, that the O_3, OH, and isoprene differences are minimized with the emissions sensitivity approach (Fig. 4.S1). We use this fire sensitivity source-attribution approach throughout this study.

To translate the concentrations of reactive compounds to calculated OHR (cOHR) at atmospheric ambient conditions, we define cOHR as the sum of the pressure- and temperature-dependent OH rate constant of a species (from the GEOS-Chem mechanism) with its concentration as follows:

$$cOHR\ (s^{-1}) = k_{OH,CH_4}[CH_4] + k_{OH,CO}[CO] + k_{OH,NO_2}[NO_2] + \Sigma k_{OH,NMOG_i}[NMOG_i] + \cdots \quad (1)$$

where *i* indicates various NMOG species.

4.3 Updating and expanding fire NMOGs in GEOS-Chem

We update and expand the fire NMOGs in GEOS-Chem by updating existing EFs and then considering additional emissions and chemistry. First, we update our EFs from Akagi et al. (2011) to the newer Andreae (2019) compilation. Total NMOG emissions do not change substantially between the two inventories – in 2019, they decrease by 3.4% from Akagi et al. to Andreae. There is, however, more variation across the different species with, for example, Akagi et al. providing larger savanna EFs for glycolaldehyde (0.25 g/kg DM vs. 0.13 g/kg DM) and glyoxal while Andreae specifies higher values for benzene (0.33 g/kg DM vs. 0.20 g/kg DM), toluene, and xylenes (see Fig. 4.S4 in the SI).

The standard GEOS-Chem model includes fire emissions of 15 NMOG species. The number of possible additional NMOGs from fires is quite large (Akagi et al., 2011). We focus on the feasibility and utility of adding fire NMOGs that Coggon et al. (2019) (building on Koss et al., (2018)) identify as accounting for 95% of fire OHR. We first identify the fire NMOGs already represented in GEOS-Chem (black circles in Fig. 4.1), then those additional species for which EFs are available from the recently updated compilation by Andreae (2019) in blue, and finally those species for which EFs are only available for western US fuel types as measured during the FIREX lab study (Koss et al., 2018) in red. We size the symbols in Fig. 4.1a by their EFs for savanna (EFs for other fuel types generally provide a similar relative ranking) to identify the largest NMOG emissions. We order the species in Fig. 4.1a by their decreasing lifetime against OH with values ranging from 1 hour for sesquiterpenes to over a month for ethane. For context, we provide the same plot by their lifetimes against two other important oxidants, O_3 and NO_3, in the SI (Fig. 4.S5). To explore how chemical lifetimes of these fire NMOGs compare with their physical lifetime in a model grid box, we estimate the approximate lifetime of transport out of a global 2° × 2.5° grid box (~20 hours) and for a nested grid box at 0.5° × 0.625° (~5 hours) using 3 m/s as the surface wind speed (shown as the grey shaded region).

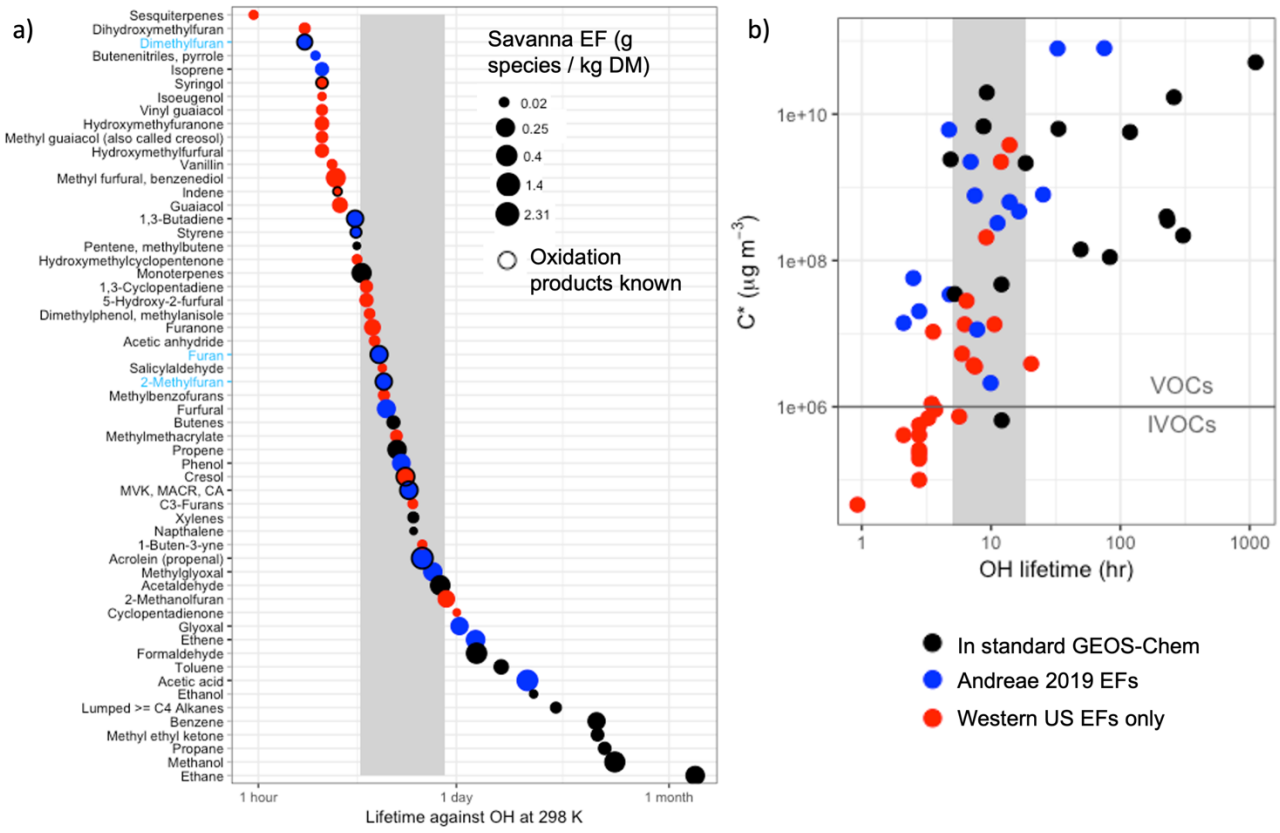

Figure 4.1. (a) NMOGs emitted from fires, shown in descending order of chemical lifetime due to oxidation by OH (at 298 K). Only the species responsible for 95% of OHR from fires are shown (following Coggon et al., 2019). NMOGs included in the standard GEOS-Chem model are in black, species not included in the standard GEOS-Chem model but where emissions factors are available in Andreae (2019) are in blue, and species that are only available for western US fuel types from Koss et al. (2018) are in red. The y-axis tick marks are in black for fire NMOGs added to GEOS-Chem in this study and in blue (with blue labels) when both the fire NMOG and its oxidation chemistry were added. The points are sized by their relative savanna and grassland (labeled "savanna") emission factor in g species / kg DM burned. The grey vertical box represents an approximate physical lifetime against transport out of a nested 0.5° × 0.625° grid box (~5 hours) and a 2° × 2.5° grid box (~20 hours). CA stands for crotonaldehyde. (b) Plot of volatility (C*) against OH lifetime for the species shown in (a) using the same color conventions. The horizontal line separates VOCs from IVOCs based on their C*.

In Fig. 4.1, most species with chemical lifetimes that exceed the transport timescale out of a model grid box are already included in the model. Using Andreae (2019) EFs, we add fire emissions of eight species already included in the model for which fire emissions were previously neglected: phenol, methyl vinyl ketone (MVK), ethene, isoprene, acetic acid, methylglyoxal, glyoxal, and lumped aldehydes with three or more carbon atoms, which does not include furfural (RCHO). We also add fire emissions of 1,3-butadiene to the tracer representing alkenes with greater or equal to three carbons (PRPE). Furans from fires are important for atmospheric reactivity (Koss et al., 2018; Coggon et al., 2019). We add a new lumped furan tracer, called FURA, that combines the pyrogenic emissions of furan, 2-methylfuran, and 2,5-dimethylfuran and uses the OH rate constant of furan (k_{OH} = 1.32 x 10^{-11} x $e^{\frac{-334}{RT}}$) (furan and 2-methylfuran dominate emissions and have very similar lifetimes against OH). In the model, the oxidation of FURA with OH produces butenedial since that has been shown experimentally with an estimated carbon balance of 100% C (Bierbach et al., 1995). Thus, we add fire emissions for almost all the species for which we have Andreae EFs (12 species) to GEOS-Chem. For 2019, these added global fire emissions (19.6 Tg C) are roughly equivalent to the fire NMOG emissions already in the model (21.8 Tg C) (see Table 4.S1 for species total emissions). The only species with Andreae (2019) EFs that we do not add to GEOS-Chem are: (1) butenenitriles, which have a very small EF and a short lifetime against OH, (2) styrene, which also has a chemical lifetime less than the grid box physical transport time, and (3) furfural. There is a wide spectrum of lesser abundant furans (+ furfural) (Zhao and Wang, 2017) that contribute to furan reactivity; therefore, the representation in this model constitutes a lower bound on furan contributions to total reactivity. We do not include species where EFs are only available for western US fuel types from Koss et al. (2018). Figure 4.1a suggests that nearly all these species are very reactive and short-lived as evidenced by the red circles being within or below the physical transport time of the grid box.

Fig. 4.1b shows the volatility of these same NMOG species. The species for which we have global EFs available are almost entirely very volatile and above a commonly held cutoff threshold for intermediate volatility compounds (IVOCs) versus VOCs (C^*=1 × 10^6 μg m^{-3} (Ahern et al., 2019 and references therein)). This suggests that both the standard model and our expanded treatment of NMOGs neglect many NMOG precursors for secondary organic aerosol.

This study focuses on the OHR of NMOG from fires; further work is needed to constrain the EFs (Fig 4.1b suggests that global EFs are not available for most IVOCs) and oxidation chemistry of NMOG species relevant to SOA formation from fires.

Species whose chemical lifetimes are shorter than the physical transport lifetimes (Fig. 4.1a) contribute strongly to near-field reactivity but are likely not exported from the grid box of emission. For these species, oxidation rapidly converts emitted species into secondary products, and it is these products that are exported away from the fire source. However, a detailed knowledge of the oxidative chemistry of many of these species is lacking (as evidenced by the small number of black circled species, indicating "oxidation products known" in Fig. 4.1a). In particular, we note that we do not include several very reactive species (e.g., furfurals, guaiacol) (Coggon et al., 2019). Hence our model represents a lower limit of reactivity from fires, despite our inclusion of longer-lived NMOG.

To characterize the amount of carbon mass and reactivity represented in our current model and the potential shortfall in NMOG emissions, we use EFs as proxies for emissions. We first calculate the total carbon mass based on the sum of the savanna and temperate forest EFs (the only EFs we have for all species in Fig. 4.1), and we compare that number to the sum of the savanna and temperate forest EFs for different subsets (standard GEOS-Chem and updated GEOS-Chem) of species included in Fig. 4.1. We note that here and throughout the manuscript, NMOG % values refer to percentage by carbon mass. We find that the standard GEOS-Chem model represents 49% of the total carbon mass emissions potential of NMOGs suggested in Fig. 4.1. Our additions to the model increase this to 72%. We then multiply these EFs by the rate constants with OH at 298 K to represent a proxy for reactivity. From this, we calculate that the standard model includes 28% of the potential emitted reactivity of savanna and temperate forest fuel type emissions; our model updates add an additional 17% (for a total of 45% of the potential reactivity). This suggests that the sum of these minor species for which global EFs are not defined, and therefore that we do not include in our model, contribute over half of the emitted reactivity from fires. We note that all these fractions are relative to speciated NMOGs from Coggon et al. (2019); unspeciated or unidentified NMOG would increase our model shortfall.

We use the Andreae (2019) EFs applied to the GFED4s DM and the chemistry updates noted here for the rest of this analysis unless specifically noted.

4.4 Exploring observational constraints on fire NMOGs

There are limited observational constraints on fire-influenced NMOGs and OHR. We use observations of OHR made at the Amazon Tall Tower Observatory (ATTO) and of VOCs from the FIREX and ARCTAS campaigns in addition to measurements of both VOCs and OHR from the Deep Convective Clouds and Chemistry (DC3) campaign. Previous work has shown that the plume-chasing sampling strategy of the WE-CAN 2018 field campaign limits the suitability of this dataset for 3D model evaluation (Carter et al., 2021). While the KORUS-AQ campaign included airborne OHR measurements and some fire influence (median concentration of acetonitrile, a biomass burning tracer (Lobert et al., 1990), ~165 ppt, Fig. 4.S6), the campaign is dominated by anthropogenic sources, which recent work shows may confound the acetonitrile signal (Huangfu et al., 2021); and therefore we do not include this campaign in our analysis. We explore observations of OHR taken during ATom-1 off the coast of western Africa, during which Strode et al. (2018) identified fire influence. However, the aircraft sampled air masses more than 3000 km away from the continental fire source. As a result, most short-lived NMOG have reacted away, and the modeled cOHR is low and dominated by CO (Fig. 4.S7). Thus, ATom-1 is not a good constraint on fire cOHR and the impact of NMOG. There are no other airborne campaigns that we are aware of that have deployed OHR instrumentation in fire-influenced environments.

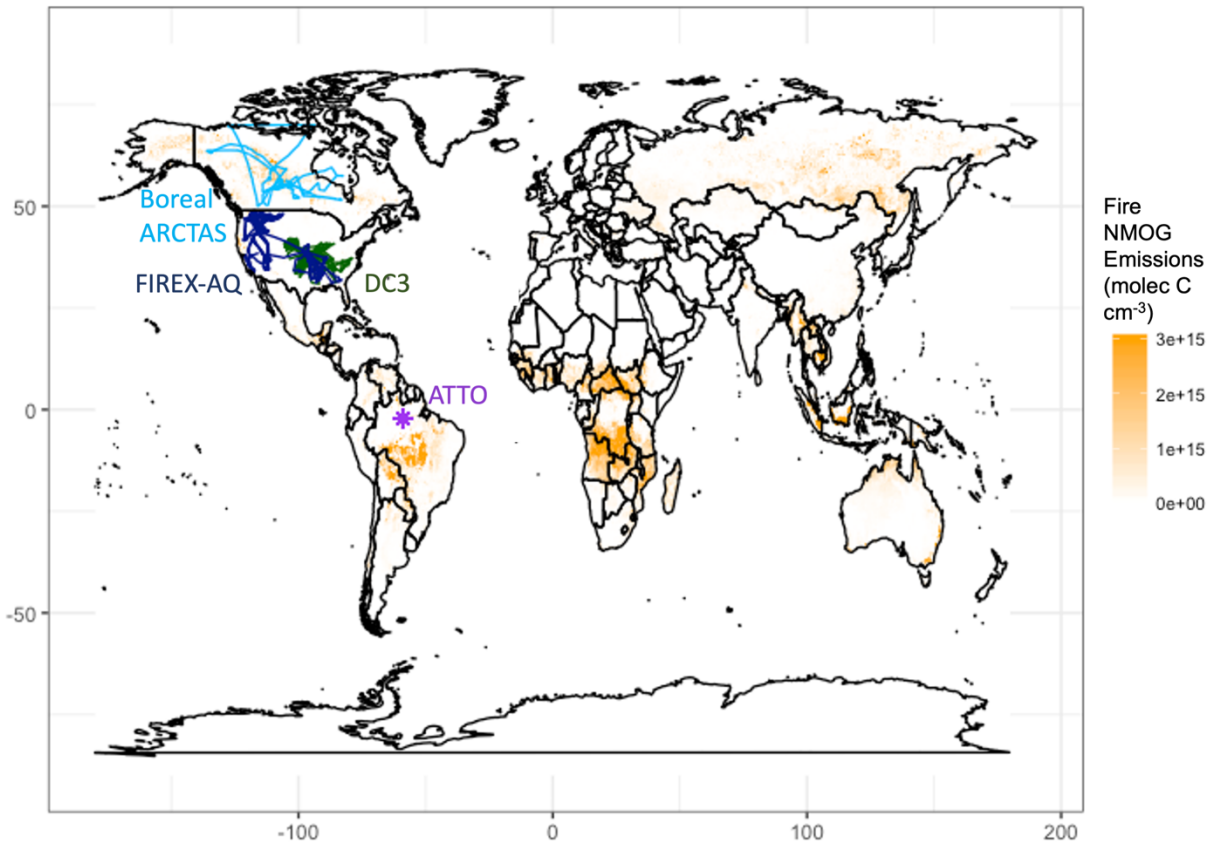

Figure 4.2. Measurement locations of campaigns used in this analysis overlaid on annual mean NMOG emissions from fires across 1997 – 2019 from GFED4s. Boreal ARCTAS is in light blue, FIREX-AQ in dark blue, DC3 in dark green, and ATTO in purple.

We use observations from campaigns that sampled fire-influenced air masses in different regions around the world (Fig. 4.2). For tower and aircraft campaigns, the model is sampled to the nearest grid box of the measurements both temporally and spatially using the entire 1-min merge of observational data. We then average both the model and the observations to the model grid box.

To evaluate our simulation of NMOGs in the US, we explore observations from the NASA DC-8 during the Fire Influence on Regional to Global Environments and Air Quality (FIREX-AQ) campaign, which deployed in the western and eastern US from 15 July through 5 September 2019 with a large suite of NMOG instrumentation aboard. The campaign investigated the chemistry and transport of smoke from both wildfires and prescribed burns in the western and

eastern US with flights originating from both Boise, ID, and Salina, KS. CO was measured using a modified commercial off-axis ICOS instrument (Los Gatos Research (LGR) N_2O/CO-30-EP; Baer et al. 2002) at ~ 4.6 μm. Precision was estimated to be 0.4 ppb, and uncertainty for the dry air mole fraction of CO for mixing ratios below 1 ppm to be ± (2.0 ppb + 2%). More details are available from Bourgeois et al. (2022). MVK, furan, 2-methylfuran, and 2,5-dimethylfuran were measured using the NCAR Trace Organic Gas Analyzer with a Time-of-Flight MS (TOGA-TOF) (Apel et al., 2015; Wang et al., 2021b). The TOGA-TOF measurements are reported with a detection limit of 0.5 ppt and an uncertainty (accuracy and precision) of 20%. Phenol was measured using the NOAA PTR Time-of-Flight MS (PTR-ToF-MS) with accuracy of 25% (Müller et al., 2014; de Gouw and Warneke, 2007) and by the California Institute of Technology Chemical Ionization Mass Spectrometer (CIT-CIMS) with an accuracy of 30% (Xu et al., 2021). During the western part of the campaign, the phenol measurements by PTR were affected by a contamination issue above 8 km, so those data have been removed. Generally, the model captures the differing fire influence in the eastern and the western US. For example, in the eastern US, the model captures vertical profiles of CO well (Fig. 4.3) while in the western US, the model matches the general shape but underestimates the magnitude of the observations and likely the influence of more sporadic fires in the region. Recent papers have also shown that GEOS-Chem struggles to fully capture large wildfires in the western US (e.g., Carter et al., 2021; O'Dell et al., 2019; Zhang et al., 2014) in part because the DM estimates may be underestimated (Carter et al., 2020) and because GEOS-Chem and other air quality models with a fairly coarse resolution have trouble resolving sub grid processes (Eastham and Jacob, 2017; Rastigejev et al., 2010), including those involved in fire plumes (Wang et al., 2021b; Stockwell et al., 2022).

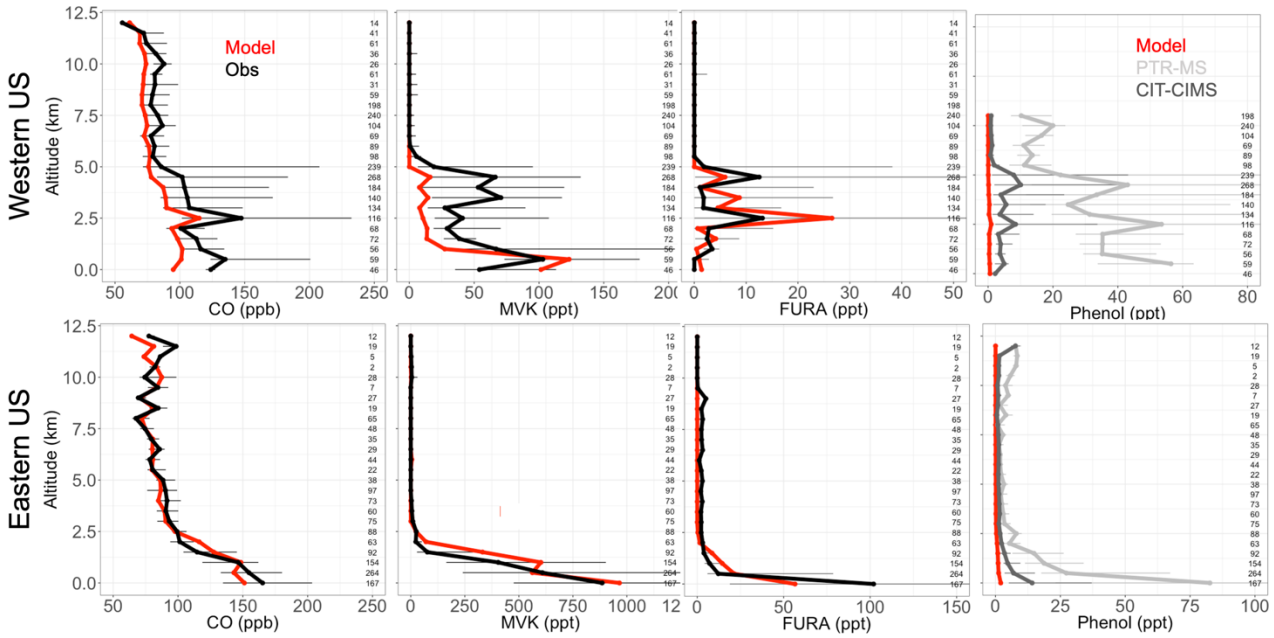

Figure 4.3. Binned observed (black) and simulated (red) median vertical profiles of CO, MVK, lumped furan species (FURA = furan + 2-methylfuran + 2,5-dimethylfuran), and phenol concentrations from the FIREX-AQ campaign. For phenol, observations using the PTR-MS are in light grey and those from the CIT-CIMS in dark grey. Horizontal bars show the 25th–75th percentile range of measurements in each vertical 0.5-km bin. The number of observations in each bin is shown on the right side of each panel.

The FIREX-AQ measurements can also be used to evaluate some of our model updates. Figure 4.3 shows that MVK, an example NMOG for which we added fire emissions in the model, follows similar model performance as CO. We note that more than 80% of simulated MVK during FIREX-AQ comes from fires. The FIREX-AQ summed observations of the same three furan species suggest that our new lumped "furan" (FURA) tracer with only fire sources performs well in the eastern and western US (Fig. 4.4). This suggests that the furan EFs for US fires like those sampled are accurately captured in the Andreae (2019) compilation; although, they may also be overestimated and thus compensating for an underestimate in the DM burned in GFED4s. Fig. 4.3 shows that our addition of fire emissions of phenol still underestimates observed concentrations across all altitudes in the western US and at the surface in the eastern US. Phenol observations from the CIT-CIMS (dark grey) instrument are a factor of 3 lower than the PTR-MS (light grey). The model underestimates the lower phenol concentration (CIT-CIMS)

by a factor of 8 in the eastern US and 15 in the western US. Given that both instruments were calibrated for phenol, the difference between two measurements is not yet accounted for. The measurements of phenol and other less-studied compounds have substantial uncertainties as indicated by these instrument differences, and more work is needed to understand these uncertainties. However, Taraborrelli et al. (2021) suggest that anthropogenic and fire sources contribute roughly equally to phenol emissions at the global scale. Therefore, both higher phenol emission factors from fires and emissions from anthropogenic sources in the US are likely needed to help resolve the discrepancy seen in Fig 4.3.

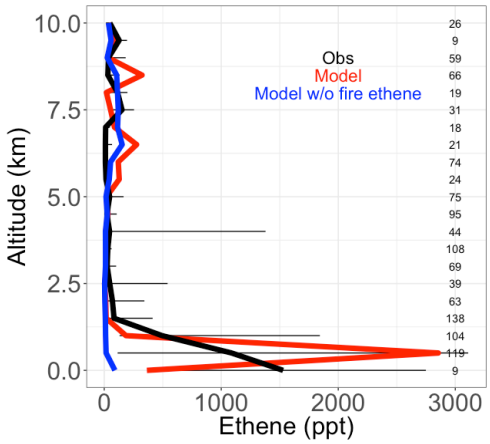

Fig 4.4. Median vertical profiles of binned ethene mixing ratios, including observed (black), simulated (red), and simulated in a sensitivity model run without fire ethene emissions (blue) during the boreal part of the ARCTAS campaign. Horizontal bars show the 25th–75th percentile range of measurements in each vertical 0.5-km bin. The number of observations in each vertical bin is shown on the right side of each panel.

In this study, we add fire emissions of ethene to the model, which may be important in certain regions. We turn to the boreal component of the Arctic Research of the Composition of the Troposphere from Aircraft and Satellites (ARCTAS) campaign to test the fidelity of this addition because the boreal EFs for ethene are high (1.54 g/kg DM, compared to 0.83 g/kg DM for savanna) and there is less anthropogenic influence in the boreal regions to confound a fire-focused model evaluation. The ARCTAS campaign sampled the Arctic region with an emphasis on forest fire smoke plumes using the NASA DC-8 aircraft from 18 June to 13 July 2008 (Jacob et al., 2010). We use observations of ethene from the UC Irvine Whole Air Sampler (WAS). This measurement has a limit of detection of 3 ppt, 3% precision, and 5% accuracy. See Simpson et

al. (2011); Colman et al. (2001) for more details. We show that the model (in red), filtered to remove the least fire-influenced points, captures the observed vertical profile of ethene concentrations well, including the large enhancement at the surface (Fig. 4.4). This is an improvement over a simulation without fire emissions of ethene (shown in blue), which shows negligible ethene throughout the vertical profile.

Figure 4.5 compares OHR measurements made at the ATTO site during the fire seasons in October 2018 and September 2019 (Pfannerstill et al., 2021) with the updated GEOS-Chem model simulation. ATTO is situated ~150 km northeast of Manaus, Brazil. We use total OHR measurements taken at 80, 150, and 320m on the tower during two intensive observation periods in October 2018 and September 2019 using the Comparative Reactivity Method (CRM, Sinha et al., 2008), which is described in more detail by Pfannerstill et al., (2021). We confirm that simulated OHR is mostly driven by isoprene during this campaign as Pfannerstill et al. (2021) show for the observations and find that the model (in red; median = 21.5 s^{-1}) captures the overall observed (in black; median = 22.4 s^{-1}) cOHR (Fig. 4.5a). Pfannerstill et al. (2021) assessed that fires contribute 17% of their OHR measurements (shown in black in Fig. 4.5b). Our updated simulation with the Andreae (2019) EFs and new chemistry (red in Fig. 4.5b) underestimates this fire contribution by a factor of ~5. Reddington et al. (2016, 2019) suggested that the FINN1/1.5 and GFED3/4s fire inventories underestimate fire emissions by a factor of 2-3 in parts of the Amazon with FINN emissions generally less biased than GFED. Following their analysis, we perform a sensitivity simulation where we use FINN1.5 instead for fire emissions and scale up the emissions to match what was used in the Reddington et al. studies. This simulation (purple) greatly improves model-observations agreement with a mean fire cOHR contribution of 17% (Fig. 4.5b). Excluding our additions to the NMOG model description (purple and white hatching) does not substantially degrade the agreement with observed OHR from fires, suggesting that underlying biomass burned may be a more important uncertainty in fire NMOG OHR than missing reactive species in this region.

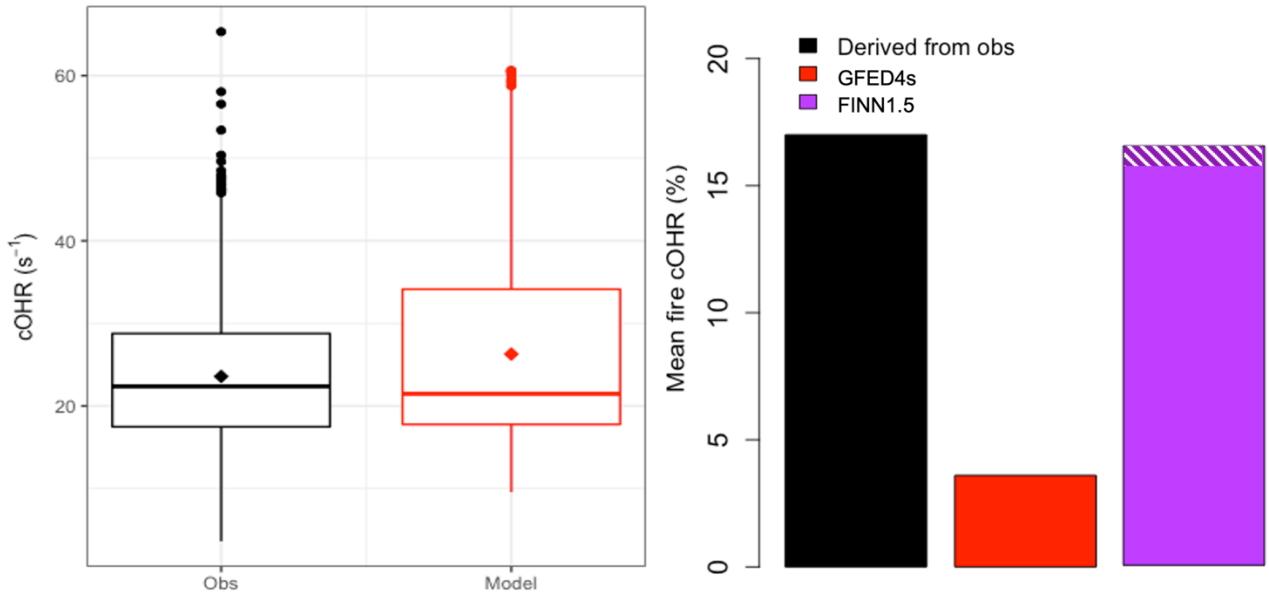

Figure 4.5. (Left) Boxplots of cOHR during the October 2018 and September 2019 measurement periods at ATTO with observations in black and the model in red with medians shown as a horizontal line and means as diamonds. (Right) The mean percentage contribution from fires during the same time period to cOHR with that derived from observations in black, the model with GFED4s in red, and a simulation using scaled-up FINN1.5 in purple. The white hatching on the FINN1.5 simulation indicates the increase in percentage contribution due to of new EFs and chemistry.

We also compare observations of NMOGs and OHR during the DC3 campaign, which sampled in the southeastern and south central US in 18 May – 22 June 2012 (Barth et al., 2015). Acetonitrile was measured using a PTR-MS (Hansel et al., 1995; Wisthaler et al., 2002). The OHR measurement is described in detail in Brune et al., (2018); Mao et al., (2009) with a limit of detection for 20s measurements estimated to be ~ 0.6 s^{-1}. This campaign was influenced by numerous sources, including fires. Here we explore how well GEOS-Chem captures observed OHR as a function of fire influence. Figure 4.6 shows the model skill in reproducing OHR (model minus observations) against CO and acetonitrile. We find that model skill degrades generally monotonically with increasing acetonitrile and CO concentrations. No similar trend is observed with anthropogenic tracers such as benzene, suggesting that the model underestimates fire sources of reactivity. This confirms that we are likely missing emitted fire NMOGs and/or secondary products during this campaign beyond what is currently represented in the model, as

suggested in Section 4.3. Thus, while previous comparisons shown in Section 4.4 indicate that the additions we have made to the model have improved our simulation of fire NMOGs, Figure 4.6 confirms further work is needed to fully capture the impact of fires on OH reactivity.

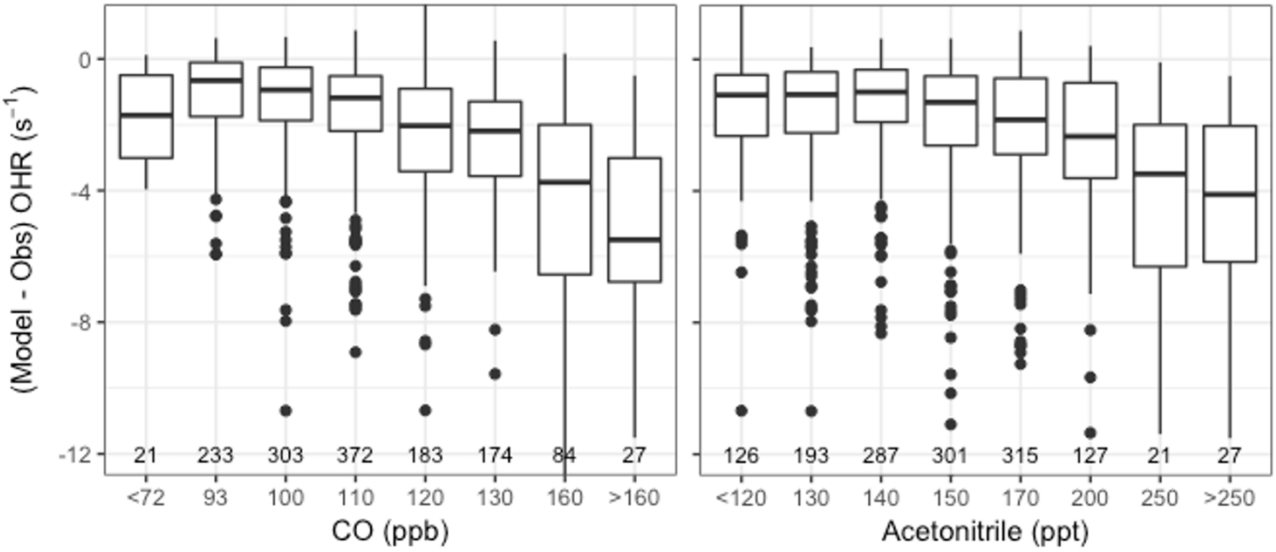

Figure 4.6. Boxplots of the model minus observed OHR or OHR difference during the DC3 campaign against binned CO (left) and acetonitrile (right) observations. The number of observations in each bin is shown on the bottom of the panel.

4.5 Characterizing fire contribution to global NMOG and atmospheric reactivity

The first estimates of global simulated cOHR highlight the strong gradients in reactivity from source regions to background (Safieddine et al., 2017; Lelieveld et al., 2016). To date, there has been no effort to attribute simulated cOHR to sources. Here we use the source-attribution approach described in Sect. 4.2.1 to assess the contribution of fire emissions to global NMOG and cOHR. We note that, given the discussion of Sect. 4.3, this global simulation should be taken as a lower limit for fire NMOG and cOHR, particularly in fire source regions.

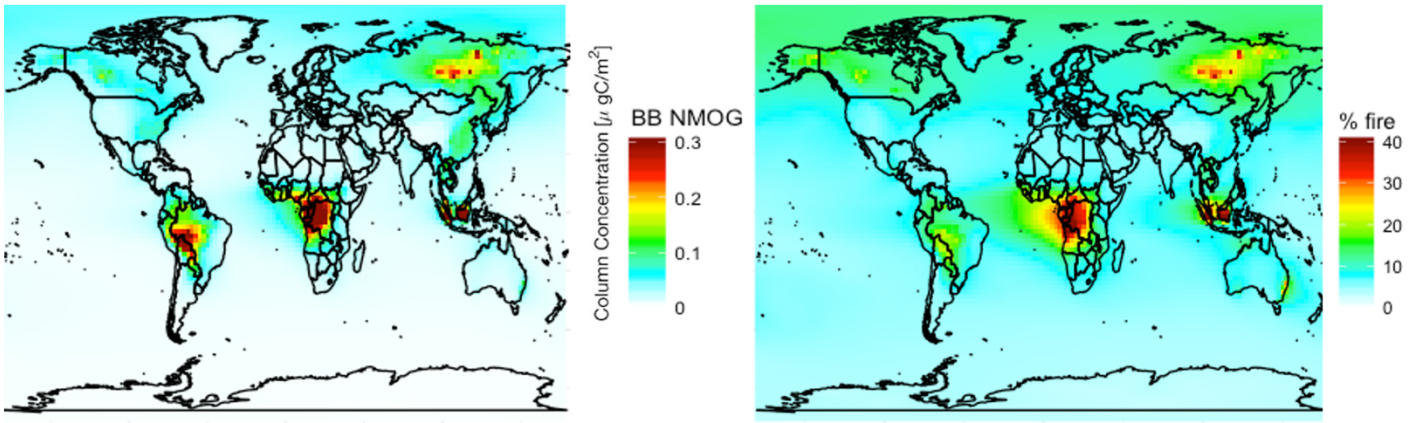

Figure 4.7. 2019 annual mean simulated (Left) NMOG total column concentrations from fires and (Right) percent contribution of NMOG total column concentrations from fires

Figure 4.7 shows simulated annual mean 2019 NMOG total column concentrations and percent contribution from fires. Fires exceed 40% of NMOG annually, not just in the fire seasons, in several fire source regions (e.g., Siberia, central Africa, and Southeast Asia) with elevated levels (~25%) across large parts of the northern hemisphere downwind of sources. Fires also contribute more than 5% of NMOGs nearly everywhere globally, including the remote ocean, driven by RCHO, acetaldehyde, ethene, propene, and DMS.

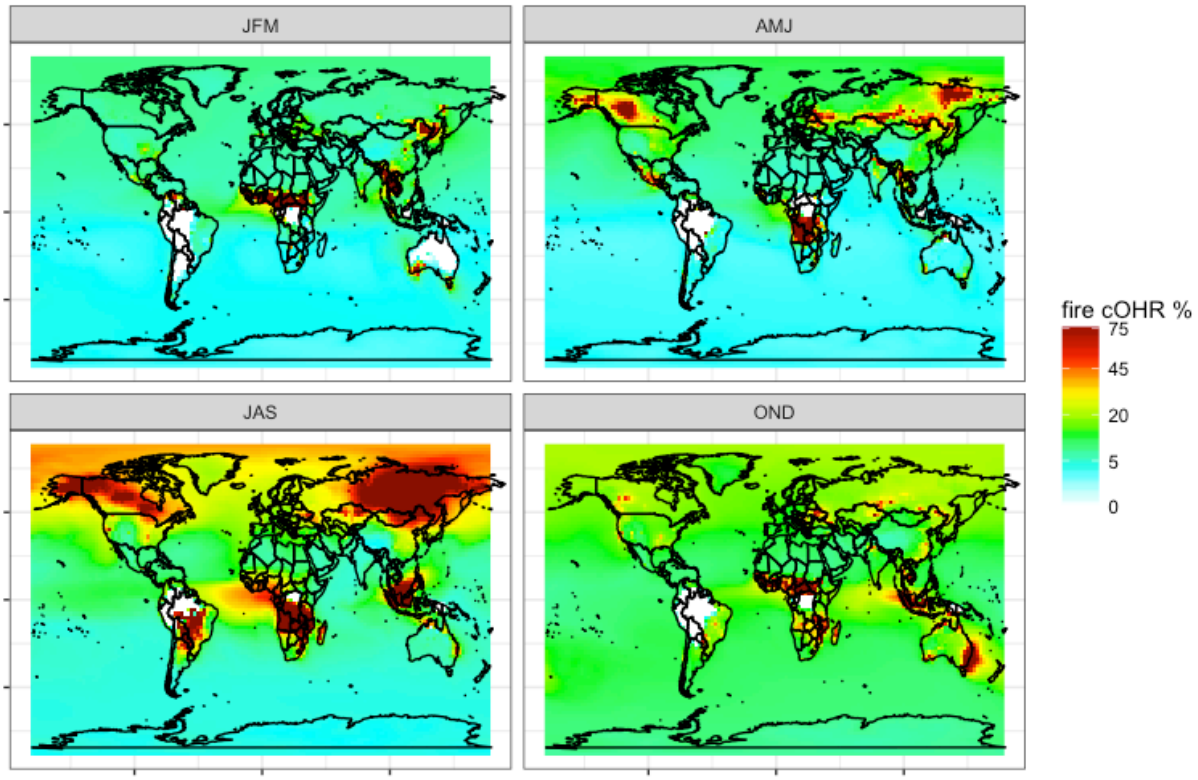

Figure 4.8. Percent surface cOHR seasonally from fires in 2019 from updated GEOS-Chem simulation (see Sect. 4.3) using GFED4s DM with Andreae (2019) emission factors. JFM is January, February, March; AMJ is April, May, June; JAS is July, August, September; and OND is October, November, December.

Figure 4.8 shows that the contribution of fires to seasonal surface cOHR in 2019 is substantial, exceeding 75% in large fire source regions. The large fire contribution in July, August, September (JAS) and, to a lesser extent, in other seasons, contributes to cOHR beyond the immediate fire emission region. We note that these values are year dependent, and, for example, 2019 was a low fire year in the western US where we might expect a larger fire contribution in other years (see Fig. 4.12 for more discussion of interannual variability). Longer-lived fire species (particularly CO) contribute 10-25% of the background cOHR, peaking in October, November, and December (OND). Globally in 2019, the annual average simulated fraction of surface reactivity from fires is 15%. The relative export of OH reactivity from fire source regions is expected to vary with the mix of emissions (i.e., chemical reactivity) and the oxidative environment. This can be explored in fire-dominated regions with strong zonal winds, which produce a clear fire plume. Fig. 4.S8 suggests that the cOHR from fires decays more slowly in

plumes from boreal source regions (Canada and Siberia) compared to the tropics (Central Africa), likely reflecting differences in the oxidative loss.

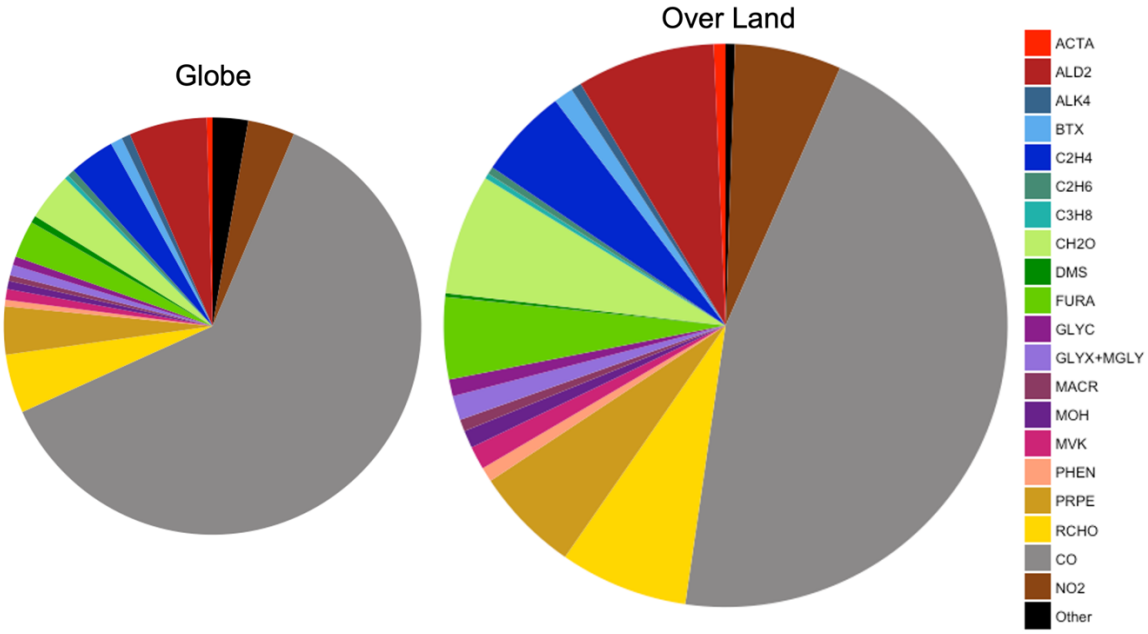

Figure 4.9. Average global annual mean contribution of chemical species and species groups to simulated surface fire cOHR in 2019 using GFED4s DM for the entire globe and over land only. The two pie charts are approximately sized by their relative fire cOHR (0.16 s^{-1} globally and 0.29 s^{-1} over land). BTX is benzene, toluene, and xylenes. Other(n=56) includes species where their annual mean fire cOHR is equal or less than 0.0004, which includes ozone.

Figure 4.9 shows that NMOGs make up 48% of the annual mean surface fire cOHR over land (and 33% over the whole globe), with CO and NO_2 providing the bulk of the remaining cOHR. Of the non-CO annual mean surface fire cOHR, NMOGs make up roughly 90% (colors in Fig. 4.9). Particularly important NMOG contributors to fire reactivity include acetaldehyde (ALD2 in dark red; 15% of non-CO fire cOHR), formaldehyde (CH_2O in light green; 13% of non-CO fire cOHR), and fire emissions of several NMOG species added in this work – lumped furan (FURA in lime green; 9% of non-CO fire cOHR), ethene (C_2H_4 in royal blue; 10% of non-CO fire cOHR), propene and higher carbon alkenes (PRPE in tan; 11% of non-CO fire cOHR), and lumped aldehydes greater than or equal to three carbons (RCHO in yellow; 14% of non-CO fire cOHR).

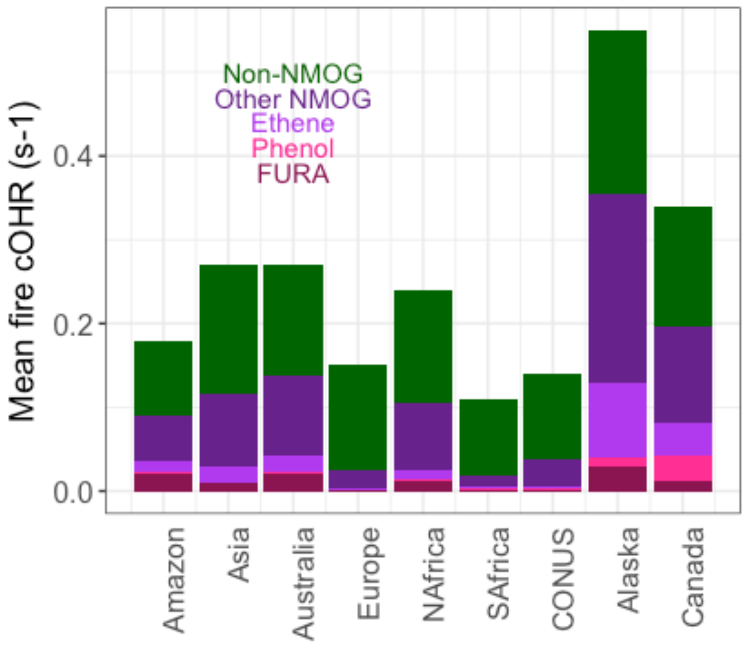

Figure 4.10. Mean simulated surface fire cOHR in 2019 using GFED4s DM regionally for the Amazon, Asia, Australia, Europe, northern hemispheric Africa (NAfrica), southern hemispheric Africa (SAfrica), the contiguous US (CONUS), Alaska, and Canada.

Because fires and fuel types differ regionally, Fig. 4.10 shows the simulated annual mean fire cOHR in several large fire regions. The addition of fire emissions of lumped furans, phenol, and ethene contribute significantly to fire cOHR depending on region, consistent with their EFs. Lumped furans, "FURA" (dark red), contribute the most in the Amazon (11%), Australia (7%), and Alaska (5%) and the least in Europe (1%), southern Africa (2%), and CONUS (2%). The boreal regions (Alaska and Canada) show larger contributions from phenol (bright pink) (2% and 9%, respectively) and ethene (light purple) (16% and 12%, respectively) consistent with high boreal EFs. Other NMOGs (dark purple) also contribute substantial cOHR in most regions except Europe, southern Africa, and CONUS where the contribution from CO is dominant. We note that given our observational analysis for the Amazon (Fig. 5), fire emissions, and thus the fire cOHR, in this region, and possibly other tropical regions, are likely drastically underestimated in our simulation. We do not adjust regional fire emissions here given that large uncertainties remain on fire emissions in the Amazon and tropics more generally; therefore, the

values shown in Fig. 4.10 should certainly be considered a lower estimate (in the Amazon by more than a factor of 3, following Fig. 4.5).

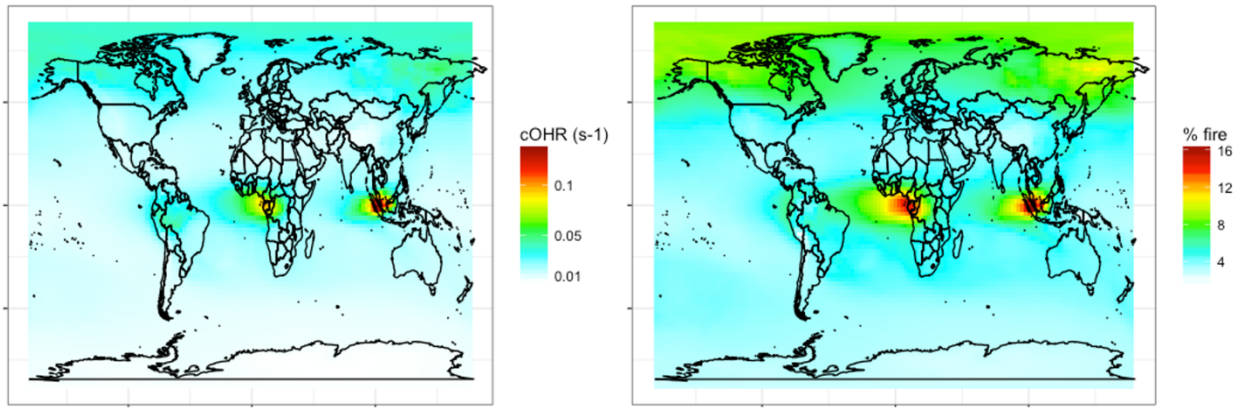

Figure 4.11. Annual mean simulated (left) fire cOHR and (right) percent of cOHR from fires using GFED4s DM in 2019 at 500 hPa.

NMOGs and associated reactivity in the free troposphere are relevant to the global oxidative capacity, long-range transport, and climate. Figure 4.11 shows that the simulated contribution of fires in the mid troposphere (500 hPa) to cOHR is 5% globally but reaches ~15% in the tropics. Fires also contribute more reactivity (~10% annually) in the boreal region. We undertake a similar analysis for 2017 (not shown) where the magnitudes and spatial trends discussed in Figs. 4.7-4.11 are similar.

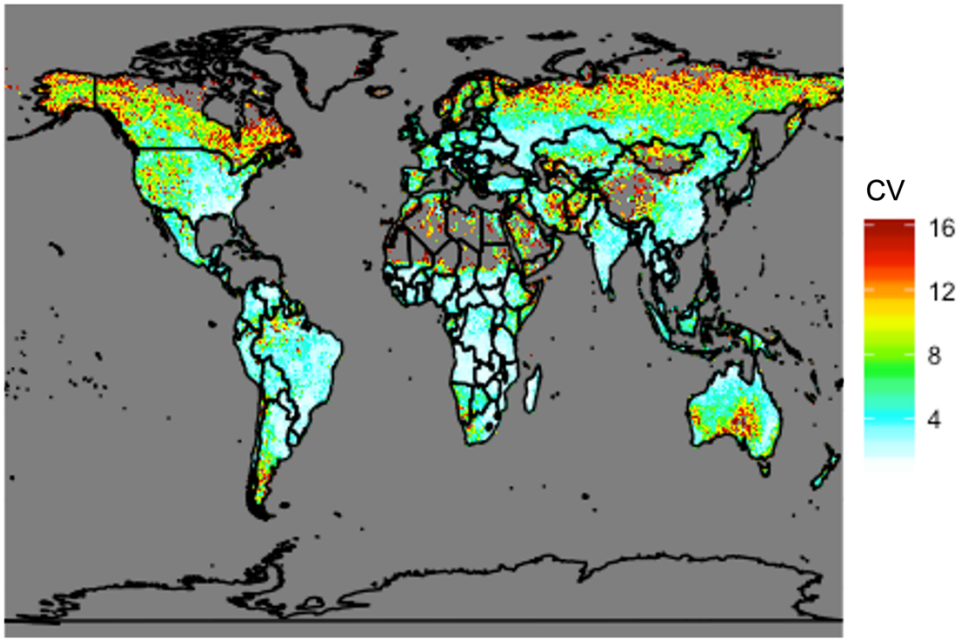

Figure 4.12. Coefficient of variation (CV) of total annual carbon emissions from fires from 1997 to 2019 using GFED4s DM. Coefficient of variation is defined as the standard deviation of a quantity divided by the mean, which is a statistical measure of the relative dispersion of the dataset about the mean.

The analysis presented above is for a single year (2019). Fire location and magnitudes vary substantially year to year. The global total carbon emissions of NMOGs from the GFED4s inventory from 1997 to 2019 range from 27 to 48 Tg C yr^{-1} with 41 Tg C emitted in 2019 and also the mean across years. This suggests that our estimates of fire's contribution in the preceding analysis is representative of average conditions at the global scale but may increase or decrease by roughly a third in different years. Therefore, across years, the annual global average fraction of surface reactivity due to fires likely ranges from ~10 – 20% with large uncertainties due to the magnitudes of other anthropogenic and biogenic emissions in any given fire region. To understand interannual variability at a more local scale, Fig. 4.12 shows the coefficient of variation, a statistical measure of the relative dispersion of the data about the mean, for total carbon emissions from fires across the same years. Given their propensity for large wildfires, the boreal regions, the western US, and Australia show greater year to year variability, which would translate to high variability in fire contributions to surface cOHR. Conversely, Africa shows very little variation consistent with human-ignited savanna and agricultural burning each year,

suggesting that our single year estimates of fire contributions to cOHR are generally robust in this region.

4.6 Conclusions

Recent work has suggested that NMOGs from fires may be a large source but noted that we did not yet have a framework in our models to fully characterize them and their reactivity (Akagi et al., 2011). Our work provides a first estimate of fire NMOGs globally and regionally and their contribution to reactivity. We updated fire NMOG EFs to Andreae (2019) from Akagi et al. (2011). We also expanded the model representation by adding new fire NMOGs (e.g., lumped furans, phenol, ethene), prioritized for their reactivity using data from the FIREX lab studies and their chemistry. We used a suite of recent observations from the lab (FIREX) to towers (ATTO) to aircraft campaigns (FIREX-AQ, ARCTAS, DC3) to constrain and test our model representation. We show that observations support the additions made to the model.

Our model suggests that fires are a major contributor to NMOG concentrations, especially near fire source regions and downwind of them. We show that fires provide more than 75% of cOHR in large parts of the northern hemisphere and that fires contribute to a high background (~25%) reactivity beyond their source regions, mostly driven by CO and other long-lived species. We also show that 90% of non-CO annual surface OHR is from NMOGs and that FURA (furan, 2-methylfuran, and 2,5-dimethylfuran) and ethene are important globally for reactivity with phenol more important at a local level in the boreal regions. To our knowledge, this is the first quantification and characterization of the impact and importance of fire for atmospheric reactivity and the first representation of both lumped furans and phenol from fires in GEOS-Chem. However, our analysis is almost certainly a lower limit on the magnitude of reactivity from fire NMOGs because we do not comprehensively include all species emitted from fires, given that for many of these their global EFs and product formation are not well understood. To further improve the representation of fire NMOGs in models, more measurements of speciated NMOG and total OHR are needed to help constrain both the total emissions and reactivity of NMOGs, particularly during field campaigns with fire influence. Further development of oxidative chemical mechanisms for highly reactive NMOGs are also needed to ensure that models better capture the exported reactivity from fires. Finally, while we substantially increase

the mass and reactivity from fire NMOGs represented in our model, more work is needed to constrain low-volatility NMOGs that are precursors to SOA.

As fires become more intense in the western US and in other temperate and boreal regions due to climate change (e.g., Westerling, 2016; Westerling et al., 2006; Abatzoglou and Williams, 2016; Senande-Rivera et al., 2022) and human forcing leads to different burned area trends globally (Andela et al., 2017), it is becoming ever more important to improve our understanding of fire emissions, their reactivity, and their impact globally. Our work shows that NMOGs from fires contribute substantially to atmospheric reactivity, both locally and globally, highlighting the urgent need to further constrain the sources and transformations of these species.

Chapter 5 Large mitigation potential of smoke $PM_{2.5}$ in the US from human-ignited wildfires and agricultural fires

Adapted from: Carter, T.S., C. L. Heald, and N. Selin, Large mitigation potential of smoke $PM_{2.5}$ in the US from human-ignited wildfires and agricultural fires, in prep for Env. Res. Letters.

5.1. Introduction

Fires threaten human lives, infrastructure, and ecosystems and are also a major cause of air quality degradation. Concentrations of $PM_{2.5}$ from fires alone can exceed both daily and annual air quality standards from the Environmental Protection Agency (EPA) and World Health Organization (WHO) (Carter et al., 2020; Pai et al., 2022; David et al., 2021). These high levels of fire $PM_{2.5}$ can negatively impact health in many ways (respiratory infections, asthma, lung cancer, and heart disease) (Chen et al., 2021; Pope and Dockery, 2006; Brook et al., 2010; Liu et al., 2015; Reid et al., 2016; Williamson et al., 2016). Using observational data from southern California, Aguilera et al., (2021) found that fire $PM_{2.5}$ is more toxic (quantified through respiratory hospitalizations) than $PM_{2.5}$ from other sources. The economic damages of wildfires and their associated health impacts can be enormous; Wang et al. (2021) estimate that the 2018 California wildfires incurred $32.2 billion in smoke-related health costs and $116.3 billion in other losses. This same study showed that the United States beyond California also suffered substantial indirect supply chain damage ($45.9 billion) related to the 2018 California fires, demonstrating that the impacts of wildfires are a statewide, regional, and even national challenge.

Fire frequency, extent, and severity are all growing in the western US due to climate change. Increasing wildfire activity in the west is strongly associated with warming temperatures and earlier spring snowmelt (Westerling et al., 2006; Westerling, 2016; Abatzoglou and Williams, 2016). Over the past three decades, climate change has increased the length of the fire weather season across much of the globe, including in regions of the US, by a couple of weeks (Abatzoglou and Williams, 2016; Jolly et al., 2015). As fire activity intensifies under climate change, smoke is expected to play a larger role in the degradation of air quality and may

overwhelm improvements from decreasing anthropogenic emissions (Fuzzi et al., 2015; Ford et al., 2018; Val Martin et al., 2015; Sarangi et al., 2022) and indeed already has (Kalashnikov et al., 2022; McClure and Jaffe, 2018).

The effects of climate change on fires are indirectly driven by humans, but it can be challenging to directly attribute fires to human versus natural causes and thus characterize the potential for near term smoke mitigation. In particular, an assessment of the contribution of fires to $PM_{2.5}$ concentrations, especially near population centers, can be complicated because humans impact so many different parts of the fire system and separating the natural versus anthropogenic drivers is difficult (Fuzzi et al., 2015; Pai et al., 2022). Humans dominate fire ignitions in several large fire regions in the US (Balch et al., 2017) and Africa (Andela et al., 2017); depending on the region, this includes both wildfires and agricultural and prescribed burns. While understanding how humans have impacted ignitions is complicated (Bowman et al., 2011), in the US, human ignitions are often correlated with railroads (sparks and equipment use) and agricultural activities (Fusco et al., 2016), and these human-ignited wildfires result in more extreme fire behavior and ecosystem impacts (Hantson et al., 2022). Agricultural expansion and intensification has fragmented natural landscapes (Marlon et al., 2008) leading to globally decreasing burned area (Andela et al., 2017). Changing demographic patterns also affect human exposure to smoke. For example, over the last 40 years, ~91% of the world's population has been living at the wildland-urban interface (WUI), and this number is expected to increase toward the end of the century (Knorr et al., 2016). The recent California fires provide a poignant example of the associated impacts of smoke-diminished air quality and of increasing threats to life and property (Wang et al., 2021a). Wu et al., (2022) highlighted that human actions (ignitions and suppression) can be at least as important as climate change in setting future fire regimes. In a study that focused on future smoke exposure, Knorr et al. (2016) found that future increases in human exposure to wildfires were mainly due to projected population increases in areas with frequent fires, and not due to a large increase in burned area. In the US specifically, the WUI accounts for 9% of total land area (Radeloff et al., 2018) with this percentage projected to double by 2030, mostly in the West (Theobald and Romme, 2007).

It is essential to quantify, where possible, the human levers on smoke to better assess the prospects for mitigation. In this study, we focus on two anthropogenic drivers: agricultural fires and human-ignitions of wildfires, both of which have clear associated management potential (Syphard and Keeley, 2015). We use the GEOS-Chem chemical transport model to quantify the effects of these two human drivers on downstream smoke exposure in the contiguous US (CONUS). This work, by design, attributes the impacts of natural vs. human ignition of fires over the last two decades; it does not address the question of how human impacts on land use and suppression has affected fire susceptibility, spread, and duration.

5.2. Data and methods

5.2.1 Agricultural versus non-agricultural dry matter burned

To analyze the contribution of agricultural fires to smoke, we use the underlying dry matter (DM) burned from agricultural versus not agricultural fires in the Global Fire Emissions Database version 4 with small fires (GFED4s) from 1997 to 2018 at 0.25° x 0.25° spatial resolution (Fig. 5.S1). Agricultural fires are prominent in the Central Valley in California and in the southeastern US.

5.2.2 US Forest Service Fire Program Analysis-Fire Occurrence Database (FPA-FOD)

To understand how human ignitions of wildfires have changed over time, we explore the FPA-FOD (Short, 2021), which includes information on 2.17 million geo-referenced wildfire records in the US from 1992 – 2018 in a spatial database. See Balch et al., (2017) for an extensive characterization of this dataset. At a minimum, this database includes discovery, and often containment, dates; final fire size; a point location; and a general cause classification (Human, Natural, or Missing data/not specified/undetermined). We characterize the information in this database and break down the human ignition categories with more granularity in Fig. 5.S2. Arson decreases from 27% to 14% of human ignitions from 2003 to 2018 while the contribution of debris and open burning increases from 34% to 45%. While the size of all fires varies both regionally and annually, naturally ignited fires are generally larger in size (Fig. 5.S3), particularly in Alaska.

Figure 5.S4 shows that, with substantial year-to-year variability, the percentage of human ignited wildfires has increased from 79 to 89% from 1992 to 2018. Concurrently, total fire $PM_{2.5}$ emissions increased in CONUS from 1992 to 2018 (Fig. 5.S4). We attribute daily GFED4s dry matter (DM) in each grid cell to the corresponding fire ignition type in the FPA-FOD to estimate emissions of human ignited wildfire $PM_{2.5}$. This method captures 90% of GFED4s fires in 2018 and 83% in 2003. This is inherently a lower estimate of fire emissions in CONUS because it thus excludes 10% and 17% of GFED4s DM in 20018 and 2003, respectively, mostly associated with small fires, which previous literature has shown GFED underestimates (Giglio et al., 2013; van der Werf et al., 2017; Stockwell et al., 2022). We select these two years to span the potential human-driven smoke source: Figure 5.1 shows that 2018 is both a high fire $PM_{2.5}$ emissions and high human ignitions year while 2003 is low for both. Consistent with Brey et al., (2018), we find that human ignited wildfire $PM_{2.5}$ emissions from the FPA-FOD are of a similar magnitude in the western and southeastern US. Human ignited wildfires show low interannual variability across the Southeast and high variability across the West, consistent with their episodic nature.

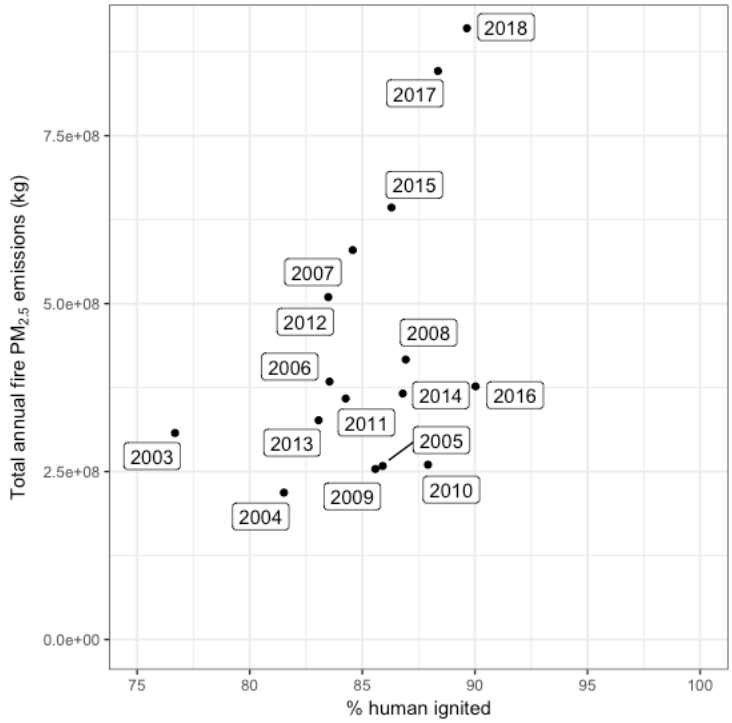

Figure 5.1: Scatter plot of each year's total fire $PM_{2.5}$ emissions against the percentage of fires ignited by humans from 2003 to 2018 in CONUS.

5.2.3 The GEOS-Chem model

We use a chemical transport model, GEOS-Chem version 13.3.3, to simulate $PM_{2.5}$ globally at a horizontal grid resolution of 2x2.5° and to generate boundary conditions for nested simulations over North America at 0.5x0. 625°. The model is driven by MERRA2 meteorology and fire emissions from GFED4s (see SI for more details). We compare the nested model simulation of $PM_{2.5}$ with IMPROVE observations, and we find that, in both years, the model matches observations well, particularly the medians, with a small high bias (normalized mean bias equals 19% in 2003 and 14% in 2018) (Fig. 5.S6).

$$PM_{2.5} = (NH_4 + NO_3 + SO_4) * 1.10 + BCPI + BCPO + \big(OCPO + (OCPI * 1.05)\big) * 2.1 + DST1 + DST2 * 0.30 + SALA * 1.86 + SOA * 1.05,$$

Where BCPI is hydrophilic black carbon (BC), BCPO is hydrophobic BC, OCPO is hydrophobic organic aerosol (OA), OCPI is hydrophilic OA, DST1 is dust aerosol with r_{eff} = 0.7 microns, DST2 is dust with r_{eff} = 1.4 microns, and SALA is fine sea salt.

We run different emissions scenarios to isolate fire, agricultural fire, and human-ignited wildfire $PM_{2.5}$ concentrations in the model.

To calculate population-weighted $PM_{2.5}$ concentrations, we use year-specific population estimates from the Gridded Population of the World (Gridded Population of the World (GPW), v4 | SEDAC, 2022). Details on the health impact calculation follow the methodology of Freese et al., (2022); Vohra et al., (2021); Vodonos et al., (2018) and are provided in the SI in addition to the 95% confidence intervals (CI).

5.3. Results and discussion

Figure 5.2 shows that agricultural fires contribute substantially to simulated fire $PM_{2.5}$ in some US regions, including the Central Valley and along the Mississippi River, with maximum annual mean concentrations reaching ~2 μg m^{-3}, accounting for more than a third of the $PM_{2.5}$ from fires in both years (Table 5.S1 and Fig. 5.S7). However, their contribution to total annual mean $PM_{2.5}$ across CONUS is much smaller (<1%) (Table 5.S1). 2003 and 2018 show similar spatial

patterns, but agricultural fire $PM_{2.5}$ concentrations are higher in the southeast in 2003 and in the west in 2018.

$PM_{2.5}$ concentrations from human-ignited wildfires in CONUS dominate fire $PM_{2.5}$, accounting for more than 67% of annual mean fire $PM_{2.5}$ in both years. These concentrations range from 0.3 μg m^{-3} to 20 μg m^{-3} across CONUS in 2003 and 0.6 μg m^{-3} to 99 μg m^{-3} in 2018 (Fig. 5.2 and Table 5.S1). We find that human-ignited wildfires are responsible for most fire $PM_{2.5}$ across all of CONUS except for the upper-Midwest where agricultural fires are more significant (Fig. 5.S7). The highest human-ignited wildfire $PM_{2.5}$ concentrations in 2003 are centered in Oregon, while in 2018, very high concentrations are simulated across northern California (Fig. 5.2). However, the footprint of human-ignited wildfire smoke is distributed beyond these source regions, responsible for ~15% of annual mean $PM_{2.5}$ across much of the intermountain west and 10% across the rest of CONUS. In 2003 and 2018, human-driven smoke (agricultural fires and human-ignited wildfires combined) is responsible for 3 and 9%, respectively, of average annual total $PM_{2.5}$ across CONUS (Table 5.S1).

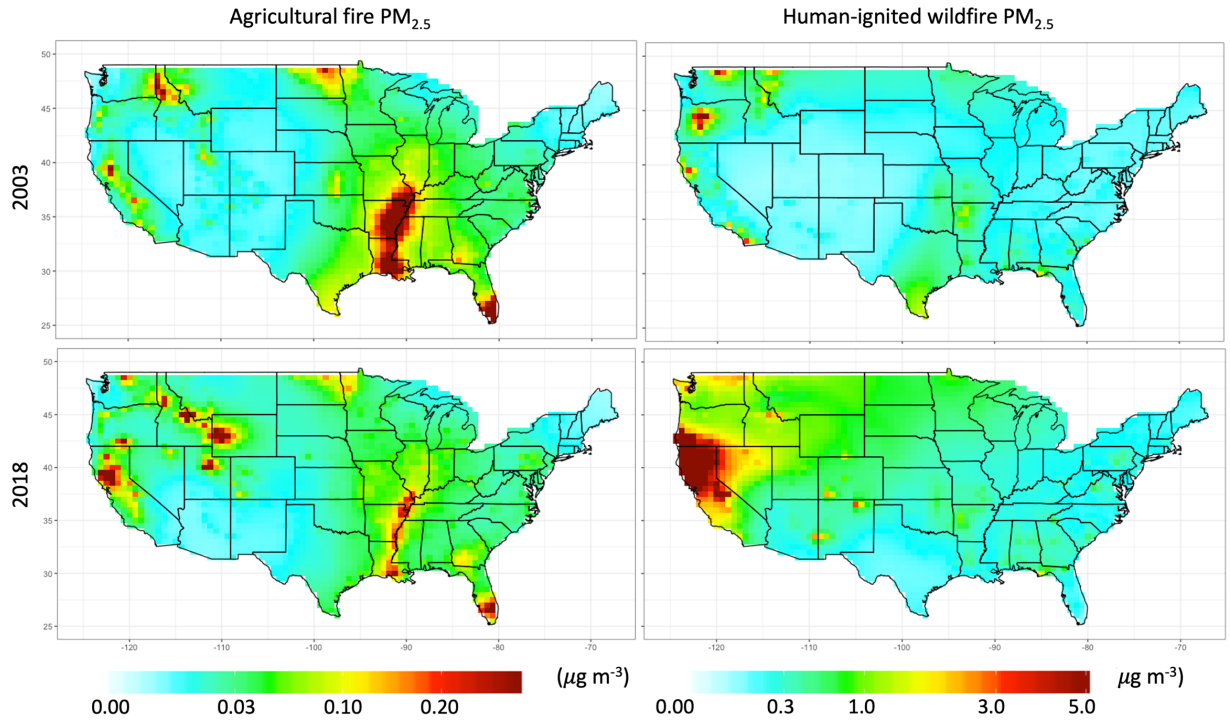

Figure 5.2: Annual mean concentration of agricultural fire (left) and human-ignited wildfire (right) $PM_{2.5}$ in 2003 (top) and 2018 (bottom). Note the different scales.

To better understand the impact of human-driven fires on regional daily $PM_{2.5}$ concentrations, we focus on the southeastern US where agricultural fires are important and northern California where human ignited wildfires were dominant in 2018 (humans ignited 90% of fires that year per the FPA-FOD). Figure 5.3 shows that simulated $PM_{2.5}$ total concentrations (black) are much lower in the southeastern US (max ~ 62 μg m^{-3}) than in northern CA where daily $PM_{2.5}$ concentrations reach nearly 5000 μg m^{-3}, far higher than the EPA daily air quality standard of 35 μg m^{-3} (indicated in the grey box). Although the southeastern US is the region where agricultural fires are most prevalent, agricultural fire $PM_{2.5}$ (tan) is low (max = 20 μg m^{-3}); however, when added on top of other sources, it does contribute to unhealthy air quality (responsible for ~0.03% of grid box days with exceedances in the region in 2018). In the southeast, fires (red) are not always the dominant driver of high $PM_{2.5}$ while in northern CA fires, human-ignited wildfires (dark blue), account for all the simulated exceedances of the EPA daily air quality standard. These northern CA exceedances are driven by large human-ignited wildfires in July to September (e.g., the Mendocino Complex Fire) and in November (e.g., by Camp Fire). In 2018, human-ignited wildfire $PM_{2.5}$ by itself leads to exceedances in more than 4% of all grid box days in northern CA with an additional 7% of grid box days exceeding the daily standard when human-ignited wildfire $PM_{2.5}$ is combined with other sources (Fig. 5.S8). Consistent with our earlier analyses, other regions, except the southern Great Plains and southeast, experience some daily exceedances due to human-ignited wildfires in 2018 while in 2003 there are far fewer of these exceedances. We note that these exceedances generally do not count toward non-attainment designations since they are considered exceptional events.

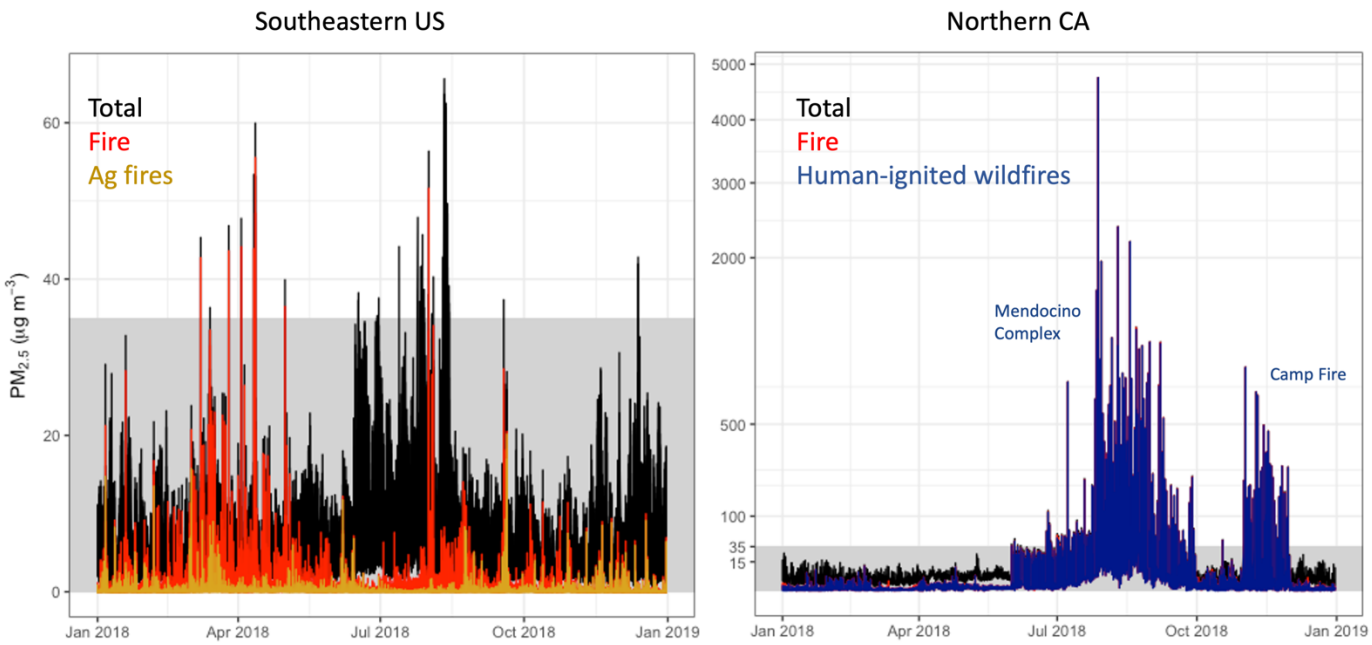

Figure 5.3: Daily $PM_{2.5}$ in the southeastern US (left) and Northern California) in 2018. Total $PM_{2.5}$ is in black, fire $PM_{2.5}$ in red, agricultural fire $PM_{2.5}$ in tan, and human-ignited wildfire $PM_{2.5}$ in dark blue. A grey shaded bar up to 35 µg m^{-3} indicates the daily $PM_{2.5}$ standard set by the EPA.

Figure 5.4: Annual average population-weighted exposure in eight regions with the background of each subset corresponding to the color of its region on its label for 2003 (a low fire emissions and human ignition year [low]) and for 2018 (a high fire emissions and human ignition year [high]). Total $PM_{2.5}$ is shown in black, lighting-ignited wildfire $PM_{2.5}$ in orange, agricultural fire $PM_{2.5}$ in light red, and human-ignited wildfire $PM_{2.5}$ in dark red. A horizontal bar at 12 µg m^{-3} indicates the EPA annual standard. The regional selections follow those designated in the Fourth National Climate Assessment.

We assess the annual average population-weighted exposure associated with non-fire (black), lightning ignited wildfire (orange), and human-driven (agricultural (magenta) and human-ignited wildfire (dark red)) $PM_{2.5}$ in both 2003 and 2018 regionally in CONUS (Fig. 5.4). Total $PM_{2.5}$ decreases across all regions from 2003 to 2018 with the largest decreases in the Northeast, Southeast, and Midwest, generally reflecting decreasing anthropogenic emissions (Fuzzi et al.,

2015). Therefore, fires (variability here represented by 2003 versus 2018) increasingly contribute a larger fraction of $PM_{2.5}$ (Fuzzi et al., 2015)(and in California can even fully compensate for anthropogenic decreases per Val Martin et al., (2015)). Smoke exposure from agricultural fires is a negligible component of the annual means throughout the United States. Lightning-ignited wildfires make an important contribution in the Northwest (where the annual mean exposure associated with them is ~ ¼ and ½ that of human-ignited $PM_{2.5}$ in 2003 and 2018, respectively) and Northern Great Plains (where their contribution is roughly comparable to that from human-ignited wildfires in both years; see Table 5.S2). However, exposure in California in 2018 is dominated by $PM_{2.5}$ from human-ignited wildfires (41% of all $PM_{2.5}$). Regions generally see larger contributions from human levers in 2018 than 2003, driven by human ignitions, with, for example, the percentage of total $PM_{2.5}$ exposure from human levers higher in 2018 (41%) relative to 2003 (7%) in California, 13 and 2%, respectively, in the Southwest, and 29 and 10% in the Northwest (Table 5.S2). More details on each of the underlying components of population-weighted exposure are given in Table 5.S2.

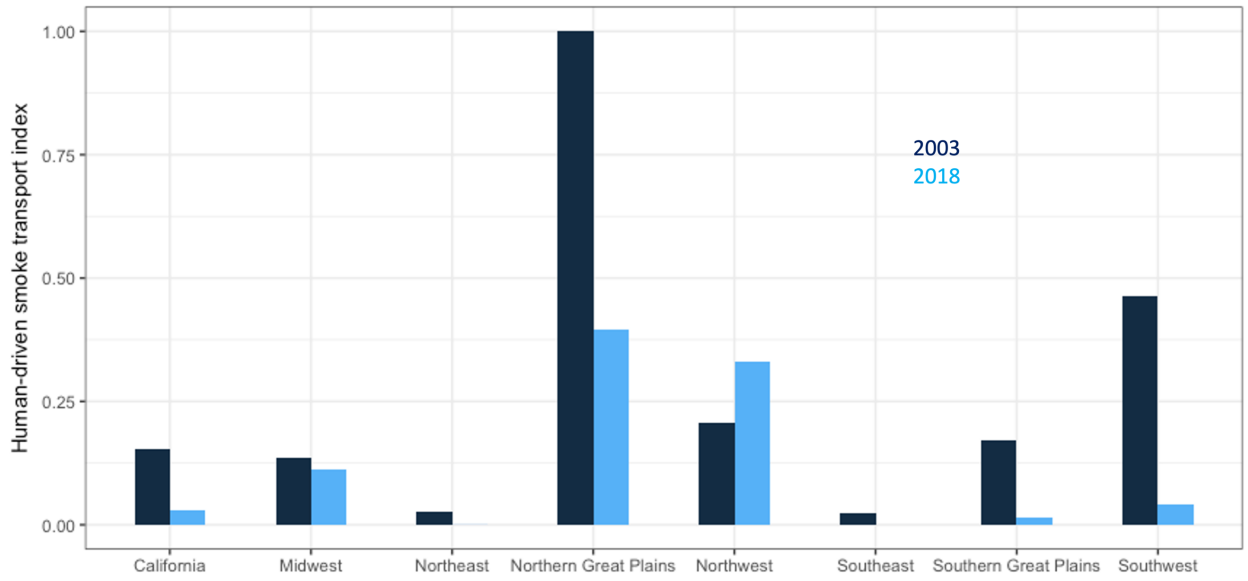

Figure 5.5: Normalized values of the human-driven smoke transport index defined as the average concentrations of $PM_{2.5}$ from agricultural fires and human-ignited wildfires divided by their corresponding emissions in each region in 2003 (dark blue) and 2018 (light blue).

To better understand the contribution of transported smoke to local exposure, we develop a human-driven smoke transport index, defined as the average of the concentration of $PM_{2.5}$ from agricultural fires and human-ignited wildfires fires divided by their corresponding emissions by region (Fig. 5.5). A high index indicates more imported fire impacts, suggesting that a reduction of fire $PM_{2.5}$ would require fire mitigation in up-wind regions, while a lower number generally means more local smoke and the potential for local mitigation. The highest smoke transport values are associated with the states downstream of the west coast, especially the Intermountain West (Northern Great Plains, Southern Great Plains, and Southwest), with some interannual variability (Fig. 5.5), suggesting that most smoke impacts in these regions are imported. The Northwest shows somewhat lower index values because smoke from fires in California can be transported here, particularly apparent in 2018, but local smoke is also important. California shows middle of the road values because of its high concentrations and emissions and thus is dominated by local smoke. The need for mitigation of local human-driven fires is particularly high in these regions. The Northeast and the Southeast show the lowest indices because they are less impacted by human-driven smoke and, in the case of the Southeast, higher agricultural smoke concentrations are balanced by their local emission source.

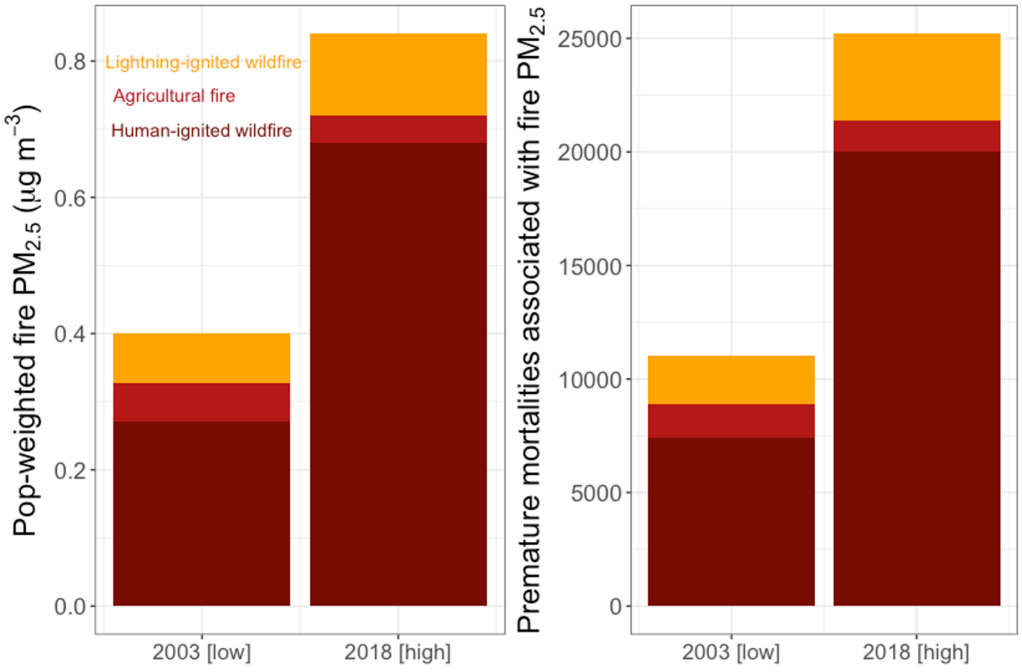

Figure 5.6: Annual average population-weighted exposure in CONUS from fire-associated $PM_{2.5}$ in 2003 and 2018 (left) and premature mortalities associated with those $PM_{2.5}$ concentrations (right). Human-ignited wildfire $PM_{2.5}$ is in dark red, agricultural $PM_{2.5}$ is in light red, and lightning-ignited wildfire $PM_{2.5}$ is in orange.

Across CONUS, human levers on fire account for 82% and 86% in 2003 and 2018, respectively, of the simulated population-weighted exposure to fire $PM_{2.5}$ (Fig. 5.6) (or 83 and 79% of not population-weighted fire $PM_{2.5}$ exposure). This is dominated by human-ignited wildfires (responsible for 68% and 81% of fire-associated exposure). Human-driven smoke contributes 14% of annual mean total $PM_{2.5}$ exposure across CONUS in 2018 and 6% in 2003. Population-weighted $PM_{2.5}$ exposure associated with agricultural fires (0.057 $\mu g\ m^{-3}$) in 2003 is comparable to that associated with lightning-ignited fires (0.073 $\mu g\ m^{-3}$) and a factor of three lower in 2018 (Table 5.S2).

Over 80% (81% in 2003 and 85% in 2018) of fire $PM_{2.5}$ -associated premature deaths come from human levers (agricultural fires + human-ignited wildfires) in both years (Fig. 5.6 and Table 5.S3). This number is insensitive to population estimates (i.e., using the 2018 $PM_{2.5}$ concentrations with 2003 population values and distribution gives the same percentage of fire $PM_{2.5}$ exposure from human levers). Agricultural fires have little interannual variability, so they lead to similar premature deaths in both years (1500 in 2003 and 1400 in 2018). We estimate that human-ignited wildfire smoke was responsible for 20,000 premature deaths in 2018 and 7,400 premature deaths in 2003, a smaller fire year (Table 5.S3). Other work has attributed similar numbers of premature deaths to fire $PM_{2.5}$ (Ford et al., 2018); we show here that the anthropogenic drivers dominate these premature mortalities.

5.4. Conclusions

While the dialogue around intensifying fires and their impacts has centered on anthropogenic climate change driving increases in frequency and severity (Westerling et al., 2006; Westerling, 2016; Abatzoglou and Williams, 2016), our work shows that direct human levers (agricultural fires and human ignitions of wildfires) are controlling the majority of fires in CONUS. Over 80% of the population-weighted annual exposure and premature deaths associated with fire $PM_{2.5}$ are from

these two human levers – both of which have substantial mitigation potential. Our results are likely a lower limit on fire impacts because of a known underestimate of fires with GFED4s and because our attribution of ignition type with the FPA-FOD misses ~15% of DM in GFED4s. Other fire-related emissions (e.g., CO_2 VOCs, and NO_x) and resulting secondary pollutants (e.g., O_3) could also be reduced with mitigation of these human levers.

Mitigation of $PM_{2.5}$ exposure from agricultural fire has been extensively studied, see e.g., Zhou et al., 2018; Holder et al., 2017. Therefore, we focus here on the benefits and possible first steps for mitigating human-ignited wildfires. Using a hybrid optimization/simulation model, Lee and Lee, (2018) examine the tradeoffs between firefighting resources (and fire suppression) versus fire ignition prevention efforts in the Republic of Korea, where most fires are anthropogenic, a regime like large parts of CONUS, particularly California. They find that the marginal benefit of ignition prevention was larger than that of firefighting helicopters, suggesting that ignition prevention may be more cost effective or at a minimum should be used in concert with fire suppression efforts.

Efforts to limit human ignitions are challenging but could be focused on certain ignition types and geographic areas to maximize effect. For example, Wang et al., (2021) discuss how health costs and indirect losses associated with future fires could be diminished by focusing fire prevention on areas upwind of large population centers or near important industry or transit infrastructure. Knorr et al., (2016) suggest that future human exposure to wildfires will increase primarily because of population growth close to areas with frequent wildfires (not because of an increase in burned area), implying that suppressing human ignitions close to high density population centers will only grow in importance. Other work (e.g., Abatzoglou et al., 2020; Collins et al., 2016) highlights that, while power line ignitions are a small number of ignitions in the US (Fig. S2) and in Australia, respectively, they pose greater risk to homes, and initiatives in California are already underway to underground particularly susceptible lines. At the local level, more detailed source attribution of fire $PM_{2.5}$ due to ignition type (as available in the FPA-FOD) would also be useful to target mitigation strategies.

The substantial contributions of humans to smoke $PM_{2.5}$ in CONUS may become even more important in the future. This is because, while climate change has lengthened the duration of the fire weather season in parts of CONUS by ~two weeks over the past thirty years (Abatzoglou and Williams, 2016; Jolly et al., 2015), human ignitions extended the fire season in CONUS by more than three months (Balch et al., 2017). In California, where humans now dominate ignitions, these human ignitions combine with extreme fire weather to catastrophic effect, and, as fire weather days become more frequent, mitigating these coincident human ignitions will be key for smoke mitigation (Hantson et al., 2022). We do not investigate the role of international smoke, but the importance of long-range transport may grow in the future as fires intensify in other regions like Siberia.

Fires and society are a complicated interwoven system, and it is impossible to know the counterfactual of human ignitions (i.e., we don't know if human ignitions were reduced if lightning induced fires would increase). Future work on how the expansion of prescribed burning to limit wildfires, especially in the West, changes $PM_{2.5}$ exposure and air quality more broadly in CONUS would help to inform other mitigation avenues. A study focused on fire-prone European regions investigated thinning and prescribed burning to manage fire risk and found that both reduced fire intensity and its risks to human health and well-being but that the increased fire emissions associated with prescribed burning could contribute to respiratory problems (Rabin et al., 2022). While fire and human interactions are complex, our work suggest that there is considerable potential for mitigating the public health burden associated with smoke exposure.

Chapter 6. Conclusions and Implications

This thesis introduces and describes a four-part research effort designed to fill knowledge gaps and reduce uncertainty in the current understanding of how smoke from fires impacts air quality and climate. As stated in the Introduction, Chapter 1, we have shown that how we represent smoke in models can have substantial implications for downstream effects on the atmosphere, the Earth System, and humans.

In Chapter 2, we find that four commonly used smoke emissions inventories differ by a factor of 2-7 in their estimates of BC and OA from fires globally and in North America, in particular. We explore which inventory drives GEOS-Chem closest to surface, aircraft, and satellite observations and show that GFED4s and GFAS1.2 provide the best model-observation agreement. Finally, we calculate a sizeable range in the health effects (population-weighted annual mean exposure and daily concentrations) and in the global DRE of smoke when driven by different inventories. Our results provide strong evidence for the need to think more critically about how assumptions around smoke alter the output from our air quality and climate models and subsequent decision making.

Chapters 3, 4, and 5 all build upon this initial work, which characterized GFED4s as the generally best performing inventory against observations in North America. Subsequent work in another region, Australia, also found that GFED4s pushes the model closest to observations (Desservettaz et al., 2022). GFED4s is based on a well-known biogeochemical model (CASA) and is updated frequently (van der Werf et al., 2017; Giglio et al., 2018, 2013). While in this dissertation we generally use GFED4s as our base inventory, we follow our own recommendations laid out in Chapter 2 and explore how other inventories could alter the results in specific cases. For example, in Chapter 3, we discuss how GFAS emissions in Africa are within 25% of GFED4s, allowing us to compare our results to other studies in the region that used GFAS. In Chapter 4, we undertake a sensitivity analysis and find that FINN performs better than GFED4s at simulating fires in the Amazon consistent with other work in the literature.

In Chapter 3, we use three recent aircraft campaigns that flew in the western US (WE-CAN) and off Africa (ORACLES and CLARIFY) to better understand how different fuels and fire conditions affect carbonaceous aerosol and its absorption properties. We find that BC and/or BrC absorption is substantially higher down wind of Africa relative to that in smoke in the western US. We also show that parameterizations that vary BrC absorptivity with the BC:OA ratio generally improve model-observation agreement but do not sufficiently differentiate absorption characteristics at short wavelengths. These dynamic properties have implications for remote sensing algorithms where retrievals assume constant properties, which could introduce artifacts. Finally, we show that photochemical whitening of BrC decreases the burden and DRE substantially globally. On a regional level, our comparison with WE-CAN observations suggests that whitening is required in the western US, but the importance for African fires cannot be confirmed.

Qualitative comparisons with the OMI UV aerosol index show that our standard BrC whitening scheme may be too fast over Africa and that a universal 1-day whitening time scale is more appropriate. Using our best estimate of a universal 1-day timescale for whitening (not dependent on OH), we find a global DRE of BBA of −0.02 W m^{-2}, neglecting whitening results in a considerably more warming DRE for fires (+0.19 W m^{-2}). The 5th IPCC report concludes that the DRE from fires is essentially zero. However, most of the underlying models used do not have an explicit representation of BrC, which we have shown can be important in some regions. Even when including 1-day whitening, the DRE for BrC is +0.08 W m^{-2}, which could be enough to shift some of these model estimates of fire net DRE to warming. More observations are needed to constrain this question.

In a subsequent study (Schnitzler et al. in review), we collaborated with experimentalists who had found that BrC whitening is inhibited by viscosity and correspondingly occurs in warm and humid conditions below ~1km only in the atmosphere. I implemented this constraint in GEOS-Chem, and we showed that this produces a BrC DRE in between the “no whitening” and the baseline whitening case from Carter et al., (2021) (Fig. 6.1). This project serves as a concrete example of the benefits of working at the intersection of modeling and experimental work, using

each to inform the other. The observations make our model more realistic, and the model is essential for showing the regional and global importance of this physical process.

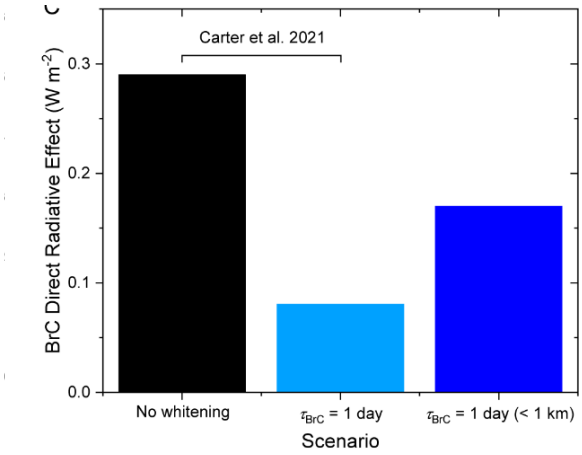

Figure 6.1: Adapted from Schnitzler et al. in review, the global mean all-sky top-of-atmosphere BrC direct radiative effect (DRE) in 2018 for each scheme, the no-whitening scheme (black), the 1-day whitening scheme (light blue), and the 1-day whitening below 1 km only scheme (dark blue).

Chapter 4, to our knowledge, is the first characterization of fire NMOGs and their reactivity in a global chemical transport model. We show that the available observations generally support our updates to fire NMOGs (new EFs and additional species) in the model. While almost certainly a lower limit, we find that fires provide more than 75% of surface cOHR in large parts of the northern hemisphere. Fires also provide ~25% of the reactivity in regions beyond their source regions, mostly driven by CO and other long-lived species. In this work, we did not explore the impact of fire NMOGs on O_3 and SOA, and that would be a natural follow-on study. In Chapter 2, we showed that we cannot determine the importance of SOA from fires using a "top down" approach because of uncertainty in POA emissions. Chapter 4 suggests that it is also challenging to represent fire SOA from a bottom up perspective because the emissions and chemistry of precursors are not well understood. More work should also further explore which species are necessary to represent in order to capture the atmospheric reactivity stemming from fires. For example, would additional lumping of similar NMOGs or even a lumped total NMOG tracer and associated reactivity provide enough information for several use cases?

In Chapter 5, we investigate how important human-driven smoke (agricultural fires and human-ignited wildfires) is in CONUS for air quality and health impacts and assess its near-term mitigation potential. This was, in part, motivated by work that showed several parts of the world would struggle to meet revised WHO air quality guidelines (5 μg m^{-3}) due to fire $PM_{2.5}$ (Pai, Carter et al., 2022). We find that human-driven smoke dominates fire $PM_{2.5}$ across years and makes meaningful contributions to total $PM_{2.5}$. We also calculate that across CONUS more than 80% of fire $PM_{2.5}$ population weighted exposure and premature mortalities are associated with human drivers. This indicates that management choices could have a large effect on smoke impacts. Future work should explore other human drivers of smoke (e.g., changing demographic patterns) and other regions as possible to compare (this ignitions dataset was only available for the US).

In Chapter 3, Chapter 5, and Pai, Carter et al. (2022), we discuss how differentiating anthropogenic and natural fires is incredibly challenging for several reasons. For example, humans have directly or indirectly touched nearly every part of the fire system, and counterfactuals are not testable (e.g., if a human ignition did not happen, would a lightning ignition?). This designation is also important for whether or not fires (or which fires) are included (in) DRF calculations because, per its definition, the DRF is the anthropogenic influence on DRE from pre-industrial to present day. Chapter 5 is the first time, to our knowledge, that a database like the FPA-FOD has been applied to fire emissions and used to estimate specific human drivers on smoke in the US. Chapter 3 also provides insights that can be used to mitigate the warming potential of fires. Because we have found that smoke coming from African fires is more warming than that in the western US, efforts to combat climate change could be focused on those fires with the largest warming impacts.

Uncertainties abound in the interconnected system of fires, the atmosphere, and humans; my work has made substantial contributions to characterize and minimize many of them. Using observations to constrain our models, we have shown that GFED4s and GFAS drive GEOS-Chem closest to observations, that a parameterization that differentiates BrC absorption from different fire types better matches lab and field observations than a fixed contribution , that a

whitening timescale of 1 day not tied to oxidant levels matches satellite observations and the literature, and that using lab studies to improve our models helps us to better match field observations. We have also pointed out areas where more observations will continue to enable modeling insights and vice versa. In Chapter 4 and 5, we introduced the CV metric as a useful way to investigate interannual variability of fires, which is a larger concern in areas dominated by wildfires, like the boreal regions, the western US, and Australia. We used this metric to discuss how our findings for the importance of fires for atmospheric reactivity are robust across years in large fire regions with low interannual variability like Africa and the Amazon. Since the CV we discuss in Chapter 4 is total carbon emissions from 1997 to 2019, which includes the years of our other studies, similar conclusions could be drawn for our other work, including that our findings for African smoke absorption should be consistent across years.

Representing fires and their smoke in air quality and climate models and other decision-making tools will only grow in importance as climate change and other human drivers interact with the natural system. Fire research communities are often somewhat siloed, so thinking critically about what we can learn from the past, present, and the future around both fire modeling and its air quality and climate impacts is essential. A comprehensive investigation of which fire processes we need to include in models (depending on which impacts one is interested in) would move both atmospheric chemistry and informed decision making forward. To do this, the modeling and observational (lab, field, and satellite) communities should plan studies and campaigns together to target large uncertainties like injection height, aerosol optical properties, and emissions.

Several topics that have come up during this dissertation that need additional research include estimates of DM burned, a more detailed understanding of the WUI, the timescale of BrC whitening, model resolution impacts on fire-related parameterizations and representation, and injection heights. In Chapter 2, we discuss how most fire $PM_{2.5}$ emissions uncertainty comes from the DM estimates and not EFs. Better estimates of DM burned are still needed because spatially the main fire emissions inventories disagree. An improved small fires representation would also improve our emissions estimates; the next version of GFED (GFED5) is expected to double emissions mostly because of improved small fires (personal comm.). Improvements in remote sensing will help to address this topic in addition to more work quantifying other

variables that allow us to estimate emissions, such as combustion completeness, fuel load, and land cover type, particularly in less studied regions. As the WUI grows, we need inventories that can capture the burned materials emitted into the atmosphere from this type of fire. This necessitates updated fire emissions inventories that estimate the DM burned of human structures and the EFs of human-made materials. Since all our smoke inventories are not perfect, the different inventory developers and other experts beyond atmospheric chemistry should come together to ponder lessons learned. As of June 2022, IGAC was considering standing up a new working group to do just that and to host a workshop at EGU 2023.

Chapter 3 provided insights on differing absorption of BrC from different fires and fuels and suggested that the timescale of its whitening in smoke is likely around a day. More work is needed to pin down if OH concentrations or photolysis are controlling parameters. Because fires are nearly always a sub grid process at the horizontal resolutions that we run GEOS-Chem, limitations and questions exist around model resolution affecting our representation of fires and many fire-related parameterizations.

In Chapters 2 and 3, we undertook sensitivity tests with the baseline injection height parametrization in GEOS-Chem (Fischer et al., 2014); a substantial difference was not seen in either case. Multi-angle Imaging SpectroRadiometer (MISR) provides globally distributed wildfire smoke plume injection heights with some limitations. Zhu et al., (2018) integrated monthly MISR observations into a new injection height scheme for GEOS-Chem and tested it against ARCTAS observations. More evaluations of this and other new injection schemes are essential because smoke injection can impact long range transport.

More observations in large fire regions, especially understudied ones like Africa, Siberia, Australia, etc. and in clearly defined fire outflow regions over long timescales would help us constrain many of these areas of future research. The ability to focus on clearly visible fire plumes, such as the outflow from Africa explored in Chapter 3, enables us to think about changes in chemistry and transport over time, and so more measurements in these regions are useful. The imminent deployment of several geostationary satellites, including TEMPO in the US, should

provide a spatial and temporal resolution also helpful to answering questions around fires and urban air quality.

The societal implications of our work are only growing as is the importance of work at the intersection of air quality and climate (and the health impacts of both). Human impacts on these natural systems and vice versa are complicated but essential to try to understand. We will need to bring together scientists and practitioners working on fire (atmospheric scientists, health experts, wildland managers, firefighters, etc.) to comprehensively address large scale questions around smoke, air quality, and climate. For example, more work is needed thinking about tradeoffs between prescribed burns and wildfires and their smoke from both an atmospheric science perspective but also urban planning, environmental justice, and ecosystem services.

References

Abatzoglou, J. T. and Williams, A. P.: Impact of anthropogenic climate change on wildfire across western US forests, Proc Natl Acad Sci USA, 113, 11770–11775, https://doi.org/10.1073/pnas.1607171113, 2016.

Abatzoglou, J. T., Smith, C. M., Swain, D. L., Ptak, T., and Kolden, C. A.: Population exposure to pre-emptive de-energization aimed at averting wildfires in Northern California, Environ. Res. Lett., 15, 094046, https://doi.org/10.1088/1748-9326/aba135, 2020.

Aguilera, R., Corringham, T., Gershunov, A., and Benmarhnia, T.: Wildfire smoke impacts respiratory health more than fine particles from other sources: observational evidence from Southern California, Nat Commun, 12, 1493, https://doi.org/10.1038/s41467-021-21708-0, 2021.

Ahern, A. T., Robinson, E. S., Tkacik, D. S., Saleh, R., Hatch, L. E., Barsanti, K. C., Stockwell, C. E., Yokelson, R. J., Presto, A. A., Robinson, A. L., Sullivan, R. C., and Donahue, N. M.: Production of Secondary Organic Aerosol During Aging of Biomass Burning Smoke From Fresh Fuels and Its Relationship to VOC Precursors, Journal of Geophysical Research: Atmospheres, 124, 3583–3606, https://doi.org/10.1029/2018JD029068, 2019.

Akagi, S., Yokelson, R., Wiedinmyer, C., Alvarado, M., Reid, J., Karl, T., Crounse, J., and Wennberg, P.: Emission Factors for Open and Domestic Biomass Burning for Use in Atmospheric Models, Atmospheric Chemistry and Physics, 4039–4072, 2011.

Akagi, S. K., Craven, J. S., Taylor, J. W., McMeeking, G. R., Yokelson, R. J., Burling, I. R., Urbanski, S. P., Wold, C. E., Seinfeld, J. H., Coe, H., Alvarado, M. J., and Weise, D. R.: Evolution of trace gases and particles emitted by a chaparral fire in California, Atmos. Chem. Phys., 12, 1397–1421, https://doi.org/10.5194/acp-12-1397-2012, 2012.

Alvarado, M. J., Logan, J. A., Mao, J., Apel, E., Riemer, D., Blake, D., Cohen, R. C., Browne, C., Wooldridge, P. J., Diskin, G. S., Sachse, G. W., Fuelberg, H., Sessions, W. R., Harrigan, D. L., Huey, G., Liao, J., Case-Hanks, A., Jimenez, J. L., Cubison, M. J., Vay, S. A., Weinheimer, A. J., Knapp, D. J., Flocke, F. M., Pollack, I. B., Wennberg, P. O., Kurten, A., Crounse, J., Clair, J. M. S., Wisthaler, A., Mikoviny, T., Yantosca, R. M., Carouge, C. C., and Sager, P. L.: Nitrogen oxides and PAN in plumes from boreal fires during ARCTAS-B and their impact on ozone: an integrated analysis of aircraft and satellite observations, Atmos. Chem. Phys., 22, 2010.

Andela, N., Morton, D. C., Giglio, L., Chen, Y., Werf, G. R. van der, Kasibhatla, P. S., DeFries, R. S., Collatz, G. J., Hantson, S., Kloster, S., Bachelet, D., Forrest, M., Lasslop, G., Li, F., Mangeon, S., Melton, J. R., Yue, C., and Randerson, J. T.: A human-driven decline in global burned area, Science, 356, 1356–1362, https://doi.org/10.1126/science.aal4108, 2017.

Andreae, M. O.: Emission of trace gases and aerosols from biomass burning – an updated assessment, Atmospheric Chemistry and Physics, 19, 8523–8546, https://doi.org/10.5194/acp-19-8523-2019, 2019.

Andreae, M. O. and Merlet, P.: Emission of trace gases and aerosols from biomass burning, Global Biogeochemical Cycles, 15, 955–966, https://doi.org/10.1029/2000GB001382, 2001.

Ozone and Your Health | Air | CDC: https://www.cdc.gov/air/ozone.html, last access: 20 June 2022.

Gridded Population of the World (GPW), v4 | SEDAC: https://sedac.ciesin.columbia.edu/data/collection/gpw-v4, last access: 14 June 2022.

Apel, E. C., Hornbrook, R. S., Hills, A. J., Blake, N. J., Barth, M. C., Weinheimer, A., Cantrell, C., Rutledge, S. A., Basarab, B., Crawford, J., Diskin, G., Homeyer, C. R., Campos, T., Flocke, F., Fried, A., Blake, D. R., Brune, W., Pollack, I., Peischl, J., Ryerson, T., Wennberg, P. O., Crounse, J. D., Wisthaler, A., Mikoviny, T., Huey, G., Heikes, B., O'Sullivan, D., and Riemer, D. D.: Upper tropospheric ozone production from lightning NOx-impacted convection: Smoke ingestion case study from the DC3 campaign, Journal of Geophysical Research: Atmospheres, 120, 2505–2523, https://doi.org/10.1002/2014JD022121, 2015.

Aruffo, E., Biancofiore, F., Di Carlo, P., Busilacchio, M., Verdecchia, M., Tomassetti, B., Dari-Salisburgo, C., Giammaria, F., Bauguitte, S., Lee, J., Moller, S., Hopkins, J., Punjabi, S., Andrews, S. J., Lewis, A. C., Palmer, P. I., Hyer, E., Le Breton, M., and Percival, C.: Impact of biomass burning emission on total peroxy nitrates: fire plume identification during the BORTAS campaign, Atmospheric Measurement Techniques, 9, 5591–5606, https://doi.org/10.5194/amt-9-5591-2016, 2016.

Baer, D. S., Paul, J. B., Gupta, M., and O'Keefe, A.: Sensitive absorption measurements in the near-infrared region using off-axis integrated-cavity-output spectroscopy, Appl Phys B, 75, 261–265, https://doi.org/10.1007/s00340-002-0971-z, 2002.

Bahreini, R., Ervens, B., Middlebrook, A. M., Warneke, C., Gouw, J. A. de, DeCarlo, P. F., Jimenez, J. L., Brock, C. A., Neuman, J. A., Ryerson, T. B., Stark, H., Atlas, E., Brioude, J., Fried, A., Holloway, J. S., Peischl, J., Richter, D., Walega, J., Weibring, P., Wollny, A. G., and Fehsenfeld, F. C.: Organic aerosol formation in urban and industrial plumes near Houston and Dallas, Texas, Journal of Geophysical Research: Atmospheres, 114, https://doi.org/10.1029/2008JD011493, 2009.

Bakhshaii, A. and Johnson, E. A.: A review of a new generation of wildfire–atmosphere modeling, Can. J. For. Res., 49, 565–574, https://doi.org/10.1139/cjfr-2018-0138, 2019.

Balch, J. K., Bradley, B. A., Abatzoglou, J. T., Nagy, R. C., Fusco, E. J., and Mahood, A. L.: Human-started wildfires expand the fire niche across the United States, PNAS, 114, 2946–2951, https://doi.org/10.1073/pnas.1617394114, 2017.

Barth, M. C., Cantrell, C. A., Brune, W. H., Rutledge, S. A., Crawford, J. H., Huntrieser, H., Carey, L. D., MacGorman, D., Weisman, M., Pickering, K. E., Bruning, E., Anderson, B., Apel, E., Biggerstaff, M., Campos, T., Campuzano-Jost, P., Cohen, R., Crounse, J., Day, D. A., Diskin, G., Flocke, F., Fried, A., Garland, C., Heikes, B., Honomichl, S., Hornbrook, R., Huey, L. G., Jimenez, J. L., Lang, T., Lichtenstern, M., Mikoviny, T., Nault, B., O'Sullivan, D., Pan, L. L., Peischl, J., Pollack, I., Richter, D., Riemer, D., Ryerson, T., Schlager, H., St. Clair, J., Walega, J., Weibring, P., Weinheimer, A., Wennberg, P., Wisthaler, A., Wooldridge, P. J., and Ziegler, C.: The Deep Convective Clouds and Chemistry (DC3) Field Campaign, Bull. Amer. Meteor. Soc., 96, 1281–1309, https://doi.org/10.1175/BAMS-D-13-00290.1, 2015.

Bates, K. H., Jacob, D. J., Li, K., Ivatt, P. D., Evans, M. J., Yan, Y., and Lin, J.: Development and evaluation of a new compact mechanism for aromatic oxidation in atmospheric models, Atmos. Chem. Phys., 21, 18351–18374, https://doi.org/10.5194/acp-21-18351-2021, 2021.

Bernath, P., Boone, C., and Crouse, J.: Wildfire smoke destroys stratospheric ozone, Science, 375, 1292–1295, https://doi.org/10.1126/science.abm5611, 2022.

Bierbach, A., Barnes, I., and Becker, K. H.: Product and kinetic study of the oh-initiated gas-phase oxidation of Furan, 2-methylfuran and furanaldehydes at ≈ 300 K, Atmospheric Environment, 29, 2651–2660, https://doi.org/10.1016/1352-2310(95)00096-H, 1995.

Bond, T. C. and Bergstrom, R. W.: Light Absorption by Carbonaceous Particles: An Investigative Review, Aerosol Science and Technology, 40, 27–67, https://doi.org/10.1080/02786820500421521, 2006.

Bond, T. C., Anderson, T. L., and Campbell, D.: Calibration and Intercomparison of Filter-Based Measurements of Visible Light Absorption by Aerosols, Aerosol Science and Technology, 30, 582–600, https://doi.org/10.1080/027868299304435, 1999.

Bond, T. C., Habib, G., and Bergstrom, R. W.: Limitations in the enhancement of visible light absorption due to mixing state, Journal of Geophysical Research (Atmospheres), 111, D20211, https://doi.org/10.1029/2006JD007315, 2006.

Bond, T. C., Doherty, S. J., Fahey, D. W., Forster, P. M., Berntsen, T., DeAngelo, B. J., Flanner, M. G., Ghan, S., Kärcher, B., Koch, D., Kinne, S., Kondo, Y., Quinn, P. K., Sarofim, M. C., Schultz, M. G., Schulz, M., Venkataraman, C., Zhang, H., Zhang, S., Bellouin, N., Guttikunda, S. K., Hopke, P. K., Jacobson, M. Z., Kaiser, J. W., Klimont, Z., Lohmann, U., Schwarz, J. P., Shindell, D., Storelvmo, T., Warren, S. G., and Zender, C. S.: Bounding the role of black carbon in the climate system: A scientific assessment, Journal of Geophysical Research: Atmospheres, 118, 5380–5552, https://doi.org/10.1002/jgrd.50171, 2013.

Bourgeois, I., Peischl, J., Neuman, J. A., Brown, S. S., Thompson, C. R., Aikin, K. C., Allen, H. M., Angot, H., Apel, E. C., Baublitz, C. B., Brewer, J. F., Campuzano-Jost, P., Commane, R., Crounse, J. D., Daube, B. C., DiGangi, J. P., Diskin, G. S., Emmons, L. K., Fiore, A. M., Gkatzelis, G. I., Hills, A., Hornbrook, R. S., Huey, L. G., Jimenez, J. L., Kim, M., Lacey, F., McKain, K., Murray, L. T., Nault, B. A., Parrish, D. D., Ray, E., Sweeney, C., Tanner, D., Wofsy, S. C., and Ryerson, T. B.: Large contribution of biomass burning emissions to ozone throughout the global remote troposphere, PNAS, 118, https://doi.org/10.1073/pnas.2109628118, 2021.

Bourgeois, I., Peischl, J., Neuman, J. A., Brown, S. S., Allen, H. M., Campuzano-Jost, P., Coggon, M. M., DiGangi, J. P., Diskin, G. S., Gilman, J. B., Gkatzelis, G. I., Guo, H., Halliday, H., Hanisco, T. F., Holmes, C. D., Huey, L. G., Jimenez, J. L., Lamplugh, A. D., Lee, Y. R., Lindaas, J., Moore, R. H., Nowak, J. B., Pagonis, D., Rickly, P. S., Robinson, M. A., Rollins, A. W., Selimovic, V., St. Clair, J. M., Tanner, D., Vasquez, K. T., Veres, P. R., Warneke, C., Wennberg, P. O., Washenfelder, R. A., Wiggins, E. B., Womack, C. C., Xu, L., Zarzana, K. J., and Ryerson, T. B.: Comparison of airborne measurements of NO, NO₂, HONO, NO_y and CO during FIREX-AQ, Gases/In Situ Measurement/Instruments and Platforms, https://doi.org/10.5194/amt-2021-432, 2022.

Bowman, D. M. J. S., Balch, J., Artaxo, P., Bond, W. J., Cochrane, M. A., D'Antonio, C. M., DeFries, R., Johnston, F. H., Keeley, J. E., Krawchuk, M. A., Kull, C. A., Mack, M., Moritz, M. A., Pyne, S., Roos, C. I., Scott, A. C., Sodhi, N. S., and Swetnam, T. W.: The human dimension of fire regimes on Earth, Journal of Biogeography, 38, 2223–2236, https://doi.org/10.1111/j.1365-2699.2011.02595.x, 2011.

Brey, S. J., Ruminski, M., Atwood, S. A., and Fischer, E. V.: Connecting smoke plumes to sources using Hazard Mapping System (HMS) smoke and fire location data over North America, Atmos. Chem. Phys., 18, 1745–1761, https://doi.org/10.5194/acp-18-1745-2018, 2018a.

Brey, S. J., Barnes, E. A., Pierce, J. R., Wiedinmyer, C., and Fischer, E. V.: Environmental Conditions, Ignition Type, and Air Quality Impacts of Wildfires in the Southeastern and Western United States, Earth's Future, 6, 1442–1456, https://doi.org/10.1029/2018EF000972, 2018b.

Brook, R. D., Rajagopalan, S., Pope, C. A., Brook, J. R., Bhatnagar, A., Diez-Roux, A. V., Holguin, F., Hong, Y., Luepker, R. V., Mittleman, M. A., Peters, A., Siscovick, D., Smith, S. C., Whitsel, L., and Kaufman, J. D.: Particulate Matter Air Pollution and Cardiovascular Disease: An Update to the Scientific Statement From the American Heart Association, Circulation, 121, 2331–2378, https://doi.org/10.1161/CIR.0b013e3181dbece1, 2010.

Brown, H., Liu, X., Pokhrel, R., Murphy, S., Lu, Z., Saleh, R., Mielonen, T., Kokkola, H., Bergman, T., Myhre, G., Skeie, R. B., Watson-Paris, D., Stier, P., Johnson, B., Bellouin, N., Schulz, M., Vakkari, V., Beukes, J. P., van Zyl, P. G., Liu, S., and Chand, D.: Biomass burning aerosols in most climate models are too absorbing, Nature Communications, 12, 277, https://doi.org/10.1038/s41467-020-20482-9, 2021.

Brune, W. H., Ren, X., Zhang, L., Mao, J., Miller, D. O., Anderson, B. E., Blake, D. R., Cohen, R. C., Diskin, G. S., Hall, S. R., Hanisco, T. F., Huey, L. G., Nault, B. A., Peischl, J., Pollack, I., Ryerson, T. B., Shingler, T., Sorooshian, A., Ullmann, K., Wisthaler, A., and Wooldridge, P. J.: Atmospheric oxidation in the presence of clouds during the Deep Convective Clouds and Chemistry (DC3) study, Atmos. Chem. Phys., 18, 14493–14510, https://doi.org/10.5194/acp-18-14493-2018, 2018.

Canagaratna, M. R., Jayne, J. T., Jimenez, J. L., Allan, J. D., Alfarra, M. R., Zhang, Q., Onasch, T. B., Drewnick, F., Coe, H., Middlebrook, A., Delia, A., Williams, L. R., Trimborn, A. M., Northway, M. J., DeCarlo, P. F., Kolb, C. E., Davidovits, P., and Worsnop, D. R.: Chemical and microphysical characterization of ambient aerosols with the

aerodyne aerosol mass spectrometer, Mass Spectrometry Reviews, 26, 185–222, https://doi.org/10.1002/mas.20115, 2007.

Cappa, C. D., Onasch, T. B., Massoli, P., Worsnop, D. R., Bates, T. S., Cross, E. S., Davidovits, P., Hakala, J., Hayden, K. L., Jobson, B. T., Kolesar, K. R., Lack, D. A., Lerner, B. M., Li, S.-M., Mellon, D., Nuaaman, I., Olfert, J. S., Petäjä, T., Quinn, P. K., Song, C., Subramanian, R., Williams, E. J., and Zaveri, R. A.: Radiative Absorption Enhancements Due to the Mixing State of Atmospheric Black Carbon, Science, 337, 1078–1081, https://doi.org/10.1126/science.1223447, 2012.

Cappa, C. D., Lim, C. Y., Hagan, D. H., Coggon, M., Koss, A., Sekimoto, K., de Gouw, J., Onasch, T. B., Warneke, C., and Kroll, J. H.: Biomass-burning-derived particles from a wide variety of fuels – Part 2: Effects of photochemical aging on particle optical and chemical properties, Atmospheric Chemistry and Physics, 20, 8511–8532, https://doi.org/10.5194/acp-20-8511-2020, 2020.

Carter, T. S., Heald, C. L., Jimenez, J. L., Campuzano-Jost, P., Kondo, Y., Moteki, N., Schwarz, J. P., Wiedinmyer, C., Darmenov, A. S., da Silva, A. M., and Kaiser, J. W.: How emissions uncertainty influences the distribution and radiative impacts of smoke from fires in North America, Atmospheric Chemistry & Physics, 20, 2073–2097, https://doi.org/10.5194/acp-20-2073-2020, 2020.

Carter, T. S., Heald, C. L., Cappa, C. D., Kroll, J. H., Campos, T. L., Coe, H., Cotterell, M. I., Davies, N. W., Farmer, D. K., Fox, C., Garofalo, L. A., Hu, L., Langridge, J. M., Levin, E. J. T., Murphy, S. M., Pokhrel, R. P., Shen, Y., Szpek, K., Taylor, J. W., and Wu, H.: Investigating Carbonaceous Aerosol and Its Absorption Properties From Fires in the Western United States (WE-CAN) and Southern Africa (ORACLES and CLARIFY), Journal of Geophysical Research: Atmospheres, 126, e2021JD034984, https://doi.org/10.1029/2021JD034984, 2021.

Chan Miller, C., Jacob, D. J., Marais, E. A., Yu, K., Travis, K. R., Kim, P. S., Fisher, J. A., Zhu, L., Wolfe, G. M., Hanisco, T. F., Keutsch, F. N., Kaiser, J., Min, K.-E., Brown, S. S., Washenfelder, R. A., González Abad, G., and Chance, K.: Glyoxal yield from isoprene oxidation and relation to formaldehyde: chemical mechanism, constraints from SENEX aircraft observations, and interpretation of OMI satellite data, Atmospheric Chemistry and Physics, 17, 8725–8738, https://doi.org/10.5194/acp-17-8725-2017, 2017.

Chen, H., Samet, J. M., Bromberg, P. A., and Tong, H.: Cardiovascular health impacts of wildfire smoke exposure, Particle and Fibre Toxicology, 18, 2, https://doi.org/10.1186/s12989-020-00394-8, 2021.

Chin, M., Ginoux, P., Kinne, S., Torres, O., Holben, B. N., Duncan, B. N., Martin, R. V., Logan, J. A., Higurashi, A., and Nakajima, T.: Tropospheric Aerosol Optical Thickness from the GOCART Model and Comparisons with Satellite and Sun Photometer Measurements, Journal of the Atmospheric Sciences, 59, 461–483, https://doi.org/10.1175/1520-0469(2002)059<0461:TAOTFT>2.0.CO;2, 2002.

Chow, J. C., Watson, J. G., Chen, L.-W. A., Chang, M. C. O., Robinson, N. F., Trimble, D., and Kohl, S.: The IMPROVE_A Temperature Protocol for Thermal/Optical Carbon Analysis: Maintaining Consistency with a Long-Term Database, Journal of the Air & Waste Management Association, 57, 1014–1023, https://doi.org/10.3155/1047-3289.57.9.1014, 2007.

Chung, C. E., Ramanathan, V., and Decremer, D.: Observationally constrained estimates of carbonaceous aerosol radiative forcing, Proceedings of the National Academy of Sciences, 109, 11624–11629, https://doi.org/10.1073/pnas.1203707109, 2012.

Coggon, M. M., Lim, C. Y., Koss, A. R., Sekimoto, K., Yuan, B., Gilman, J. B., Hagan, D. H., Selimovic, V., Zarzana, K. J., Brown, S. S., Roberts, J. M., Müller, M., Yokelson, R., Wisthaler, A., Krechmer, J. E., Jimenez, J. L., Cappa, C., Kroll, J. H., de Gouw, J., and Warneke, C.: OH chemistry of non-methane organic gases (NMOGs) emitted from laboratory and ambient biomass burning smoke: evaluating the influence of furans and oxygenated aromatics on ozone and secondary NMOG formation, Atmos. Chem. Phys., 19, 14875–14899, https://doi.org/10.5194/acp-19-14875-2019, 2019.

Collier, S., Zhou, S., Onasch, T. B., Jaffe, D. A., Kleinman, L., Sedlacek, A. J., Briggs, N. L., Hee, J., Fortner, E., Shilling, J. E., Worsnop, D., Yokelson, R. J., Parworth, C., Ge, X., Xu, J., Butterfield, Z., Chand, D., Dubey, M. K., Pekour, M. S., Springston, S., and Zhang, Q.: Regional Influence of Aerosol Emissions from Wildfires Driven by Combustion Efficiency: Insights from the BBOP Campaign, Environ. Sci. Technol., 50, 8613–8622, https://doi.org/10.1021/acs.est.6b01617, 2016.

Collins, K. M., Penman, T. D., and Price, O. F.: Some Wildfire Ignition Causes Pose More Risk of Destroying Houses than Others, PLOS ONE, 11, e0162083, https://doi.org/10.1371/journal.pone.0162083, 2016.

Colman, J. J., Swanson, A. L., Meinardi, S., Sive, B. C., Blake, D. R., and Rowland, F. S.: Description of the Analysis of a Wide Range of Volatile Organic Compounds in Whole Air Samples Collected during PEM-Tropics A and B, Anal. Chem., 73, 3723–3731, https://doi.org/10.1021/ac010027g, 2001.

Cooke, W. F., Liousse, C., Cachier, H., and Feichter, J.: Construction of a 1° × 1° fossil fuel emission data set for carbonaceous aerosol and implementation and radiative impact in the ECHAM4 model, Journal of Geophysical Research: Atmospheres, 104, 22137–22162, https://doi.org/10.1029/1999JD900187, 1999.

Cotterell, M. I., Szpek, K., Haywood, J. M., and Langridge, J. M.: Sensitivity and accuracy of refractive index retrievals from measured extinction and absorption cross sections for mobility-selected internally mixed light absorbing aerosols, Aerosol Science and Technology, 54, 1034–1057, https://doi.org/10.1080/02786826.2020.1757034, 2020.

Cotterell, M. I., Szpek, K., Tiddeman, D. A., Haywood, J. M., and Langridge, J. M.: Photoacoustic studies of energy transfer from ozone photoproducts to bath gases following Chappuis band photoexcitation, Phys. Chem. Chem. Phys., 23, 536–553, https://doi.org/10.1039/D0CP05056C, 2021.

Cubison, M., Ortega, A., Hayes, P., Farmer, D., Day, D., Lechner, M., Brune, W., Apel, E., Diskin, G., Fisher, J., Fuelberg, H., Hecobian, A., Knapp, D., Mikoviny, T., Riemer, D., Sachse, G., Sessions, W., Weber, R., Weinheimer, A., Wisthaler, A., and Jimenez, J.: Effects of aging on organic aerosol from open biomass burning smoke in aircraft and laboratory studies, Faculty of Science - Papers (Archive), 12049–12064, https://doi.org/10.5194/acp-11-12049-2011, 2011.

The Quick Fire Emissions Dataset (QFED) – Documentation of versions 2.1, 2.2 and 2.4, NASA Technical Report Series on Global Modeling and Data Assimilation, NASA TM-2013-104606: https://scholar.google.com/scholar?lookup=0&q=The+Quick+Fire+Emissions+Dataset+(QFED):+Documentation+of+versions+2.1,+2.2+and+2.4.%22+NASA+Technical+Report+Series+on+Global+Modeling+and+Data+Assimilation&hl=en&as_sdt=0,22, last access: 16 June 2020.

David, L. M., Ravishankara, A. R., Brey, S. J., Fischer, E. V., Volckens, J., and Kreidenweis, S.: Could the exception become the rule? “Uncontrollable” air pollution events in the U.S. due to wildland fires, Environ. Res. Lett., https://doi.org/10.1088/1748-9326/abe1f3, 2021.

Davies, N. W., Cotterell, M. I., Fox, C., Szpek, K., Haywood, J. M., and Langridge, J. M.: On the accuracy of aerosol photoacoustic spectrometer calibrations using absorption by ozone, Atmospheric Measurement Techniques, 11, 2313–2324, https://doi.org/10.5194/amt-11-2313-2018, 2018.

Davies, N. W., Fox, C., Szpek, K., Cotterell, M. I., Taylor, J. W., Allan, J. D., Williams, P. I., Trembath, J., Haywood, J. M., and Langridge, J. M.: Evaluating biases in filter-based aerosol absorption measurements using photoacoustic spectroscopy, Atmospheric Measurement Techniques, 12, 3417–3434, https://doi.org/10.5194/amt-12-3417-2019, 2019.

DeCarlo, P. F., Kimmel, J. R., Trimborn, A., Northway, M. J., Jayne, J. T., Aiken, A. C., Gonin, M., Fuhrer, K., Horvath, T., Docherty, K. S., Worsnop, D. R., and Jimenez, J. L.: Field-Deployable, High-Resolution, Time-of-Flight Aerosol Mass Spectrometer, Anal. Chem., 78, 8281–8289, https://doi.org/10.1021/ac061249n, 2006.

DeCarlo, P. F., Dunlea, E. J., Kimmel, J. R., Aiken, A. C., Sueper, D., Crounse, J., Wennberg, P. O., Emmons, L., Shinozuka, Y., Clarke, A., Zhou, J., Tomlinson, J., Collins, D. R., Knapp, D., Weinheimer, A. J., Montzka, D. D., Campos, T., and Jimenez, J. L.: Fast airborne aerosol size and chemistry measurements above Mexico City and Central Mexico during the MILAGRO campaign, Atmos. Chem. Phys., 8, 4027–4048, https://doi.org/10.5194/acp-8-4027-2008, 2008.

Denjean, C., Bourrianne, T., Burnet, F., Mallet, M., Maury, N., Colomb, A., Dominutti, P., Brito, J., Dupuy, R., Sellegri, K., Schwarzenboeck, A., Flamant, C., and Knippertz, P.: Overview of aerosol optical properties over southern West Africa from DACCIWA aircraft measurements, Atmospheric Chemistry and Physics, 20, 4735–4756, https://doi.org/10.5194/acp-20-4735-2020, 2020.

Desservettaz, M. J., Fisher, J. A., Luhar, A. K., Woodhouse, M. T., Bukosa, B., Buchholz, R. R., Wiedinmyer, C., Griffith, D. W. T., Krummel, P. B., Jones, N. B., Deutscher, N. M., and Greenslade, J. W.: Australian Fire Emissions of Carbon Monoxide Estimated by Global Biomass Burning Inventories: Variability and Observational Constraints, Journal of Geophysical Research: Atmospheres, 127, e2021JD035925, https://doi.org/10.1029/2021JD035925, 2022.

Drury, E., Jacob, D. J., Spurr, R. J. D., Wang, J., Shinozuka, Y., Anderson, B. E., Clarke, A. D., Dibb, J., McNaughton, C., and Weber, R.: Synthesis of satellite (MODIS), aircraft (ICARTT), and surface (IMPROVE, EPA-AQS, AERONET) aerosol observations over eastern North America to improve MODIS aerosol retrievals and constrain surface aerosol concentrations and sources, Journal of Geophysical Research: Atmospheres, 115, https://doi.org/10.1029/2009JD012629, 2010.

Dunlea, E. J., DeCarlo, P. F., Aiken, A. C., Kimmel, J. R., Peltier, R. E., Weber, R. J., Tomlinson, J., Collins, D. R., Shinozuka, Y., McNaughton, C. S., Howell, S. G., Clarke, A. D., Emmons, L. K., Apel, E. C., Pfister, G. G., van Donkelaar, A., Martin, R. V., Millet, D. B., Heald, C. L., and Jimenez, J. L.: Evolution of Asian aerosols during transpacific transport in INTEX-B, Atmos. Chem. Phys., 31, 2009.

Eastham, S. D. and Jacob, D. J.: Limits on the ability of global Eulerian models to resolve intercontinental transport of chemical plumes, Atmos. Chem. Phys., 17, 2543–2553, https://doi.org/10.5194/acp-17-2543-2017, 2017.

European Union: Council Directive 1999/13/EC of 11 March 1999 on the limitation of emissions of volatile organic compounds due to the use of organic solvents in certain activities and installations, OJ L, 085, 1999.

Fairlie, Duncan T., Jacob, D. J., and Park, R. J.: The impact of transpacific transport of mineral dust in the United States, Atmospheric Environment, 41, 1251–1266, https://doi.org/10.1016/j.atmosenv.2006.09.048, 2007.

Feng, Y., Ramanathan, V., and Kotamarthi, V. R.: Brown carbon: a significant atmospheric absorber of solar radiation?, Atmospheric Chemistry and Physics, 13, 8607–8621, https://doi.org/10.5194/acp-13-8607-2013, 2013.

Fischer, E. V., Jacob, D. J., Yantosca, R. M., Sulprizio, M. P., Millet, D. B., Mao, J., Paulot, F., Singh, H. B., Roiger, A., Ries, L., Talbot, R. W., Dzepina, K., and Pandey Deolal, S.: Atmospheric peroxyacetyl nitrate (PAN): a global budget and source attribution, Atmos. Chem. Phys., 14, 2679–2698, https://doi.org/10.5194/acp-14-2679-2014, 2014.

Ford, B., Martin, M. V., Zelasky, S. E., Fischer, E. V., Anenberg, S. C., Heald, C. L., and Pierce, J. R.: Future Fire Impacts on Smoke Concentrations, Visibility, and Health in the Contiguous United States, GeoHealth, 2, 229–247, https://doi.org/10.1029/2018GH000144, 2018.

Forestieri, S. D., Staudt, S. M., Kuborn, T. M., Faber, K., Ruehl, C. R., Bertram, T. H., and Cappa, C. D.: Establishing the impact of model surfactants on cloud condensation nuclei activity of sea spray aerosol mimics, Atmospheric Chemistry and Physics, 18, 10985–11005, https://doi.org/10.5194/acp-18-10985-2018, 2018.

Forrister, H., Liu, J., Scheuer, E., Dibb, J., Ziemba, L., Thornhill, K. L., Anderson, B., Diskin, G., Perring, A. E., Schwarz, J. P., Campuzano-Jost, P., Day, D. A., Palm, B. B., Jimenez, J. L., Nenes, A., and Weber, R. J.: Evolution of brown carbon in wildfire plumes, Geophysical Research Letters, 42, 4623–4630, https://doi.org/10.1002/2015GL063897, 2015.

Foster, K., Pokhrel, R., Burkhart, M., and Murphy, S.: A novel approach to calibrating a photoacoustic absorption spectrometer using polydisperse absorbing aerosol, Atmos. Meas. Tech., 12, 3351–3363, https://doi.org/10.5194/amt-12-3351-2019, 2019.

Fountoukis, C. and Nenes, A.: ISORROPIA II: a computationally efficient thermodynamic equilibrium model for K+?Ca2+?Mg2+?NH4+?Na+?SO42??NO3??Cl??H2O aerosols, 48, 2007.

Freese, L. M., Chossière, G. P., Eastham, S., Jenn, A., and Selin, N. E.: Nuclear and Coal Power Generation Phaseouts Redistribute U.S. Air Quality and Climate Related Mortality Risk, Environmental Sciences, https://doi.org/10.1002/essoar.10510994.1, 2022.

Fuller, K. A., Malm, W. C., and Kreidenweis, S. M.: Effects of mixing on extinction by carbonaceous particles, Journal of Geophysical Research: Atmospheres, 104, 15941–15954, https://doi.org/10.1029/1998JD100069, 1999.

Fusco, E. J., Abatzoglou, J. T., Balch, J. K., Finn, J. T., and Bradley, B. A.: Quantifying the human influence on fire ignition across the western USA, Ecological Applications, 26, 2390–2401, https://doi.org/10.1002/eap.1395, 2016.

Fuzzi, S., Baltensperger, U., Carslaw, K., Decesari, S., Denier van der Gon, H., Facchini, M. C., Fowler, D., Koren, I., Langford, B., Lohmann, U., Nemitz, E., Pandis, S., Riipinen, I., Rudich, Y., Schaap, M., Slowik, J. G., Spracklen, D. V., Vignati, E., Wild, M., Williams, M., and Gilardoni, S.: Particulate matter, air quality and climate: lessons learned and future needs, Atmospheric Chemistry and Physics, 15, 8217–8299, https://doi.org/10.5194/acp-15-8217-2015, 2015.

Garofalo, L. A., Pothier, M. A., Levin, E. J. T., Campos, T., Kreidenweis, S. M., and Farmer, D. K.: Emission and Evolution of Submicron Organic Aerosol in Smoke from Wildfires in the Western United States, ACS Earth Space Chem., 3, 1237–1247, https://doi.org/10.1021/acsearthspacechem.9b00125, 2019.

GBD 2019 Risk Factors Collaborators: Global burden of 87 risk factors in 204 countries and territories, 1990-2019: a systematic analysis for the Global Burden of Disease Study 2019, Lancet, 396, 1223–1249, https://doi.org/10.1016/S0140-6736(20)30752-2, 2020.

Giglio, L., Van Der Werf, G. R., Randerson, J. T., Collatz, G. J., and Kasibhatla, P.: Global estimation of burned area using MODIS active fire observations, Atmospheric Chemistry and Physics, 6, 957–974, 2006.

Giglio, L., Randerson, J. T., and Werf, G. R. van der: Analysis of daily, monthly, and annual burned area using the fourth-generation global fire emissions database (GFED4), Journal of Geophysical Research: Biogeosciences, 118, 317–328, https://doi.org/10.1002/jgrg.20042, 2013.

Giglio, L., Boschetti, L., Roy, D. P., Humber, M. L., and Justice, C. O.: The Collection 6 MODIS burned area mapping algorithm and product, Remote Sensing of Environment, 217, 72–85, https://doi.org/10.1016/j.rse.2018.08.005, 2018.

Gilman, J. B., Lerner, B. M., Kuster, W. C., Goldan, P. D., Warneke, C., Veres, P. R., Roberts, J. M., de Gouw, J. A., Burling, I. R., and Yokelson, R. J.: Biomass burning emissions and potential air quality impacts of volatile organic compounds and other trace gases from fuels common in the US, Atmospheric Chemistry and Physics, 15, 13915–13938, https://doi.org/10.5194/acp-15-13915-2015, 2015.

Goldstein, A. H. and Galbally, I. E.: in the Earth's Atmosphere, 8, 2007.

de Gouw, J. and Warneke, C.: Measurements of volatile organic compounds in the earth's atmosphere using proton-transfer-reaction mass spectrometry, Mass Spectrom Rev, 26, 223–257, https://doi.org/10.1002/mas.20119, 2007.

Grieshop, A. P., Logue, J. M., Donahue, N. M., and Robinson, A. L.: Laboratory investigation of photochemical oxidation of organic aerosol from wood fires 1: measurement and simulation of organic aerosol evolution, Atmos. Chem. Phys., 9, 1263–1277, https://doi.org/10.5194/acp-9-1263-2009, 2009.

Guenther, A. B., Jiang, X., Heald, C. L., Sakulyanontvittaya, T., Duhl, T., Emmons, L. K., and Wang, X.: The Model of Emissions of Gases and Aerosols from Nature version 2.1 (MEGAN2.1): an extended and updated framework for modeling biogenic emissions, Geoscientific Model Development, 5, 1471–1492, https://doi.org/10.5194/gmd-5-1471-2012, 2012.

Hammer, M. S., Martin, R. V., van Donkelaar, A., Buchard, V., Torres, O., Ridley, D. A., and Spurr, R. J. D.: Interpreting the ultraviolet aerosol index observed with the OMI satellite instrument to understand absorption by organic aerosols: implications for atmospheric oxidation and direct radiative effects, Atmospheric Chemistry and Physics, 16, 2507–2523, https://doi.org/10.5194/acp-16-2507-2016, 2016.

Hammer, M. S., Martin, R. V., Li, C., Torres, O., Manning, M., and Boys, B. L.: Insight into global trends in aerosol composition from 2005 to 2015 inferred from the OMI Ultraviolet Aerosol Index, Atmos. Chem. Phys., 18, 8097–8112, https://doi.org/10.5194/acp-18-8097-2018, 2018.

Hansel, A., Jordan, A., Holzinger, R., Prazeller, P., Vogel, W., and Lindinger, W.: Proton transfer reaction mass spectrometry: on-line trace gas analysis at the ppb level, International Journal of Mass Spectrometry and Ion Processes, 149–150, 609–619, https://doi.org/10.1016/0168-1176(95)04294-U, 1995.

Hansen, A. D. A., Rosen, H., and Novakov, T.: Aethalometer - an instrument for the real-time measurement of optical absorption by aerosol particles, Lawrence Berkeley Lab., CA (USA), 1983.

Hantson, S., Andela, N., Goulden, M. L., and Randerson, J. T.: Human-ignited fires result in more extreme fire behavior and ecosystem impacts, Nat Commun, 13, 2717, https://doi.org/10.1038/s41467-022-30030-2, 2022.

Haslett, S. L., Taylor, J. W., Evans, M., Morris, E., Vogel, B., Dajuma, A., Brito, J., Batenburg, A. M., Borrmann, S., Schneider, J., Schulz, C., Denjean, C., Bourrianne, T., Knippertz, P., Dupuy, R., Schwarzenböck, A., Sauer, D., Flamant, C., Dorsey, J., Crawford, I., and Coe, H.: Remote biomass burning dominates southern West African air pollution during the monsoon, Atmospheric Chemistry and Physics, 19, 15217–15234, https://doi.org/10.5194/acp-19-15217-2019, 2019.

Hatch, L. E., Luo, W., Pankow, J. F., Yokelson, R. J., Stockwell, C. E., and Barsanti, K. C.: Identification and quantification of gaseous organic compounds emitted from biomass burning using two-dimensional gas chromatography–time-of-flight mass spectrometry, Atmospheric Chemistry and Physics, 15, 1865–1899, https://doi.org/10.5194/acp-15-1865-2015, 2015.

Hayden, K., Li, S.-M., Liggio, J., Wheeler, M., Wentzell, J., Leithead, A., Brickell, P., Mittermeier, R., Oldham, Z., Mihele, C., Staebler, R., Moussa, S., Darlington, A., Steffen, A., Wolde, M., Thompson, D., Chen, J., Griffin, D., Eckert, E., Ditto, J., He, M., and Gentner, D.: Reconciling the total carbon budget for boreal forest wildfire emissions using airborne observations, Atmospheric Chemistry and Physics Discussions, 1–62, https://doi.org/10.5194/acp-2022-245, 2022.

Haywood, J. M., Abel, S. J., Barrett, P. A., Bellouin, N., Blyth, A., Bower, K. N., Brooks, M., Carslaw, K., Che, H., Coe, H., Cotterell, M. I., Crawford, I., Cui, Z., Davies, N., Dingley, B., Field, P., Formenti, P., Gordon, H., de Graaf, M., Herbert, R., Johnson, B., Jones, A. C., Langridge, J. M., Malavelle, F., Partridge, D. G., Peers, F., Redemann, J., Stier, P., Szpek, K., Taylor, J. W., Watson-Parris, D., Wood, R., Wu, H., and Zuidema, P.: Overview: The CLoud-Aerosol-Radiation Interaction and Forcing: Year-2017 (CLARIFY-2017) measurement campaign, Atmospheric Chemistry and Physics Discussions, 1–49, https://doi.org/10.5194/acp-2020-729, 2020.

Haywood, J. M., Abel, S. J., Barrett, P. A., Bellouin, N., Blyth, A., Bower, K. N., Brooks, M., Carslaw, K., Che, H., Coe, H., Cotterell, M. I., Crawford, I., Cui, Z., Davies, N., Dingley, B., Field, P., Formenti, P., Gordon, H., de Graaf, M., Herbert, R., Johnson, B., Jones, A. C., Langridge, J. M., Malavelle, F., Partridge, D. G., Peers, F., Redemann, J., Stier, P., Szpek, K., Taylor, J. W., Watson-Parris, D., Wood, R., Wu, H., and Zuidema, P.: The CLoud–Aerosol–Radiation Interaction and Forcing: Year 2017 (CLARIFY-2017) measurement campaign, Atmos. Chem. Phys., 21, 1049–1084, https://doi.org/10.5194/acp-21-1049-2021, 2021.

Heald, C. L., Ridley, D. A., Kroll, J. H., Barrett, S. R. H., Cady-Pereira, K. E., Alvarado, M. J., and Holmes, C. D.: Contrasting the direct radiative effect and direct radiative forcing of aerosols, Atmospheric Chemistry and Physics, 14, 5513–5527, https://doi.org/10.5194/acp-14-5513-2014, 2014.

Hennigan, C. J., Miracolo, M. A., Engelhart, G. J., May, A. A., Presto, A. A., Lee, T., Sullivan, A. P., McMeeking, G. R., Coe, H., Wold, C. E., Hao, W.-M., Gilman, J. B., Kuster, W. C., de Gouw, J., Schichtel, B. A., Collett, J. L., Kreidenweis, S. M., and Robinson, A. L.: Chemical and physical transformations of organic aerosol from the photo-oxidation of open biomass burning emissions in an environmental chamber, Atmos. Chem. Phys., 11, 7669–7686, https://doi.org/10.5194/acp-11-7669-2011, 2011.

Hobbs, P. V., Sinha, P., Yokelson, R. J., Christian, T. J., Blake, D. R., Gao, S., Kirchstetter, T. W., Novakov, T., and Pilewskie, P.: Evolution of gases and particles from a savanna fire in South Africa, Journal of Geophysical Research: Atmospheres, 108, https://doi.org/10.1029/2002JD002352, 2003.

Hodshire, A. L., Akherati, A., Alvarado, M. J., Brown-Steiner, B., Jathar, S. H., Jimenez, J. L., Kreidenweis, S. M., Lonsdale, C. R., Onasch, T. B., Ortega, A. M., and Pierce, J. R.: Aging Effects on Biomass Burning Aerosol Mass and Composition: A Critical Review of Field and Laboratory Studies, Environ. Sci. Technol., https://doi.org/10.1021/acs.est.9b02588, 2019.

Hoesly, R. M., Smith, S. J., Feng, L., Klimont, Z., Janssens-Maenhout, G., Pitkanen, T., Seibert, J. J., Vu, L., Andres, R. J., Bolt, R. M., Bond, T. C., Dawidowski, L., Kholod, N., Kurokawa, J., Li, M., Liu, L., Lu, Z., Moura, M. C. P., O'Rourke, P. R., and Zhang, Q.: Historical (1750–2014) anthropogenic emissions of reactive gases and aerosols from the Community Emissions Data System (CEDS), Geoscientific Model Development, 11, 369–408, https://doi.org/10.5194/gmd-11-369-2018, 2018.

Holder, A. L., Gullett, B. K., Urbanski, S. P., Elleman, R., O'Neill, S., Tabor, D., Mitchell, W., and Baker, K. R.: Emissions from prescribed burning of agricultural fields in the Pacific Northwest, Atmospheric Environment, 166, 22–33, https://doi.org/10.1016/j.atmosenv.2017.06.043, 2017.

Hsu, N. C., Tsay, S.-C., King, M. D., and Herman, J. R.: Deep Blue Retrievals of Asian Aerosol Properties During ACE-Asia, IEEE Transactions on Geoscience and Remote Sensing, 44, 3180–3195, https://doi.org/10.1109/TGRS.2006.879540, 2006.

Huang, M., Carmichael, G. R., Pierce, R. B., Jo, D. S., Park, R. J., Flemming, J., Emmons, L. K., Bowman, K. W., Henze, D. K., Davila, Y., Sudo, K., Jonson, J. E., Tronstad Lund, M., Janssens-Maenhout, G., Dentener, F. J., Keating, T. J., Oetjen, H., and Payne, V. H.: Impact of intercontinental pollution transport on North American ozone air pollution: an HTAP phase 2 multi-model study, Atmos. Chem. Phys., 17, 5721–5750, https://doi.org/10.5194/acp-17-5721-2017, 2017.

Huangfu, Y., Yuan, B., Wang, S., Wu, C., He, X., Qi, J., de Gouw, J., Warneke, C., Gilman, J. B., Wisthaler, A., Karl, T., Graus, M., Jobson, B. T., and Shao, M.: Revisiting Acetonitrile as Tracer of Biomass Burning in Anthropogenic-Influenced Environments, Geophysical Research Letters, 48, e2020GL092322, https://doi.org/10.1029/2020GL092322, 2021.

Iacono, M. J., Delamere, J. S., Mlawer, E. J., Shephard, M. W., Clough, S. A., and Collins, W. D.: Radiative forcing by long-lived greenhouse gases: Calculations with the AER radiative transfer models, Journal of Geophysical Research: Atmospheres, 113, https://doi.org/10.1029/2008JD009944, 2008.

African Biomass Burning and Its Atmospheric Impacts:

Ichoku, C. and Kaufman, Y. J.: A method to derive smoke emission rates from MODIS fire radiative energy measurements, IEEE Transactions on Geoscience and Remote Sensing, 43, 2636–2649, https://doi.org/10.1109/TGRS.2005.857328, 2005.

Intergovernmental Panel on Climate Change: AR5 Synthesis Report: Climate Change 2014 — IPCC, 2014.

Jacob, D. J., Crawford, J. H., Maring, H., Clarke, A. D., Dibb, J. E., Emmons, L. K., Ferrare, R. A., Hostetler, C. A., Russell, P. B., Singh, H. B., Thompson, A. M., Shaw, G. E., McCauley, E., Pederson, J. R., and Fisher, J. A.: The Arctic Research of the Composition of the Troposphere from Aircraft and Satellites (ARCTAS) mission: design, execution, and first results, Atmos. Chem. Phys., 10, 5191–5212, https://doi.org/10.5194/acp-10-5191-2010, 2010.

Jacobson, M. Z.: A physically-based treatment of elemental carbon optics: Implications for global direct forcing of aerosols, Geophysical Research Letters, 27, 217–220, https://doi.org/10.1029/1999GL010968, 2000.

Jaeglé, L., Quinn, P. K., Bates, T. S., Alexander, B., and Lin, J.-T.: Global distribution of sea salt aerosols: new constraints from in situ and remote sensing observations, Atmospheric Chemistry and Physics, 11, 3137–3157, https://doi.org/10.5194/acp-11-3137-2011, 2011.

Jaffe, D., Chand, D., Hafner, W., Westerling, A., and Spracklen, D.: Influence of Fires on O3 Concentrations in the Western U.S., Environ. Sci. Technol., 42, 5885–5891, https://doi.org/10.1021/es800084k, 2008.

Jaffe, D. A., Wigder, N., Downey, N., Pfister, G., Boynard, A., and Reid, S. B.: Impact of Wildfires on Ozone Exceptional Events in the Western U.S., Environ. Sci. Technol., 47, 11065–11072, https://doi.org/10.1021/es402164f, 2013.

Jaffe, D. A., Cooper, O. R., Fiore, A. M., Henderson, B. H., Tonnesen, G. S., Russell, A. G., Henze, D. K., Langford, A. O., Lin, M., and Moore, T.: Scientific assessment of background ozone over the U.S.: Implications for air quality management, Elementa: Science of the Anthropocene, 6, 56, https://doi.org/10.1525/elementa.309, 2018.

Jen, C. N., Hatch, L. E., Selimovic, V., Yokelson, R. J., Weber, R., Fernandez, A. E., Kreisberg, N. M., Barsanti, K. C., and Goldstein, A. H.: Speciated and total emission factors of particulate organics fromburning western U.S. wildland fuels and their dependence oncombustion efficiency, Aerosols/Laboratory Studies/Troposphere/Chemistry (chemical composition and reactions), https://doi.org/10.5194/acp-2018-840, 2018.

Jo, D. S., Park, R. J., Lee, S., Kim, S.-W., and Zhang, X.: A global simulation of brown carbon: implications for photochemistry and direct radiative effect, Atmos. Chem. Phys., 16, 3413–3432, https://doi.org/10.5194/acp-16-3413-2016, 2016.

Johnston Fay H., Henderson Sarah B., Chen Yang, Randerson James T., Marlier Miriam, DeFries Ruth S., Kinney Patrick, Bowman David M.J.S., and Brauer Michael: Estimated Global Mortality Attributable to Smoke from Landscape Fires, Environmental Health Perspectives, 120, 695–701, https://doi.org/10.1289/ehp.1104422, 2012.

Jolleys, M. D., Coe, H., McFiggans, G., McMeeking, G. R., Lee, T., Kreidenweis, S. M., Collett, J. L., and Sullivan, A. P.: Organic aerosol emission ratios from the laboratory combustion of biomass fuels, Journal of Geophysical Research: Atmospheres, 119, 12,850-12,871, https://doi.org/10.1002/2014JD021589, 2014.

Jolly, W. M., Cochrane, M. A., Freeborn, P. H., Holden, Z. A., Brown, T. J., Williamson, G. J., and Bowman, D. M. J. S.: Climate-induced variations in global wildfire danger from 1979 to 2013, Nat Commun, 6, 7537, https://doi.org/10.1038/ncomms8537, 2015.

Jones, B. A.: Are we underestimating the economic costs of wildfire smoke? An investigation using the life satisfaction approach, Journal of Forest Economics, 27, 80–90, https://doi.org/10.1016/j.jfe.2017.03.004, 2017.

Kahnert, M. and Kanngießer, F.: Modelling optical properties of atmospheric black carbon aerosols, Journal of Quantitative Spectroscopy and Radiative Transfer, 244, 106849, https://doi.org/10.1016/j.jqsrt.2020.106849, 2020.

The MACC Global Fire Assimilation System: First Emission Products (GFASv0):

Kaiser, J. W., Heil, A., Andreae, M. O., Benedetti, A., Chubarova, N., Jones, L., Morcrette, J.-J., Razinger, M., Schultz, M. G., Suttie, M., and van der Werf, G. R.: Biomass burning emissions estimated with a global fire

assimilation system based on observed fire radiative power, Biogeosciences, 9, 527–554, https://doi.org/10.5194/bg-9-527-2012, 2012.

Kalashnikov, D. A., Schnell, J. L., Abatzoglou, J. T., Swain, D. L., and Singh, D.: Increasing co-occurrence of fine particulate matter and ground-level ozone extremes in the western United States, Science Advances, 8, eabi9386, https://doi.org/10.1126/sciadv.abi9386, 2022.

Kim, P. S., Jacob, D. J., Fisher, J. A., Travis, K., Yu, K., Zhu, L., Yantosca, R. M., Sulprizio, M. P., Jimenez, J. L., Campuzano-Jost, P., Froyd, K. D., Liao, J., Hair, J. W., Fenn, M. A., Butler, C. F., Wagner, N. L., Gordon, T. D., Welti, A., Wennberg, P. O., Crounse, J. D., St. Clair, J. M., Teng, A. P., Millet, D. B., Schwarz, J. P., Markovic, M. Z., and Perring, A. E.: Sources, seasonality, and trends of southeast US aerosol: an integrated analysis of surface, aircraft, and satellite observations with the GEOS-Chem chemical transport model, Atmospheric Chemistry and Physics, 15, 10411–10433, https://doi.org/10.5194/acp-15-10411-2015, 2015.

Kloster, S., Mahowald, N. M., Randerson, J. T., and Lawrence, P. J.: The impacts of climate, land use, and demography on fires during the 21st century simulated by CLM-CN, Biogeosciences, 9, 509–525, https://doi.org/10.5194/bg-9-509-2012, 2012.

Knorr, W., Arneth, A., and Jiang, L.: Demographic controls of future global fire risk, Nature Climate Change, 6, 781–785, https://doi.org/10.1038/nclimate2999, 2016.

Ko, J., Krasowsky, T., and Ban-Weiss, G.: Measurements to determine the mixing state of black carbon emitted from the 2017–2018 California wildfires and urban Los Angeles, Atmospheric Chemistry and Physics, 20, 15635–15664, https://doi.org/10.5194/acp-20-15635-2020, 2020.

Kondo, Y., Matsui, H., Moteki, N., Sahu, L., Takegawa, N., Kajino, M., Zhao, Y., Cubison, M. J., Jimenez, J. L., Vay, S., Diskin, G. S., Anderson, B., Wisthaler, A., Mikoviny, T., Fuelberg, H. E., Blake, D. R., Huey, G., Weinheimer, A. J., Knapp, D. J., and Brune, W. H.: Emissions of black carbon, organic, and inorganic aerosols from biomass burning in North America and Asia in 2008, Journal of Geophysical Research: Atmospheres, 116, https://doi.org/10.1029/2010JD015152, 2011.

Köpke, P., Hess, M., Schult, I., and Shettle, E. P.: Global aerosol data set, Max-Planck-Inst. für Meteorologie, 1997.

Koss, A. R., Sekimoto, K., Gilman, J. B., Selimovic, V., Coggon, M. M., Zarzana, K. J., Yuan, B., Lerner, B. M., Brown, S. S., Jimenez, J. L., Krechmer, J., Roberts, J. M., Warneke, C., Yokelson, R. J., and Gouw, J. de: Non-methane organic gas emissions from biomass burning: identification, quantification, and emission factors from PTR-ToF during the FIREX 2016 laboratory experiment, Atmospheric Chemistry and Physics, 18, 3299–3319, https://doi.org/10.5194/acp-18-3299-2018, 2018.

Kumar, V., Chandra, B. P., and Sinha, V.: Large unexplained suite of chemically reactive compounds present in ambient air due to biomass fires, Sci Rep, 8, 626, https://doi.org/10.1038/s41598-017-19139-3, 2018.

Kwan, A. J., Crounse, J. D., Clarke, A. D., Shinozuka, Y., Anderson, B. E., Crawford, J. H., Avery, M. A., McNaughton, C. S., Brune, W. H., Singh, H. B., and Wennberg, P. O.: On the flux of oxygenated volatile organic compounds from organic aerosol oxidation, Geophysical Research Letters, 33, https://doi.org/10.1029/2006GL026144, 2006.

Kwon, H.-A., Park, R. J., Oak, Y. J., Nowlan, C. R., Janz, S. J., Kowalewski, M. G., Fried, A., Walega, J., Bates, K. H., Choi, J., Blake, D. R., Wisthaler, A., and Woo, J.-H.: Top-down estimates of anthropogenic VOC emissions in South Korea using formaldehyde vertical column densities from aircraft during the KORUS-AQ campaign, Elementa: Science of the Anthropocene, 9, 00109, https://doi.org/10.1525/elementa.2021.00109, 2021.

Lack, D. A., Cappa, C. D., Covert, D. S., Baynard, T., Massoli, P., Sierau, B., Bates, T. S., Quinn, P. K., Lovejoy, E. R., and Ravishankara, A. R.: Bias in Filter-Based Aerosol Light Absorption Measurements Due to Organic Aerosol

Loading: Evidence from Ambient Measurements, Aerosol Science and Technology, 42, 1033–1041, https://doi.org/10.1080/02786820802389277, 2008.

Lack, D. A., Langridge, J. M., Bahreini, R., Cappa, C. D., Middlebrook, A. M., and Schwarz, J. P.: Brown carbon and internal mixing in biomass burning particles, PNAS, 109, 14802–14807, https://doi.org/10.1073/pnas.1206575109, 2012.

Lapina, K., Heald, C. L., Spracklen, D. V., Arnold, S. R., Allan, J. D., Coe, H., McFiggans, G., Zorn, S. R., Drewnick, F., Bates, T. S., Hawkins, L. N., Russell, L. M., Smirnov, A., O'Dowd, C. D., and Hind, A. J.: Investigating organic aerosol loading in the remote marine environment, Atmospheric Chemistry and Physics, 11, 8847–8860, https://doi.org/10.5194/acp-11-8847-2011, 2011.

Laskin, A., Laskin, J., and Nizkorodov, S. A.: Chemistry of Atmospheric Brown Carbon, Chem. Rev., 115, 4335–4382, https://doi.org/10.1021/cr5006167, 2015.

Lee, Y. and Lee, B.: Tradeoff between the number of firefighting resources and the level of fire ignition prevention efforts in the Republic of Korea, J. Mt. Sci., 15, 144–155, https://doi.org/10.1007/s11629-016-4264-0, 2018.

Lelieveld, J., Gromov, S., Pozzer, A., and Taraborrelli, D.: Global tropospheric hydroxyl distribution, budget and reactivity, Atmospheric Chemistry and Physics, 16, 12477–12493, https://doi.org/10.5194/acp-16-12477-2016, 2016.

Levin, E. J. T., McMeeking, G. R., Carrico, C. M., Mack, L. E., Kreidenweis, S. M., Wold, C. E., Moosmüller, H., Arnott, W. P., Hao, W. M., Collett, J. L., and Malm, W. C.: Biomass burning smoke aerosol properties measured during Fire Laboratory at Missoula Experiments (FLAME), Journal of Geophysical Research: Atmospheres, 115, https://doi.org/10.1029/2009JD013601, 2010.

Levy, R. C., Remer, L. A., Mattoo, S., Vermote, E. F., and Kaufman, Y. J.: Second-generation operational algorithm: Retrieval of aerosol properties over land from inversion of Moderate Resolution Imaging Spectroradiometer spectral reflectance, Journal of Geophysical Research: Atmospheres, 112, https://doi.org/10.1029/2006JD007811, 2007.

Levy, R. C., Remer, L. A., Kleidman, R. G., Mattoo, S., Ichoku, C., Kahn, R., and Eck, T. F.: Global evaluation of the Collection 5 MODIS dark-target aerosol products over land, Atmos. Chem. Phys., 10, 10399–10420, https://doi.org/10.5194/acp-10-10399-2010, 2010.

Levy, R. C., Mattoo, S., Munchak, L. A., Remer, L. A., Sayer, A. M., Patadia, F., and Hsu, N. C.: The Collection 6 MODIS aerosol products over land and ocean, Atmos. Meas. Tech., 6, 2989–3034, https://doi.org/10.5194/amt-6-2989-2013, 2013.

Lim, C. Y., Hagan, D. H., Coggon, M. M., Koss, A. R., Sekimoto, K., Gouw, J. de, Warneke, C., Cappa, C. D., and Kroll, J. H.: Secondary organic aerosol formation from the laboratory oxidation of biomass burning emissions, Atmospheric Chemistry and Physics, 19, 12797–12809, https://doi.org/10.5194/acp-19-12797-2019, 2019.

Lin, G., Penner, J. E., Flanner, M. G., Sillman, S., Xu, L., and Zhou, C.: Radiative forcing of organic aerosol in the atmosphere and on snow: Effects of SOA and brown carbon, Journal of Geophysical Research: Atmospheres, 119, 7453–7476, https://doi.org/10.1002/2013JD021186, 2014.

Liu, D., He, C., Schwarz, J. P., and Wang, X.: Lifecycle of light-absorbing carbonaceous aerosols in the atmosphere, npj Climate and Atmospheric Science, 3, 1–18, https://doi.org/10.1038/s41612-020-00145-8, 2020.

Liu, J., Fan, S., Horowitz, L. W., and Levy, H.: Evaluation of factors controlling long-range transport of black carbon to the Arctic, Journal of Geophysical Research: Atmospheres, 116, https://doi.org/10.1029/2010JD015145, 2011.

Liu, J. C., Pereira, G., Uhl, S. A., Bravo, M. A., and Bell, M. L.: A systematic review of the physical health impacts from non-occupational exposure to wildfire smoke, Environmental Research, 136, 120–132, https://doi.org/10.1016/j.envres.2014.10.015, 2015a.

Liu, X., Zhang, Y., Huey, L. G., Yokelson, R. J., Wang, Y., Jimenez, J. L., Campuzano-Jost, P., Beyersdorf, A. J., Blake, D. R., Choi, Y., St. Clair, J. M., Crounse, J. D., Day, D. A., Diskin, G. S., Fried, A., Hall, S. R., Hanisco, T. F., King, L. E., Meinardi, S., Mikoviny, T., Palm, B. B., Peischl, J., Perring, A. E., Pollack, I. B., Ryerson, T. B., Sachse, G., Schwarz, J. P., Simpson, I. J., Tanner, D. J., Thornhill, K. L., Ullmann, K., Weber, R. J., Wennberg, P. O., Wisthaler, A., Wolfe, G. M., and Ziemba, L. D.: Agricultural fires in the southeastern U.S. during SEAC4RS: Emissions of trace gases and particles and evolution of ozone, reactive nitrogen, and organic aerosol, Journal of Geophysical Research: Atmospheres, 7383–7414, https://doi.org/10.1002/2016JD025040@10.1002/(ISSN)2169-8996.SEAFOURC1, 2015b.

Liu, X., Huey, L. G., Yokelson, R. J., Selimovic, V., Simpson, I. J., Müller, M., Jimenez, J. L., Campuzano-Jost, P., Beyersdorf, A. J., Blake, D. R., Butterfield, Z., Choi, Y., Crounse, J. D., Day, D. A., Diskin, G. S., Dubey, M. K., Fortner, E., Hanisco, T. F., Hu, W., King, L. E., Kleinman, L., Meinardi, S., Mikoviny, T., Onasch, T. B., Palm, B. B., Peischl, J., Pollack, I. B., Ryerson, T. B., Sachse, G. W., Sedlacek, A. J., Shilling, J. E., Springston, S., Clair, J. M. S., Tanner, D. J., Teng, A. P., Wennberg, P. O., Wisthaler, A., and Wolfe, G. M.: Airborne measurements of western U.S. wildfire emissions: Comparison with prescribed burning and air quality implications, Journal of Geophysical Research: Atmospheres, 122, 6108–6129, https://doi.org/10.1002/2016JD026315, 2017.

Lobert, J. M., Scharffe, D. H., Hao, W. M., and Crutzen, P. J.: Importance of biomass burning in the atmospheric budgets of nitrogen-containing gases, Nature, 346, 552–554, https://doi.org/10.1038/346552a0, 1990.

Lu, Z., Streets, D. G., Winijkul, E., Yan, F., Chen, Y., Bond, T. C., Feng, Y., Dubey, M. K., Liu, S., Pinto, J. P., and Carmichael, G. R.: Light Absorption Properties and Radiative Effects of Primary Organic Aerosol Emissions, Environ. Sci. Technol., 49, 4868–4877, https://doi.org/10.1021/acs.est.5b00211, 2015.

Luo, G., Yu, F., and Schwab, J.: Revised treatment of wet scavenging processes dramatically improves GEOS-Chem 12.0.0 simulations of surface nitric acid, nitrate, and ammonium over the United States, Geoscientific Model Development, 12, 3439–3447, https://doi.org/10.5194/gmd-12-3439-2019, 2019.

Malm, W. C. and Hand, J. L.: An examination of the physical and optical properties of aerosols collected in the IMPROVE program, Atmospheric Environment, 41, 3407–3427, https://doi.org/10.1016/j.atmosenv.2006.12.012, 2007.

Mao, J., Ren, X., Brune, W. H., Olson, J. R., Crawford, J. H., Fried, A., Huey, L. G., Cohen, R. C., Heikes, B., Singh, H. B., Blake, D. R., Sachse, G. W., Diskin, G. S., Hall, S. R., and Shetter, R. E.: Airborne measurement of OH reactivity during INTEX-B, Atmos. Chem. Phys., 11, 2009.

Mao, J., Paulot, F., Jacob, D. J., Cohen, R. C., Crounse, J. D., Wennberg, P. O., Keller, C. A., Hudman, R. C., Barkley, M. P., and Horowitz, L. W.: Ozone and organic nitrates over the eastern United States: Sensitivity to isoprene chemistry, Journal of Geophysical Research: Atmospheres, 118, 11,256-11,268, https://doi.org/10.1002/jgrd.50817, 2013.

Marais, E. A. and Wiedinmyer, C.: Air Quality Impact of Diffuse and Inefficient Combustion Emissions in Africa (DICE-Africa), Environ. Sci. Technol., 50, 10739–10745, https://doi.org/10.1021/acs.est.6b02602, 2016.

Marais, E. A., Jacob, D. J., Jimenez, J. L., Campuzano-Jost, P., Day, D. A., Hu, W., Krechmer, J., Zhu, L., Kim, P. S., Miller, C. C., Fisher, J. A., Travis, K., Yu, K., Hanisco, T. F., Wolfe, G. M., Arkinson, H. L., Pye, H. O. T., Froyd, K. D., Liao, J., and McNeill, V. F.: Aqueous-phase mechanism for secondary organic aerosol formation from isoprene: application to the southeast United States and co-benefit of SO $_2$ emission controls, Atmos. Chem. Phys., 16, 1603–1618, https://doi.org/10.5194/acp-16-1603-2016, 2016.

Marlon, J. R., Bartlein, P. J., Carcaillet, C., Gavin, D. G., Harrison, S. P., Higuera, P. E., Joos, F., Power, M. J., and Prentice, I. C.: Climate and human influences on global biomass burning over the past two millennia, Nature Geosci, 1, 697–702, https://doi.org/10.1038/ngeo313, 2008.

Marlon, J. R., Bartlein, P. J., Gavin, D. G., Long, C. J., Anderson, R. S., Briles, C. E., Brown, K. J., Colombaroli, D., Hallett, D. J., Power, M. J., Scharf, E. A., and Walsh, M. K.: Long-term perspective on wildfires in the western USA, Proceedings of the National Academy of Sciences, 109, E535–E543, https://doi.org/10.1073/pnas.1112839109, 2012.

Martin, R. V., Jacob, D. J., Yantosca, R. M., Chin, M., and Ginoux, P.: Global and regional decreases in tropospheric oxidants from photochemical effects of aerosols, Journal of Geophysical Research: Atmospheres, 108, https://doi.org/10.1029/2002JD002622, 2003.

May, A. A., McMeeking, G. R., Lee, T., Taylor, J. W., Craven, J. S., Burling, I., Sullivan, A. P., Akagi, S., Collett, J. L., Flynn, M., Coe, H., Urbanski, S. P., Seinfeld, J. H., Yokelson, R. J., and Kreidenweis, S. M.: Aerosol emissions from prescribed fires in the United States: A synthesis of laboratory and aircraft measurements, Journal of Geophysical Research: Atmospheres, 119, 11,826-11,849, https://doi.org/10.1002/2014JD021848, 2014.

May, A. A., Lee, T., McMeeking, G. R., Akagi, S., Sullivan, A. P., Urbanski, S., Yokelson, R. J., and Kreidenweis, S. M.: Observations and analysis of organic aerosol evolution in some prescribed fire smoke plumes, Atmos. Chem. Phys. Discuss., 15, 1953–1988, https://doi.org/10.5194/acpd-15-1953-2015, 2015.

McClure, C. D. and Jaffe, D. A.: US particulate matter air quality improves except in wildfire-prone areas, Proc. Natl. Acad. Sci. U.S.A., 115, 7901–7906, https://doi.org/10.1073/pnas.1804353115, 2018.

McClure, C. D., Lim, C. Y., Hagan, D. H., Kroll, J. H., and Cappa, C. D.: Biomass-burning-derived particles from a wide variety of fuels – Part 1: Properties of primary particles, Atmospheric Chemistry and Physics, 20, 1531–1547, https://doi.org/10.5194/acp-20-1531-2020, 2020.

McDuffie, E. E., Smith, S. J., O'Rourke, P., Tibrewal, K., Venkataraman, C., Marais, E. A., Zheng, B., Crippa, M., Brauer, M., and Martin, R. V.: A global anthropogenic emission inventory of atmospheric pollutants from sector- and fuel-specific sources (1970–2017): an application of the Community Emissions Data System (CEDS), Earth System Science Data, 12, 3413–3442, https://doi.org/10.5194/essd-12-3413-2020, 2020.

McMeeking, G. R., Kreidenweis, S. M., Baker, S., Carrico, C. M., Chow, J. C., Collett, J. L., Hao, W. M., Holden, A. S., Kirchstetter, T. W., Malm, W. C., Moosmüller, H., Sullivan, A. P., and Wold, C. E.: Emissions of trace gases and aerosols during the open combustion of biomass in the laboratory, Journal of Geophysical Research: Atmospheres, 114, https://doi.org/10.1029/2009JD011836, 2009.

McMeeking, G. R., Fortner, E., Onasch, T. B., Taylor, J. W., Flynn, M., Coe, H., and Kreidenweis, S. M.: Impacts of nonrefractory material on light absorption by aerosols emitted from biomass burning, Journal of Geophysical Research: Atmospheres, 119, 12,272-12,286, https://doi.org/10.1002/2014JD021750, 2014.

Moffet, R. C. and Prather, K. A.: In-situ measurements of the mixing state and optical properties of soot with implications for radiative forcing estimates, PNAS, 106, 11872–11877, https://doi.org/10.1073/pnas.0900040106, 2009.

Mohr, C., Lopez-Hilfiker, F. D., Zotter, P., Prévôt, A. S. H., Xu, L., Ng, N. L., Herndon, S. C., Williams, L. R., Franklin, J. P., Zahniser, M. S., Worsnop, D. R., Knighton, W. B., Aiken, A. C., Gorkowski, K. J., Dubey, M. K., Allan, J. D., and Thornton, J. A.: Contribution of Nitrated Phenols to Wood Burning Brown Carbon Light Absorption in Detling, United Kingdom during Winter Time, Environ. Sci. Technol., 47, 6316–6324, https://doi.org/10.1021/es400683v, 2013.

Müller, M., Mikoviny, T., Feil, S., Haidacher, S., Hanel, G., Hartungen, E., Jordan, A., Märk, L., Mutschlechner, P., Schottkowsky, R., Sulzer, P., Crawford, J. H., and Wisthaler, A.: A compact PTR-ToF-MS instrument for airborne measurements of volatile organic compounds at high spatiotemporal resolution, Atmospheric Measurement Techniques, 7, 3763–3772, https://doi.org/10.5194/amt-7-3763-2014, 2014.

Nowell, H. K., Holmes, C. D., Robertson, K., Teske, C., and Hiers, J. K.: A New Picture of Fire Extent, Variability, and Drought Interaction in Prescribed Fire Landscapes: Insights From Florida Government Records, Geophysical Research Letters, 45, 7874–7884, https://doi.org/10.1029/2018GL078679, 2018.

O'Dell, K., Ford, B., Fischer, E. V., and Pierce, J. R.: Contribution of Wildland-Fire Smoke to US PM2.5 and Its Influence on Recent Trends, Environ. Sci. Technol., 53, 1797–1804, https://doi.org/10.1021/acs.est.8b05430, 2019.

O'Dell, K., Hornbrook, R. S., Permar, W., Levin, E. J. T., Garofalo, L. A., Apel, E. C., Blake, N. J., Jarnot, A., Pothier, M. A., Farmer, D. K., Hu, L., Campos, T., Ford, B., Pierce, J. R., and Fischer, E. V.: Hazardous Air Pollutants in Fresh and Aged Western US Wildfire Smoke and Implications for Long-Term Exposure, Environ. Sci. Technol., 54, 11838–11847, https://doi.org/10.1021/acs.est.0c04497, 2020.

Ogren, J. A., Wendell, J., Andrews, E., and Sheridan, P. J.: Continuous light absorption photometer for long-term studies, Atmos. Meas. Tech., 10, 4805–4818, https://doi.org/10.5194/amt-10-4805-2017, 2017.

Oliveira, S., Rocha, J., and Sá, A.: Wildfire risk modeling, Current Opinion in Environmental Science & Health, 23, 100274, https://doi.org/10.1016/j.coesh.2021.100274, 2021.

OMI Team: Ozone Monitoring Instrument (OMI) Data User's Guide, 2012.

Ortega, A. M., Day, D. A., Cubison, M. J., Brune, W. H., Bon, D., de Gouw, J. A., and Jimenez, J. L.: Secondary organic aerosol formation and primary organic aerosol oxidation from biomass-burning smoke in a flow reactor during FLAME-3, Atmospheric Chemistry and Physics, 13, 11551–11571, https://doi.org/10.5194/acp-13-11551-2013, 2013.

Pai, S. J., Heald, C. L., Pierce, J. R., Farina, S. C., Marais, E. A., Jimenez, J. L., Campuzano-Jost, P., Nault, B. A., Middlebrook, A. M., Coe, H., Shilling, J. E., Bahreini, R., Dingle, J. H., and Vu, K.: An evaluation of global organic aerosol schemes using airborne observations, Atmospheric Chemistry and Physics, 20, 2637–2665, https://doi.org/10.5194/acp-20-2637-2020, 2020.

Pai, S. J., Carter, T. S., Heald, C. L., and Kroll, J. H.: Updated World Health Organization Air Quality Guidelines Highlight the Importance of Non-anthropogenic PM2.5, Environ. Sci. Technol. Lett., 9, 501–506, https://doi.org/10.1021/acs.estlett.2c00203, 2022.

Palm, B. B., Peng, Q., Fredrickson, C. D., Lee, B. H., Garofalo, L. A., Pothier, M. A., Kreidenweis, S. M., Farmer, D. K., Pokhrel, R. P., Shen, Y., Murphy, S. M., Permar, W., Hu, L., Campos, T. L., Hall, S. R., Ullmann, K., Zhang, X., Flocke, F., Fischer, E. V., and Thornton, J. A.: Quantification of organic aerosol and brown carbon evolution in fresh wildfire plumes, Proc Natl Acad Sci USA, 202012218, https://doi.org/10.1073/pnas.2012218117, 2020.

Park, R. J., Jacob, D. J., Chin, M., and Martin, R. V.: Sources of carbonaceous aerosols over the United States and implications for natural visibility, Journal of Geophysical Research: Atmospheres, 108, https://doi.org/10.1029/2002JD003190, 2003.

Park, R. J., Jacob, D. J., Field, B. D., Yantosca, R. M., and Chin, M.: Natural and transboundary pollution influences on sulfate-nitrate-ammonium aerosols in the United States: Implications for policy, Journal of Geophysical Research: Atmospheres, 109, https://doi.org/10.1029/2003JD004473, 2004.

Park, R. J., Kim, M. J., Jeong, J. I., Youn, D., and Kim, S.: A contribution of brown carbon aerosol to the aerosol light absorption and its radiative forcing in East Asia, Atmospheric Environment, 44, 1414–1421, https://doi.org/10.1016/j.atmosenv.2010.01.042, 2010.

Perring, A. E., Schwarz, J. P., Markovic, M. Z., Fahey, D. W., Jimenez, J. L., Campuzano-Jost, P., Palm, B. D., Wisthaler, A., Mikoviny, T., Diskin, G., Sachse, G., Ziemba, L., Anderson, B., Shingler, T., Crosbie, E., Sorooshian, A., Yokelson, R., and Gao, R.-S.: In situ measurements of water uptake by black carbon-containing aerosol in wildfire

plumes, Journal of Geophysical Research: Atmospheres, 122, 1086–1097, https://doi.org/10.1002/2016JD025688, 2017.

Petrenko, M., Kahn, R., Chin, M., Soja, A., Kucsera, T., and Harshvardhan: The use of satellite-measured aerosol optical depth to constrain biomass burning emissions source strength in the global model GOCART, Journal of Geophysical Research: Atmospheres, 117, https://doi.org/10.1029/2012JD017870, 2012.

Pfannerstill, E. Y., Reijrink, N. G., Edtbauer, A., Ringsdorf, A., Zannoni, N., Araújo, A., Ditas, F., Holanda, B. A., Sá, M. O., Tsokankunku, A., Walter, D., Wolff, S., Lavrič, J. V., Pöhlker, C., Sörgel, M., and Williams, J.: Total OH reactivity over the Amazon rainforest: variability with temperature, wind, rain, altitude, time of day, season, and an overall budget closure, Atmospheric Chemistry and Physics, 21, 6231–6256, https://doi.org/10.5194/acp-21-6231-2021, 2021.

Pfister, G. G., Avise, J., Wiedinmyer, C., Edwards, D. P., Emmons, L. K., Diskin, G. D., Podolske, J., and Wisthaler, A.: CO source contribution analysis for California during ARCTAS-CARB, Atmos. Chem. Phys., 11, 7515–7532, https://doi.org/10.5194/acp-11-7515-2011, 2011.

Pham, B. T., Jaafari, A., Avand, M., Al-Ansari, N., Dinh Du, T., Yen, H. P. H., Phong, T. V., Nguyen, D. H., Le, H. V., Mafi-Gholami, D., Prakash, I., Thi Thuy, H., and Tuyen, T. T.: Performance Evaluation of Machine Learning Methods for Forest Fire Modeling and Prediction, Symmetry, 12, 1022, https://doi.org/10.3390/sym12061022, 2020.

Philip, S., Martin, R. V., and Keller, C. A.: Sensitivity of chemistry-transport model simulations to the duration of chemical and transport operators: a case study with GEOS-Chem v10-01, Geoscientific Model Development, 9, 1683–1695, https://doi.org/10.5194/gmd-9-1683-2016, 2016.

Pistone, K., Redemann, J., Doherty, S., Zuidema, P., Burton, S., Cairns, B., Cochrane, S., Ferrare, R., Flynn, C., Freitag, S., Howell, S. G., Kacenelenbogen, M., LeBlanc, S., Liu, X., Schmidt, K. S., Sedlacek III, A. J., Segal-Rozenhaimer, M., Shinozuka, Y., Stamnes, S., van Diedenhoven, B., Van Harten, G., and Xu, F.: Intercomparison of biomass burning aerosol optical properties from in situ and remote-sensing instruments in ORACLES-2016, Atmospheric Chemistry and Physics, 19, 9181–9208, https://doi.org/10.5194/acp-19-9181-2019, 2019.

Pokhrel, R. P., Beamesderfer, E. R., Wagner, N. L., Langridge, J. M., Lack, D. A., Jayarathne, T., Stone, E. A., Stockwell, C. E., Yokelson, R. J., and Murphy, S. M.: Relative importance of black carbon, brown carbon, and absorption enhancement from clear coatings in biomass burning emissions, Atmos. Chem. Phys., 17, 5063–5078, https://doi.org/10.5194/acp-17-5063-2017, 2017.

Pollack, I. B., Lindaas, J., Roscioli, J. R., Agnese, M., Permar, W., Hu, L., and Fischer, E. V.: Evaluation of ambient ammonia measurements from a research aircraft using a closed-path QC-TILDAS operated with active continuous passivation, Atmos. Meas. Tech., 26, 2019.

Pope, C. A. and Dockery, D. W.: Health Effects of Fine Particulate Air Pollution: Lines that Connect, Journal of the Air & Waste Management Association, 56, 709–742, https://doi.org/10.1080/10473289.2006.10464485, 2006.

Rabin, S. S., Melton, J. R., Lasslop, G., Bachelet, D., Forrest, M., Hantson, S., Kaplan, J. O., Li, F., Mangeon, S., Ward, D. S., Yue, C., Arora, V. K., Hickler, T., Kloster, S., Knorr, W., Nieradzik, L., Spessa, A., Folberth, G. A., Sheehan, T., Voulgarakis, A., Kelley, D. I., Prentice, I. C., Sitch, S., Harrison, S., and Arneth, A.: The Fire Modeling Intercomparison Project (FireMIP), phase 1: experimental and analytical protocols with detailed model descriptions, Geoscientific Model Development, 10, 1175–1197, https://doi.org/10.5194/gmd-10-1175-2017, 2017.

Rabin, S. S., Gérard, F. N., and Arneth, A.: The influence of thinning and prescribed burning on future forest fires in fire-prone regions of Europe, Environ. Res. Lett., 17, 055010, https://doi.org/10.1088/1748-9326/ac6312, 2022.

Radeloff, V. C., Helmers, D. P., Kramer, H. A., Mockrin, M. H., Alexandre, P. M., Bar-Massada, A., Butsic, V., Hawbaker, T. J., Martinuzzi, S., Syphard, A. D., and Stewart, S. I.: Rapid growth of the US wildland-urban interface

raises wildfire risk, Proceedings of the National Academy of Sciences, 115, 3314–3319, https://doi.org/10.1073/pnas.1718850115, 2018.

Ramo, R., Roteta, E., Bistinas, I., Wees, D. van, Bastarrika, A., Chuvieco, E., and Werf, G. R. van der: African burned area and fire carbon emissions are strongly impacted by small fires undetected by coarse resolution satellite data, PNAS, 118, https://doi.org/10.1073/pnas.2011160118, 2021.

Randerson, J. T., Chen, Y., Werf, G. R. van der, Rogers, B. M., and Morton, D. C.: Global burned area and biomass burning emissions from small fires, Journal of Geophysical Research: Biogeosciences, 117, https://doi.org/10.1029/2012JG002128, 2012.

Rap, A., Scott, C. E., Spracklen, D. V., Bellouin, N., Forster, P. M., Carslaw, K. S., Schmidt, A., and Mann, G.: Natural aerosol direct and indirect radiative effects, Geophysical Research Letters, 40, 3297–3301, https://doi.org/10.1002/grl.50441, 2013.

Rastigejev, Y., Park, R., Brenner, M. P., and Jacob, D. J.: Resolving intercontinental pollution plumes in global models of atmospheric transport, Journal of Geophysical Research: Atmospheres, 115, https://doi.org/10.1029/2009JD012568, 2010.

Reddington, C. L., Spracklen, D. V., Artaxo, P., Ridley, D. A., Rizzo, L. V., and Arana, A.: Analysis of particulate emissions from tropical biomass burning using a global aerosol model and long-term surface observations, Atmospheric Chemistry and Physics, 16, 11083–11106, 2016.

Reddington, C. L., Morgan, W. T., Darbyshire, E., Brito, J., Coe, H., Artaxo, P., Scott, C. E., Marsham, J., and Spracklen, D. V.: Biomass burning aerosol over the Amazon: analysis of aircraft, surface and satellite observations using a global aerosol model, Atmos. Chem. Phys., 19, 9125–9152, https://doi.org/10.5194/acp-19-9125-2019, 2019.

Reid Colleen E., Brauer Michael, Johnston Fay H., Jerrett Michael, Balmes John R., and Elliott Catherine T.: Critical Review of Health Impacts of Wildfire Smoke Exposure, Environmental Health Perspectives, 124, 1334–1343, https://doi.org/10.1289/ehp.1409277, 2016.

Remer, L. A., Kaufman, Y. J., Tanré, D., Mattoo, S., Chu, D. A., Martins, J. V., Li, R.-R., Ichoku, C., Levy, R. C., Kleidman, R. G., Eck, T. F., Vermote, E., and Holben, B. N.: The MODIS Aerosol Algorithm, Products, and Validation, J. Atmos. Sci., 62, 947–973, https://doi.org/10.1175/JAS3385.1, 2005.

Ridley, D. A., Heald, C. L., and Ford, B.: North African dust export and deposition: A satellite and model perspective, Journal of Geophysical Research: Atmospheres, 117, https://doi.org/10.1029/2011JD016794, 2012.

Robinson, A. L., Donahue, N. M., Shrivastava, M. K., Weitkamp, E. A., Sage, A. M., Grieshop, A. P., Lane, T. E., Pierce, J. R., and Pandis, S. N.: Rethinking Organic Aerosols: Semivolatile Emissions and Photochemical Aging, Science, 315, 1259–1262, https://doi.org/10.1126/science.1133061, 2007.

Safieddine, S. A., Heald, C. L., and Henderson, B. H.: The global nonmethane reactive organic carbon budget: A modeling perspective, Geophys. Res. Lett., 44, 3897–3906, https://doi.org/10.1002/2017GL072602, 2017.

Saide, P. E., Spak, S. N., Pierce, R. B., Otkin, J. A., Schaack, T. K., Heidinger, A. K., da Silva, A. M., Kacenelenbogen, M., Redemann, J., and Carmichael, G. R.: Central American biomass burning smoke can increase tornado severity in the U.S., Geophysical Research Letters, 956–965, https://doi.org/10.1002/2014GL062826@10.1002/(ISSN)1944-8007.2015EdHighlights, 2016.

Saleh, R., Robinson, E. S., Tkacik, D. S., Ahern, A. T., Liu, S., Aiken, A. C., Sullivan, R. C., Presto, A. A., Dubey, M. K., Yokelson, R. J., Donahue, N. M., and Robinson, A. L.: Brownness of organics in aerosols from biomass burning linked to their black carbon content, Nature Geosci, 7, 647–650, https://doi.org/10.1038/ngeo2220, 2014.

Sarangi, C., Qian, Y., Leung, R., Zhang, Y., Zou, Y., and Wang, Y.: Projected increases in wildfires may challenge regulatory curtailment of $PM_{2.5}$ over the eastern US by 2050, Atmospheric Chemistry and Physics Discussions, 1–30, https://doi.org/10.5194/acp-2022-324, 2022.

Sayer, A. M., Munchak, L. A., Hsu, N. C., Levy, R. C., Bettenhausen, C., and Jeong, M.-J.: MODIS Collection 6 aerosol products: Comparison between Aqua's e-Deep Blue, Dark Target, and "merged" data sets, and usage recommendations, Journal of Geophysical Research: Atmospheres, 119, 13,965-13,989, https://doi.org/10.1002/2014JD022453, 2014.

Schwarz, J. P., Spackman, J. R., Fahey, D. W., Gao, R. S., Lohmann, U., Stier, P., Watts, L. A., Thomson, D. S., Lack, D. A., Pfister, L., Mahoney, M. J., Baumgardner, D., Wilson, J. C., and Reeves, J. M.: Coatings and their enhancement of black carbon light absorption in the tropical atmosphere, Journal of Geophysical Research: Atmospheres, 113, https://doi.org/10.1029/2007JD009042, 2008a.

Schwarz, J. P., Gao, R. S., Spackman, J. R., Watts, L. A., Thomson, D. S., Fahey, D. W., Ryerson, T. B., Peischl, J., Holloway, J. S., Trainer, M., Frost, G. J., Baynard, T., Lack, D. A., Gouw, J. A. de, Warneke, C., and Negro, L. A. D.: Measurement of the mixing state, mass, and optical size of individual black carbon particles in urban and biomass burning emissions, Geophysical Research Letters, 35, https://doi.org/10.1029/2008GL033968, 2008b.

Schwarz, J. P., Samset, B. H., Perring, A. E., Spackman, J. R., Gao, R. S., Stier, P., Schulz, M., Moore, F. L., Ray, E. A., and Fahey, D. W.: Global-scale seasonally resolved black carbon vertical profiles over the Pacific, Geophysical Research Letters, 40, 5542–5547, https://doi.org/10.1002/2013GL057775, 2013.

Sekimoto, K., Koss, A. R., Gilman, J. B., Selimovic, V., Coggon, M. M., Zarzana, K. J., Yuan, B., Lerner, B. M., Brown, S. S., Warneke, C., Yokelson, R. J., Roberts, J. M., and de Gouw, J.: High- and low-temperature pyrolysis profiles describe volatile organic compound emissions from western US wildfire fuels, Atmos. Chem. Phys., 18, 9263–9281, https://doi.org/10.5194/acp-18-9263-2018, 2018.

Selimovic, V., Yokelson, R. J., Warneke, C., Roberts, J. M., Gouw, J. de, Reardon, J., and Griffith, D. W. T.: Aerosol optical properties and trace gas emissions by PAX and OP-FTIR for laboratory-simulated western US wildfires during FIREX, Atmospheric Chemistry and Physics, 18, 2929–2948, https://doi.org/10.5194/acp-18-2929-2018, 2018.

Senande-Rivera, M., Insua-Costa, D., and Miguez-Macho, G.: Spatial and temporal expansion of global wildland fire activity in response to climate change, Nat Commun, 13, 1208, https://doi.org/10.1038/s41467-022-28835-2, 2022.

Sherwen, T., Schmidt, J. A., Evans, M. J., Carpenter, L. J., Großmann, K., Eastham, S. D., Jacob, D. J., Dix, B., Koenig, T. K., Sinreich, R., Ortega, I., Volkamer, R., Saiz-Lopez, A., Prados-Roman, C., Mahajan, A. S., and Ordóñez, C.: Global impacts of tropospheric halogens (Cl, Br, I) on oxidants and composition in GEOS-Chem, Atmospheric Chemistry and Physics, 16, 12239–12271, https://doi.org/10.5194/acp-16-12239-2016, 2016.

Shinozuka, Y., Saide, P. E., Ferrada, G. A., Burton, S. P., Ferrare, R., Doherty, S. J., Gordon, H., Longo, K., Mallet, M., Feng, Y., Wang, Q., Cheng, Y., Dobracki, A., Freitag, S., Howell, S. G., LeBlanc, S., Flynn, C., Segal-Rosenhaimer, M., Pistone, K., Podolske, J. R., Stith, E. J., Bennett, J. R., Carmichael, G. R., Silva, A. da, Govindaraju, R., Leung, R., Zhang, Y., Pfister, L., Ryoo, J.-M., Redemann, J., Wood, R., and Zuidema, P.: Modeling the smoky troposphere of the southeast Atlantic: a comparison to ORACLES airborne observations from September of 2016, Atmospheric Chemistry and Physics Discussions, 1–77, https://doi.org/10.5194/acp-2019-678, 2019.

Shinozuka, Y., Saide, P. E., Ferrada, G. A., Burton, S. P., Ferrare, R., Doherty, S. J., Gordon, H., Longo, K., Mallet, M., Feng, Y., Wang, Q., Cheng, Y., Dobracki, A., Freitag, S., Howell, S. G., LeBlanc, S., Flynn, C., Segal-Rosenhaimer, M., Pistone, K., Podolske, J. R., Stith, E. J., Bennett, J. R., Carmichael, G. R., da Silva, A., Govindaraju, R., Leung, R., Zhang, Y., Pfister, L., Ryoo, J.-M., Redemann, J., Wood, R., and Zuidema, P.: Modeling the smoky troposphere of the southeast Atlantic: a comparison to ORACLES airborne observations from September of 2016, Atmospheric Chemistry and Physics, 20, 11491–11526, https://doi.org/10.5194/acp-20-11491-2020, 2020.

Short, K. C.: Spatial wildfire occurrence data for the United States, 1992-2018 [FPA_FOD_20210617] (5th Edition), https://doi.org/10.2737/RDS-2013-0009.5, 2021.

Shrivastava, M., Cappa, C. D., Fan, J., Goldstein, A. H., Guenther, A. B., Jimenez, J. L., Kuang, C., Laskin, A., Martin, S. T., Ng, N. L., Petaja, T., Pierce, J. R., Rasch, P. J., Roldin, P., Seinfeld, J. H., Shilling, J., Smith, J. N., Thornton, J. A., Volkamer, R., Wang, J., Worsnop, D. R., Zaveri, R. A., Zelenyuk, A., and Zhang, Q.: Recent advances in understanding secondary organic aerosol: Implications for global climate forcing, Reviews of Geophysics, 55, 509–559, https://doi.org/10.1002/2016RG000540, 2017.

Simone, N. W., Stettler, M. E. J., and Barrett, S. R. H.: Rapid estimation of global civil aviation emissions with uncertainty quantification, Transportation Research Part D: Transport and Environment, 25, 33–41, https://doi.org/10.1016/j.trd.2013.07.001, 2013.

Simpson, I. J., Akagi, S. K., Barletta, B., Blake, N. J., Choi, Y., Diskin, G. S., Fried, A., Fuelberg, H. E., Meinardi, S., Rowland, F. S., Vay, S. A., Weinheimer, A. J., Wennberg, P. O., Wiebring, P., Wisthaler, A., Yang, M., Yokelson, R. J., and Blake, D. R.: Boreal forest fire emissions in fresh Canadian smoke plumes: C₁-C₁₀ volatile organic compounds (VOCs), CO₂, CO, NO₂, NO, HCN and CH₃CN, Atmos. Chem. Phys., 11, 6445–6463, https://doi.org/10.5194/acp-11-6445-2011, 2011.

Sinha, V., Williams, J., Crowley, J. N., and Lelieveld, J.: The Comparative Reactivity Method – a new tool to measure total OH Reactivity in ambient air, Atmospheric Chemistry and Physics, 8, 2213–2227, https://doi.org/10.5194/acp-8-2213-2008, 2008.

Stettler, M. E. J., Eastham, S., and Barrett, S. R. H.: Air quality and public health impacts of UK airports. Part I: Emissions, Atmospheric Environment, 45, 5415–5424, https://doi.org/10.1016/j.atmosenv.2011.07.012, 2011.

Stockwell, C. E., Bela, M. M., Coggon, M. M., Gkatzelis, G. I., Wiggins, E., Gargulinski, E. M., Shingler, T., Fenn, M., Griffin, D., Holmes, C. D., Ye, X., Saide, P. E., Bourgeois, I., Peischl, J., Womack, C. C., Washenfelder, R. A., Veres, P. R., Neuman, J. A., Gilman, J. B., Lamplugh, A., Schwantes, R. H., McKeen, S. A., Wisthaler, A., Piel, F., Guo, H., Campuzano-Jost, P., Jimenez, J. L., Fried, A., Hanisco, T. F., Huey, L. G., Perring, A., Katich, J. M., Diskin, G. S., Nowak, J. B., Bui, T. P., Halliday, H. S., DiGangi, J. P., Pereira, G., James, E. P., Ahmadov, R., McLinden, C. A., Soja, A. J., Moore, R. H., Hair, J. W., and Warneke, C.: Airborne Emission Rate Measurements Validate Remote Sensing Observations and Emission Inventories of Western U.S. Wildfires, Environ. Sci. Technol., https://doi.org/10.1021/acs.est.1c07121, 2022.

Stohl, A., Klimont, Z., Eckhardt, S., Kupiainen, K., Shevchenko, V. P., Kopeikin, V. M., and Novigatsky, A. N.: Black carbon in the Arctic: the underestimated role of gas flaring and residential combustion emissions, Atmos. Chem. Phys., 13, 8833–8855, https://doi.org/10.5194/acp-13-8833-2013, 2013.

Strode, S. A., Liu, J., Lait, L., Commane, R., Daube, B., Wofsy, S., Conaty, A., Newman, P., and Prather, M.: Forecasting carbon monoxide on a global scale for the ATom-1 aircraft mission: insights from airborne and satellite observations and modeling, Atmospheric Chemistry and Physics, 18, 10955–10971, https://doi.org/10.5194/acp-18-10955-2018, 2018.

Syphard, A. D. and Keeley, J. E.: Location, timing and extent of wildfire vary by cause of ignition, Int. J. Wildland Fire, 24, 37–47, https://doi.org/10.1071/WF14024, 2015.

Taraborrelli, D., Cabrera-Perez, D., Bacer, S., Gromov, S., Lelieveld, J., Sander, R., and Pozzer, A.: Influence of aromatics on tropospheric gas-phase composition, Atmospheric Chemistry and Physics, 21, 2615–2636, https://doi.org/10.5194/acp-21-2615-2021, 2021.

Taylor, J. W., Wu, H., Szpek, K., Bower, K., Crawford, I., Flynn, M. J., Williams, P. I., Dorsey, J., Langridge, J. M., Cotterell, M. I., Fox, C., Davies, N. W., Haywood, J. M., and Coe, H.: Absorption closure in highly aged biomass

burning smoke, Atmospheric Chemistry and Physics, 20, 11201–11221, https://doi.org/10.5194/acp-20-11201-2020, 2020.

Teich, M., van Pinxteren, D., Wang, M., Kecorius, S., Wang, Z., Müller, T., Močnik, G., and Herrmann, H.: Contributions of nitrated aromatic compounds to the light absorption of water-soluble and particulate brown carbon in different atmospheric environments in Germany and China, Atmospheric Chemistry and Physics, 17, 1653–1672, https://doi.org/10.5194/acp-17-1653-2017, 2017.

Theobald, D. M. and Romme, W. H.: Expansion of the US wildland–urban interface, Landscape and Urban Planning, 83, 340–354, https://doi.org/10.1016/j.landurbplan.2007.06.002, 2007.

Tkacik, D. S., Robinson, E. S., Ahern, A., Saleh, R., Stockwell, C., Veres, P., Simpson, I. J., Meinardi, S., Blake, D. R., Yokelson, R. J., Presto, A. A., Sullivan, R. C., Donahue, N. M., and Robinson, A. L.: A dual-chamber method for quantifying the effects of atmospheric perturbations on secondary organic aerosol formation from biomass burning emissions, Journal of Geophysical Research: Atmospheres, 122, 6043–6058, https://doi.org/10.1002/2016JD025784, 2017.

Tosca, M. G., Randerson, J. T., and Zender, C. S.: Global impact of smoke aerosols from landscape fires on climate and the Hadley circulation, Atmospheric Chemistry and Physics, 13, 5227–5241, https://doi.org/10.5194/acp-13-5227-2013, 2013.

Travis, K. R., Jacob, D. J., Fisher, J. A., Kim, P. S., Marais, E. A., Zhu, L., Yu, K., Miller, C. C., Yantosca, R. M., Sulprizio, M. P., Thompson, A. M., Wennberg, P. O., Crounse, J. D., St Clair, J. M., Cohen, R. C., Laughner, J. L., Dibb, J. E., Hall, S. R., Ullmann, K., Wolfe, G. M., Pollack, I. B., Peischl, J., Neuman, J. A., and Zhou, X.: Why do Models Overestimate Surface Ozone in the Southeastern United States?, Atmos Chem Phys, 16, 13561–13577, https://doi.org/10.5194/acp-16-13561-2016, 2016.

Travis, K. R., Heald, C. L., Allen, H. M., Apel, E. C., Arnold, S. R., Blake, D. R., Brune, W. H., Chen, X., Commane, R., Crounse, J. D., Daube, B. C., Diskin, G. S., Elkins, J. W., Evans, M. J., Hall, S. R., Hintsa, E. J., Hornbrook, R. S., Kasibhatla, P. S., Kim, M. J., Luo, G., McKain, K., Millet, D. B., Moore, F. L., Peischl, J., Ryerson, T. B., Sherwen, T., Thames, A. B., Ullmann, K., Wang, X., Wennberg, P. O., Wolfe, G. M., and Yu, F.: Constraining remote oxidation capacity with ATom observations, Atmospheric Chemistry and Physics, 20, 7753–7781, https://doi.org/10.5194/acp-20-7753-2020, 2020.

Turetsky, M. R., Kane, E. S., Harden, J. W., Ottmar, R. D., Manies, K. L., Hoy, E., and Kasischke, E. S.: Recent acceleration of biomass burning and carbon losses in Alaskan forests and peatlands, Nature Geoscience, 4, 27–31, https://doi.org/10.1038/ngeo1027, 2011.

Urbanski, S. P., Hao, W. M., and Nordgren, B.: The wildland fire emission inventory: western United States emission estimates and an evaluation of uncertainty, Atmos. Chem. Phys., 11, 12973–13000, https://doi.org/10.5194/acp-11-12973-2011, 2011.

Air Pollutant Emissions Trends Data: https://www.epa.gov/air-emissions-inventories/air-pollutant-emissions-trends-data, last access: 20 May 2020.

Climate Science Special Report: https://science2017.globalchange.gov/chapter/8/, last access: 16 June 2020.

Vakkari, V., Kerminen, V.-M., Beukes, J. P., Tiitta, P., Zyl, P. G. van, Josipovic, M., Venter, A. D., Jaars, K., Worsnop, D. R., Kulmala, M., and Laakso, L.: Rapid changes in biomass burning aerosols by atmospheric oxidation, Geophysical Research Letters, 41, 2644–2651, https://doi.org/10.1002/2014GL059396, 2014.

Vakkari, V., Beukes, J. P., Dal Maso, M., Aurela, M., Josipovic, M., and van Zyl, P. G.: Major secondary aerosol formation in southern African open biomass burning plumes, Nature Geoscience, 11, 580–583, https://doi.org/10.1038/s41561-018-0170-0, 2018.

Val Martin, M., Heald, C. L., Lamarque, J.-F., Tilmes, S., Emmons, L. K., and Schichtel, B. A.: How emissions, climate, and land use change will impact mid-century air quality over the United States: a focus on effects at national parks, Atmos. Chem. Phys., 15, 2805–2823, https://doi.org/10.5194/acp-15-2805-2015, 2015.

Val Martin, M., Kahn, R. A., and Tosca, M. G.: A Global Analysis of Wildfire Smoke Injection Heights Derived from Space-Based Multi-Angle Imaging, Remote Sensing, 10, 1609, https://doi.org/10.3390/rs10101609, 2018.

Van Leeuwen, T. T., Van der Werf, G. R., Hoffmann, A. A., Detmers, R. G., Rücker, G., French, N. H. F., Archibald, S., Carvalho Jr, J. A., Cook, G. D., De Groot, W. J., Hély, C., Kasischke, E. S., Kloster, S., McCarty, J. L., Pettinari, M. L., Savadogo, P., Alvarado, E. C., Boschetti, L., Manuri, S., Meyer, C. P., Siegert, F., Trollope, L. A., and Trollope, W. S. W.: Biomass burning fuel consumption rates: a field measurement database, 2014.

Veraverbeke, S., Rogers, B. M., and Randerson, J. T.: Daily burned area and carbon emissions from boreal fires in Alaska, Biogeosciences, 12, 3579–3601, https://doi.org/10.5194/bg-12-3579-2015, 2015.

Vodonos, A., Awad, Y. A., and Schwartz, J.: The concentration-response between long-term PM2.5 exposure and mortality; A meta-regression approach, Environmental Research, 166, 677–689, https://doi.org/10.1016/j.envres.2018.06.021, 2018.

Vohra, K., Vodonos, A., Schwartz, J., Marais, E. A., Sulprizio, M. P., and Mickley, L. J.: Global mortality from outdoor fine particle pollution generated by fossil fuel combustion: Results from GEOS-Chem, Environmental Research, 195, 110754, https://doi.org/10.1016/j.envres.2021.110754, 2021.

Voulgarakis, A., Naik, V., Lamarque, J.-F., Shindell, D. T., Young, P. J., Prather, M. J., Wild, O., Field, R. D., Bergmann, D., Cameron-Smith, P., Cionni, I., Collins, W. J., Dalsøren, S. B., Doherty, R. M., Eyring, V., Faluvegi, G., Folberth, G. A., Horowitz, L. W., Josse, B., MacKenzie, I. A., Nagashima, T., Plummer, D. A., Righi, M., Rumbold, S. T., Stevenson, D. S., Strode, S. A., Sudo, K., Szopa, S., and Zeng, G.: Analysis of present day and future OH and methane lifetime in the ACCMIP simulations, Atmospheric Chemistry and Physics, 13, 2563–2587, https://doi.org/10.5194/acp-13-2563-2013, 2013.

Wang, D., Guan, D., Zhu, S., Kinnon, M. M., Geng, G., Zhang, Q., Zheng, H., Lei, T., Shao, S., Gong, P., and Davis, S. J.: Economic footprint of California wildfires in 2018, Nat Sustain, 4, 252–260, https://doi.org/10.1038/s41893-020-00646-7, 2021a.

Wang, S., Coggon, M. M., Gkatzelis, G. I., Warneke, C., Bourgeois, I., Ryerson, T., Peischl, J., Veres, P. R., Neuman, J. A., Hair, J., Shingler, T., Fenn, M., Diskin, G., Huey, L. G., Lee, Y. R., Apel, E. C., Hornbrook, R. S., Hills, A. J., Hall, S. R., Ullmann, K., Bela, M. M., Trainer, M. K., Kumar, R., Orlando, J. J., Flocke, F. M., and Emmons, L. K.: Chemical Tomography in a Fresh Wildland Fire Plume: A Large Eddy Simulation (LES) Study, JGR Atmospheres, 126, https://doi.org/10.1029/2021JD035203, 2021b.

Wang, X., Heald, C. L., Ridley, D. A., Schwarz, J. P., Spackman, J. R., Perring, A. E., Coe, H., Liu, D., and Clarke, A. D.: Exploiting simultaneous observational constraints on mass and absorption to estimate the global direct radiative forcing of black carbon and brown carbon, Atmospheric Chemistry and Physics, 14, 10989–11010, https://doi.org/10.5194/acp-14-10989-2014, 2014.

Wang, X., Heald, C. L., Sedlacek, A. J., de Sá, S. S., Martin, S. T., Alexander, M. L., Watson, T. B., Aiken, A. C., Springston, S. R., and Artaxo, P.: Deriving brown carbon from multiwavelength absorption measurements: method and application to AERONET and Aethalometer observations, Atmospheric Chemistry and Physics, 16, 12733–12752, https://doi.org/10.5194/acp-16-12733-2016, 2016.

Wang, X., Heald, C. L., Liu, J., Weber, R. J., Campuzano-Jost, P., Jimenez, J. L., Schwarz, J. P., and Perring, A. E.: Exploring the observational constraints on the simulation of brown carbon, Atmospheric Chemistry and Physics, 18, 635–653, https://doi.org/10.5194/acp-18-635-2018, 2018.

Ward, D. S., Kloster, S., Mahowald, N. M., Rogers, B. M., Randerson, J. T., and Hess, P. G.: The changing radiative forcing of fires: global model estimates for past, present and future, Atmospheric Chemistry and Physics, 12, 10857–10886, https://doi.org/10.5194/acp-12-10857-2012, 2012.

van der Werf, G. R., Randerson, J. T., Giglio, L., van Leeuwen, T. T., Chen, Y., Rogers, B. M., Mu, M., van Marle, M. J. E., Morton, D. C., Collatz, G. J., Yokelson, R. J., and Kasibhatla, P. S.: Global fire emissions estimates during 1997–2016, Earth System Science Data, 9, 697–720, https://doi.org/10.5194/essd-9-697-2017, 2017.

Westerling, A. L.: Increasing western US forest wildfire activity: sensitivity to changes in the timing of spring, Phil. Trans. R. Soc. B, 371, 20150178, https://doi.org/10.1098/rstb.2015.0178, 2016.

Westerling, A. L., Hidalgo, H. G., Cayan, D. R., and Swetnam, T. W.: Warming and Earlier Spring Increase Western U.S. Forest Wildfire Activity, Science, 313, 940–943, https://doi.org/10.1126/science.1128834, 2006.

Wiedinmyer, C., Akagi, S., Yokelson, R., Emmons, L., Al-Saadi, J., Orlando, J., and Soja, A.: The Fire INventory from NCAR (FINN): A High Resolution Global Model to Estimate the Emissions from Open Burning, Geoscientific Model Development, 625–641, 2011.

Wiedinmyer, C., Yokelson, R. J., and Gullett, B. K.: Global Emissions of Trace Gases, Particulate Matter, and Hazardous Air Pollutants from Open Burning of Domestic Waste, Environ. Sci. Technol., 48, 9523–9530, https://doi.org/10.1021/es502250z, 2014.

Williamson, G. J., Bowman, D. M. J. S., Price, O. F., Henderson, S. B., and Johnston, F. H.: A transdisciplinary approach to understanding the health effects of wildfire and prescribed fire smoke regimes, Environ. Res. Lett., 11, 125009, https://doi.org/10.1088/1748-9326/11/12/125009, 2016.

Wisthaler, A., Hansel, A., Dickerson, R. R., and Crutzen, P. J.: Organic trace gas measurements by PTR-MS during INDOEX 1999, Journal of Geophysical Research: Atmospheres, 107, INX2 23-1-INX2 23-11, https://doi.org/10.1029/2001JD000576, 2002.

Womack, C. C., Manfred, K. M., Wagner, N. L., Adler, G., Franchin, A., Lamb, K. D., Middlebrook, A. M., Schwarz, J. P., Brock, C. A., Brown, S. S., and Washenfelder, R. A.: Complex refractive indices in the ultraviolet and visible spectralregion for highly absorbing non-spherical biomass burning aerosol, Aerosols/Field Measurements/Troposphere/Physics (physical properties and processes), https://doi.org/10.5194/acp-2020-1200, 2020.

Wooster, M. J.: Small-scale experimental testing of fire radiative energy for quantifying mass combusted in natural vegetation fires, Geophysical Research Letters, 29, 23-1-23–4, https://doi.org/10.1029/2002GL015487, 2002.

Wooster, M. J., Roberts, G., Perry, G. L. W., and Kaufman, Y. J.: Retrieval of biomass combustion rates and totals from fire radiative power observations: FRP derivation and calibration relationships between biomass consumption and fire radiative energy release, Journal of Geophysical Research: Atmospheres, 110, https://doi.org/10.1029/2005JD006318, 2005.

WRAP: Development of 2000-04 Baseline Period and 2018 Projection Year Emission Inventories, Prepared by Air Sciences, Inc. Project No. 178-8, 32, 2005.

Wu, C., Sitch, S., Huntingford, C., Mercado, L. M., Venevsky, S., Lasslop, G., Archibald, S., and Staver, A. C.: Reduced global fire activity due to human demography slows global warming by enhanced land carbon uptake, Proc. Natl. Acad. Sci. U.S.A., 119, e2101186119, https://doi.org/10.1073/pnas.2101186119, 2022.

Wu, H., Taylor, J. W., Szpek, K., Langridge, J. M., Williams, P. I., Flynn, M., Allan, J. D., Abel, S. J., Pitt, J., Cotterell, M. I., Fox, C., Davies, N. W., Haywood, J., and Coe, H.: Vertical variability of the properties of highly aged biomass burning aerosol transported over the southeast Atlantic during CLARIFY-2017, Atmospheric Chemistry and Physics, 20, 12697–12719, https://doi.org/10.5194/acp-20-12697-2020, 2020.

Wu, H., Taylor, J. W., Langridge, J. M., Yu, C., Allan, J. D., Szpek, K., Cotterell, M. I., Williams, P. I., Flynn, M., Barker, P., Fox, C., Allen, G., Lee, J., and Coe, H.: Rapid transformation of ambient absorbing aerosols from West African biomass burning, Atmospheric Chemistry and Physics Discussions, 1–37, https://doi.org/10.5194/acp-2021-49, 2021.

Xu, L., Crounse, J. D., Vasquez, K. T., Allen, H., Wennberg, P. O., Bourgeois, I., Brown, S. S., Campuzano-Jost, P., Coggon, M. M., Crawford, J. H., DiGangi, J. P., Diskin, G. S., Fried, A., Gargulinski, E. M., Gilman, J. B., Gkatzelis, G. I., Guo, H., Hair, J. W., Hall, S. R., Halliday, H. A., Hanisco, T. F., Hannun, R. A., Holmes, C. D., Huey, L. G., Jimenez, J. L., Lamplugh, A., Lee, Y. R., Liao, J., Lindaas, J., Neuman, J. A., Nowak, J. B., Peischl, J., Peterson, D. A., Piel, F., Richter, D., Rickly, P. S., Robinson, M. A., Rollins, A. W., Ryerson, T. B., Sekimoto, K., Selimovic, V., Shingler, T., Soja, A. J., Clair, J. M. S., Tanner, D. J., Ullmann, K., Veres, P. R., Walega, J., Warneke, C., Washenfelder, R. A., Weibring, P., Wisthaler, A., Wolfe, G. M., Womack, C. C., and Yokelson, R. J.: Ozone chemistry in western U.S. wildfire plumes, Science Advances, https://doi.org/10.1126/sciadv.abl3648, 2021.

Yang, Y., Shao, M., Wang, X., Nölscher, A. C., Kessel, S., Guenther, A., and Williams, J.: Towards a quantitative understanding of total OH reactivity: A review, Atmospheric Environment, 134, 147–161, https://doi.org/10.1016/j.atmosenv.2016.03.010, 2016.

Yokelson, R. J., Christian, T. J., Karl, T. G., and Guenther, A.: The tropical forest and fire emissions experiment: laboratory fire measurements and synthesis of campaign data, Atmospheric Chemistry and Physics, 8, 3509–3527, https://doi.org/10.5194/acp-8-3509-2008, 2008.

Yokelson, R. J., Crounse, J. D., DeCarlo, P. F., Karl, T., Urbanski, S., Atlas, E., Campos, T., Shinozuka, Y., Kapustin, V., Clarke, A. D., Weinheimer, A., Knapp, D. J., Montzka, D. D., Holloway, J., Weibring, P., Flocke, F., Zheng, W., Toohey, D., Wennberg, P. O., Wiedinmyer, C., Mauldin, L., Fried, A., Richter, D., Walega, J., Jimenez, J. L., Adachi, K., Buseck, P. R., Hall, S. R., and Shetter, R.: Emissions from biomass burning in the Yucatan, Atmos. Chem. Phys., 28, 2009.

Yuan, W., Huang, R.-J., Yang, L., Guo, J., Chen, Z., Duan, J., Wang, T., Ni, H., Han, Y., Li, Y., Chen, Q., Chen, Y., Hoffmann, T., and O'Dowd, C.: Characterization of the light-absorbing properties, chromophore composition and sources of brown carbon aerosol in Xi'an, northwestern China, Atmospheric Chemistry and Physics, 20, 5129–5144, https://doi.org/10.5194/acp-20-5129-2020, 2020.

Yue, X., Mickley, L. J., Logan, J. A., and Kaplan, J. O.: Ensemble projections of wildfire activity and carbonaceous aerosol concentrations over the western United States in the mid-21st century, Atmospheric Environment, 77, 767–780, https://doi.org/10.1016/j.atmosenv.2013.06.003, 2013.

Zhang, F., Wang, J., Ichoku, C., Hyer, E. J., Yang, Z., Ge, C., Su, S., Zhang, X., Kondragunta, S., Kaiser, J. W., Wiedinmyer, C., and Silva, A. da: Sensitivity of mesoscale modeling of smoke direct radiative effect to the emission inventory: a case study in northern sub-Saharan African region, Environ. Res. Lett., 9, 075002, https://doi.org/10.1088/1748-9326/9/7/075002, 2014a.

Zhang, L., Jacob, D. J., Yue, X., Downey, N. V., Wood, D. A., and Blewitt, D.: Sources contributing to background surface ozone in the US Intermountain West, Atmospheric Chemistry and Physics, 14, 5295–5309, https://doi.org/10.5194/acp-14-5295-2014, 2014b.

Zhao, X. and Wang, L.: Atmospheric Oxidation Mechanism of Furfural Initiated by Hydroxyl Radicals, J. Phys. Chem. A, 121, 3247–3253, https://doi.org/10.1021/acs.jpca.7b00506, 2017.

Zhou, L., Baker, K. R., Napelenok, S. L., Pouliot, G., Elleman, R., O'Neill, S. M., Urbanski, S. P., and Wong, D. C.: Modeling crop residue burning experiments to evaluate smoke emissions and plume transport, Science of The Total Environment, 627, 523–533, https://doi.org/10.1016/j.scitotenv.2018.01.237, 2018.

Zhu, L., Val Martin, M., Gatti, L. V., Kahn, R., Hecobian, A., and Fischer, E. V.: Development and implementation of a new biomass burning emissions injection height scheme (BBEIH v1.0) for the GEOS-Chem model (v9-01-01), Geoscientific Model Development, 11, 4103–4116, 2018.

Zuidema, P., Sedlacek, A. J., Flynn, C., Springston, S., Delgadillo, R., Zhang, J., Aiken, A. C., Koontz, A., and Muradyan, P.: The Ascension Island Boundary Layer in the Remote Southeast Atlantic is Often Smoky, Geophysical Research Letters, 45, 4456–4465, https://doi.org/10.1002/2017GL076926, 2018.

Appendix 1. Supplement to Chap. 2: How emissions uncertainty influences the distribution and radiative impacts of smoke from fires in North America

Emissions across other large biomass burning regions (Asia, the Amazon, and Africa)

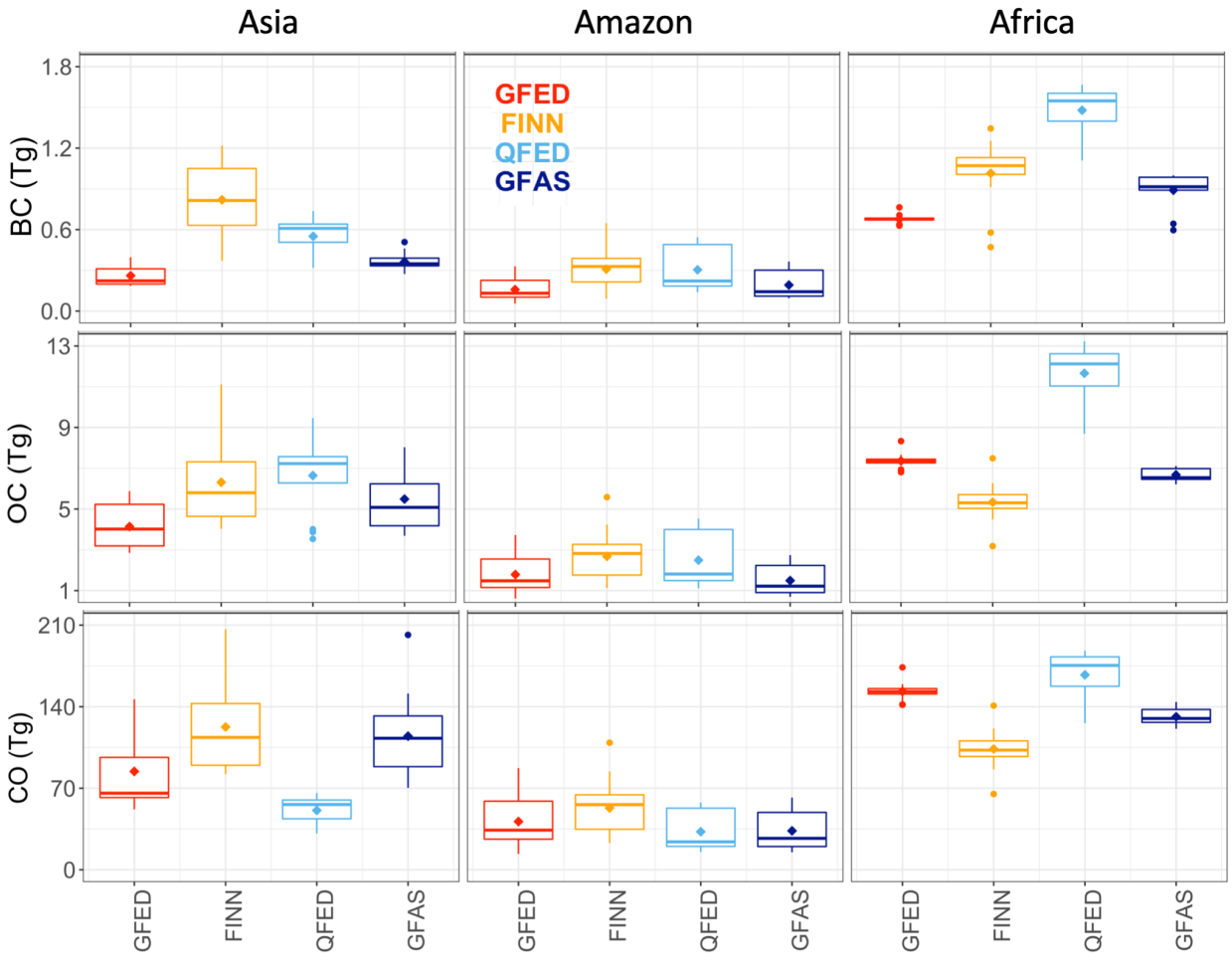

Figure 2.S1: Boxplot summaries of each inventory's total annual emissions of BC, OC, and CO for Asia, the Amazon, and Africa from 2004 to 2016. Diamonds indicate means. The horizontal bar is the median. The box shows the 25th to the 75th percentile, and the whiskers show 1.5 times the interquartile range. Points outside 1.5 times the interquartile range are shown as dots. GFED4s emissions are in red, FINN1.5 in orange, QFED2.4 in light blue, and GFAS1.2 in dark blue.

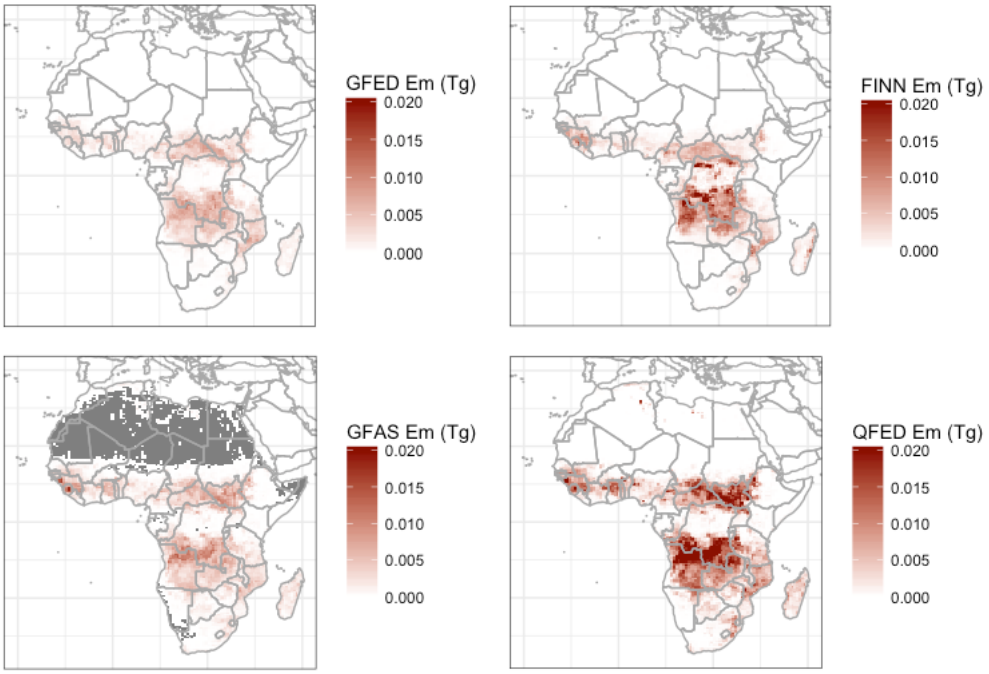

Figure 2.S2a: Because African emissions showed a larger range across inventories than emissions in Asia and the Amazon, we show the spatial extent of African black carbon emissions here summed from 2004-2014 (Fig. 2.S2a) and for OC emissions (Fig. 2.S2b) below.

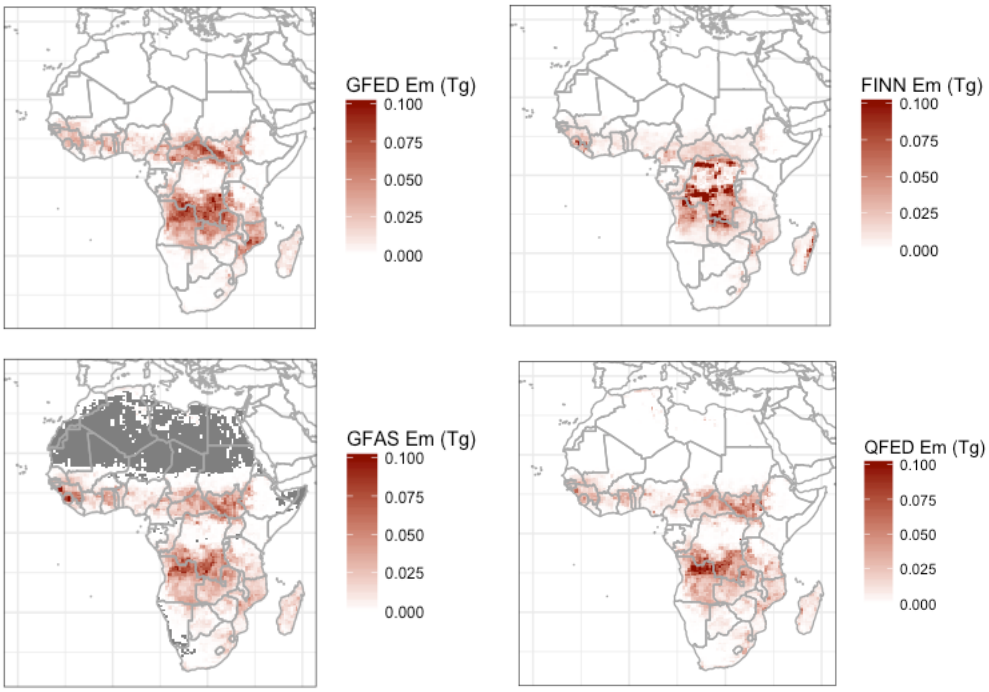

Figure 2.S2b: Spatial extent of African organic carbon emissions summed from 2004-2014. Across both BC and OC emissions, it appears that variability among the inventories is driven more by central African emissions than emissions in the Sahel area with QFED2.4 nearly always

much higher than the other three inventories for BC and less so for OC since those emissions have been scaled down to account for our different OM:OC ratio.

Biomass burning injection height scheme sensitivity test

Slight improvements in model-observation agreement, especially aloft and in the most fire-influenced points, are seen when a simple injection height scheme (Fischer et al. 2014) is used. More work is needed on fire injection schemes in chemical transport models.

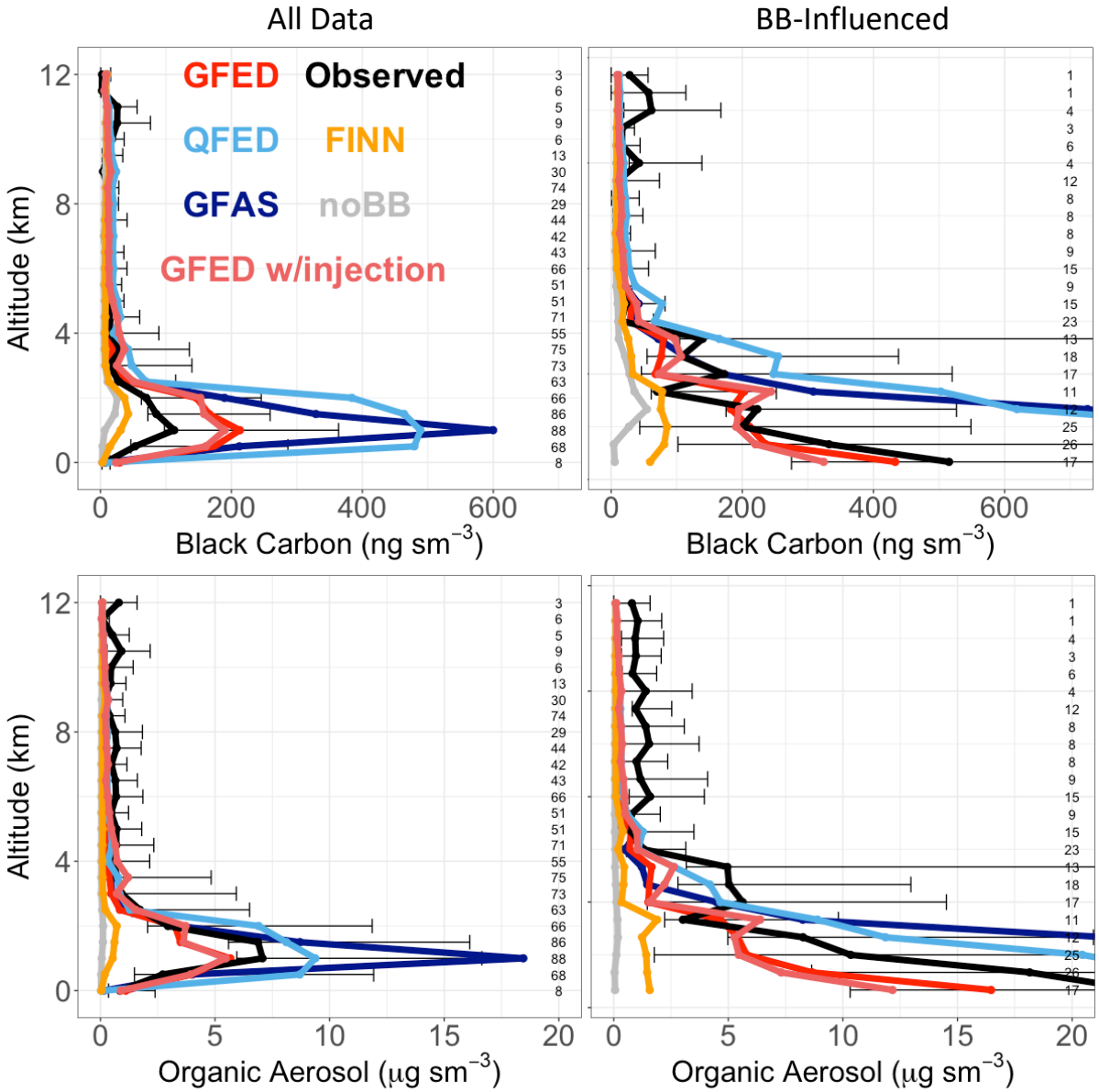

Figure 2.S3: Boreal ARCTAS vertical profiles (shown in 0.5km bins) with injection height scheme (65% into PBL and 35% into the free troposphere). Observations (black) are compared with the five inventory simulations – "GFED4s with injection height scheme" (pink), "GFED4s" (red), "FINN1.5" (orange), "QFED2.4" (light blue), and "GFAS1.2" (dark blue) and a noBB simulation in grey. Error bars show the 25th to 75th percentiles of measurements and simulations

averaged in each vertical bin. The left column shows medians of the total results from the campaign while the right column is filtered by the top 25th percentile observed acetonitrile. This sensitivity test was run at 2x2.5°.

Inventory effect on model agreement with aerosol optical depth (AOD)

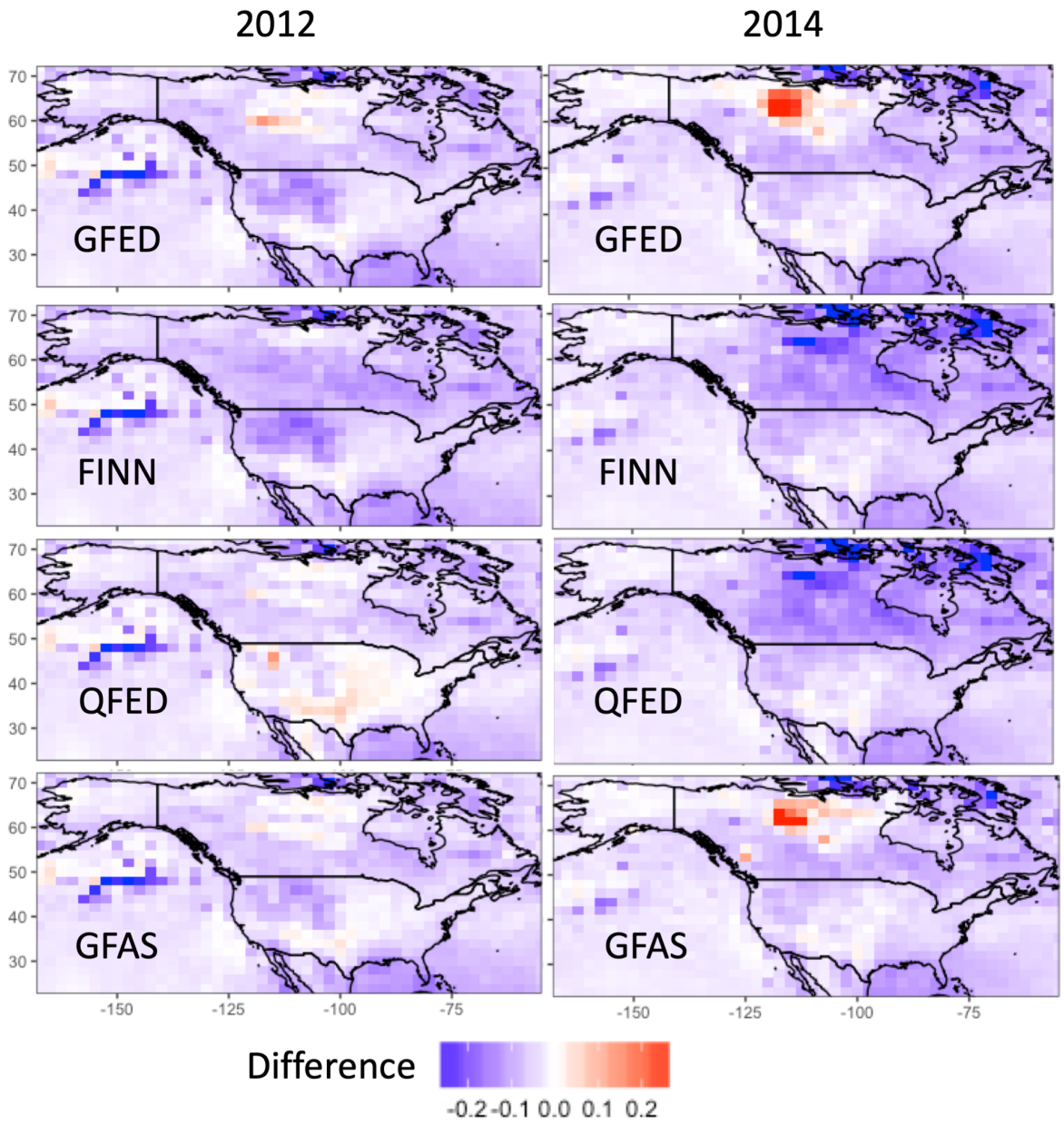

Figure 2.S4: Maps of the difference between the simulated AOD driven by each inventory and MODIS-observed AOD from the Aqua satellite during the mean Northern Hemispheric fire season (May – September) in 2012 and 2014.

Impacts on air quality

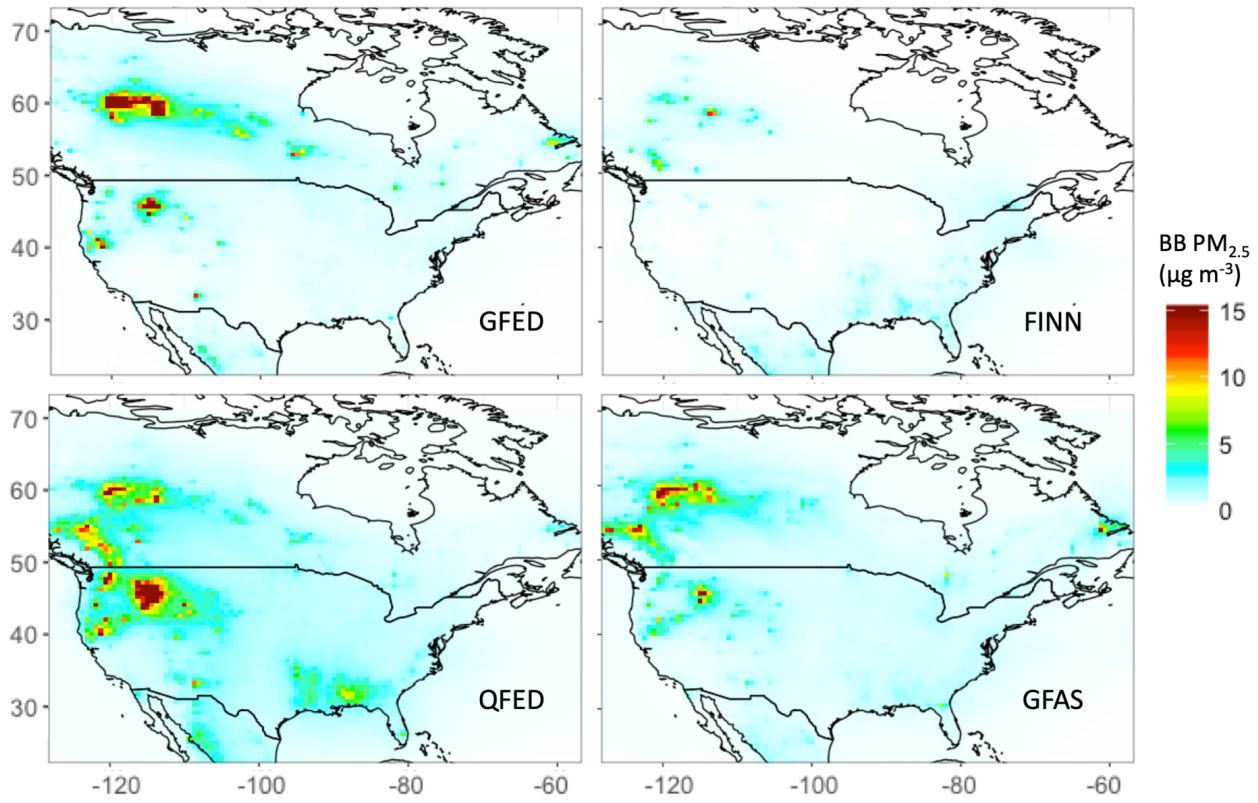

Figure 2.S5: Maps of surface 2012 annual mean fire (BC+OA) PM2.5 concentrations driven by each inventory at nested resolution. GFED4s is top left, FINN1.5 top right, QFED2.4 bottom left, and GFAS1.2 bottom right. The color bar is saturated at 15 ug m^{-3} for all panels. See below for an analysis of each year from 2012 – 2014.

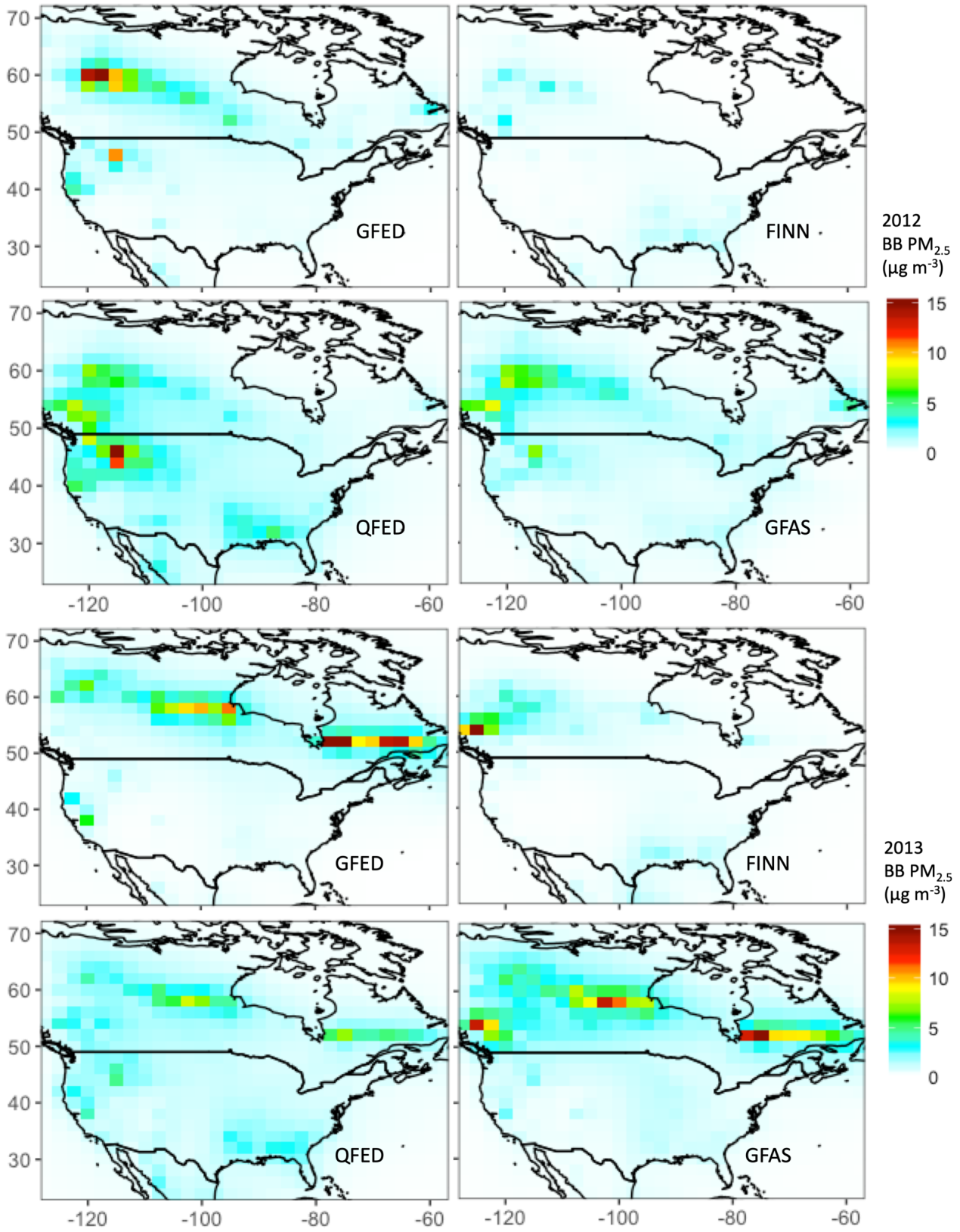
GFED
FINN
QFED
GFAS
2012
BB PM2.5
(µg m-3)
15
10
5
0
70
60
50
40
30
-120
-100
-80
-60
GFED
FINN
QFED
GFAS
2013
BB PM2.5
(µg m-3)
15
10
5
0

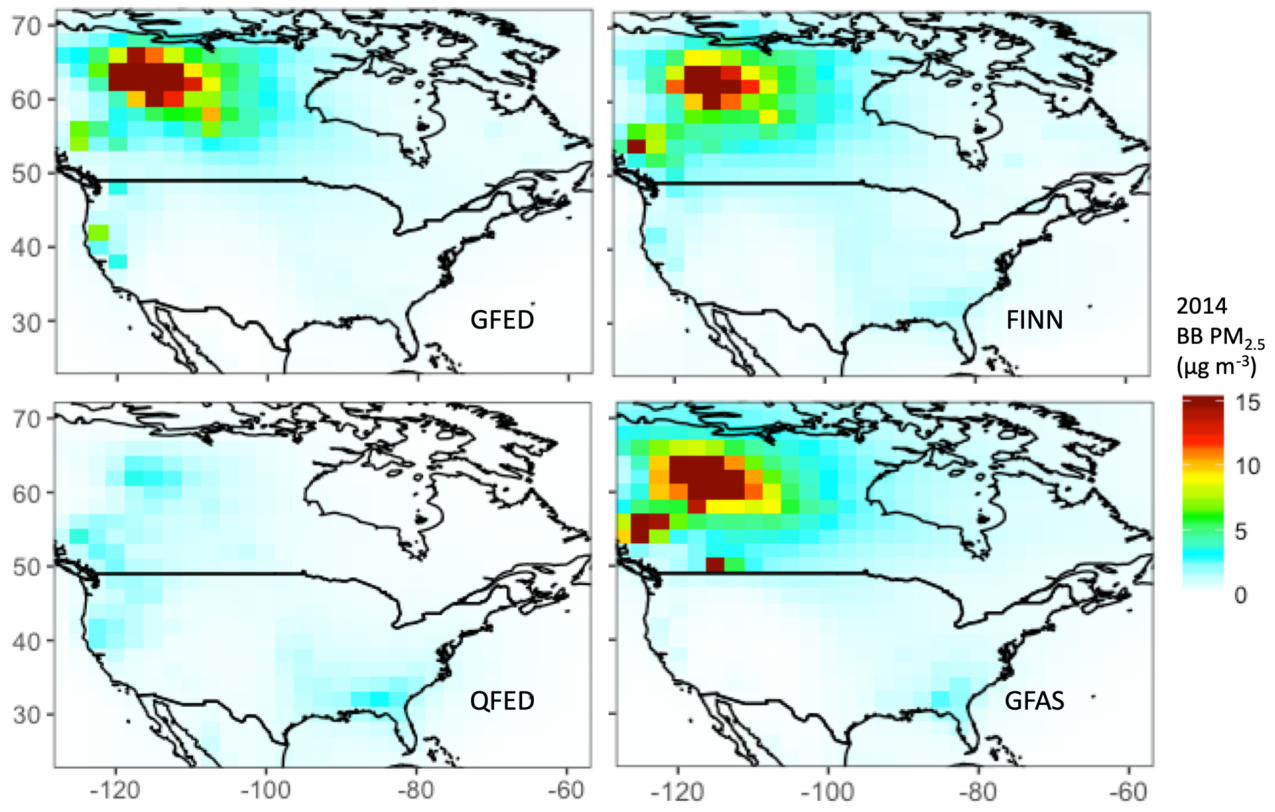

Figure 2.S6: Maps of surface annual mean fire (BC+OA) PM2.5 concentrations from 2012 to 2014 driven by each inventory at 2x2.5°. GFED4s is top left, FINN1.5 top right, QFED2.4 bottom left, and GFAS1.2 bottom right. The color bar is saturated at 15 ug/m^3 for all panels.

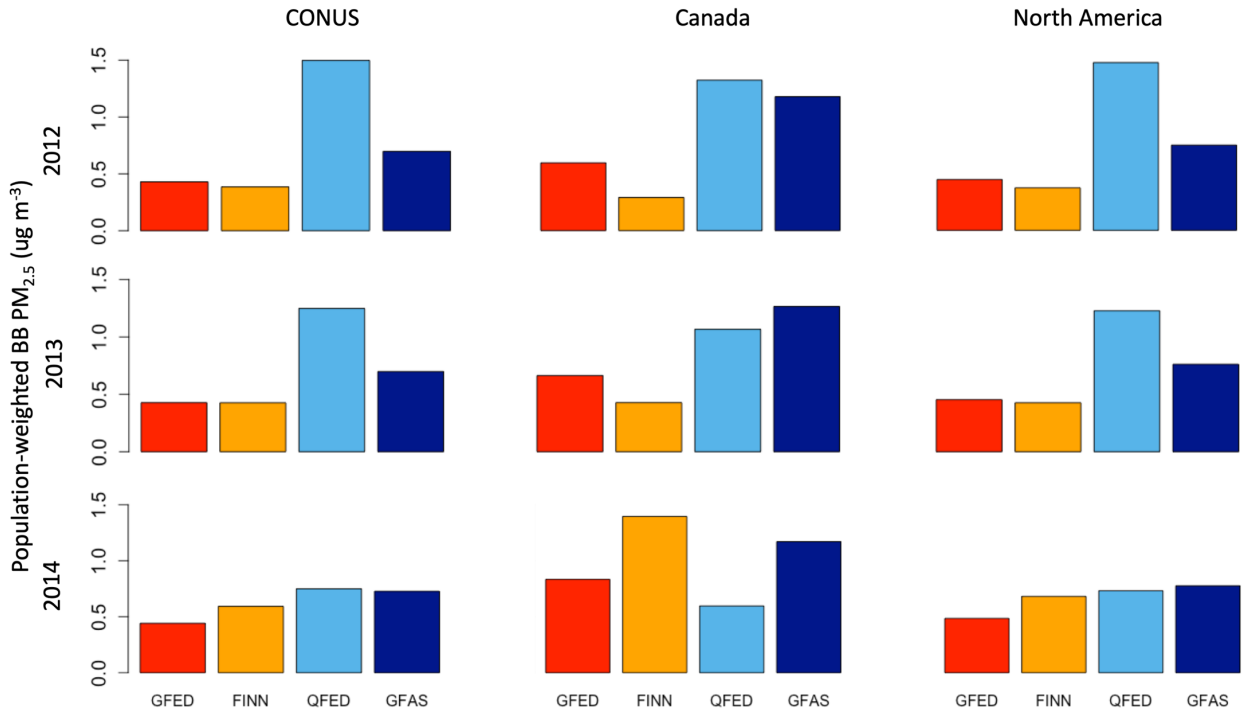

Figure 2.S7: Bar plots of the annual mean population-weighted fire PM2.5 exposure across the four inventories (GFED4s in red, FINN1.5 in orange, QFED2.4 in light blue, and GFAS1.2 in dark blue) for the US (left panel), Canada (middle panel), and North America (right panel) at 2x2.5° from 2012 - 2014.

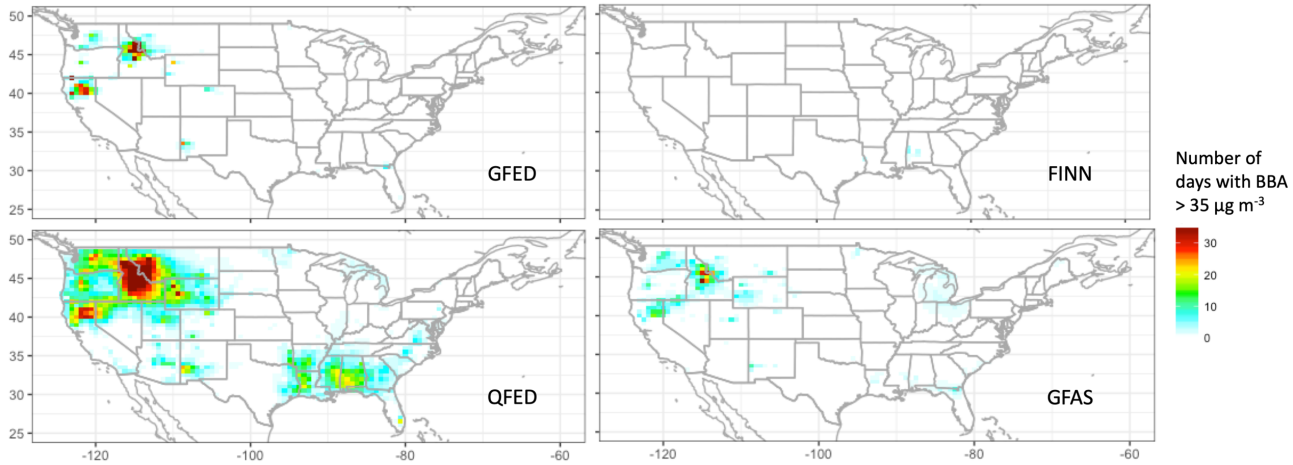

Figure 2.S8: Number of exceedances of the 24-hour average $PM_{2.5}$ standard (35 ug m^{-3}) from only surface BBA in 2012. Note that the color bar is saturated at 35 days.

Impacts on the direct radiative effect

Differences in emissions carry over to the DRE of both BC and OA with QFED2.4 generally the largest and FINN1.2 the smallest. Significant variability across the inventories is seen across years, especially in the OA DRE in boreal North America.

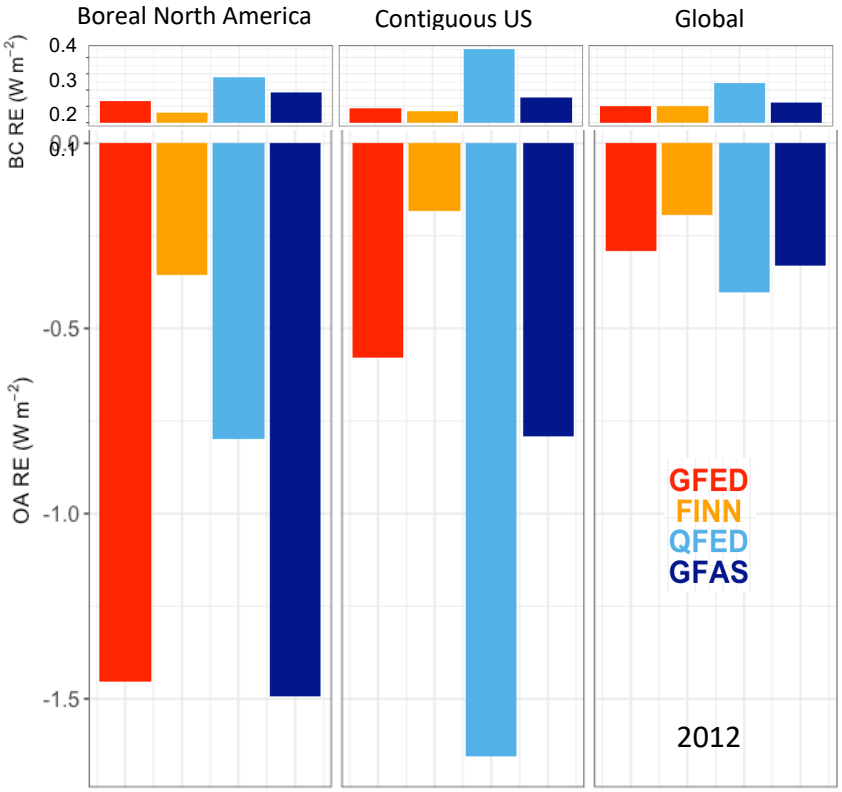
Boreal North America
Contiguous US
Global
BC RE (W m^{-2})
OA RE (W m^{-2})
0.4
0.3
0.2
0.1
0.0
-0.5
-1.0
-1.5
GFED
FINN
QFED
GFAS
2012

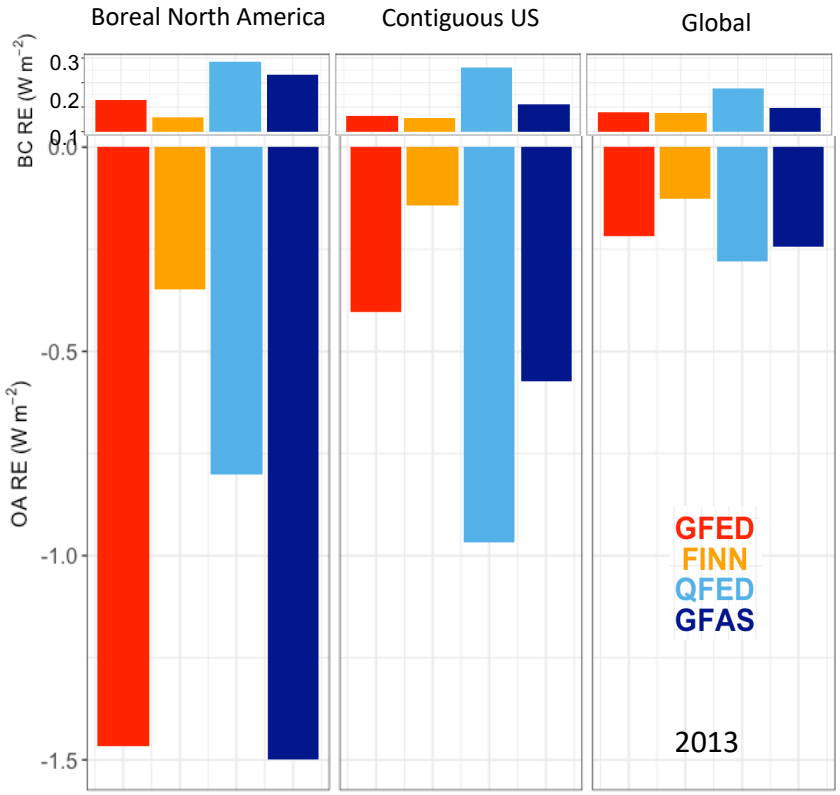
Boreal North America
Contiguous US
Global
BC RE (W m^{-2})
OA RE (W m^{-2})
0.3
0.2
0.1
0.0
-0.5
-1.0
-1.5
GFED
FINN
QFED
GFAS
2013

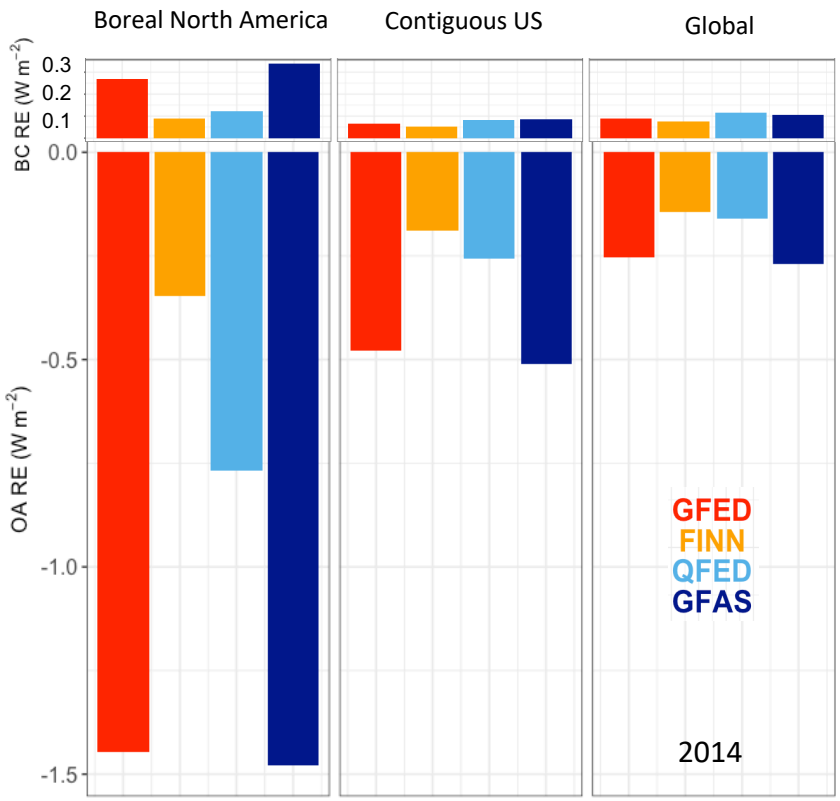
Boreal North America
Contiguous US
Global
BC RE (W m^{-2})
0.3
0.2
0.1
0.0
OA RE (W m^{-2})
-0.5
-1.0
-1.5
GFED
FINN
QFED
GFAS
2014

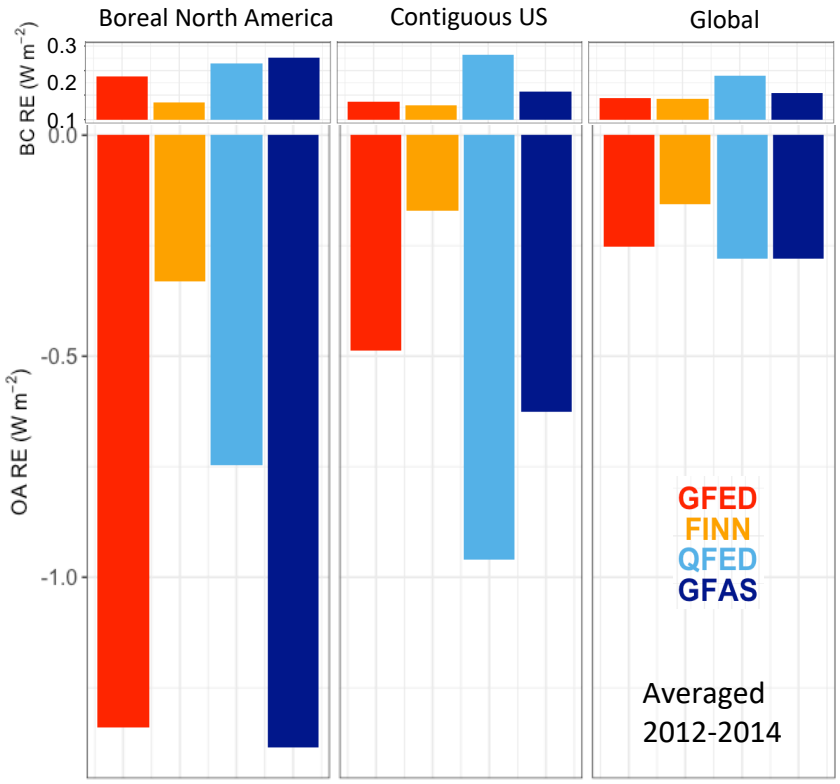
Boreal North America
Contiguous US
Global
BC RE (W m^{-2})
0.3
0.2
0.1
0.0
OA RE (W m^{-2})
-0.5
-1.0
GFED
FINN
QFED
GFAS
Averaged
2012-2014

Figure 2.S9: Northern Hemisphere fire season (May – September) top of atmosphere (TOA) all-sky direct radiative effect of BB-only BC and OA for each year from 2012-2014 individually and averaged over the three years in BONA, CONUS, and globally. GFED4s is shown in red, FINN1.5 orange, QFED2.4 light blue, and GFAS1.2 dark blue. (The size of BC versus OA panels is not to scale).

Table 2.S1: Biomass burning aerosol (BC and OA) mean 2012 DRE in boreal North America, CONUS, and globally

	BONA		CONUS		Global		Global BBA DRE
	BC	OA	BC	OA	BC	OA	
GFED4s	0.08	-0.42	0.058	-0.27	0.072	-0.16	-0.088
FINN1.5	0.057	-0.11	0.063	-0.14	0.082	-0.13	-0.048
QFED2.4	0.15	-0.43	0.23	-0.82	0.18	-0.28	-0.10
GFAS1.2	0.11	-0.43	0.093	-0.40	0.095	-0.20	-0.11

Appendix 2. Supplement to Chap. 3: Investigating Carbonaceous Aerosol and its Absorption Properties from Fires in the western US (WE-CAN) and southern Africa (ORACLES and CLARIFY)

Adapted from: JGR: Atmospheres

Supporting Information for

Investigating Carbonaceous Aerosol and its Absorption Properties from Fires in the western US (WE-CAN) and southern Africa (ORACLES and CLARIFY)

Therese S. Carter[1], Colette L. Heald[1,2], Christopher D. Cappa[3], Jesse H. Kroll[1,4], Teresa L. Campos[5], Hugh Coe[6], Michael I. Cotterell[7], Nicholas W. Davies[8,9], Delphine K. Farmer[10], Cathyrn Fox[9], Lauren A. Garofalo[10], Lu Hu[11], Justin M. Langridge[9], Ezra J.T. Levin[12,13], Shane M. Murphy[14], Rudra P. Pokhrel[14, a], Yingjie Shen[14], Kate Szpek[9], Jonathan W. Taylor[6], Huihui Wu[6]

[1]Civil and Environmental Engineering Department, Massachusetts Institute of Technology, Cambridge, MA 02139, USA [2]Earth, Atmospheric and Planetary Sciences, Massachusetts Institute of Technology, Cambridge, MA 02139, USA [3]Department of Civil and Environmental Engineering, University of California at Davis, Davis, CA 95616, USA [4]Department of Chemical Engineering, Massachusetts Institute of Technology, Cambridge, MA 02139, USA [5]Atmospheric Chemistry Division, National Center for Atmospheric Research, Boulder, Colorado 80301, United States [6]Department of Earth and Environmental Sciences, University of Manchester, Manchester, UK [7]School of Chemistry, University of Bristol, Bristol, United Kingdom [8]College of Engineering, Mathematics and Physical Sciences, University of Exeter, Exeter, EX4 4QF, UK [9]Met Office, Fitzroy Road, Exeter, EX1 3PB, UK [10]Department of Chemistry, Colorado State University, Fort Collins, Colorado 80523, USA [11]Department of Chemistry and Biochemistry, University of Montana, Missoula, MT 59812, USA [12]Department of Atmospheric Science, Colorado State University, Fort Collins, CO 80523, USA [13]Handix Scientific, Boulder CO 80301 [14]Department of Atmospheric Science, University of Wyoming, Laramie, WY 82071, USA [a] Current address: Department of Physics, North Carolina A&T State University, Greensboro, NC, 27411

Contents of this file

Text 3.S1 to 3.S3
Figures 3.S1 to 3.S2

Introduction

Supplemental text provides more details on two previously published BC:OA parameterizations to represent BrC absorption. Supplemental figures provide supporting evidence for an overestimate of anthropogenic BC emissions in NEI2011.

Text 3.S1.

The Saleh et al. (2014) parameterization describes the varying degree of absorption for BrC as a function of the BC:OA ratio as follows:

$$\omega = \frac{0.21}{\frac{BC}{OA} + 0.07} \quad (1)$$

$$k_{550} = 0.016\, log\left(\frac{BC}{OA}\right) + 0.04, \quad (2)$$

$$k_\lambda = k_{550} \times \left(\frac{550}{\lambda}\right)^{\omega}, \quad (3)$$

where ω refers to the wavelength dependence of the imaginary part of the refractive index (k) and k_{550} refers to the imaginary part of the refractive index at 550 nm. We use the k value along with size distribution and density information to calculate the MAC for OA applied in GEOS-Chem (Table 3.1).

Text 3.S2.

McClure et al. (2020) showed that a sigmoidal fit provides for a more robust relationship over a wider range of BC:OA values (Table S2 in McClure et al. 2020):

$$\log(\text{MACBrC}, 405\text{ nm}) = 1.072 + \frac{-1.519}{1 + \frac{\exp(0.053 - x)}{0.732}}, \quad (4)$$

$$AAE_{405-532} = 1.25 + \frac{7.81}{1 + \frac{\exp(2.298 - x)}{0.554}}, \quad (5)$$

$$\log(\text{MACBrC}, 660\text{ nm}) = 0.87355 + \frac{-3.33745}{1 + \frac{\exp(1.08638 - x)}{1.3639}}, \quad (6)$$

where x is the log(OA/BC).

Text 3.S3.

Despite the large difference in the BC:OA ratio between the campaigns, the estimated BrC absorption efficiency is only 20-30% higher downwind of Africa at short wavelengths. This is the result of equation 1 in Text 3.S1, which modifies the AAE or the wavelength dependence of absorption ω. In particular, because the $AAE_{550\text{-}405}$ calculated for WE-CAN (~1.79) using the Saleh parameterization is roughly twice that calculated for ORACLES-2016 (~1.05), even with a factor of ~4 difference between the median BC:OA of the two, the calculated imaginary part of the refractive index (responsible for absorption) for OA at 405 nm is roughly the same (~0.03) despite their significantly different burn conditions and fuel types. Compared to the baseline properties, the Saleh et al. parameterization results in slightly less absorbing OA at 660 nm that is consistent across all regions (Table 3.1).

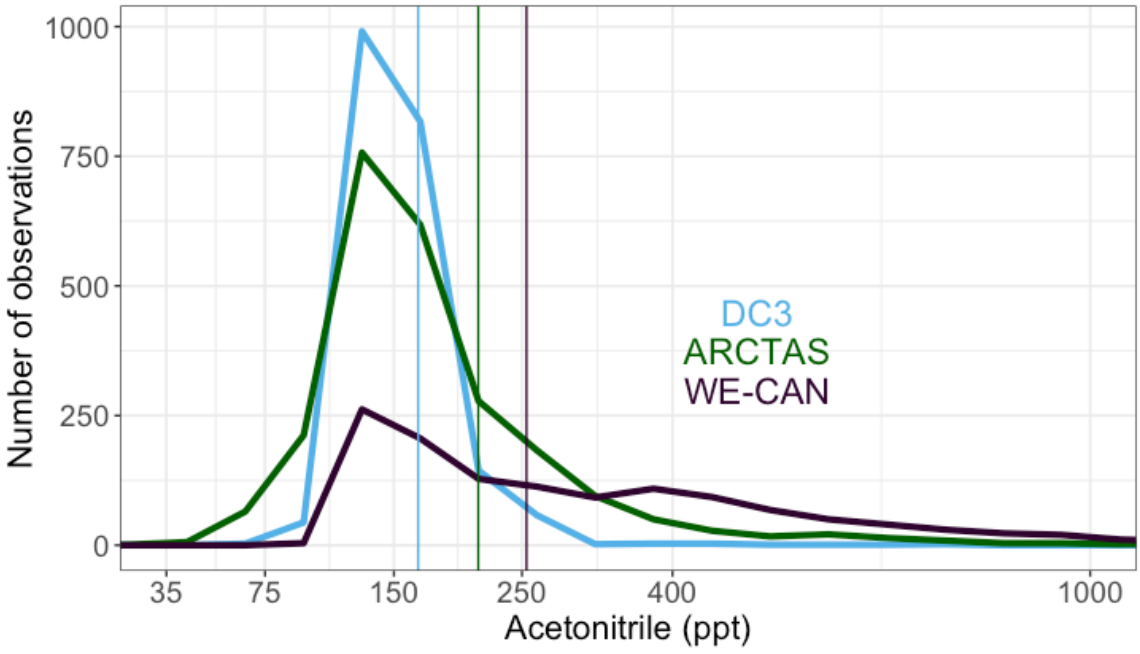

Figure 3.S1. Comparison of observed acetonitrile histograms across fire-influenced campaigns (DC3 in light blue, boreal component of ARCTAS in green, and WE-CAN in purple). Vertical lines mark the median for each campaign. Note that the *x* axis has been transformed by a square-root function and truncated, but observations go up to 7050 ppt.

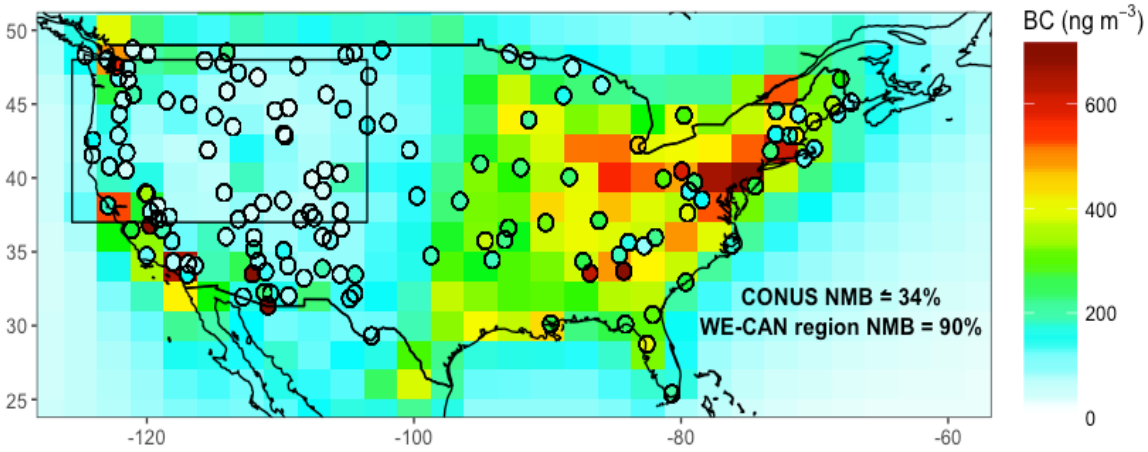

Figure 3.S2. Winter (December 2017 – February 2018) model mean surface BC concentrations in CONUS; the mean observed surface concentrations at IMPROVE sites are overlaid as circles. The WE-CAN region is enclosed by a box. The color bar is saturated at maximum values.

Appendix 3. Supplement to Chap. 4: An Improved Representation of Fire Non-Methane Organic Gases (NMOGs) in Models: Emissions to Reactivity

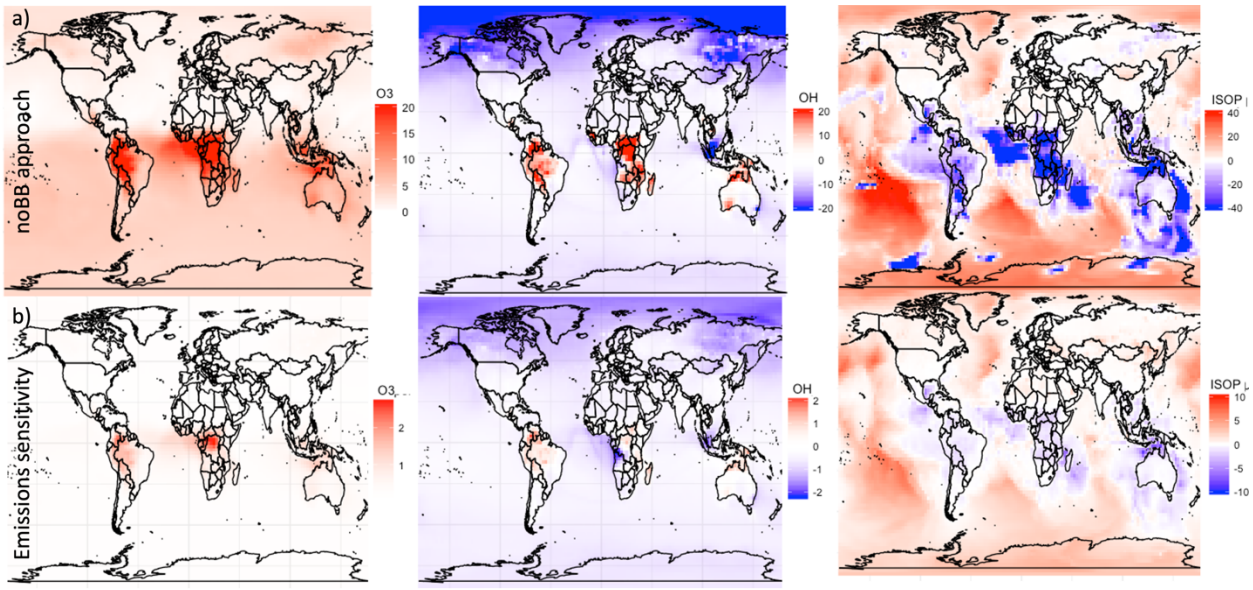

Fig 4.S1: Annual 2019 surface mean ozone, OH, and ISOP (isoprene) concentration percent differences attributed to fires using two approaches a) subtracting out no fire simulation versus b) emissions sensitivity runs of 1.05 and 0.95 times fire emissions scaled up to equal an 100% perturbation

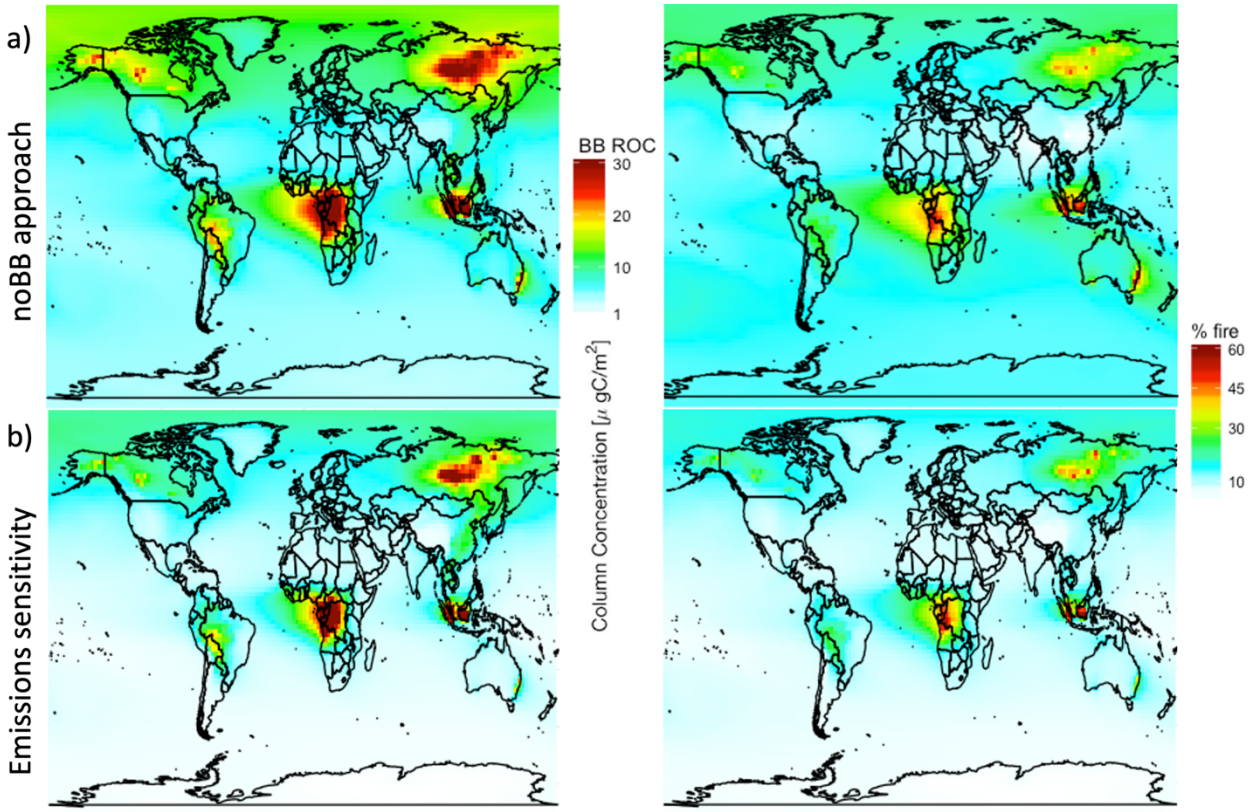

Fig 4.S2: Annual 2019 mean simulated ROC column concentrations and percent ROC attributed to fires using two approaches a) subtracting out no fire simulation versus b) emissions sensitivity runs of 1.05 and 0.95 times fire emissions scaled up to equal an 100% perturbation

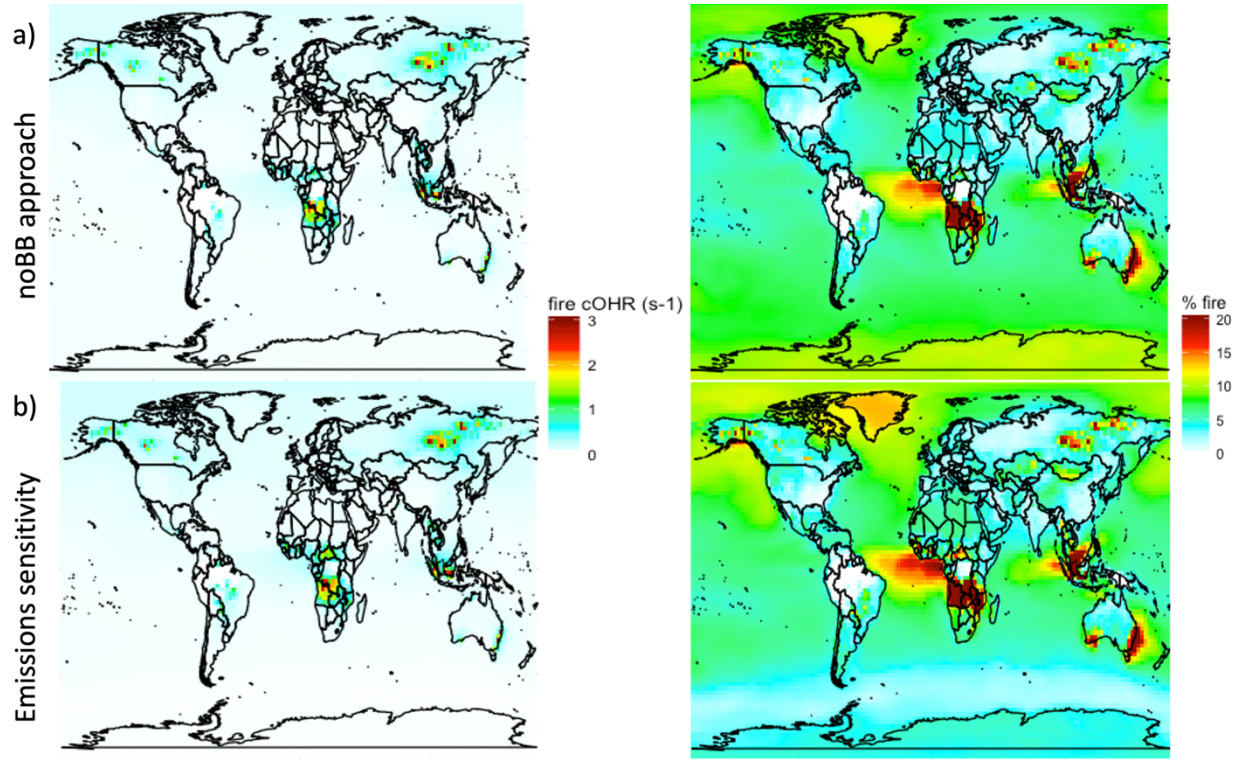

Fig 4.S3: Annual 2019 mean surface OHR and percent OHR attributed to fires using two approaches a) subtracting out no fire simulation versus b) emissions sensitivity runs of 1.05 and 0.95 times fire emissions scaled up to equal an 100% perturbation

a) Savanna, grassland, shrub

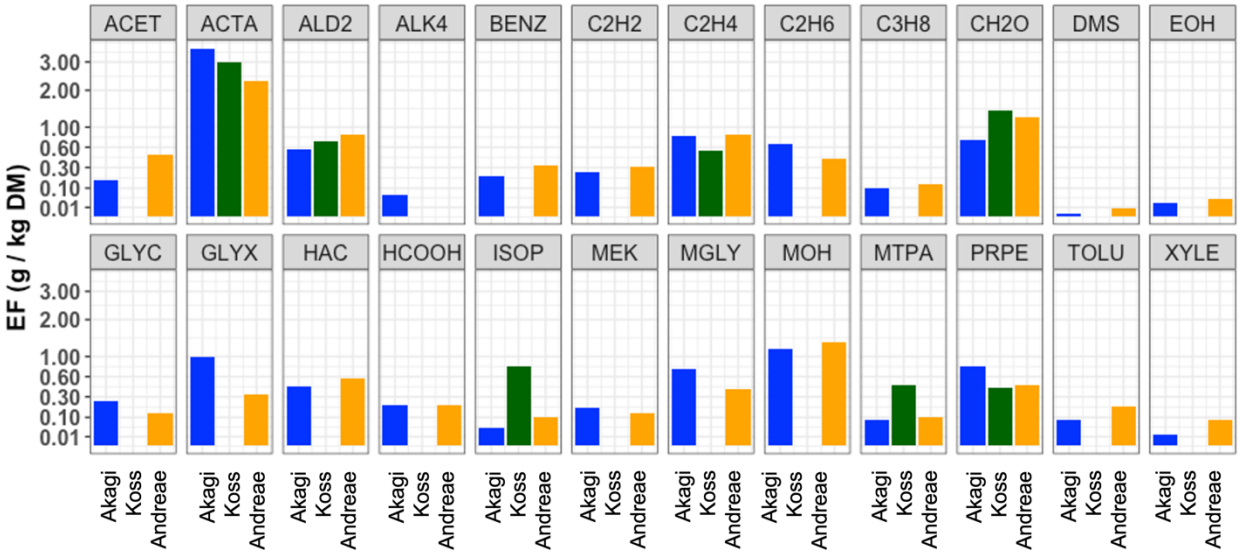

b) Temperate forest

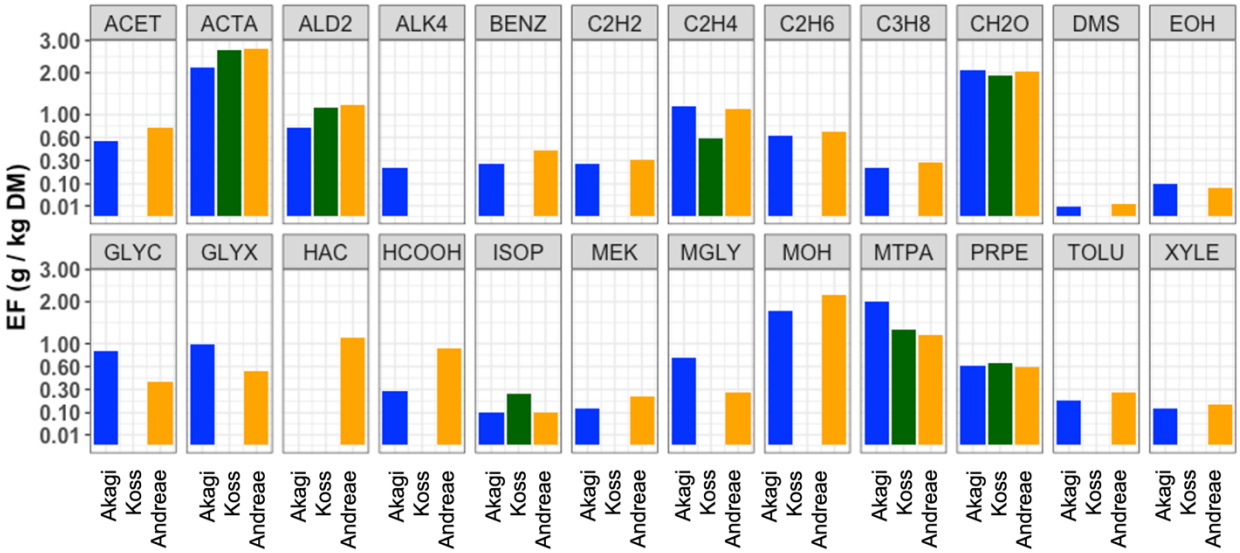

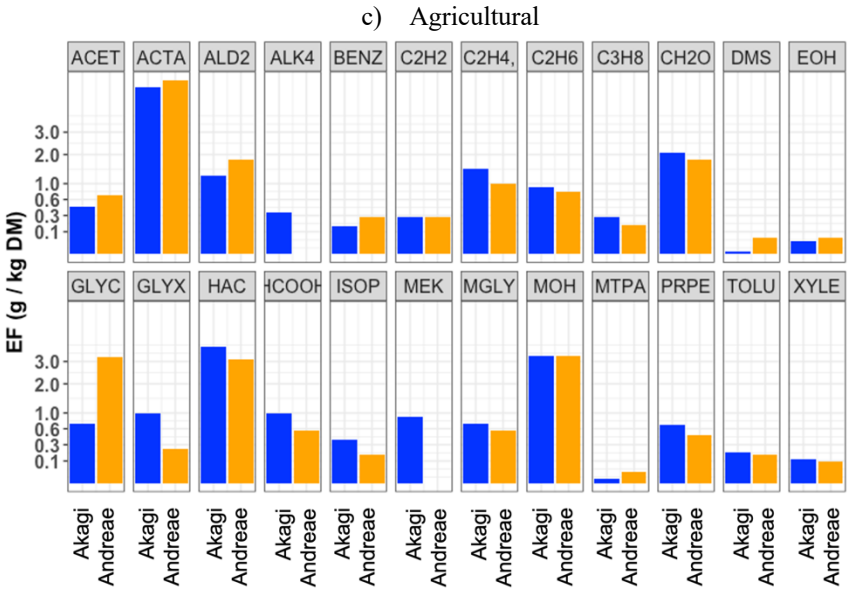

Fig 4.S4: Emission factors of common NMOGs from the Akagi et al. (2011) in dark blue, Koss et al. (2018) in green, and Andreae 2019 paper in orange for a) savanna, grassland, shrub fuel types, b) temperate forests, and c) agricultural fires

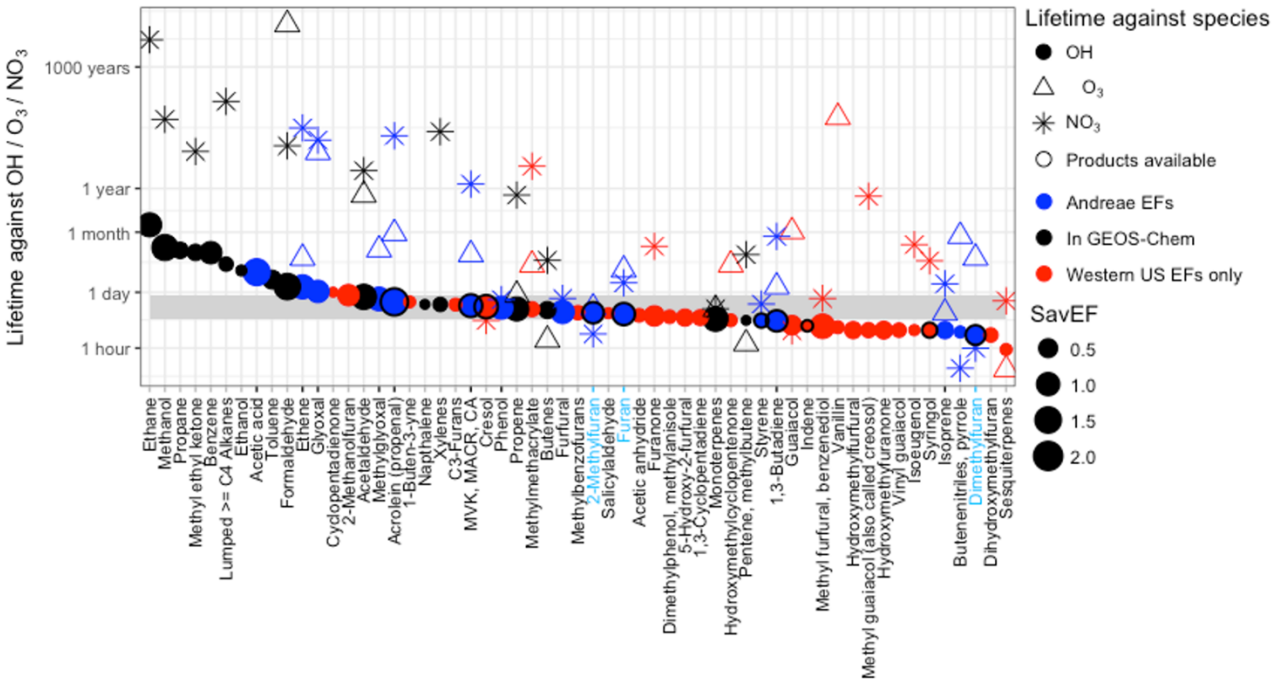

Fig 4.S5: Following Coggon et al. (2019), the species responsible for 95% of OHR in addition to species already represented as emitted from fires in GFED4s in GEOS-Chem are plotted in descending order of their lifetime against OH, NO_3, and O_3. Those already in GEOS-Chem are in black, species not yet in GEOS-Chem but where emissions factors were available in Andreae 2019 are in blue, and species that are only available for western US fuel types from Koss et al. (2018) are in red. The circles are sized by their relative savanna and grassland emission factor in g species / kg DM burned. The grey horizontal box represents an approximate physical lifetime against transport out of a nested 0.5° × 0.625° grid box (~5 hours) and a 2x2.5 grid box (~20 hours).

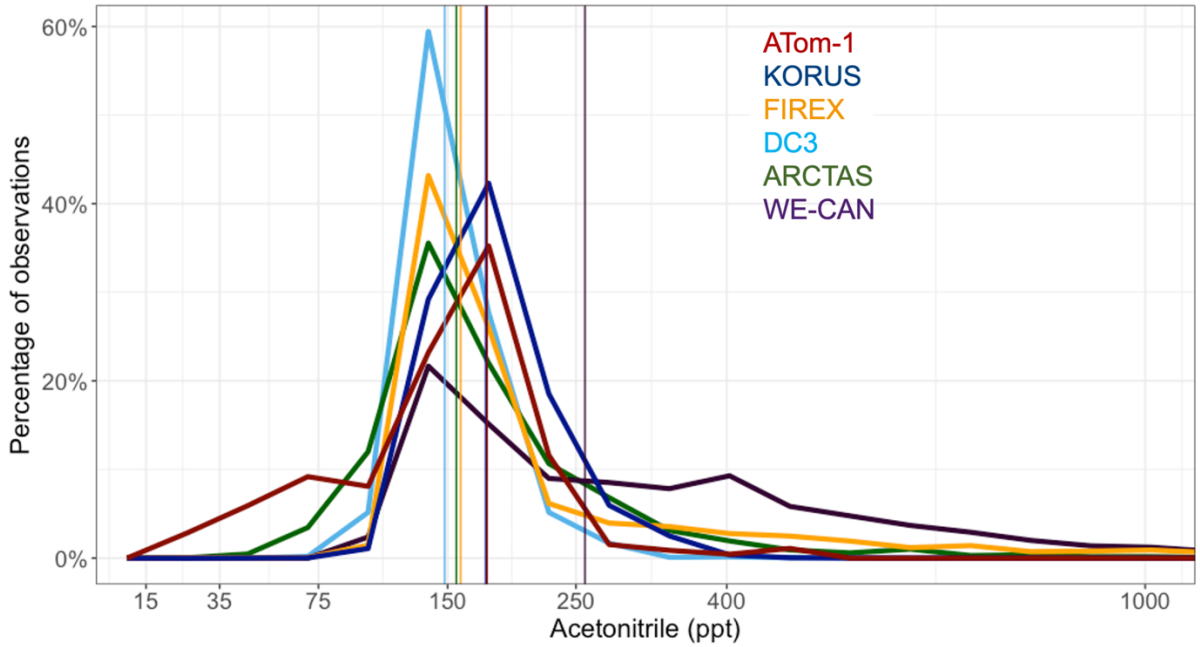

Figure 4.S6: Percentage of observations by their acetonitrile concentrations for the first intensive of ATom from July to August 2016 (dark red), KORUS from April to June 2016 (dark blue), FIREX from July to September 2019 (orange), DC3 in May to June 2012 (light blue), ARCTAS in June to July 2008 (green), and WE-CAN in July to September 2018 (purple).

The Atmospheric Tomography Mission deployment 1 (ATom-1) took place from 29 July to 23 August 2016, originated in Palmsdale, CA, and sampled around the globe, including in the east Atlantic off the coast of Africa. In our analysis, we focus on this area since previous work has documented its fire influence (Travis et al., 2020; Strode et al., 2018), and we include points between 35° N and 50° S and greater than 32° W to focus on this fire outflow region. Table 2 in (Travis et al., 2020) describes the OHR and NMOG measurements used to calculate observed cOHR. We follow the convention established in Travis et al. (2020) of including species in cOHR where at least 20% of possible available measurements below 3km are not missing.

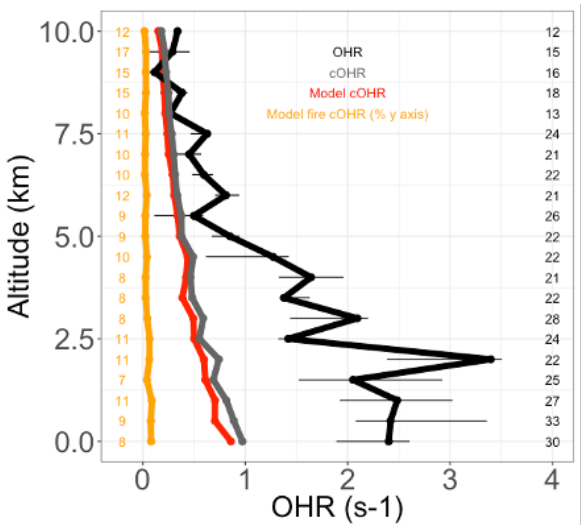

Figure 4.S7: Vertical profile of measured total OHR in black, calculated observed OHR in grey, modeled calculated OHR in red, and modeled calculated OHR from fires in orange. Horizontal bars show the 25th–75th percentile range of measurements in each vertical 0.5-km bin. The number of observations in each bin is shown on the right side of each panel.

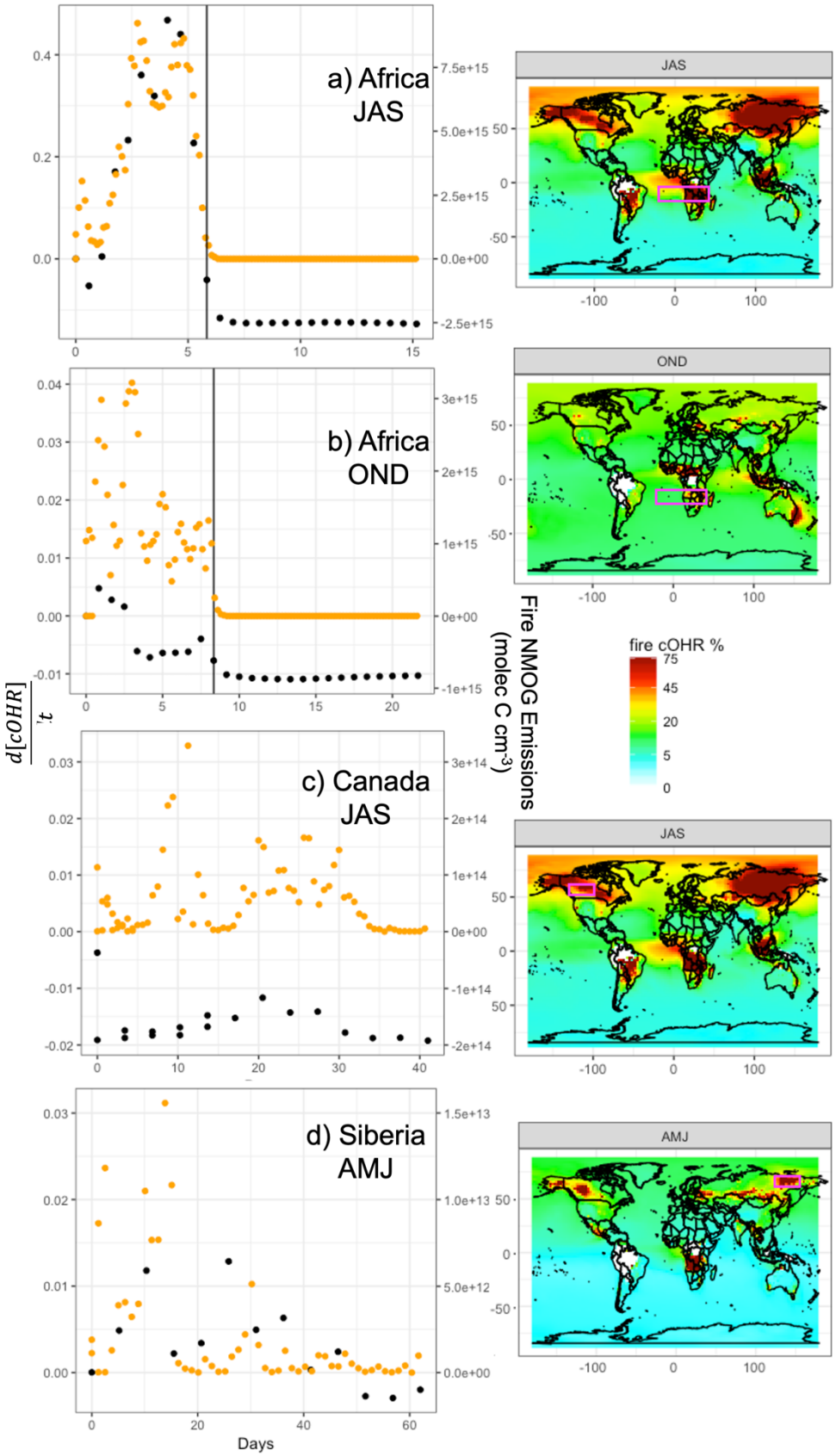
a) Africa JAS
b) Africa OND
c) Canada JAS
d) Siberia AMJ
JAS
OND
JAS
AMJ
fire cOHR %
75
45
20
5
0
Fire NMOG Emissions (molec C cm-3)
d[cOHR]/dt
Days

Figure 4.S8: The simulated decay of cOHR (black) in outflow from fires in (a) Africa during July, August, September (JAS), (b) Africa during October, November, December (OND), (c) Canada in JAS, and (d) Siberia in April, May, June (AMJ). Distance is converted to time using zonal average wind speeds. Fire NMOG emissions are also plotted in orange. For the Africa plots, the approximate Atlantic coastline edge is indicated with a black vertical line. In the right column, we show the seasonal average contribution from fires to cOHR and box the regions of interest in magenta.

Appendix 4. Supplement to Chap. 5: Large mitigation potential of smoke $PM_{2.5}$ in the US from human-ignited wildfires and agricultural fires

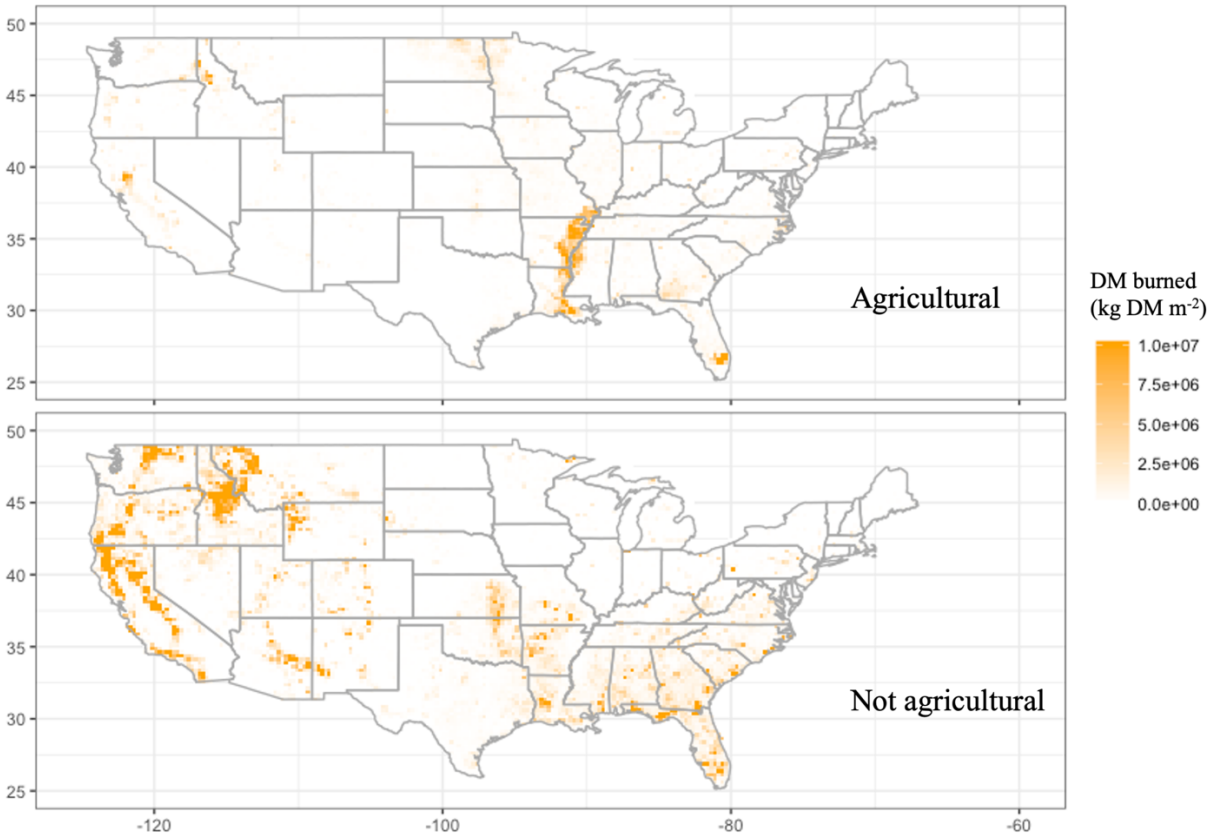

Figure 5.S1. Mean annual dry matter burned from 1997 – 2018 from agriculture (Agricultural) and all other fire types (not agricultural) from GFED4s.

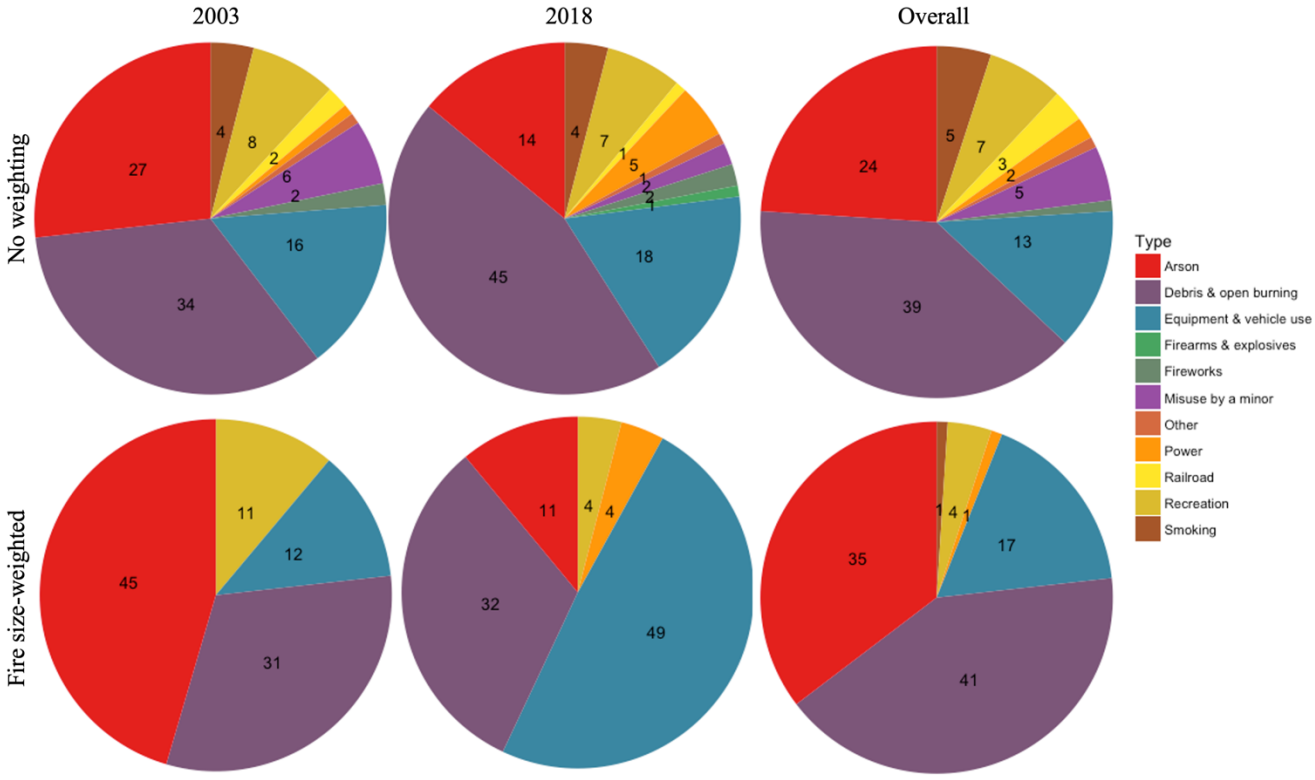

Figure 5.S2. Pie charts for 2003, 2018, and the whole dataset of the contribution of underlying human ignition fire categories without weighting by fire size (top row) and weighted by fire size (bottom row).

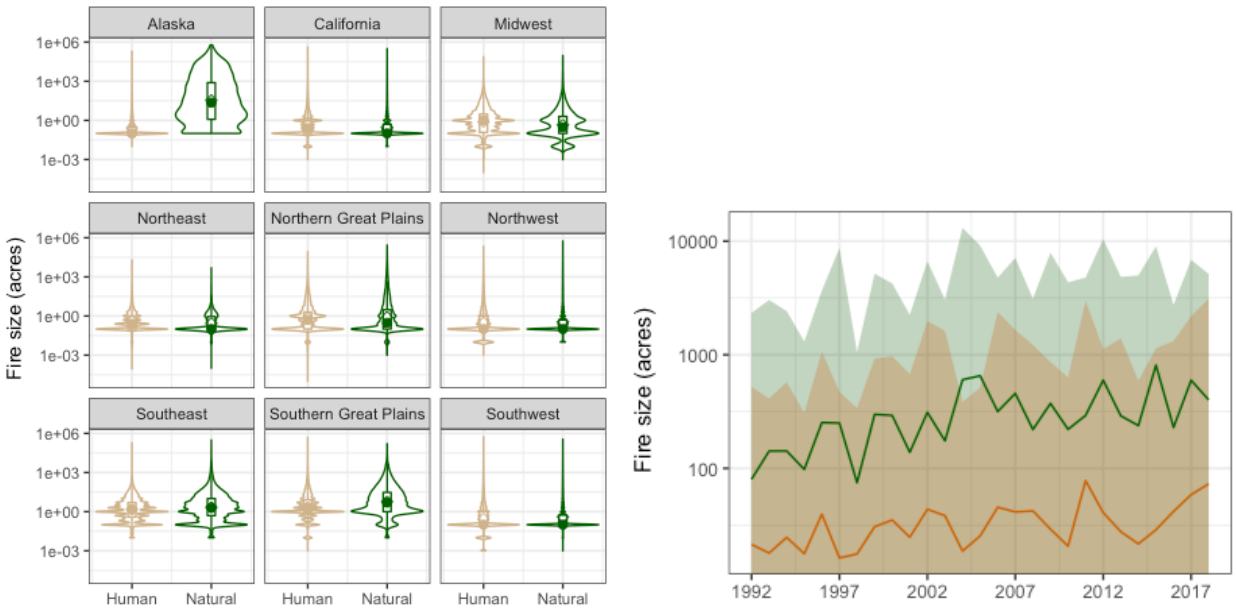

Figure 5.S3. From the FPA-FOD, (left) violin and boxplots of fire size of human (tan) and naturally (green) ignited wildfires by region and (right) annual mean fire size of both fire types from 1992 to 2018 with their standard deviations shown as shaded envelopes.

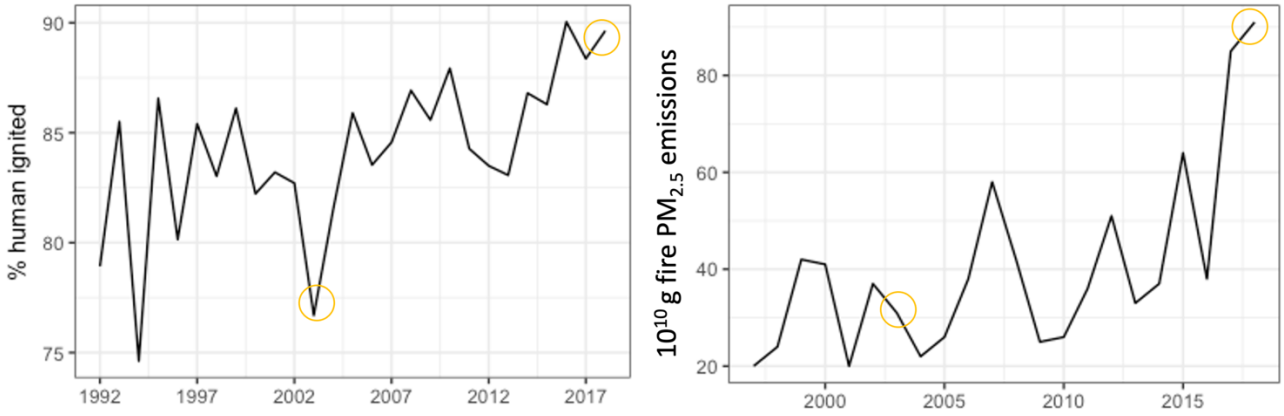

Figure 5.S4. (left) The percentage of fire in the FPA FOD that are human ignited from 1992 to 2018 and (right) fire $PM_{2.5}$ emissions in CONUS from GFED4s from 1997 to 2018. 2003 and 2018 are circled as representative low (high) human-ignition and low (high) fire emission for 2003 and 2018, respectively.

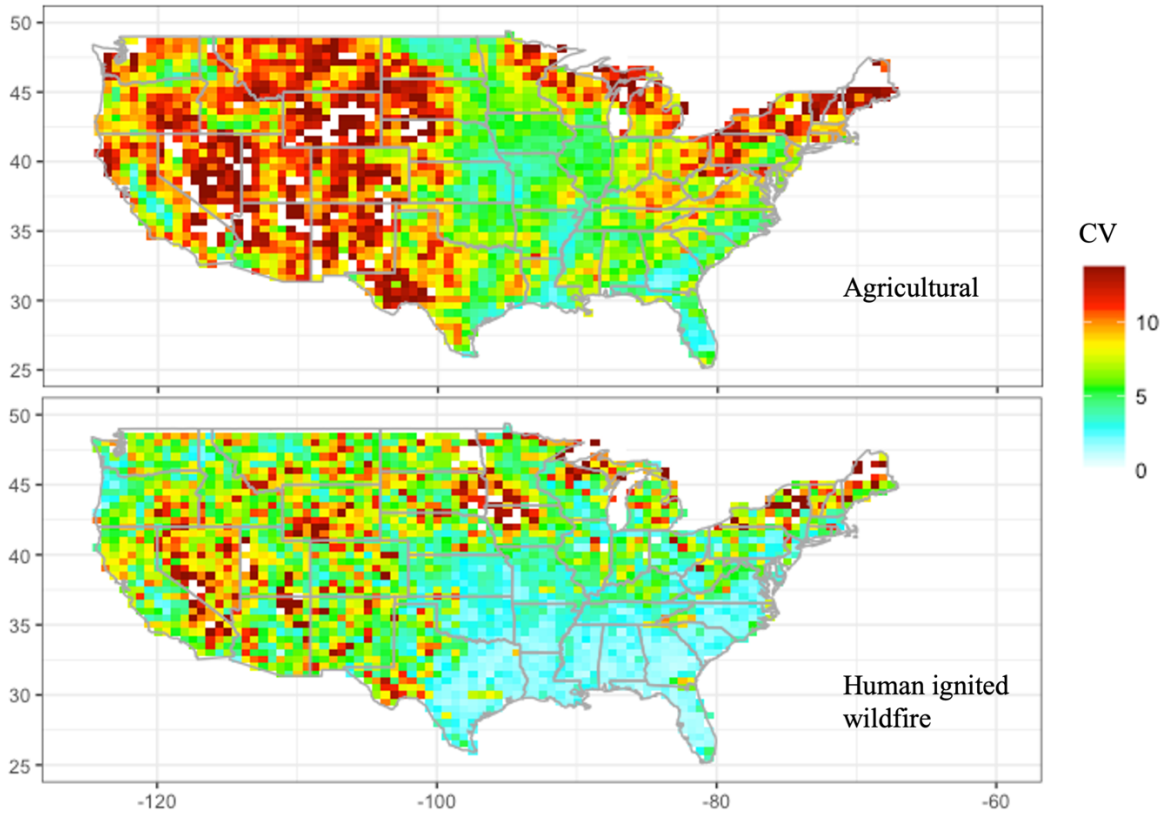

Figure 5.S5. The coefficient of variation (CV) of agricultural fire $PM_{2.5}$ emissions (top) and human-ignited wildfire $PM_{2.5}$ emissions (bottom) from 2003 – 2018. Coefficient of variation is

defined as the standard deviation of a quantity divided by the mean, which is a statistical measure of the relative dispersion of the dataset about the mean.

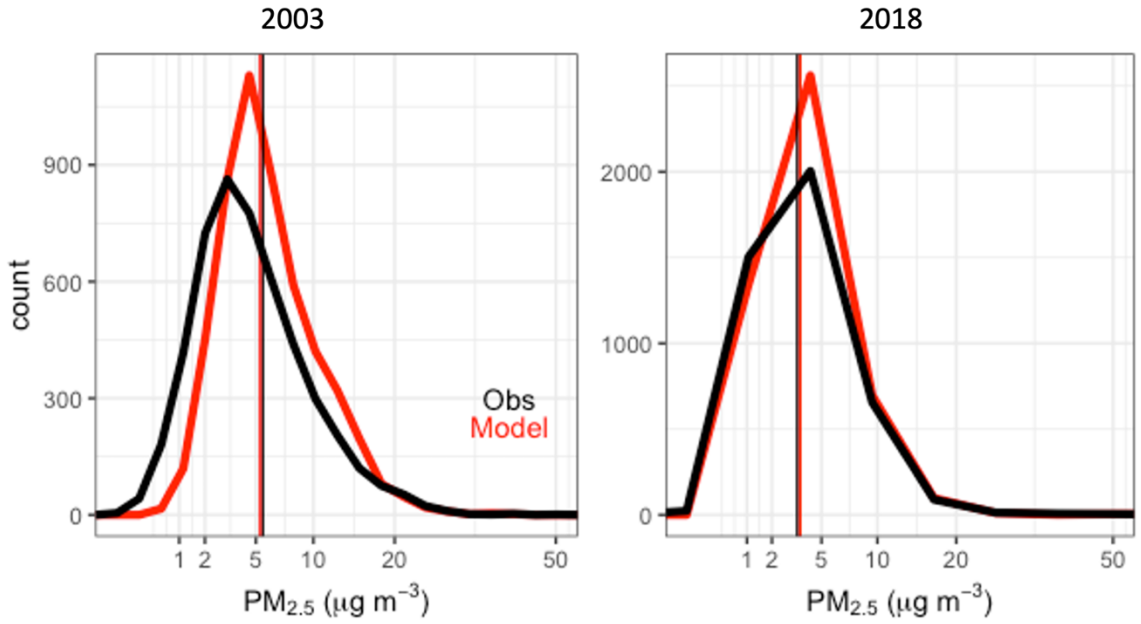

Figure 5.S6. Probability distribution functions of modelled (red) and observed (black) $PM_{2.5}$ at CONUS IMPROVE sites in 2003 and 2018. Vertical lines show the medians.

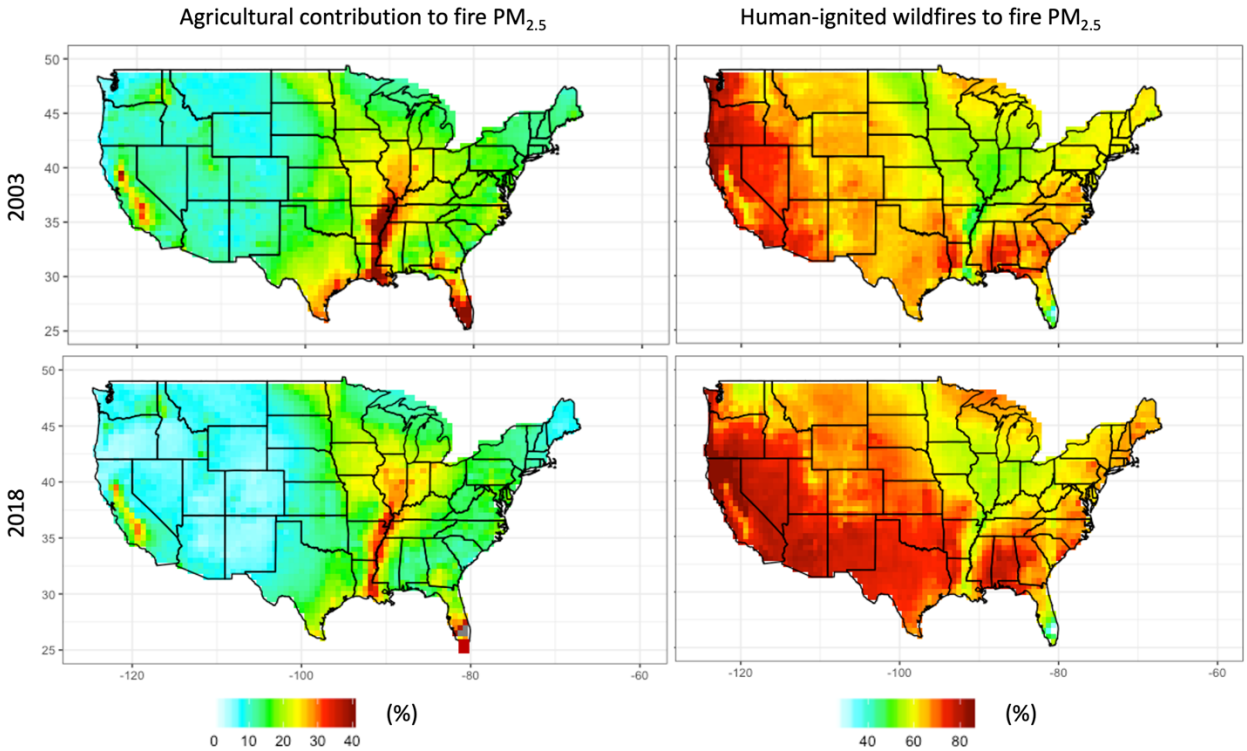

Figure 5.S7: Annual mean contribution of agricultural fires (left) and human-ignited wildfires (right) to fire $PM_{2.5}$ for 2003 (top) and 2018 (bottom).

Figure 5.S8: The percentage of grid box days where human-ignited wildfire $PM_{2.5}$ by itself exceeds the EPA daily standard of 35 µg m^{-3} in dark red ("Fire Alone") and where it combines with other sources of $PM_{2.5}$ to exceed that standard in pink ("In Combo") in 2003 (top) and 2018 (bottom). Note that the two panels have different y axes.

	Average annual % of fire $PM_{2.5}$		**Max annual % of fire $PM_{2.5}$**		**Average annual % of total $PM_{2.5}$**		**Max annual % of total $PM_{2.5}$**	
Year	*2003*	*2018*	*2003*	*2018*	*2003*	*2018*	*2003*	*2018*
Agricultural fires	17	13	100	100	0.42	0.51	87	94
Human ignited wildfires	67	70	100	100	3	6	99.7	100

Table 5.S1. Average and max percent contribution of agricultural fires and human ignited wildfires to fire and total $PM_{2.5}$ concentrations in CONUS in 2003 and 2018 per grid box.

Region	**Agricultural fires (µg m^{-3})**		**Human-ignited wildfires (µg m^{-3})**		**Lightning-ignited wildfires (µg m^{-3})**		**Non-fire (µg m^{-3})**		**% human levers of total**	
Year	*2003*	*2018*	*2003*	*2018*	*2003*	*2018*	*2003*	*2018*	*2003*	*2018*
Northwest	0.033	0.033	0.48	1.62	0.11	0.72	4.71	3.22	10	29

Northern Great Plains	0.033	0.042	0.25	0.64	0.51	0.43	5.03	2.91	5	17
Midwest	0.049	0.046	0.21	0.32	0.12	0.14	11.09	5.98	2	6
California	0.050	0.066	0.59	3.38	0.009	0.034	8.96	4.85	7	41
Northeast	0.019	0.023	0.14	0.24	0.084	0.076	13.13	6.93	1	4
Southwest	0.017	0.025	0.11	0.53	0.053	0.25	5.57	3.58	2	13
Southern Great Plains	0.057	0.032	0.47	0.21	0.028	0.037	8.97	4.97	6	5
Southeast	0.12	0.06	0.22	0.26	0.034	0.058	10.99	5.61	3	5
CONUS	0.057	0.04	0.27	0.68	0.073	0.12	10.0	5.49	3	11

Table 5.S2. Component concentrations and percentages associated with the annual average population-weighted exposure in eight regions and CONUS in 2003 and 2018 shown in Fig. 4.

Premature mortality from $PM_{2.5}$ (95% CI)	**Ag fires**	**Human-ignited wildfires**	**Fires**	**Human lever % of fire $PM_{2.5}$**	**Human lever % of total $PM_{2.5}$**
2003	1,500 (1,200 – 1,700)	7400 (6100 - 8500)	11,000 (8,900 – 13,100)	81%	3%
2018	1,400 (1,000 – 1,700)	20,000 (14,900 – 24,200)	25,200 (18,700 – 30,600)	85%	10%

Table 5.S3. Premature mortalities associated with agricultural fires, human ignited wildfires, and total fires in 2003 and 2018 and their lower and upper 95% CI and the percentage of fire and total $PM_{2.5}$ associated with human levers.

Model Configuration

We use the GEOS-Chem, a global chemical transport model, (www.geos-chem.org) to simulate $PM_{2.5}$ concentrations in 2003 and 2018 with 6-month spin-up simulations. GEOS-Chem is driven by assimilated meteorology from the Modern-Era Retrospective analysis for Research and Applications, Version 2 (MERRA-2), at the NASA Global Modeling and Assimilation Office (GMAO). We run version 13.3.3 with 47 vertical levels. GEOS-Chem employs SO_4^{2-}–NO_3^-–NH_4^+ thermodynamics (Fountoukis and Nenes, 2007) coupled to an ozone-NO_x-VOC-oxidant chemical mechanism (Mao et al., 2013; Travis et al., 2016; Miller et al., 2017). The simulation of important aerosol species are described in previous work: black carbon (Park et al., 2003); organic carbon (OC), using the simple scheme for SOA (Chin et al., 2002; Cooke et al., 1999; Pai et al., 2020); sulfate, nitrate, and ammonium (Park et al., 2004); sea salt (Jaeglé et al., 2011); and mineral dust (Fairlie, et al., 2007; Ridley et al., 2012). Total organic aerosol mass is calculated using an organic matter to OC ratio of 1.4 for hydrophobic and 2.1 for hydrophilic.

Anthropogenic emissions are from the global CEDS inventory (McDuffie et al., 2020). Biogenic emissions are calculated online using the MEGANv2.1 framework (Guenther et al., 2012).

Health Impact Assessment

We calculate the annual mean $PM_{2.5}$ concentrations associated with all $PM_{2.5}$, all fires, agricultural fires, and human ignited wildfires. Following Freese et al., (2022) and Vohra et al., (2021), we calculate the mortalities due to these changes in $PM_{2.5}$ exposure using the concentration response function (CRF) in Fig. 2 from a recent meta-analysis (Vodonos et al., 2018). For each grid box, we calculate $\bar{\beta}(PM_{2.5})$, the long-term $PM_{2.5}$ concentration response:

$$\bar{\beta}(PM_{2.5}) = \frac{1}{\Delta PM_{2.5}} \int_{PM_{2.5_a}}^{PM_{2.5_b}} \beta(PM'_{2.5}) \delta(PM'_{2.5})$$

Where β is based on Figure 2 in Vodonos et al., (2018) and its value is based on $\Delta PM_{2.5}$, a is the base scenario and b is each fire scenario, and $\Delta PM_{2.5}$ is the annual average $PM_{2.5}$ change between a and b. We also calculate the 95% confidence interval (CI) for $\bar{\beta}(PM_{2.5})$ using the same method and the upper and lower bounds on the 95% CI from Vodonos et al.

We then calculate the incidence, I, for each grid box:

$$I = \frac{exp^{\bar{\beta}\Delta PM_{2.5}} - 1}{exp^{\bar{\beta}\Delta PM_{2.5}}}$$

Based on the change in concentration and incidence, we then calculate the change in all-cause mortality for each grid box:

$$\Delta M = p_{af} I M_0$$

Where p_{af} is the population affected from the Gridded Population of the World (Gridded Population of the World (GPW), v4 | SEDAC, 2022) for all ages, and M_0 is the United States' baseline all-cause mortality from the 2017 Global Burden of Disease Study (GBD 2019 Risk Factors Collaborators, 2020).). We linearly interpolate the gridded UN-adjusted population count dataset, which has a native resolution of 30 arc-seconds and provides population estimates for 2000, 2005, 2010, 2015, and 2020, to 2003 and 2018 and grid the data to the GEOS-Chem nested grid (0.5x0.625°).

Appendix 5. A brief investigation of using fire temperature from a geostationary satellite to parameterize fire volatile organic compound emissions

Recent work has hinted at the ability to use fire temperature as a proxy for NMOG emissions (Sekimoto et al., 2018). They showed that high (> 500 °C) and low-temperature (300 – 500 °C) pyrolysis processes produce NMOGs with different average atmospheric properties (OHR, volatility, etc.) and that this appears consistent across fuel types. We briefly explored this tantalizing possibility, which would potentially improve our diurnal representation of NMOGs. Using GOES-16 observations of fire temperature (Fig. A5.1) did not provide the granularity of information to use this in a global CTM. This may be because the fire dynamics within a given fire do not linearly proceed through the burning stages (i.e., all types of burning can occur simultaneously within a given fire), so a much more sophisticated high resolution fire dynamics model would be needed to implement this idea.

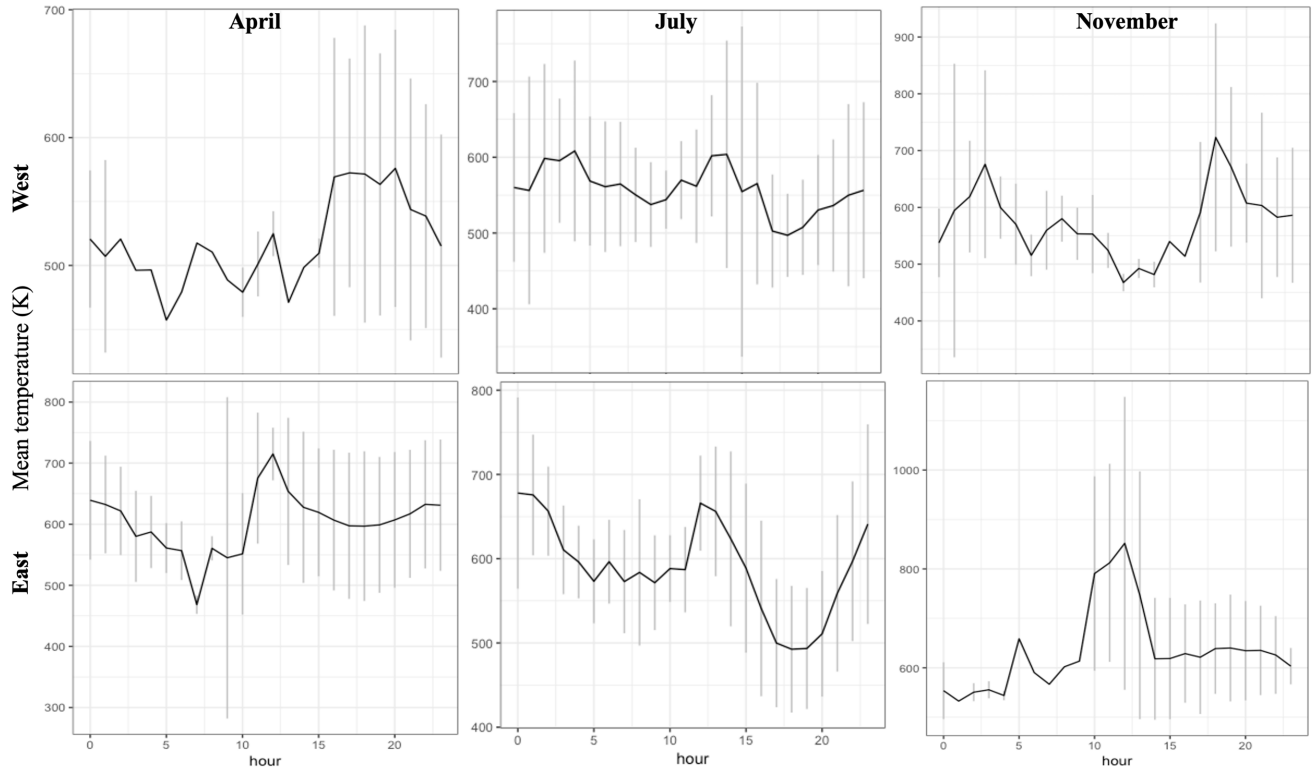

Figure A5.1: Mean fire temperature (in Kelvin) in the western (top) and eastern (bottom) contiguous US in April, July, and November from the Geostationary Operational Environmental Satellite (GOES-16).

As a first check in GEOS-Chem, we ran a sensitivity analysis for the FIREX campaign in summer 2019 where we emitted all NMOGs in the morning. Figure A5.2 shows that, across several species, the timing of emissions does not change the overall shape of the vertical profiles substantially. Very small differences at the surface are observed with propane and formaldehyde.

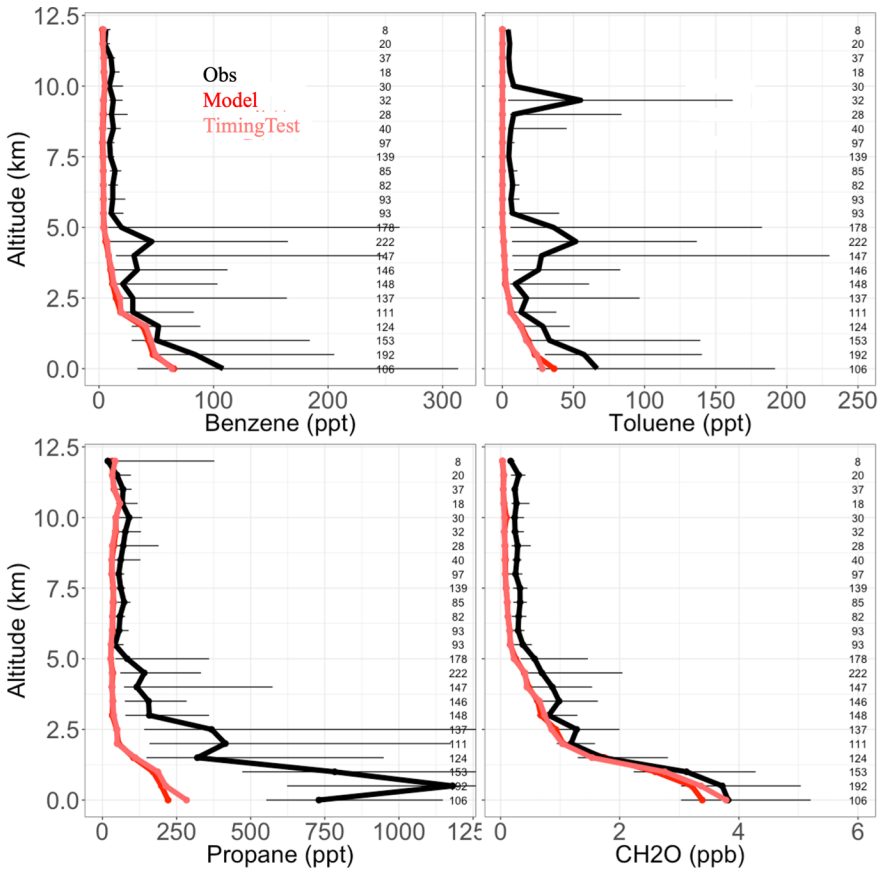

Figure A5.2: Vertical profiles of observed (black) and modeled (red) NMOGs with a sensitivity simulation where all NMOGs are emitted in the morning in pink during the western flights of FIREX in 2019. Horizontal bars show the 25th–75th percentile range of measurements in each vertical 0.5-km bin. The number of observations in each bin is shown on the right side of each panel.